



University  
of Glasgow

Tesson, Mathias Christian Stephane (2013) Copper-dependent enhancement of targeted radiotherapy by combination with the radiosensitiser disulfiram. PhD

<http://theses.gla.ac.uk/4760/>

Copyright and moral rights for this thesis are retained by the author

A copy can be downloaded for personal non-commercial research or study, without prior permission or charge

This thesis cannot be reproduced or quoted extensively from without first obtaining permission in writing from the Author

The content must not be changed in any way or sold commercially in any format or medium without the formal permission of the Author

When referring to this work, full bibliographic details including the author, title, awarding institution and date of the thesis must be given.

Copper-dependent enhancement of targeted  
radiotherapy by combination with the  
radiosensitiser disulfiram

Mathias Christian Stéphane Tesson

A thesis submitted in fulfilment of the requirements for the degree of  
Doctor of Philosophy

College of Medical, Veterinary and Life Sciences,  
Institute of Cancer Sciences,  
University of Glasgow.

November, 2013

## **Declaration**

I am the sole author of this thesis. All references have been consulted by myself in the preparation of this manuscript. Unless otherwise acknowledged, all the work presented in this thesis was performed personally.

## **Dedication**

*À Papa, à Maman, pour le soutien inconditionnel quels que furent mes choix.*

*À Christiane, mon ange-gardien.*

## **Acknowledgments**

The work which forms the basis of this thesis has been carried out at the Radiation Oncology laboratory, Institute of Cancer Research, College of Medical, Veterinary and Life Sciences, University of Glasgow. I am grateful to Molecular Insight Pharmaceuticals, Inc., Cambridge, Massachusetts for supporting this project academically and financially.

I want to thank my supervisor Professor Rob Mairs for providing me with the opportunity of working in his lab, for the enlightening conversations about targeted radiotherapy, for his patience and devotion to improve my literary skills and for the free pints and lunches. I also want to thank my co-workers Sharon and Colin for the feedback on my work.

This thesis would have not been possible without the early teaching from Anne-Marie, Lesley, Annette and Tony. Notably, thank you Tony for introducing me to the wonderful world of combination analyses... I actually love it now! A special mention to Colin Nixon and his team for the support and expertise with histological procedures and to Sue Champion for her patience in teaching radiochemistry to a biologist. Also, statistical analyses were made possible thanks to Dr Wilson Angerson.

Last but not least, I want to thank my partner Jen for the care and daily support but also for introducing me to the clinical world, the endpoint of translational research. And finally, Glad, Caro, Flo and Karyn, thank you for keeping me sane!

# Table of content

Declaration	2
Dedication	3
Acknowledgment	4
Table of content	5
List of tables	13
List of figures	14
Abbreviations	18
Abstract	25

## **1 Introduction.....27**

### **1.1 Radiation, radiotherapy and targeted radiotherapy ....27**

1.1.1 Definition of radiation.....	27
1.1.2 Limitations of external beam radiotherapy of cancer .....	27
1.1.3 Targeted radiotherapy .....	27
1.1.4 Current use of targeted radiotherapy.....	28
1.1.4.1 Na <sup>131</sup> I for the treatment of thyroid conditions.....	28
1.1.4.2 Radionuclides for the treatment of bone metastasis.....	29
1.1.4.3 Radioimmunotherapy of haematopoietic malignancies .....	29
1.1.4.4 Somatostatin analogues for the treatment of neuroendocrine tumours....	30
1.1.4.5 Neuroblastoma .....	30
1.1.4.6 Prostate cancer (PCa) .....	32
1.1.5 The biological effect of IR.....	35
1.1.5.1 The formation of free radicals.....	35
1.1.5.2 Cellular responses to radiation.....	35
1.1.5.2.1 Antioxidant responses .....	36
1.1.5.2.2 Cell cycle regulation in response to radiation .....	37
1.1.5.2.3 DNA damage and DNA repair .....	37
1.1.6 Radiosensitisation .....	38
1.1.7 A strategy to improve targeted radiotherapy.....	41

### **1.2 Disulfiram (DSF).....42**

1.2.1 The nomenclature of DSF and its derivatives .....	42
1.2.2 The origins of DSF.....	43

1.2.3	Alcoholism, DSF and cancer.....	44
1.2.4	The biological targets of DSF .....	44
1.2.4.1	Increasing oxidative stress .....	44
1.2.4.2	The proteasome/NF- $\kappa$ B axis .....	46
1.2.4.3	Is DSF an oxidising agent or an antioxidant? .....	48
1.2.5	DSF acts as an anti-viral agent and as an immunomodulator .....	49
1.2.6	DSF in combination with chemotherapy.....	50
1.2.7	Cancer stem cells and ALDH.....	51
1.2.8	Angiogenesis .....	52
1.2.9	DSF targets cancer cells .....	52
1.2.10	Pharmacology and toxicity of DSF.....	53
1.2.11	Old drugs, new tricks .....	54
1.2.12	Clinical trials involving DSF .....	54
1.2.13	DSF, a radiation modifier.....	55
1.2.13.1	The mixed disulphide theory.....	57
1.2.13.2	Radioprotection .....	57
1.2.13.3	Radiosensitisation .....	58
1.2.13.4	All about scheduling?.....	59
1.2.14	Conclusion .....	60
<b>2</b>	<b>Thesis aims.....</b>	<b>61</b>
<b>3</b>	<b>The Cu-dependent toxicity of DSF to tumour cells grown as monolayers.....</b>	<b>62</b>
<b>3.1</b>	<b>Introduction.....</b>	<b>62</b>
3.1.1	The cytotoxic activity of DSF is imperfectly understood .....	62
3.1.2	The importance of defining the concentration-effect relationship of DSF on the basis of pharmacological laws. ....	64
<b>3.2</b>	<b>Aims.....</b>	<b>65</b>
<b>3.3</b>	<b>Materials and methods.....</b>	<b>65</b>
3.3.1	Cell culture .....	65
3.3.2	Drugs and drugs treatments.....	65
3.3.3	Viability assay .....	66

3.3.4	Clonogenic assay.....	66
3.3.5	The median effect principle .....	67
3.3.6	Absorbance measurement .....	68
3.3.7	Proteasome assay .....	68
3.3.8	Fluorescence-activated cell sorting (FACS) analysis of the cell cycle .....	68
3.3.9	Statistical analysis .....	69
<b>3.4</b>	<b>Results .....</b>	<b>69</b>
3.4.1	The biphasic response profile of DSF.....	69
3.4.2	The effect of the molar ratio of DSF or DETC to Cu on the cytotoxicity of DSF and DETC .....	70
3.4.3	The chelation of Cu by DSF and DETC .....	73
3.4.4	The determination of the dose-response relationship of DSF in the presence or in the absence of Cu .....	77
3.4.5	Proteasome activity .....	79
3.4.6	Cell cycle.....	81
<b>3.5</b>	<b>Discussion and summary of the results .....</b>	<b>82</b>
<b>4</b>	<b>The radiosensitising effect of DSF:Cu .....</b>	<b>88</b>
<b>4.1</b>	<b>Introduction.....</b>	<b>88</b>
4.1.1	Assessing the efficacy of the combination of drugs with radiation .....	88
4.1.2	The linear-quadratic model .....	89
4.1.3	Isobologram and combination index methods of synergy analysis .....	90
<b>4.2</b>	<b>Aims.....</b>	<b>91</b>
<b>4.3</b>	<b>Materials and methods.....</b>	<b>91</b>
4.3.1	Tissue culture .....	91
4.3.2	$\gamma$ -radiation treatment .....	91
4.3.3	Clonogenic assay.....	91
4.3.4	The linear-quadratic model .....	91
4.3.4.1	The linear-quadratic equation .....	91
4.3.4.2	Calculation of the IC <sub>50</sub> .....	92
4.3.4.3	Calculation of DEF .....	93
4.3.4.4	Drug treatment .....	93
4.3.5	The median effect principle .....	93

4.3.6	Isobologram analysis.....	94
4.3.6.1	Mode I isobologram analysis .....	94
4.3.6.2	Mode II isobologram analysis.....	94
4.3.6.3	Determination and interpretation of the isoeffect points.....	96
4.3.6.4	Drug treatment .....	98
4.3.7	Combination index analysis .....	98
4.3.7.1	Combination index analysis .....	98
4.3.7.2	Drug treatment .....	100
<b>4.4</b>	<b>Results .....</b>	<b>101</b>
4.4.1	Mathematical modelling of the effect of $\gamma$ -radiation as a single agent using the linear-quadratic model .....	101
4.4.2	Determination of the radiosensitising effect of disulfiram using the linear-quadratic model.....	101
4.4.2.1	The effect of DSF:Cu on the survival of $\gamma$ -irradiated SK-N-BE(2c) clonogens .....	102
4.4.2.2	The effect of DSF on the survival of SK-N-BE(2c) clonogens following $\gamma$ -radiation treatment.....	102
4.4.2.3	The effect of DSF:Cu on the survival of UVW/NAT clonogens following $\gamma$ -radiation treatment.....	103
4.4.2.4	The effect of DSF on the survival of UVW/NAT clonogens following $\gamma$ -radiation treatment .....	104
4.4.2.5	Conclusions .....	105
4.4.3	Determination of the nature of the radiosensitising effect of DSF:Cu and DSF	105
4.4.3.1	Isobologram analysis.....	106
4.4.3.1.1	Isobologram analysis of DSF:Cu or DSF in combination with $\gamma$ -radiation in SK-N-BE(2c) cells.....	106
4.4.3.1.2	Isobologram analysis of DSF:Cu and DSF in combination with $\gamma$ -radiation in UVW/NAT cells .....	109
4.4.3.2	Combination index analysis .....	111
4.4.3.2.1	Combination index analysis of DSF:Cu in combination with $\gamma$ -radiation in SK-N-BE(2c) cells.....	111
4.4.3.2.2	The combination index analysis of DSF in combination with $\gamma$ -radiation in SK-N-BE(2c) cells.....	112

4.4.3.2.3	The combination index analysis of DSF:Cu in combination with $\gamma$ -radiation in UVW/NAT cells .....	113
4.4.3.2.4	The combination index analysis of DSF in combination with $\gamma$ -radiation in UVW/NAT cells .....	114
4.4.3.3	Conclusions .....	115
<b>4.5</b>	<b>Discussion.....</b>	<b>116</b>
<b>5</b>	<b>A hypothesised mechanism for the radiosensitisation induced by DSF:Cu.....</b>	<b>124</b>
<b>5.1</b>	<b>Introduction.....</b>	<b>124</b>
<b>5.2</b>	<b>Aims.....</b>	<b>124</b>
<b>5.3</b>	<b>Materials and methods .....</b>	<b>125</b>
5.3.1	Tissue culture .....	125
5.3.2	$\gamma$ -radiation treatment .....	125
5.3.3	Serum starvation.....	125
5.3.4	DSF:Cu treatment in combination with $\gamma$ -radiation .....	125
5.3.5	Cell cycle analysis.....	125
5.3.6	Statistical analysis .....	126
<b>5.4</b>	<b>Results .....</b>	<b>126</b>
5.4.1	The effect of serum starvation on cell cycle distribution.....	126
5.4.2	Cell cycle arrest in response to $\gamma$ -radiation treatment .....	127
5.4.3	The effect of DSF:Cu on G2 arrest following $\gamma$ -radiation treatment .....	128
<b>5.5</b>	<b>Discussion.....</b>	<b>132</b>
<b>6</b>	<b>Characterisation of multicellular tumour spheroids (MTS) for the study of combination treatments .....</b>	<b>135</b>
<b>6.1</b>	<b>Introduction.....</b>	<b>135</b>
6.1.1	Spheroids.....	135
6.1.2	Considerations for targeted radiotherapy .....	136
6.1.3	A mathematical approach to the quantification of spheroid growth delay ....	137
<b>6.2</b>	<b>Aims.....</b>	<b>137</b>

<b>6.3</b>	<b>Materials and methods .....</b>	<b>137</b>
6.3.1	Spheroid initiation.....	137
6.3.2	DSF:Cu treatment .....	138
6.3.3	Spheroid volume measurement.....	138
6.3.4	Calculation of the growth delay ( $\tau_2$ ) and the doubling time (DT) .....	138
6.3.5	Calculation of the area under the curve (AUC) .....	140
6.3.6	Statistical analysis .....	140
6.3.7	Regression analysis .....	141
6.3.8	Immunocytochemistry.....	141
6.3.9	Pimonidazole treatment.....	141
6.3.10	Staining of pimonidazole adducts .....	142
6.3.11	Heamatoxylin and eosin.....	142
<b>6.4</b>	<b>Results .....</b>	<b>142</b>
6.4.1	The morphology of spheroids is dependent on their size.....	142
6.4.2	Spheroid growth rate is dependent on initial size .....	146
6.4.2.1	LNCaP.....	146
6.4.2.2	SK-N-BE(2c).....	148
6.4.2.3	UVW/NAT.....	149
6.4.3	Determination of the dose-response relationship using the spheroid model..	151
6.4.4	The influence of spheroid size on DSF:Cu cytotoxicity .....	154
6.4.5	The effect of confluency on DSF:Cu cytotoxicity.....	156
<b>6.5</b>	<b>Discussion/summary of the results.....</b>	<b>161</b>
<b>7</b>	<b>The enhancement of the effect of radiopharmaceuticals by DSF:Cu.....</b>	<b>165</b>
<b>7.1</b>	<b>Introduction.....</b>	<b>165</b>
7.1.1	Study model .....	166
<b>7.2</b>	<b>Aims.....</b>	<b>166</b>
<b>7.3</b>	<b>Materials and methods.....</b>	<b>167</b>
7.3.1	Spheroid initiation.....	167
7.3.2	Spheroid treatments.....	167
7.3.2.1	DSF:Cu treatment .....	167

7.3.2.2	$\gamma$ -radiation treatment .....	167
7.3.2.3	Radiopharmaceutical treatment.....	167
7.3.2.4	Combination treatment.....	168
7.3.3	[ <sup>131</sup> I]MIP-1095 uptake.....	168
7.3.4	Protein extraction and quantification .....	168
7.3.5	Spheroid measurement .....	169
7.3.6	Calculation of $\tau_2$ and DT values.....	169
7.3.7	Calculation of AUC values .....	169
7.3.8	Statistical analyses .....	169
7.3.8.1	Statistical analysis of single agent dose-response effects .....	169
7.3.8.2	Statistical analysis of the effect of 2-(phosphonomethyl)pentanedioic acid (PMPA) on the spheroid growth delay induced by [ <sup>131</sup> I]MIP-1095 .....	170
7.3.8.3	Statistical analysis of the potentiation of radiation kill.....	170
7.3.9	Calculation of the combination index CI .....	171
7.3.9.1	Calculation of IC <sub>50</sub> and m parameters.....	171
7.3.9.2	Calculation of the CI value .....	171

## **7.4 Results ..... 172**

7.4.1	The radiosensitising effect of DSF:Cu in combination with $\gamma$ -radiation treatment in LNCaP spheroids .....	172
7.4.2	Determination of the mechanism of [ <sup>131</sup> I]MIP-1095 uptake in LNCaP spheroids .....	175
7.4.3	Determination of PSMA-specific [ <sup>131</sup> I]MIP-1095-induced LNCaP spheroid growth delay.....	178
7.4.4	The effect of DSF:Cu in combination with [ <sup>131</sup> I]MIP-1095 in LNCaP spheroids .....	181
7.4.5	The effect of treatment schedules of DSF:Cu and [ <sup>131</sup> I]MIP-1095 on the growth of LNCaP spheroids.....	182
7.4.6	The effect of DSF:Cu in combination with [ <sup>131</sup> I]mIBG on the growth of SK-N-BE(2c) and UVW/NAT spheroids .....	185
7.4.6.1	The effect of DSF:Cu on the growth of SK-N-BE(2c) and UVW/NAT spheroids	185
7.4.6.2	The effect of [ <sup>131</sup> I]mIBG on the growth of SK-N-BE(2c) and UVW/NAT spheroids	187
7.4.7	The effect of DSF:Cu in combination with [ <sup>131</sup> I]mIBG in SK-N-BE(2c) and UVW/NAT spheroids .....	189

<b>7.5</b>	<b>Discussion and summary of the results .....</b>	<b>191</b>
<b>8</b>	<b>Comparison of the ability of drugs to potentiate the growth delay induced by <math>\gamma</math>-radiation and [<math>^{131}\text{I}</math>]MIP-1095 in spheroids</b>	<b>197</b>
<b>8.1</b>	<b>Introduction.....</b>	<b>197</b>
8.1.1	Nutlin-3 .....	197
8.1.2	Olaparib.....	198
8.1.3	AZD7762 .....	198
8.1.4	Topotecan.....	198
8.1.5	Bortezomib.....	199
8.1.6	Justification of the concentrations of the drugs examined.....	199
<b>8.2</b>	<b>Aim .....</b>	<b>200</b>
<b>8.3</b>	<b>Materials and methods .....</b>	<b>200</b>
8.3.1	Spheroid formation and analysis.....	200
8.3.2	Combined treatments of drugs with $\gamma$ -radiation or [ $^{131}\text{I}$ ]MIP-1095 .....	200
8.3.3	Calculation of specific growth delay SGD .....	200
8.3.4	Statistical analysis of the drug-induced potentiation of $\gamma$ -radiation or [ $^{131}\text{I}$ ]MIP-1095 .....	201
8.3.5	Test for outlying results .....	201
<b>8.4</b>	<b>Results .....</b>	<b>202</b>
8.4.1	Enhancement of the growth delay induced by $\gamma$ -radiation or [ $^{131}\text{I}$ ]MIP-1095	202
8.4.1.1	Nutlin-3 .....	202
8.4.1.2	Olaparib.....	203
8.4.1.3	AZD7762 .....	207
8.4.1.4	Topotecan.....	210
8.4.1.5	Bortezomib.....	213
8.4.2	Comparison of enhancement of [ $^{131}\text{I}$ ]MIP-1095-induced and $\gamma$ -radiation-induced growth delay by drugs .....	216
<b>8.5</b>	<b>Discussion and summary of the results .....</b>	<b>217</b>

<b>9</b>	<b>Summary and future work .....</b>	<b>223</b>
<b>10</b>	<b>Appendix .....</b>	<b>226</b>
<b>11</b>	<b>List of references .....</b>	<b>227</b>

## List of tables

Table 1 DNA metabolism-targeting drugs used in anti-cancer therapy.....	41
Table 2 The pro- and anti-oxidative properties of DSF and its derivatives.....	49
Table 3 Clinical trials investigating DSF as an anti-cancer therapeutic .....	55
Table 4 The conflicting literature on the modification of the radiation effect by DSF and DETC .....	56
Table 5 The interpretation of the combination index (CI) according to Chou <sup>214</sup> .....	100
Table 6 Experimental design of the combination treatment intensities in combination index analysis.....	100
Table 7 Comparison between DEF, isobologram analysis and combination index analysis for the evaluation of the interaction between DSF:Cu or DSF with $\gamma$ -radiation.....	118
Table 8 The $\tau_2$ , DT and AUC <sub>log</sub> values of the effect of spheroid size on the DSF:Cu- induced spheroid growth delay .....	156
Table 9 Summary of the metabolic characteristics of spheroids at day 0 and at day 21 ...	162
Table 10 The $\tau_2$ , DT and AUC <sub>log</sub> values from Figure 61 .....	180
Table 11 The plasma concentrations of the evaluated drugs .....	200
Table 12 Critical Z values at the 1%, 2.5% and 5% levels of significance for dataset containing n observations.....	202

## List of figures

Figure 1 The chemical structures of meta-iodobenzylguanidine (mIBG) and noradrenaline .....	32
Figure 2 The chemical structures of PSMA-targeting compounds.....	35
Figure 3 The chemical reactions of the conversion of superoxide to hydrogen peroxide by SOD.....	36
Figure 4 The chemical structures of the dithiocarbamate family members .....	43
Figure 5 The Fenton reaction using $\text{Fe}^{2+}$ as an electron donor .....	45
Figure 6 The non-enzymatic conversion of DSF to DETC by glutathione (GSH), adapted from Nagendra et al. (1991) <sup>119</sup> .....	46
Figure 7 The two-mechanisms hypothesis of the particular concentration-effect of DSF ..	63
Figure 8 The biphasic response of SK-N-BE(2c) clonogens to treatment with DSF .....	70
Figure 9 The effect of ratios of DSF to Cu on the viability of SK-N-BE(2c), UVW/NAT and LNCaP cells.....	71
Figure 10 The effect of ratios of DETC to Cu on the viability of SK-N-BE(2c), UVW/NAT and LNCaP cells.....	72
Figure 11 The absorption spectrum of DETC, Cu, DETC + Cu and $\text{Cu}[\text{DETC}]_2$ .....	73
Figure 12 The requirement of a reducing agent for the formation of the Cu-chelated form of DSF (DSF:Cu) .....	75
Figure 13 The effect of excess DETC or DSF relative to Cu on the formation of $\text{DETC}_2\text{:Cu}$ or DSF:Cu .....	76
Figure 14 DSF:Cu is present in cells exposed to DSF and Cu.....	77
Figure 15 The effect of equimolar concentrations of DSF and Cu (DSF:Cu) on the clonogenic capacity of SK-N-BE(2c) and UVW/NAT cells .....	78
Figure 16 The effect of DSF alone on the clonogenic capacity of SK-N-BE(2c) and UVW/NAT.....	79
Figure 17 The effect of DSF:Cu on the chymotrypsin-like catalytic activity of the proteasome in LNCaP, SK-N-BE(2c) and UVW/NAT cells.....	80
Figure 18 The effect of bortezomib on the chymotrypsin-like catalytic activity of the proteasome in LNCaP, SK-N-BE(2c) and UVW/NAT cells .....	81
Figure 19 The effect of DSF:Cu on the distribution of cells throughout the phases of the cell cycle.....	82
Figure 20 The planar structure of the elesclomol:Cu complex, adapted from Lianming Wu et al. (2011) <sup>229</sup> .....	84

Figure 21 The effect of a radiosensitiser on the survival of clonogens following radiation treatment.....	89
Figure 22 The determination of additivity by mode I, IIa and IIb in the construction of an isobologram at the 50% level of cytotoxicity .....	96
Figure 23 Determination of isoeffect points .....	97
Figure 24 The significance of plotted isoeffect points relative to the envelope of additivity .....	98
Figure 25 The effect of $\gamma$ -radiation on the clonogenic survival of SK-N-BE(2c) and UVW/NAT cells.....	101
Figure 26 The radiosensitising effect of DSF:Cu and DSF in SK-N-BE(2c) cells.....	103
Figure 27 The radiosensitising effect of DSF:Cu and DSF in UVW/NAT cells.....	104
Figure 28 Median effect analysis of the combination of DSF:Cu or DSF with $\gamma$ -radiation in SK-N-BE(2c) cells .....	107
Figure 29 Isobologram analysis of the combination of DSF:Cu or DSF with $\gamma$ -radiation in SK-N-BE(2c) cells .....	108
Figure 30 The effect of imbalance in the contribution of two agents on synergistic interaction.....	109
Figure 31 Median effect analysis of the combination of DSF:Cu or DSF with $\gamma$ -radiation in UVW/NAT cells.....	110
Figure 32 Isobologram analysis of the combination of DSF:Cu or DSF with $\gamma$ -radiation in UVW/NAT cells.....	111
Figure 33 The combination index analysis of the combination of DSF:Cu with $\gamma$ -radiation in SK-N-BE(2c) cells .....	112
Figure 34 The combination index analysis of the combination of DSF with $\gamma$ -radiation in SK-N-BE(2c) cells .....	113
Figure 35 The combination index analysis of the combination of DSF:Cu with $\gamma$ -radiation in UVW/NAT cells .....	114
Figure 36 The combination index analysis of the combination of DSF with $\gamma$ -radiation in UVW/NAT cells.....	115
Figure 37 The effect of the modification of the linear ( $\alpha$ ) or the quadratic ( $\beta$ ) component of radiation cell killing on the survival curve.....	121
Figure 38 Absence of an effect of serum starvation on the distribution of SK-N-BE(2c) and UVW/NAT cells throughout the phases of the cell cycle .....	127
Figure 39 Time-dependency of G2 arrest after $\gamma$ -radiation treatment.....	128

Figure 40 The effect of DSF:Cu on the redistribution of SK-N-BE(2c) cells throughout the phases of the cell cycle following $\gamma$ -radiation treatment.....	129
Figure 41 The effect of DSF:Cu on the redistribution of UVW/NAT cells throughout the phases of the cell cycle following $\gamma$ -radiation treatment.....	130
Figure 42 The effect of DSF:Cu on the redistribution of LNCaP cells throughout the phases of the cell cycle following $\gamma$ -radiation treatment .....	131
Figure 43 The effect of DSF:Cu on the redistribution of HCT116 p53+/+ cells throughout the phases of the cell cycle following $\gamma$ -radiation treatment.....	131
Figure 44 The effect of DSF:Cu on the redistribution of HCT116 p53-/- cells throughout the phases of the cell cycle following $\gamma$ -radiation treatment.....	132
Figure 45 Comparison between $\tau_2$ and DT values for the measure of spheroid growth....	139
Figure 46 Hypoxic core and proliferative outer layer in LNCaP spheroids .....	143
Figure 47 Hypoxic core and proliferative outer layer in SK-N-BE(2c) spheroids .....	144
Figure 48 Hypoxic core and proliferative outer layer in UVW/NAT spheroids.....	146
Figure 49 The effect of the initial volume ( $V_0$ ) on the growth rate of LNCaP spheroids..	147
Figure 50 The effect of the initial volume ( $V_0$ ) on the growth rate of SK-N-BE(2c) spheroids .....	149
Figure 51 The effect of the initial volume ( $V_0$ ) on the growth rate UVW/NAT spheroids. ....	150
Figure 52 The effect of the arbitrary choice of a timepoint on the variability of the surviving fractions.....	152
Figure 53 The calculation of $IC_{50}$ based on $AUC_{linear}$ or $AUC_{log}$ values .....	153
Figure 54 The effect of spheroid size on DSF:Cu-induced growth delay.....	155
Figure 55 The effect of confluency on DSF:Cu-induced toxicity to LNCaP cell monolayers .....	159
Figure 56 The effect of pH on DSF:Cu cytotoxicity in LNCaP monolayers.....	160
Figure 57 The effect of DSF:Cu on the growth of LNCaP spheroids.....	172
Figure 58 The effect of $\gamma$ -radiation on the growth of LNCaP spheroids.....	174
Figure 59 The effect of DSF:Cu on the growth delay induced by $\gamma$ -radiation in LNCaP spheroids. ....	175
Figure 60 The binding and internalisation of [ $^{131}$ I]MIP-1095 to LNCaP spheroids.....	177
Figure 61 The effect of [ $^{131}$ I]MIP-1095 on the growth of LNCaP spheroids .....	179
Figure 62 The effect of DSF:Cu on the growth delay induced by [ $^{131}$ I]MIP-1095 in LNCaP spheroids .....	182

Figure 63 The effect of treatment schedules of DSF:Cu and [ <sup>131</sup> I]MIP-1095 on the growth of LNCaP spheroids .....	184
Figure 64 The effect of DSF:Cu on the growth of SK-N-BE(2c) spheroids .....	185
Figure 65 The effect of DSF:Cu on the growth of UVW/NAT spheroids.....	186
Figure 66 The effect of [ <sup>131</sup> I]mIBG on the growth of SK-N-BE(2c) spheroids.....	187
Figure 67 The effect of [ <sup>131</sup> I]mIBG on the growth of UVW/NAT spheroids.....	188
Figure 68 The effect of DSF:Cu on the growth delay induced by [ <sup>131</sup> I]mIBG in SK-N-BE(2c) spheroids .....	189
Figure 69 The effect of DSF:Cu on the growth delay induced by [ <sup>131</sup> I]mIBG in UVW/NAT spheroids .....	190
Figure 70 Spheroid growth delay induced by treatment with $\gamma$ -radiation, [ <sup>131</sup> I]MIP-1095 or nutlin-3 as single agents or in combination.....	203
Figure 71 Absence of enhancement of $\gamma$ -radiation-induced spheroid growth delay by combined treatment with olaparib.....	205
Figure 72 Spheroid growth delay induced by treatment with [ <sup>131</sup> I]MIP-1095 or olaparib as single agents or in combination.....	206
Figure 73 Absence of enhancement of $\gamma$ -radiation-induced spheroid growth delay by combined treatment with AZD7762 .....	208
Figure 74 Absence of enhancement of [ <sup>131</sup> I]MIP-1095-induced spheroid growth delay by combined treatment with AZD7762 .....	209
Figure 75 Spheroid growth delay induced by treatment with $\gamma$ -radiation or topotecan as single agents or in combination.....	211
Figure 76 Spheroid growth delay induced by treatment with [ <sup>131</sup> I]MIP-1095 or topotecan as single agents or in combination.....	212
Figure 77 Absence of enhancement of $\gamma$ -radiation-induced spheroid growth delay by combined treatment with bortezomib.....	213
Figure 78 Spheroid growth delay induced by treatment with [ <sup>131</sup> I]MIP-1095 or bortezomib as single agents or in combination .....	215
Figure 79 Comparison of the enhancement of $\gamma$ -radiation-induced or [ <sup>131</sup> I]MIP-1095-induced the growth delay by radiosensitising drugs .....	217
Figure 80 An example of the FACS analysis carried out using FlowJo software .....	226

## Abbreviations

°C	degree centigrade
-SH	thiol group
3-D	3-dimensionnal
<sup>32</sup> P	phosphorous-32
<sup>60</sup> Co	cobalt-60
<sup>89</sup> Sr	strontium-89
<sup>90</sup> Y	yttrium-90
<sup>111</sup> In	indium-111
<sup>123</sup> I	iodine-123
[ <sup>123</sup> I]mIBG	iodine-123-labelled meta-iodobenzylguanidine
[ <sup>123</sup> I]MIP-1095	iodine-123-labelled (S)-2-(3-((S)-1-carboxy-5-(3-(4-iodophenyl)ureido)pentyl)ureido) pentanedioic acid
[ <sup>123</sup> I]MIP-1072	iodine-123-labelled (S)-2-(3-((S)-1-carboxy-5-((4-iodobenzyl)amino)pentyl)ureido) pentanedioic acid
<sup>131</sup> I	iodine-131
[ <sup>131</sup> I]mIBG	iodine-131-labelled meta-iodobenzylguanidine
[ <sup>131</sup> I]MIP-1095	iodine-131-labelled (S)-2-(3-((S)-1-carboxy-5-(3-(4-iodophenyl)ureido)pentyl)ureido) pentanedioic acid
[ <sup>131</sup> I]MIP-1072	iodine-131-labelled (S)-2-(3-((S)-1-carboxy-5-((4-iodobenzyl)amino)pentyl)ureido) pentanedioic acid
<sup>153</sup> Sm	samarium-153
<sup>186</sup> Re	renium-186
<sup>210</sup> Po	polonium-210
<sup>223</sup> Ra	radium-223
α-	alpha
ABS	absolute value
A <sub>x</sub>	absorbance at x nm
ADH	alcohol dehydrogenase
ADP	adenosine diphosphate
ADT	androgen deprivation therapy
AKT	protein kinase B
ALDH	aldehyde dehydrogenase
ANOVA	analysis of variance

AR	androgen receptor
Asc ac	ascorbic acid
ATM	ataxia telangiectasia mutated
ATP	adenosine triphosphate
ATR	ATM- and rad3-related
AU	arbitrary unit
AUC	area under the curve
β-	beta-
BCL	B-cell lymphoma 2
BCPD	bathocuproine disulfonate
BER	base excision repair
BSO	buthionine sulfoximine
CASP3	caspase 3
CCNU	1-(2-chloroethyl)3-cyclohexyl-1-nitrosourea
CD	cluster of differentiation
CDC	cell division cycle
CDK	cyclin-dependent kinase
Cd	cadmium
CFU	colony forming unit
Chk1/2	checkpoint kinase 1/2
CHQ	chloroquine
CI	combination index
Cl	chloride
cm	centimetre
CO <sub>2</sub>	carbon dioxide
CPM	count per minute
CRPC	castrate-resistant prostate cancer
CSC	cancer stem cell
Cu	copper
Cu[DETC] <sub>2</sub>	disulfiram copper complex (Section 3.3.2)
CV	coefficient of variation
Δ	discriminant of a quadratic equation
d	diameter
D	dose
DAB	3,3'-diaminobenzidine

D $\beta$ H	dopamine- $\beta$ -hydroxylase
DEF <sub>x</sub>	dose enhancement factor at the x% toxicity level
DER	disulfiram-ethanol reaction
DETC	diethyldithiocarbamate
DETC <sub>2</sub> :Cu	diethyldithiocarbamate copper complex (Section 3.3.2)
DMEM	Dulbecco's modified Eagle medium
DMI	desipramine
DMSO	dimethyl sulfoxide
DNA	deoxyribonucleic acid
DNA-PK	DNA-dependent protein kinase
DOTA	1,4,7,10-tetraazacyclododecane-1,4,7,10-tetra-acetic acid
DRI	dose reduction index
DSB	double-strand break
DSF	disulfiram
DSF:Cu	disulfiram copper complex (Section 3.3.2)
DT	doubling time
DTPA	diethylene triamine penta-acetic acid
EDTA	ethylene diamine tetraacetic acid
EBRT	external beam radiotherapy
EFS	event-free survival
exp	exponential
f <sub>a</sub>	affected fraction
FACS	fluorescence-activated cell sorting
FCS	foetal calf serum
Fe	iron
f <sub>u</sub>	unaffected fraction
FDA	food and drug administration
FGF	fibroblast growth factor
FW	formula weight
$\gamma$	gamma-
g	gravitational acceleration or gram according to context
GD2	disialoganglioside
GM-CSF	Granulocyte-macrophage colony-stimulating factor
GR	glutathione reductase
GSH	reduced glutathione

GSSG	oxidised glutathione
Gy	gray
h	hour
H•	hydrogen radical
H&E	haematoxylin and eosin
H <sub>2</sub> O <sub>2</sub>	hydrogen peroxide
HBSS	Hank's balanced salt solution
HDR	high dose rate
HIV	human immunodeficiency virus
HO•	hydroxyl radical
HR	homologous recombination
hu	humanised
IAP	inhibitor of apoptosis
IBM	international business machine
IC <sub>x</sub>	x% inhibitory concentration
IκB	NF-κB inhibitor
IL	interleukin
IMRT	intensity-modulated radiotherapy
INRG	international neuroblastoma risk group
INSS	international neuroblastoma staging system
IR	ionising radiation
KCN	potassium cyanide
K <sub>d</sub>	dissociation constant
kg	kilogram
K <sub>i</sub>	50% inhibitory constant
LDR	low dose rate
log	logarithm base 10
ln	logarithm base <i>e</i>
m	coefficient of sigmoidicity
M	molar
MATIN	<u>m</u> IBG and <u>t</u> opotecan in <u>n</u> euroblastoma clinical trial
MBq	megabecquerel
MDM2	mouse double-minute 2
MEF	mouse embryo fibroblast
MEM	minimum essential medium

mg	milligram
mM	millimolar
mIBG	meta-iodobenzylguanidine
min	minute
MIP-1072	(S)-2-(3-((S)-1-carboxy-5-((4-iodobenzyl)amino)pentyl)ureido)pentanedioic acid
MIP-1095	(S)-2-(3-((S)-1-carboxy-5-(3-(4-iodophenyl)ureido)pentyl)ureido)pentanedioic acid
MMP	matrix metalloproteinase
mol	mole
MTS	multicellular tumour spheroids
MTT	3-(4,5-Dimethylthiazol-2-yl)-2,5-diphenyltetrazolium
MYCN	myelocytomatosis viral related oncogene neuroblastoma
n	number of observation
N/A	non applicable
Na	sodium
NAAG	N-acetylaspartylglutamate
NAALADase	N-acetylated $\alpha$ -linked acidic dipeptidase
NAC	N-acetyl cysteine
NAD <sup>+</sup>	nicotinamide adenine dinucleotide (oxidised)
NADP <sup>+</sup>	nicotinamide adenosine di-nucleotide phosphate (oxidised)
NADPH	nicotinamide adenosine di-nucleotide phosphate (reduced)
NAT	noradrenaline transporter
NER	nucleotide excision repair
NET	neuroendocrine tumour
NF- $\kappa$ B	nuclear factor kappa B
NHEJ	non-homologous non-end joining
Ni	nickel
nm	nanometer
nM	nanomolar
ns	non-significant
O <sub>2</sub>	dioxygen
O <sub>2</sub> <sup>•-</sup>	superoxide radical
$\pi$	pi number – ratio of circumference of a circle to its diameter
P	phosphorous

PARP	poly-(ADP-ribose) polymerase
PBS	phosphate-buffered saline
PCa	prostate cancer
pCASP3	phosphorylated caspase 3
PDTC	pyrrolidine dithiocarbamate
P-gp	P-glycoprotein
pH	potential of hydrogen
PI	propidium iodide
PMPA	2-(phosphonomethyl) pentanedioic acid
pRB	phosphorylated retinoblastoma
PSA	prostate-specific antigen
PSMA	prostate-specific membrane antigen
r	coefficient of correlation
R <sup>2</sup>	coefficient of determination
RB	retinoblastoma
RECK	reversion-inducing-cysteine-rich protein with kazal motifs
ROS	reactive oxygen species
rpm	round per min
RPMI	Roswell Park Memorial Institute
S-S	disulphide bridge
SEM	standard error of the mean <sup>7</sup>
Ser	serine
SF	surviving fraction
SGD <sub>C</sub>	specific growth delay of a combination treatment
SGD <sub>SA</sub>	specific growth delay of a single-agent treatment
SO <sub>4</sub>	sulfuric acid
SOD	superoxide dismutase
SH	sulfhydryl group, thiol group
SPSS	software package for statistical analysis
SSB	single-strand break
SSTR	somatostatin receptor
Suc-LLVY	N-Succinyl-Leucine-Leucine-Valine-Tyrosine
t	time
T3	triiodothyronine
T4	thyroxine
TBE	Tris-buffered EDTA

Thr	threonine
TNF- $\alpha$	tumour necrosis factor $\alpha$
$\tau_x$	growth delay in days for a x-fold increase in volume
$\mu\text{g}$	microgram
UK	United Kingdom
$\mu\text{l}$	microlite
$\mu\text{M}$	micromolar
US	United States
UV	ultraviolet
v or V	volume
$V_0$	initial volume
VEGF	vascular endothelial growth factor
VIS	visible
y-int	ordinate intercept

## Abstract

The purpose of this research was to enhance the targeted radiotherapy of two metastatic malignant diseases: neuroblastoma and prostatic carcinoma.

By virtue of its high affinity for the norepinephrine transporter (NET), [<sup>131</sup>I]meta-iodobenzylguanidine ([<sup>131</sup>I]MIBG) has been used for the therapy of tumours of neuroectodermal origin for more than 25 years. Although not yet universally adopted, [<sup>131</sup>I]MIBG targeted radiotherapy remains a highly promising means of management of neuroblastoma. MIP-1095, a glutamate-urea-lysine dipeptide has high affinity for prostate-specific membrane antigen (PSMA) and has recently demonstrated exquisite specificity for PSMA-expressing, metastatic prostatic carcinoma. Preliminary imaging studies in patients, using [<sup>123</sup>I]MIP-1095, revealed tumour-selective binding and prolonged retention only in malignant sites. This indicates the therapeutic potential of this agent when labeled with Iodine-131.

Our aim is to make the most effective use of [<sup>131</sup>I]MIBG and [<sup>131</sup>I]MIP-1095 for the treatment of neuroblastoma and prostatic carcinoma by combining the [<sup>131</sup>I]-labelled radiopharmaceutical with radiosensitiser drugs.

The thiol-containing molecule disulfiram was selected for combination with targeted radiotherapy because of its reported inhibition of the 26S proteasome and NF-κB activity, its ability to chelate copper and its pro-oxidative effects. The copper-dependence of the cytotoxicity and radiosensitising activity of disulfiram was established in neuroblastoma cell models. Radiation dose enhancement values at the 50% toxicity level were 4.24 and 2.00 in SK-N-BE(2c) and UVW/NAT cells, respectively. The radiosensitising mechanism of disulfiram-copper was shown to involve the inhibition of cell cycle arrest in G2. The enhancement of the cytotoxicity of [<sup>131</sup>I]mIBG and of [<sup>131</sup>I]MIP-1095 by disulfiram-copper was demonstrated by delay of the growth of multicellular tumour spheroids.

Finally, the screening of the enhancing effect of chemotherapeutic agents on the spheroid growth delay induced by [<sup>131</sup>I]MIP-1095 indicated that combinations with topotecan, nutlin-3, bortezomib or olaparib have good prospects for therapy of metastatic prostate carcinoma. In conclusion, it is expected that DSF:Cu will enhance the outcome of patients undergoing targeted radiotherapy due to its radiosensitising properties.

# 1 Introduction

## 1.1 Radiation, radiotherapy and targeted radiotherapy

### 1.1.1 Definition of radiation

Radiation is the emission of electromagnetic waves of a specific wavelength and frequency. The electromagnetic spectrum ranges from high frequency  $\gamma$ -rays, X-rays and ultraviolet rays to low frequency microwaves and radiowaves. Ionising radiation (IR) has sufficient energy to alter the structure of an atom. IR may arise from the radioactive decay of atoms ( $\gamma$ ,  $\alpha$  and  $\beta$  radiations) or they may be produced by electrical devices (X-rays).  $\alpha$  and  $\beta$  radiations are the particulate manifestations of the radioactive decay of atoms.  $\alpha$  particles are nuclei of helium and  $\beta$  particles may be positrons ( $\beta^+$ ) or electrons ( $\beta^-$ ). Since its discovery at the end of the 19<sup>th</sup> century, IR has become an important tool in medical practice. For instance, X-ray imaging is a standard procedure in orthopaedic diagnosis and for the local treatment of tumours. Radionuclides have also been used in the clinic, such as the  $\beta$ -emitter iodine-131 ( $^{131}\text{I}$ ) for the treatment and diagnosis of thyroid diseases.

### 1.1.2 Limitations of external beam radiotherapy of cancer

Radiation treatment may be administered by an external beam directed at malignant tissue. The irradiated volume usually encompasses tumour and a proportion of non-malignant surrounding tissue. Advances have been made in external beam radiotherapy, resulting in a reduction in the exposure of non-malignant tissue. For example intensity-modulated radiotherapy (IMRT) conforms the radiation dose more precisely to the three-dimensional shape of the tumour thereby minimizing the dose to adjacent normal organs. However, external beam radiotherapy is unable to treat disseminated malignant lesions without irradiating healthy tissues.

### 1.1.3 Targeted radiotherapy

Targeted radiotherapy is the specific delivery of radiation to malignant lesions by the use of a tumour-seeking agent linked to a radionuclide. It is the radiotherapeutic treatment of choice when the cancer has metastasised, when the malignant lesions are too small to be detected or when they are located close to vital structures. Targeted radiotherapy has been devised to circumvent the limitations of external beam radiotherapy.

The specificity of the delivery of radiation by targeted radiotherapy may arise from the biological properties of the radionuclide itself. For instance, the thyroid accumulates iodine for the synthesis of the thyroid hormones. Hence, the treatment of thyroid cancer has

employed Na<sup>131</sup>I for several decades<sup>1</sup>. Alternatively, the expression of markers specific to the tumour cells can be used for the targeting of radionuclides attached to a tumour-seeking molecule. For instance, radiolabelled antibodies have been used to treat solid tumours from the breast<sup>2</sup>, prostate<sup>2</sup>, colon<sup>3</sup> and neuroblastoma<sup>4</sup> as well as haematopoietic cancers such as lymphoma and leukaemia<sup>5</sup>. However, antibodies are large molecules that may fail to penetrate tumours<sup>5</sup>. Indeed, an inverse relationship has been demonstrated between tumour uptake of radiolabelled antibodies and tumour mass<sup>6,7</sup>. Improved penetrability may be obtained by the use of antibody fragments<sup>8</sup>. Small molecules, such as the noradrenalin transporter (NAT)-targeting agent meta-iodobenzylguanidine (mIBG) for the treatment of neuroblastoma, may possess even greater tumour penetrability<sup>9-11</sup>.

The efficacy of targeted radiotherapy depends on the size of the malignant lesion and on the physical properties of the radionuclide. The ability of a radionuclide to deliver radiation to untargeted neighbouring cells within the tumour is called cross-fire and this is dependent on the path length of the radionuclide. Tumour heterogeneity limits binding and uptake of the radiopharmaceutical by cells within the tumour mass. This impediment to tumour cure may be surmounted by cross-fire irradiation<sup>12</sup> obtained through the use of long-range  $\beta$ -emitters. However, the longer the path length of the radionuclide, the greater the risk of irradiating untargeted surrounding healthy tissue which would result in undesirable toxicity. The implication is that, due to sub-optimal deposition of radiation energy within the malignant lesion, metastases smaller than the path length of the radionuclide could escape sterilisation at activity levels sufficient to eradicate metastases of a diameter similar to that of the path length. While short-range  $\alpha$ -emitters may be better therapeutic tools than  $\beta$ -emitters due to their induction of less collateral damage<sup>13</sup>, the optimal treatment of disseminated disease may consist of cocktails of radionuclides with a range of path lengths<sup>14</sup>.

#### **1.1.4 Current use of targeted radiotherapy**

This section will summarise the current use of targeted radiotherapy in medical practice with particular emphasis on neuroblastoma and prostate cancer.

##### **1.1.4.1 Na<sup>131</sup>I for the treatment of thyroid conditions**

The first radionuclide used in modern medical practice was radioiodine in the 1950s for the treatment of thyroid cancer<sup>15</sup>. Iodine is taken up by the differentiated follicular thyroid cells for the biosynthesis of the thyroid hormones triiodothyronine (T3) and thyroxine

(T4). For the treatment of thyroid cancer, radioiodine does not need to be conjugated to a tumour-targeting vehicle because iodine is specifically accumulated by thyroid cells.

The effectiveness of radioiodine has been examined in patients with high risk thyroid cancer with locoregional or distant metastases<sup>16</sup>. The study reported an important improvement of cancer-specific survival and disease progression for patients treated with radioiodine versus those who were not<sup>16</sup>. It demonstrates the beneficial use of radioiodine for the treatment of metastatic thyroid cancer or the ablation of residual disease following thyroidectomy. Radioiodine treatment of thyroid cancer is considered the greatest success of targeted radiotherapy<sup>15</sup>.

#### **1.1.4.2 Radionuclides for the treatment of bone metastasis**

The incidence of bone metastasis observed at post-mortem examination is 73% in breast cancer, 68% in prostate cancer, 42% in thyroid cancer, 36% in lung cancer, 35% in renal cancer and 5% in cancers of the gastrointestinal tract<sup>17</sup>. Morbidities associated with bone metastasis include pain, fractures and spinal cord compression<sup>17</sup>. The presence of bone metastases is also associated with poor prognosis. The relief of pain from bone metastases is achieved by the administration of bone-seeking radionuclides such as radium-223 (<sup>223</sup>Ra), strontium-89 (<sup>89</sup>Sr), samarium-153 (<sup>153</sup>Sm), rhenium-186 (<sup>186</sup>Re) or phosphorous-32 (<sup>32</sup>P) which are incorporated into regenerating bone at metastatic sites. A meta-analysis of 15 studies worldwide demonstrated that these radionuclides relieved bone pain over a 1 to 6 months period<sup>18</sup>.

#### **1.1.4.3 Radioimmunotherapy of haematopoietic malignancies**

Radioimmunotherapy is the treatment of cancer by administration of radiolabelled antibody. Despite poor tissue penetration and immunogenicity, radiolabelled antibodies have improved the outcome of haematopoietic cancers. Recently two radiolabelled antibodies have been approved by the Food and Drug Administration (FDA) for the treatment of non-Hodgkin's lymphoma. The two antibodies directed against the B cell-specific antigen CD20 and radiolabelled with yttrium-90 (<sup>90</sup>Y) or <sup>131</sup>I are <sup>90</sup>Y-ibritumomab tiuxetan (Zevalin™, Biogen-IDEc Pharmaceuticals, CA, 2002) and <sup>131</sup>I-tositumomab (Bexxar™, GlaxoSmithKline, 2003). The efficacies of <sup>90</sup>Y-ibritumomab and <sup>131</sup>I-tositumomab has been compared with the non-radiolabelled CD20-targeting antibody. These clinical trials indicated that patient outcome was improved with relatively low and manageable side-effects and that radioimmunotherapy was a successful treatment of non-Hodgkin's lymphoma<sup>19,20</sup>.

#### **1.1.4.4 Somatostatin analogues for the treatment of neuroendocrine tumours**

Neuroendocrine tumours (NETs) constitute a heterogeneous group of malignancies that originate in neuroendocrine cells. Common primary sites are the stomach, pancreas and intestines<sup>21</sup>. Despite their heterogeneous location, NETs share common features such as histology and hormone production. The somatostatin receptor subtype 2 (SSTR2) is expressed in more than 80% of all NETs<sup>22</sup>. A variety of somatostatin analogues, radiometalated using chelators such as diethylene triamine penta-acetic acid (DTPA) or 1,4,7,10-tetraazacyclododecane-1,4,7,10-tetra-acetic acid (DOTA), have been developed. Clinical trials using somatostatin analogues such as octreotide and octreotate have demonstrated good tumour control associated with acceptable side-effects<sup>23,24</sup>.

#### **1.1.4.5 Neuroblastoma**

Neuroblastoma is the most common extracranial cancer in childhood, representing 28% of all cancers in infants<sup>25</sup>. Neuroblastoma arises in cells of the neural crest during embryonal development of the nervous system. Tumours can develop in all parts of the peripheral sympathetic nervous system, most commonly in the adrenal glands.

Neuroblastoma is a heterogeneous disease with outcomes ranging from spontaneous regression or differentiation to benign ganglioneuroma to a progressive, metastatic and fatal disease. The prognosis of neuroblastoma is related to the Shimada classification of tumour histology<sup>26</sup>, the International Neuroblastoma Staging System (INSS) stage of the tumour and the age at diagnosis. Moreover, predictors of decreased overall survival are the myelocytomatosis viral related oncogene neuroblastoma-derived (MYCN) status and genetic modifications such as ploidy, 1p and 11q aberrations and 1q gain. According to the International Neuroblastoma Risk Group (INRG) risk stratification, and based on the prognostic factors described above, the high risk group of neuroblastoma children represents 36.1% of all neuroblastoma cases with a 5-year event-free survival (EFS) less than 50% despite intensive multimodal treatment<sup>27</sup>. In contrast, the very low and low risk groups represent 26.8% and 28.2% of the neuroblastoma patients with a 5-year EFS greater than 85% and 75%, respectively<sup>27</sup>. Finally, neuroblastoma tumours tend to metastasise, especially in the high risk group. The primary sites of metastases are bone marrow (70.5%), non-orbital bones (55.7%), lymph nodes (30.9%), the liver (29.6%) and the orbital bone (18.2%). Metastases to the bones, the bone marrow, the central nervous system, the orbital bone, the lungs and the pleura are associated with a significant decrease in the 3-year EFS<sup>28</sup>.

The classical treatment of high risk neuroblastoma is a 3-step regimen including induction, consolidation and maintenance<sup>29</sup>. The role of induction and consolidation therapy is to reduce the tumour burden before chemoresistance develops while maintenance therapy aims to eradicate the residual disease after intensive myeloablative therapy. In the induction phase, various combinations of chemotherapeutic agents including cisplatin, doxorubicin, vincristine, cyclophosphamide, etoposide or topotecan may be administered. Surgical resection and external beam radiation treatment of the primary or metastatic sites may be performed. Secondly, consolidation therapy consists of intensive myeloablative chemotherapy including carboplatin, etoposide, melphalan or busulphan with autologous bone marrow transplant. Finally, maintenance therapy aims to rid the body of residual disease by, for example, inducing differentiation of the neuroblastoma cells. The differentiating agent 13-cis retinoic acid has been shown to improve outcome in children with high risk neuroblastoma<sup>30</sup>. Furthermore, treatment with 13-cis retinoic acid in combination with immunotherapy (anti-GD2, IL-2 and GM-CSF) was shown to improve the 2-years EFS compared with 13-cis retinoic acid alone. However this regimen was highly toxic<sup>31</sup>.

Catecholamines are small molecules acting upon the central and peripheral nervous systems as neurotransmitters or acting systemically as hormones. At the synapse between axon and neurone, NAT is responsible for the reuptake of noradrenaline into the intracellular space in order to prevent sustained activation of the noradrenergic receptor. By virtue of its analogy of structure to noradrenaline (Figure 1), meta-iodobenzylguanidine (mIBG) can be taken up by cells that express NAT. Since 90% of neuroblastoma tumours express NAT<sup>32</sup>, mIBG labelled with iodine-131 (<sup>131</sup>I)mIBG) or with iodine-123 (<sup>123</sup>I)mIBG) has been used for the treatment and imaging of neuroblastoma, respectively. To date, the majority of clinical trials investigating the efficacy of [<sup>131</sup>I]mIBG have been carried out in cohorts of high risk neuroblastoma children who were unresponsive to classical therapy, described above, or who relapsed shortly after treatment. The studies yielded overall response rates between 30% and 58% and the major toxicity observed was myelosuppression<sup>33-40</sup>. On the other hand, it has been shown that [<sup>131</sup>I]mIBG as a first-line treatment prior to chemotherapy and surgery is an effective option for the treatment of high risk neuroblastoma<sup>41</sup>.

Finally, phase I studies have investigated [<sup>131</sup>I]mIBG in combination with chemotherapy. The combinations of [<sup>131</sup>I]mIBG with the induction regimen cisplatin, cyclophosphamide,

etoposide, vincristine and doxorubicin<sup>42</sup> or with irinotecan and vincristine<sup>43</sup> resulted in the reduction of the tumour burden with tolerable toxicities. These studies showed that [<sup>131</sup>I]mIBG can be incorporated safely into the classical chemotherapeutic treatment of high risk neuroblastoma. These studies form the rationale for the preclinical determination of new radiosensitising drugs which may improve the efficacy of [<sup>131</sup>I]mIBG<sup>44</sup>.

Despite intensive treatment regimens, children with high risk neuroblastomas continue to have a poor prognosis. The inclusion of [<sup>131</sup>I]mIBG in the treatment of neuroblastoma has shown efficacy and is promising for patients with chemo-refractory tumours. While long-term remissions have been achieved, cure is rare. Efforts to improve the outcome of the treatment of high risk neuroblastoma has focussed on the scheduling of [<sup>131</sup>I]mIBG therapy within the classical regimen<sup>41</sup>, the simultaneous administration of radiosensitising drugs with [<sup>131</sup>I]mIBG<sup>42,43</sup> and the development of new chemotherapeutic agents<sup>29</sup>.

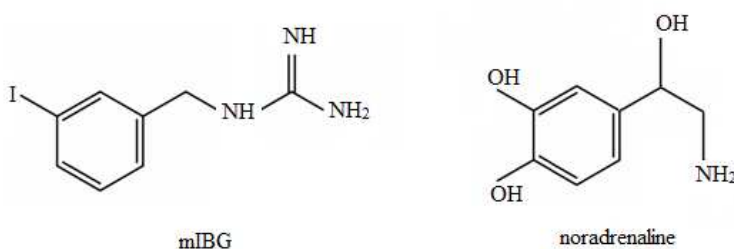


**Figure 1** The chemical structures of meta-iodobenzylguanidine (mIBG) and noradrenaline

#### **1.1.4.6 Prostate cancer (PCa)**

PCa was the fourth most common cancer in Europe in 2008 and the second most common cancer in men accounting for 89,300 deaths<sup>45</sup>. About 75% of PCa worldwide occur in men 65 years old or over<sup>46</sup>. It is a heterogeneous disease ranging from indolent tumours to aggressive, metastatic and fatal disease.

Localised PCa is confined within the prostate. Given the often indolent nature of localised PCa, which is associated with a good prognosis, active surveillance may be the preferred option for the management of patients. Other treatment options for localised PCa include radical prostatectomy, androgen deprivation therapy (ADT) or radiotherapy in the form of external beam radiotherapy and brachytherapy. However, even after complete prostatectomy, recurrence and metastases constitute an important complication of the treatment of localised PCa<sup>47</sup>.

Due to the reliance of PCa tumour growth on androgen stimulation<sup>48</sup>, the mainstay of PCa treatment is ADT. However, the tumour may progress, even under ADT, a state called castrate-resistant prostate cancer (CRPC). Furthermore, metastasis is a common complication of advanced CRPC<sup>17,49</sup>. Bone pain due to bone metastasis may be palliated by the administration of bone-seeking radionuclides such as <sup>153</sup>Sm, <sup>223</sup>Ra or <sup>89</sup>Sr but, at present, there is no curative treatment of metastatic CRPC.

The improvement of the outcome of CRPC patients is the focus of PCa research. Recent phase III trials have shown that the median survival of patients with metastatic CRPC is 1 to 2 years<sup>50-52</sup>. The main chemotherapeutic agent approved for the treatment of metastatic CRPC is docetaxel. Docetaxel in combination with prednisone has improved survival of this group of patients by 2 to 3 months compared with the previous standard treatment using mitoxantrone plus prednisone<sup>52</sup>. Furthermore, recent phase III clinical trials have confirmed the benefit of blockers of the androgen-mediated stimulation of PCa tumour growth, abiraterone<sup>53,54</sup> and enzalutamide<sup>55</sup>, in docetaxel-refractory CRPC patients.

The above studies indicated that innovative chemotherapy increased the survival of patients with metastatic CRPC only by several months, demonstrating the need for alternative therapeutic approaches in the treatment of this subset of patients. Given the survival benefit afforded by targeted radiotherapy of thyroid cancer, neuroblastoma and NETs, radiopharmaceuticals targeting PCa markers may hold promise for therapy of metastatic PCa. Furthermore, targeted radiotherapy is already in use for the treatment of painful bone metastases in PCa using bone-seeking radionuclides. However, this treatment is only palliative and does not target all malignant lesions. Therefore, the development of a PCa tumour-targeting radiopharmaceutical which could be used with a curative intent to target all malignant lesions (bone metastases, non-osseous metastases and residual disease after ablative treatment) is an appealing strategy for the treatment of metastatic CRPC.

N-acetylated  $\alpha$ -linked acidic dipeptidase (NAALADase) is a neuropeptidase that releases glutamate and N-acetylaspartate from its substrate, the neurotransmitter N-acetylaspartylglutamate (NAAG)<sup>56</sup>. Prostate specific membrane antigen (PSMA) was found to be genetically and functionally homologous to NAALADase<sup>57</sup>. It has been speculated that the role of PSMA in prostate is the cleavage of molecules with paracrine and/or autocrine activity involved in prostate homeostasis<sup>58</sup>.

While the role of PSMA in the prostate is not well understood, its potential as a target for prostate carcinoma is recognised. Increased expression of PSMA has been demonstrated in prostate carcinomas compared with normal prostate or benign prostatic hyperplasia<sup>59</sup>. Secondly, PSMA immunoreactivity was increased after ADT in 55% (11 out of 20) of the patients<sup>60</sup>. Increased PSMA immunoreactivity was also found after ADT in 100% (4 out of 4) of metastatic specimens<sup>60</sup>, suggesting that PSMA is upregulated in metastatic PCa. Thus, PSMA-targeting agents is a promising therapeutic tools for the management of disseminated PCa<sup>61</sup>.

Antibodies have been developed against the PSMA antigen<sup>2</sup>. The first commercial antibody was Indium-111 (<sup>111</sup>In)-CYT-356 (Prostascint). However this antibody recognised an intracellular epitope of PSMA and initial testing in human showed unexpected myelotoxicity<sup>62</sup>. Four other antibodies with specificity for extracellular epitopes of PSMA have also been developed<sup>63</sup>. For instance, phase I clinical trials evaluating the humanised monoclonal antibody huJ591 have demonstrated PSMA specificity and successful application as an imaging agent<sup>2</sup>.

A series of small heterodimeric compounds, which inhibit the NAALADase activity of PSMA, were developed by Molecular Insight Pharmaceuticals, Inc., Cambridge, Massachusetts<sup>64</sup>. The structures of the two lead compounds, (S)-2-(3-((S)-1-carboxy-5-((4-iodobenzyl)amino)pentyl)ureido) pentanedioic acid (MIP-1072) and (S)-2-(3-((S)-1-carboxy-5-(3-(4-iodophenyl)ureido)pentyl)ureido) pentanedioic acid (MIP-1095), consist of glutamate bound to lysine by a urea bridge (Figure 2). The benzene ring which allows iodination is linked to the nitrogen group of lysine in MIP-1072 or attached to lysine via a urea bridge in MIP-1095 (Figure 2). Both compounds have demonstrated PSMA-specific uptake in tissue distribution studies in mice bearing xenografts derived from the LNCaP and PSMA-transfected PC3 cell lines<sup>65</sup>. The pharmacokinetic characteristics and the imaging potential for prostate carcinoma of the <sup>123</sup>I-radiolabelled versions of these two compounds ([<sup>123</sup>I]MIP-1072 and [<sup>123</sup>I]MIP-1095) have been investigated in patients. It was shown that both [<sup>123</sup>I]MIP-1072 and [<sup>123</sup>I]MIP-1095 were suitable for the detection of malignant lesions in soft tissues, bones and in the prostate<sup>61</sup>. Notably, the retention of [<sup>123</sup>I]MIP-1095 within tissues was greater than that of [<sup>123</sup>I]MIP-1072 - manifest by a greater absorbed radiation dose<sup>61</sup>. This study forms the rationale for the investigation of radiolabelled MIP-1095 as an imaging tool and also as therapeutic modality for the treatment of disseminated PCa.

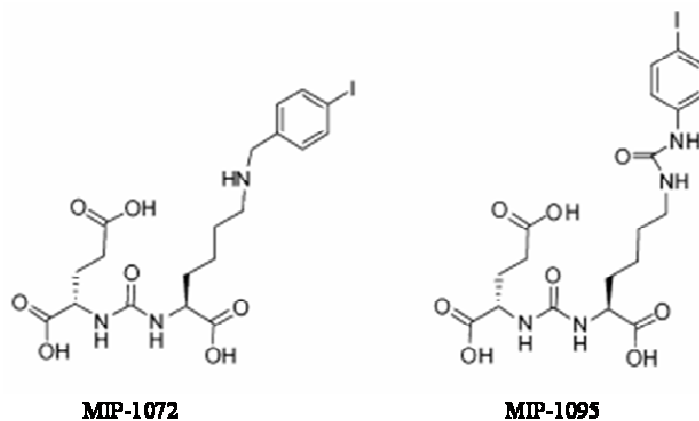


**Figure 2** The chemical structures of PSMA-targeting compounds

### 1.1.5 The biological effect of IR

#### 1.1.5.1 The formation of free radicals

The result of the interaction of IR with an atom may be the stripping of an electron. The loss of an electron by an atom or a molecule, the primary effect of IR on matter, is called oxidation. Alternatively, the target atom may become excited, resulting in one or more of its electrons being moved to a higher energy level.

A free radical is defined as an atom or a molecule containing one or more unpaired electrons<sup>66</sup>. An unpaired electron is avid for another unpaired electron, resulting in the formation of a covalent bond. Therefore, free radicals are highly reactive chemical entities. Free radicals whose unpaired electron is associated with the oxygen atom are called reactive oxygen species (ROS). The absorption of radiation energy by a molecule of water breaks the O-H bond and leads to the formation of a hydroxyl radical (HO•) and an atom of hydrogen (H•)<sup>66</sup>. Alternatively, the electron liberated by the interaction of IR with matter may reduce a molecule of oxygen to form the superoxide radical (O<sub>2</sub>•<sup>-</sup>). The peroxide O<sub>2</sub>•<sup>2-</sup> is formed if a second electron further reduces O<sub>2</sub>•<sup>-</sup>. Secondly, with the addition of two protons, O<sub>2</sub>•<sup>2-</sup> forms the non-radical oxidising agent hydrogen peroxide (H<sub>2</sub>O<sub>2</sub>). Due to the avidity of ROS for a second electron in order to form a covalent bond, ROS readily oxidise molecules in their immediate vicinity<sup>66</sup>. Therefore IR is a powerful oxidative agent, directly via the interaction with matter and indirectly via the production of ROS.

#### 1.1.5.2 Cellular responses to radiation

The structure and, consequently, the function of a protein are dependent on the intracellular oxidative status of a cell. For instance, a sulphur atom within a protein exists as a thiol

group (-SH) in a reducing environment whereas it exists as a disulphide bridge (-S-S-) in an oxidative environment. The formation of disulphide bridges between two sulphur atoms within a protein under oxidising conditions may change the conformation and the function of a protein with potentially detrimental effects for the cell. Therefore, redox homeostasis, the mechanisms responsible for the maintenance of the intracellular redox equilibrium, is required to sustain cellular metabolism. Another target of radiation is DNA. The oxidation of DNA leads to the generation of abnormal DNA bases (such as 8-oxoguanine), single-strand breaks (SSB) and double-strand breaks (DSB). These alterations to DNA may lead to mutations or cell death. Upon radiation-induced oxidative stress, the cell relies on various antioxidant defence mechanisms in order to maintain redox homeostasis and the integrity of the genome. Microarray studies have indicated that IR alters the level of expression of genes involved in DNA repair<sup>67-70</sup>, cell cycle regulation<sup>67,71,72</sup> and antioxidant defence<sup>70-72</sup>.

#### 1.1.5.2.1 Antioxidant responses

Superoxide dismutase (SOD) is an enzyme that converts  $O_2^{\bullet-}$  into  $H_2O_2$  (Figure 3). Since  $H_2O_2$  is a potentially harmful oxidising agent, catalase converts  $H_2O_2$  into water and oxygen. SOD requires a metal ion for its enzymatic activity. SOD1, located in the cytoplasm, is coupled with zinc or copper, SOD2, located in the mitochondria, is coupled with manganese and the extracellular SOD3 is also coupled with zinc or copper. The SOD/catalase system protects cells from the indirect oxidative effect of radiation by the scavenging of  $O_2^{\bullet-}$ .

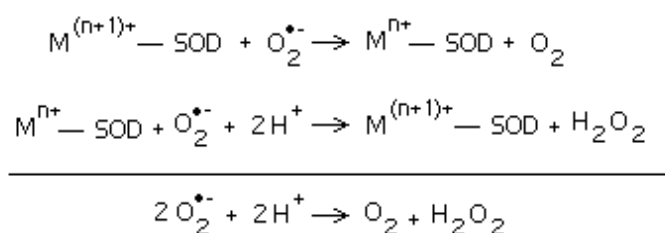


**Figure 3 The chemical reactions of the conversion of superoxide to hydrogen peroxide by SOD**  
M, metal.

Glutathione protects cells from oxidation by several mechanisms: direct scavenging ROS, the reduction of oxidised entities or by the conjugation of reduced glutathione (GSH) to oxidised moieties. Upon radiation treatment, the glutathione peroxidase gene has been found to be upregulated in fibroblasts isolated from glioma<sup>72</sup>. Glutathione peroxidase

catalyses the transfer of an electron from the reduced form of glutathione (GSH) to an oxidised moiety. This process produces the oxidised form of glutathione (GSSG) and the reduced moiety. The reverse chemical reaction, the reduction of GSSG into two GSH molecules, is catalysed by glutathione reductase, thereby recycling the cellular antioxidant pool. This reaction requires the co-factor nicotinamide adenosine dinucleotide phosphate (NADPH) for the provision of electrons.

#### **1.1.5.2.2 Cell cycle regulation in response to radiation**

The proliferation of cells is a highly controlled process requiring progression through four successive phases of the cell cycle. In every cycle, a parent cell produces two daughter cells. Cells which are in the S phase of the cell cycle are in the process of replicating their DNA in order to obtain two copies of the genome. After the entirety of the genome has been replicated, the cells may undergo mitosis, a process whereby each daughter cell inherits one copy of the parent cell's genome. The intermediate phases of the cell cycle, although not involved with DNA metabolism, are responsible for the verification of the genome's integrity. Cells which are in the G1 phase of the cell cycle, which contain N amount of DNA, have exited mitosis and are preparing to enter the S phase in order to replicate their DNA. Cells in the G2 phase of the cell cycle, which contain 2N amount of DNA, have replicated the entirety of their genome and are preparing to enter mitosis.

The presence of DNA damage such as abnormal bases or SSB during DNA replication may interfere with the progress of the replication fork leading to the formation of DSB which are strong signals for cell death if they are too numerous to be efficiently repaired. Alternatively, DSB present during mitosis may cause unequal distribution of the genome to the daughter cells resulting in their death. Moreover, the presence of DNA damage may result in an impaired alignment of the chromosomes along the spindle equator. Such unrepaired damage may prevent mitotic progression or result in cell death by a process called mitotic catastrophe<sup>73</sup>. Consequently, cells have evolved complex checkpoints which arrest cell cycle progression in order to check the integrity of the genome at the G1/S and G2/M transitions. Cell cycle checkpoints confer radioresistance upon proliferative cells because they allow time for the repair of potentially lethal radiation-induced DNA damage.

#### **1.1.5.2.3 DNA damage and DNA repair**

The absorption of radiation energy by DNA leads to the production of abnormal bases, SSB and DSB<sup>74</sup>. DSB are considered the most critical DNA lesions. Moreover, the cytotoxicity of IR on cells is known to be more potent in normoxic conditions compared

with hypoxic conditions, implicating ROS in the generation of DNA damage<sup>75</sup>. It is considered that 60-70% of radiation-induced DNA damage is caused by ROS<sup>76</sup>. The main ROS considered to react with DNA molecules is HO•. The chemical reaction of HO• with DNA leads to the same DNA lesions as those induced by the direct absorption of radiation energy<sup>77</sup>.

Nucleotide excision repair (NER) is responsible for the recognition and repair of DNA-distorting base damage, such as thymidine dimers, predominantly after ultraviolet (UV) radiation treatment. On the other hand, base excision repair (BER) is responsible for the repair of non-DNA-distorting base damage including deamination, depurination, alkylation and other oxidative damage leading to abnormal bases. Such defects are recognised by DNA glycosylases and removed by apurinic/apyrimidinic endonucleases. The gap is then filled by DNA polymerase  $\beta$  and the nick repaired by DNA ligases<sup>78</sup>. Both NER and BER are involved in the repair of ROS-induced oxidative damage of DNA<sup>79</sup> ENREF 14.

The repair of DSB of DNA is carried out by two mechanisms. Homologous recombination (HR) uses the homologous strand of DNA for the error-free synthesis of missing DNA sequences. The requirement of the homologous strand implies that this mechanism preferentially occurs in S-phase and G2, when there are two copies of each DNA strand<sup>80</sup> ENREF 15. DSB sensors and recombinases are members of the RAD51 protein family and they are upregulated after radiation treatment<sup>81</sup>. Alternatively, non-homologous end joining (NHEJ) joins the ends of two DNA strands together. Thus, NHEJ does not need the homologous DNA strand. This error-prone DNA repair machinery is therefore unable to maintain the integrity of the genome<sup>80</sup> ENREF 15. The main effectors of NHEJ are the heterodimer KU70/KU80, which is responsible for the recognition of the DSB, and DNA-dependent protein kinase (DNA-PK), which is responsible for the recruitment of ligase IV and artemis. In turn, the NHEJ complex, consisting of KU70/KU80, DNA-PK, ligase IV and artemis, joins both ends of the DNA together<sup>80</sup> ENREF 15.

### **1.1.6 Radiosensitisation**

“A true radiosensitiser is a chemical which increases the cell-killing effect of a given dose of radiation. This is achieved either by increased formation of longer-lived toxic radiation-induced radicals or modification of vulnerable, critical targets in cells, or by interference with mechanisms of repair of sublethal radiation damage”<sup>82</sup>. This definition of radiosensitisation directly involves the generation of oxidative stress and the inhibition of

the pathways leading to efficient DNA repair following irradiation. These pathways are described next.

ROS are produced in all aerobic cells via the oxidation of the constituents of the mitochondrial electron transport chain<sup>83</sup>. Therefore, due to the high metabolic rate required to sustain proliferation, cancer cells experience greater oxidative stress than normal cells proliferating at a lower rate. Degenerative oxidation of membrane phospholipids, DNA damage and the depolarisation of the mitochondrial inner membrane are thought to lead to oxidation-induced cell death. It was proposed that oxidising agents could be used therapeutically to increase the oxidative stress in cancer cells beyond a theoretical threshold corresponding to the maximal level of oxidative stress that a cancer cell can withstand. Crucially, due to the existence of greater oxidative stress in cancer cells than in healthy cells, this threshold would not be reached in healthy cells<sup>84</sup>. However, as a consequence of elevated oxidative levels, it is speculated that cancer cells may also harbour increased levels of antioxidant defences. Therefore, their depletion, which would increase the susceptibility to oxidising agents, may also be an efficient therapeutic option.

The primary effect of IR is the oxidation of molecules. Therefore, combination treatment comprising IR with an oxidising agent, or with a drug decreasing the antioxidant capacity of a cell, should result in a greater imbalance of the redox homeostasis, favouring oxidation. Oxidising agents should be radiosensitisers since they increase the cytotoxic oxidative effect of IR. Indeed, *in vitro* studies have demonstrated that the combination of 2-deoxyglucose with 6-aminonicotinamide radiosensitised cancer cells via an increase in oxidative stress. Furthermore, the enhancement of radiation cell kill was accompanied by an increased NADP<sup>+</sup>/NADPH ratio and an increased GSSG/GSH ratio<sup>85</sup>. Further evidence for the positive interaction between oxidising agents and radiotherapy has been provided by the clinical study which demonstrated the efficacy of combining the glutathione-depleting agent arsenic trioxide<sup>86</sup> with radiotherapy in patients with glioma<sup>87</sup>.

The inhibition of G1 and G2 arrest shortens the time for irradiated cells to repair DNA damage. Consequently, irradiated cells treated with cell cycle checkpoint inhibitors enter mitosis or the S phase with DNA damage. Similarly, DNA repair inhibitors increase the proportion of irradiated cells entering mitosis or the S phase with DNA damage.

DNA replication during S phase is a dynamic process requiring multiple components. Firstly, the DNA strands are separated from each other. Secondly, each strand serves as a

template for the synthesis of a complementary strand. As the replication fork advances, torsional stress in DNA is created ahead of the fork. Topoisomerase I cleaves one strand of DNA, allowing the second strand to pass through the cleavage site before re-sealing the nick. During this process, an intermediate state occurs through the formation of transient covalent bonds between topoisomerase I and the cleaved strand of DNA, the so-called “cleavable complex”.

A DNA repair inhibitor or a G1 arrest inhibitor allows the entry of irradiated cells into the S phase in the presence of extensive DNA damage. During DNA replication, SSB caused by radiation in addition to those created by topoisomerases at the replication fork may lead to the formation of DSB which are strong signals for cell death. Evidence for the transformation of SSB into DSB during DNA replication was provided recently by two separate studies. Olaparib is an inhibitor of poly(ADP-ribose) polymerase 1 (PARP-1). PARP-1 is involved in the recognition of SSB and the recruitment of the DNA repair machinery. It is also responsible for the relaxation of the chromatin structure allowing access of the DNA damage repair machinery to the DNA break site<sup>88</sup>. Olaparib is therefore an inhibitor of SSB repair. It was demonstrated that (i) aphidicolin, an inhibitor of DNA replication, prevented olaparib-mediated radiosensitisation and (ii) that the proportion of DSB in S-phase cells after 4 Gy irradiation was increased in the presence of olaparib<sup>89</sup>. Similarly, it was demonstrated that cells synchronised in S phase harboured more DSB when they were treated with the alkylating agent temozolomide in the presence of a PARP-1 inhibitor compared with treatment by temozolomide alone<sup>90</sup>. These results indicated that the inhibition of the repair of SSB by olaparib during the replication of DNA resulted in an increase in the formation of DSB after radiation treatment or treatment with an alkylating agent. They further suggested that the SSB are converted into DSB during DNA replication in the presence of a DNA repair inhibitor which leads to increased cell death.

Alternatively, a G2 arrest inhibitor allows the entry of irradiated cells into mitosis in the presence of DNA damage. Such cells may die by mitotic catastrophe.

Many drugs used in anti-cancer therapy disrupt mitotic progress or DNA metabolism (Table 1). Moreover, many of these drugs have been used successfully in combination with target radiotherapy in patients<sup>42,43,91</sup>. For example, the combination of [<sup>131</sup>I]mIBG with a radiosensitiser, the topoisomerase I inhibitor and S phase disruptor topotecan, has shown to be synergistic *in vitro* and *in vivo*. In this study, the combination of topotecan with [<sup>131</sup>I]mIBG induces a more efficient clonogenic kill and an enhancement of the delay in

DNA repair compared with [<sup>131</sup>I]mIBG treatment alone. The schedule of administration of the two agents was also shown to be crucial for synergy. The simultaneous administration of [<sup>131</sup>I]mIBG and topotecan resulted in greater delay in the growth of human tumour xenografts than [<sup>131</sup>I]mIBG administration prior to topotecan or *vice versa*<sup>92</sup>. This mIBG and topotecan in neuroblastoma (MATIN) regimen is now undergoing clinical evaluation<sup>93</sup>.

Drugs	Target	Mechanism of action
Vinca alkaloids (vinblastine, vincristine) Taxanes (paclitaxel, docetaxel)	Microtubules	Disruption of the polymerisation/depolymerisation dynamic of mitotic microtubules
Cyclophosphamide, cisplatin, melphalan, busulphan, temozolomide, carmustine, anthracyclins (doxorubicin, daunorubicin)	DNA	DNA crosslinking, alkylating and intercalating agents
Etoposide, mitoxantrone, topotecan, irinotecan	Topoisomerase I and II	Stabilisation of the cleavable complex and creation of double-strand breaks during DNA replication

**Table 1 DNA metabolism-targeting drugs used in anti-cancer therapy**

### 1.1.7 A strategy to improve targeted radiotherapy

Although targeted radiotherapy has produced promising results, the optimal way to use it has yet to be determined<sup>91,94</sup>. Indeed, the clinical trials listed in Section 1.1.4 have indicated that, despite overall response rates of 50% associated with little or manageable toxicity, cure of neuroblastoma and NETs remains elusive.

The intracellular pathways driving cell proliferation are numerous and cross talks occur among them<sup>95,96</sup>. Redundant mechanisms allow cells to survive treatment-induced alteration of a particular pathway. Resistance to therapy also develops even in initially responding patients, notably after ADT of prostate cancer<sup>97</sup>. Thus, treatment with two or more agents that act upon different oncogenic pathways or that act upon different components of the same oncogenic pathway are likely to achieve better tumour control than single agent therapies. Nowadays, cancer management employs multimodal strategies involving surgery, chemotherapy and radiotherapy. Moreover, chemotherapy may comprise multiple drugs (Section 1.1.4.5).

The limiting factor of all anticancer therapies is the toxicity to the dose limiting organ. In targeted radiotherapy, the main dose-limiting organ is the bone marrow although renal

toxicity occurs following administration of octreotide and octreotate for the treatment of patients with NET. Furthermore, neutropenia and thrombocytopenia are commonly observed after targeted radiotherapy. The anti-cancer efficacy of therapy must be balanced by toxicity to the patient. Synergistic interaction between two agents in a combination results in a supra-additive effect, i.e. a greater kill than that of the single agents. The concept of synergy has also been broadened to the therapeutic ratio in which a combination treatment is therapeutically synergistic if the side-effects are less than those of the single agents<sup>98</sup>. Theoretically, a synergistic combination kills at lower doses than those required for the single agents to achieve the same kill. Moreover, the use of low doses of a synergistic combination results in lower levels of toxicity and fewer side-effects, thereby improving the therapeutic ratio. This is of great importance in targeted radiotherapy for which bone marrow transplants are often required in order to avoid myelosuppression.

The efficacy of targeted radiotherapy may be improved by combination with radiosensitisers. One aim of the research described in this thesis was the screening of chemotherapeutic agents for synergistic interaction with targeted radiotherapy. Of particular interest was disulfiram because of its pro-oxidative properties, its ability to inhibit the proteasome/nuclear factor kappa B (NF- $\kappa$ B) pathway, its ability to chelate copper and its radiomodifying properties. A literature review of the biological effects of DSF is provided in the second part of this introduction.

## **1.2 Disulfiram (DSF)**

### **1.2.1 The nomenclature of DSF and its derivatives**

Dithiocarbamates are defined by a carbamate group in which both oxygens are substituted by sulphur atoms. A thiuram is a molecule with two dithiocarbamates linked by a disulphide bridge. DSF is a thiuram with four ethyl groups; hence DSF is also called tetraethylthiuram disulphide. The reduction of the disulphide bridge yields two diethyldithiocarbamate (DETC) molecules. One particular derivative has been extensively studied: pyrrolidine dithiocarbamate (PDTC). PDTC is a dithiocarbamate in which the nitrogen atom is engaged in a pyrrolidine cycle. DSF and its derivatives all chelate copper (Cu). The chemical structures of these compounds are shown below (Figure 4).

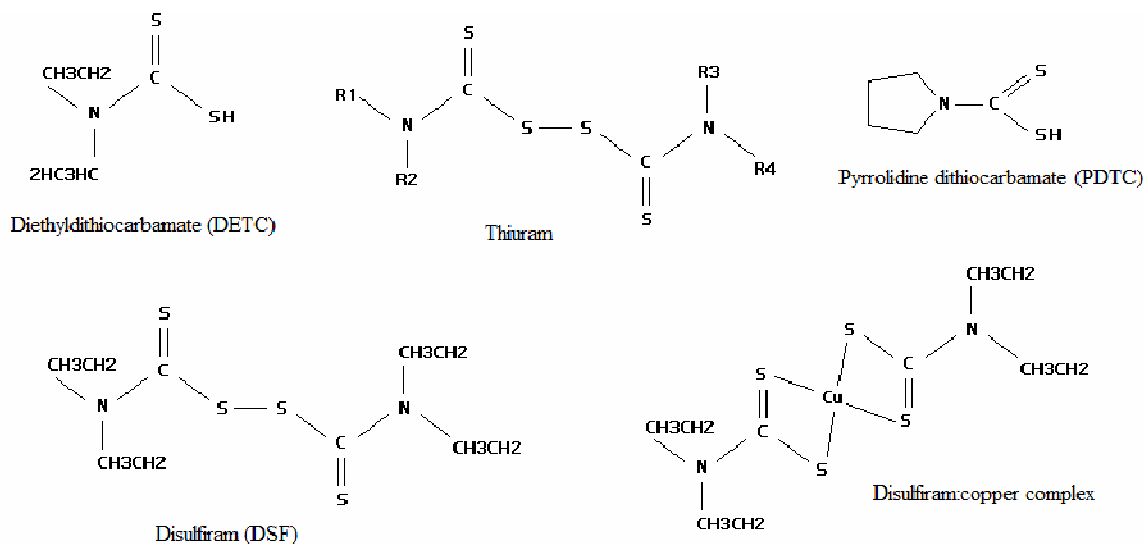


**Figure 4** The chemical structures of the dithiocarbamate family members

### 1.2.2 The origins of DSF

At the beginning of the 20<sup>th</sup> century, it was realised that workers grinding carbon disulphides in the rubber industry developed unpleasant symptoms after alcohol ingestion. The symptoms included hypotension, increased pulse rate, headache and flushing of the face. Notably, a physician published that these compounds could be the cure for alcoholism as the cited workers all became involuntary alcohol abstainers<sup>99</sup>. This finding was then extended to show that DSF is a sensitising agent to alcohol<sup>100,101</sup>. Following this pioneering work, DSF has been used for half a century to treat alcoholism. The mechanism of action of DSF in alcohol aversion therapy is thought to be the inhibition of the enzyme aldehyde dehydrogenase (ALDH). After alcohol ingestion, ethanol is oxidised to acetaldehyde by alcohol dehydrogenase (ADH). Toxic acetaldehydes are further oxidised to acetate by ALDH. It is the prolonged and elevated plasma concentration of acetaldehyde, due to DSF-induced inhibition of ALDH, which is thought to be responsible for the unpleasant symptoms, the so-called “DSF-ethanol reaction” (DER). Consequently, patients undergoing DSF treatment avoid alcohol intake for fear of an undesirable reaction.

DSF also inhibits dopamine β hydroxylase (DβH), the enzyme that catalyses the hydroxylation of dopamine to noradrenaline<sup>102</sup>. This may explain why DSF is indicated in cocaine addiction therapies<sup>103,104</sup> and may be used to treat other addictions such as pathological gambling<sup>105</sup>. The rationale is that the dopamine-noradrenaline axis is involved in rewarding and reinforcing behaviours<sup>106</sup>. The inhibition of this axis by DSF would prevent addictive behaviours. Furthermore, cocaine is a potent catecholamine re-uptake inhibitor. Increased noradrenaline levels are responsible for the euphoric feeling after

cocaine intake, and this may be reduced by the DSF-mediated reduction of noradrenaline levels.

### **1.2.3 Alcoholism, DSF and cancer**

It has been reported that the lung cancer related death of alcoholics was significantly lower in those taking DSF than in those who were not<sup>107</sup>. Although alcohol intake should be higher in DSF non-takers, the authors argued that since alcohol is not an indicated cause of lung cancer, the difference in alcohol intake could not account for the difference in lung cancer incidence. However, smoking, a habit linked to alcohol consumption and a known risk factor for lung cancer, was not taken in account in this study. The same study also found an association between lower incidence of other cancers and DSF intake but the difference was not statistically significant<sup>107</sup>. This observation raised the question whether DSF was a potential anti-cancer agent or not. A case of spontaneous remission from breast cancer in an alcoholic following DSF therapy was reported<sup>108</sup> and, more recently, DSF produced a long-term remission in an advanced stage melanoma patient<sup>109</sup>.

### **1.2.4 The biological targets of DSF**

#### **1.2.4.1 Increasing oxidative stress**

DSF is a chelator of divalent metal ions - primarily copper (Cu) but also iron (Fe)<sup>110</sup>, nickel (Ni)<sup>111</sup> and cadmium (Cd)<sup>112</sup>. DSF has been described as a Cu ionophore which exerts cytotoxic effects via Cu deposition inside cells<sup>113</sup>, a mode of action called Cu overload<sup>114</sup>. Cu only exists bound to proteins in the cytoplasm, thus, following Cu overload, cellular metabolism may be disrupted by inhibition of many proteins. Alternatively, the Cu-bound form of DSF may represent an active form of DSF which is toxic in its own right (see Section 1.2.4.2).

Due to their higher metabolic activity, tumour cells exist in a state of increased oxidative stress compared with normal cells<sup>84</sup>. According to the Cu overload theory, excess Cu reacts with the glutathione system, thus depleting the antioxidant defences of tumour cells. Also, Cu ions can cycle between two ionic forms, Cu(II) and Cu(III), in the presence of H<sub>2</sub>O<sub>2</sub> and form ROS, such as HO•, in a Fenton-like reaction (Figure 5)<sup>115</sup>. Tumour cells can produce high levels of H<sub>2</sub>O<sub>2</sub><sup>116</sup>. Thus, Cu may be capable of raising oxidative stress beyond the threshold that the tumour cell can deal with in two ways: interfering with the glutathione system and through the intermediacy of a Fenton-like reaction. Raising Cu levels within tumour cells, resulting in the disruption of multiple metabolic pathways and

elevating oxidative stress, has been suggested to be an effective anti-cancer option<sup>84</sup>. Furthermore, the Cu-mediated increase in oxidative stress could be a radiosensitising mechanism by which DSF could enhance the efficacy of radiotherapy.

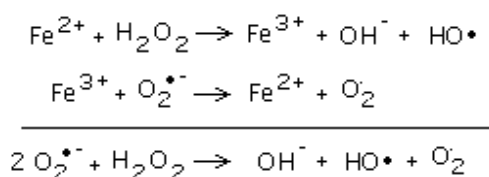


**Figure 5 The Fenton reaction using Fe<sup>2+</sup> as an electron donor**

Tumours accumulate Cu to sustain their higher metabolic demand, which results in greater Cu levels than in non-malignant cells<sup>84</sup>. For instance, Cu is a co-factor for superoxide dismutase (involved in the removal of superoxide radicals), lysyl oxidase (involved in the cross linking between collagen and elastin) and cytochrome c oxidase (involved in the production of ATP in mitochondria)<sup>84</sup>. Besides the Cu overload mechanism of action, it could be argued that Cu chelation by DSF is in itself toxic to cancer cells by interfering with tumour cellular metabolism of Cu.

SOD1 requires Cu for the detoxification of O<sub>2</sub><sup>•-</sup>. It has been shown that DETC, the product of the reduction of the disulphide bridge of DSF, inhibits SOD<sup>117</sup>. The authors argued that DETC-mediated inhibition of SOD enzymatic activity occurred via binding to Cu. Indeed, the inhibition of the enzymatic activity was reversed by Cu supplementation. Moreover, the authors observed the formation of a yellow colour following treatment of solutions of SOD with DETC, which was indicative of the formation of a complex between DETC and Cu<sup>110,118</sup>. The yellow colour was not extractable by organic solvents but extractable by treatment with CuSO<sub>4</sub><sup>117</sup>. This observation suggested that DETC probably binds to SOD via its interaction with Cu, thereby inhibiting SOD activity. Therefore, DETC inhibits a mechanism which counteracts oxidative damage created by ROS. Since DSF is broken down into DETC *in vivo*, DSF should have similar SOD-inhibitory properties to DETC. This mechanism may further contribute to the sensitisation of cancer cells to oxidative insults such as IR.

The glutathione system is responsible for the redox homeostasis of the cell by cycling between its reduced form (GSH) and its oxidised form (GSSG). This multi-step process was described previously (Section 1.1.5.2.1). DSF can interact with the glutathione system by virtue of its disulphide bridge. It has been shown that the non-enzymatic reaction



xenobiotics. The inactive form of NF- $\kappa$ B is bound to its inhibitor I $\kappa$ B and remains in the cytoplasm. Upon external stimulation (radiation, oxidative stress), I $\kappa$ B is phosphorylated, ubiquitinated and broken down by the proteasome. The degradation of I $\kappa$ B releases NF- $\kappa$ B which can then be translocated to the nucleus where it binds DNA in order to drive the transcription of its target genes. NF- $\kappa$ B is activated as part of the cellular response to oxidative stress and has anti-apoptotic properties.

The production of ROS by IR was described previously (Section 1.1.5.1). Elevated levels of ROS in the cytoplasm after irradiation create oxidative stress. The oxidation of key amino acids (e.g. cysteine) in active sites of proteins may alter the protein structure. Proteins capable of being activated in this way are called oxidative stress sensors. Once activated, oxidative stress sensors trigger the transcription of genes encoding antioxidant defences. Although the NF- $\kappa$ B activation routes are multiple and unclear, NF- $\kappa$ B was demonstrated to be an oxidative stress sensor<sup>122</sup>. NF- $\kappa$ B has been shown to be activated in response to radiation<sup>123,124</sup> and to confer upon cells radioresistant properties<sup>123,125</sup>.

NF- $\kappa$ B activation has been shown to increase the antioxidant capacity of pheochromocytoma cells by transcription of the genes encoding catalase and  $\gamma$ -glutamyl-cysteine synthetase, conferring increased protection against oxidative stress which translated into prevention of apoptosis<sup>126</sup>. Similarly, it has been demonstrated in another study that the inhibitor of apoptosis (IAP) was up-regulated after stimulation by tumour necrosis factor (TNF- $\alpha$ ), a known activator of NF- $\kappa$ B<sup>127</sup>. The mechanism of IAP-induced prevention of apoptosis was thought to be binding to and inhibition of caspases. Thus, NF- $\kappa$ B has antioxidant and anti-apoptotic properties at least through transcription of genes encoding antioxidants and IAP.

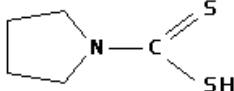
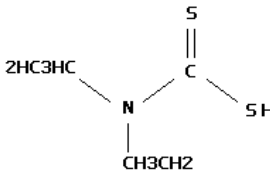
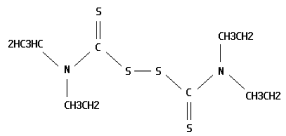
DSF and its pyrrolidine derivative, PDTC, are inhibitors of NF- $\kappa$ B activation<sup>128,129</sup>. The inhibition of NF- $\kappa$ B activation by DSF or PDTC is a sensitising mechanism to oxidative stress and apoptosis. Therefore, the inhibition of the proteasome/NF- $\kappa$ B axis by DSF represents another radiosensitising mechanism by which it could improve the efficacy of targeted radiotherapy.

### 1.2.4.3 Is DSF an oxidising agent or an antioxidant?

Despite the pro-oxidative properties of DSF described previously in Section 1.2.4.1, it has also been demonstrated that DSF and its derivatives such as PDTC and DETC have anti-oxidative properties.

In one study, PDTC, the pyrrolidine derivative of DSF with free thiols, decreased the rate of generation of ROS by fenretinide and inhibited apoptosis<sup>130</sup>, suggesting direct scavenging of ROS. In a second study, DSF prevented lipid peroxidation in isolated hepatocytes exposed to a range of oxidising agents including H<sub>2</sub>O<sub>2</sub><sup>131</sup>. These studies demonstrated the antioxidant properties of DSF and PDTC.

DSF and its derivatives have pro-oxidative properties exemplified by the transport of Cu into the cytosol, the inhibition of NF-κB and the depletion of antioxidant defences such as SOD and glutathione. Conversely, they also have anti-oxidative properties by virtue of their reduction of peroxidised lipids and the direct scavenging of ROS. A summary of these mechanisms is shown in Table 2. An attempt has been made to describe the chemistry of dithiocarbamates (PDTC, DETC and DSF) that encompasses both pro and anti-oxidative properties<sup>132</sup>. Using a HO•-generating cell-free system (H<sub>2</sub>O<sub>2</sub> and CuCl<sub>2</sub>), the authors demonstrated the scavenging of HO• by DSF, DETC and PDTC<sup>132</sup>. Secondly, using a different cell-free system comprising DETC, CuCl<sub>2</sub>, GSH, glutathione reductase (GR) and NADPH, the authors monitored the rate of oxidation of GSH into GSSG. It was demonstrated that the inclusion of CuCl<sub>2</sub> in a solution of DETC produced the oxidised compounds DSF and DETC<sub>2</sub>:Cu that led to the oxidation of GSH into GSSH<sup>132</sup>. Therefore, the authors cautiously concluded that “dithiocarbamates are radical-scavenging compounds with pro-oxidant activity; that is, they remove one-electron oxidants (free radicals) but, in doing so, induce a state of two-electron oxidative stress (GSH conversion to GSSG; NADPH oxidation to NADP<sup>+</sup>).” This conclusion indicated that dithiocarbamates are oxidising agents. The scavenging of ROS, and therefore the reducing power of dithiocarbamates, generates oxidised disulphides or oxidised Cu-complexes that are able to deplete cells of reduced glutathione.

Chemical	Chemical structure	Oxidising properties	Antioxidant properties
PDTC		NF-κB inhibition <sup>128</sup>	Scavenging of ROS <sup>132</sup>
DETC		Inhibition of SOD <sup>117</sup>	Scavenging of ROS <sup>132</sup>
DSF		NF-κB inhibition <sup>129</sup> , glutathione depletion <sup>119,132</sup> , Cu chelation and Fenton-like reaction <sup>84</sup>	Scavenging of ROS <sup>132</sup> , reduction of lipid peroxidation <sup>131</sup>

**Table 2** The pro- and anti-oxidative properties of DSF and its derivatives

### 1.2.5 DSF acts as an anti-viral agent and as an immunomodulator

The effect of DSF and its derivatives on NF-κB activation and oxidative stress is perhaps best exemplified by its use in anti-viral therapy. The effectiveness of treatment against influenza and human immunodeficiency virus (HIV) infections is impeded by high mutation rates of these viruses. Consequently, targeting of viral components is not an optimal strategy. Instead, targeting the host cellular metabolism that is misused for the benefit of viral replication and that is not subjected to high mutation rates may prove more successful. The mechanism whereby the host's NF-κB is requisitioned for viral replication is not well understood. One possibility is that virus-infected cells release pro-inflammatory cytokines, which represents an activation trigger for macrophages to produce toxic ROS in order to kill infected tissues. The release of ROS is an activation trigger for the transcription factor NF-κB which, in turn, promotes transcription of viral genes<sup>133</sup>. Several investigators have studied the potential of NF-κB inhibitors, such as PDTC, to counteract viral infections such as influenza and HIV. It has been shown that PDTC increased the survival of influenza-infected mice and reduced infiltration of immune cells into influenza-infected tissues. It also decreased the production of interferon-gamma, thus limiting macrophage-mediated release of ROS and reducing secondary tissue damage<sup>134</sup>.

NF-κB was first recognised to be a transcription factor binding to the κB chain of immunoglobulin κ enhancer gene sequence<sup>135</sup>. NF-κB is involved in many immunological processes such as immunoglobulin production, the maturation of macrophages and the maturation and proliferation of T and B cells<sup>136</sup>. Despite the requirement for NF-κB in T

and B cell development, DETC-mediated inhibition of NF- $\kappa$ B activation was shown to promote T cell maturation to fully immunocompetent cells in athymic mice<sup>137</sup>. Since the immune system may recognise tumour cells and kill them, it is encouraging that DETC did not impede immune function but, on the contrary, enhanced T cell activation.

### 1.2.6 DSF in combination with chemotherapy

The multi-drug resistance syndrome is responsible for chemoresistance due to the pumping of drugs out of the cell. Drug efflux is mediated by the membrane-bound transporter P-glycoprotein (P-gp) and this mechanism is dependent on the availability of adenosine triphosphate (ATP). DSF was shown to inhibit P-gp drug efflux by modifying thiol groups in cysteine residues located within the ATP-binding cassette of P-gp<sup>138</sup>. Another study demonstrated that two DSF metabolites, S-methyl N,N-diethylthiocarbamate sulfoxide and S-methyl N,N-diethylthiocarbamate sulfone, also inhibited P-gp drug efflux<sup>139</sup>. Therefore, DSF may enhance chemotherapy by inhibiting P-gp-mediated chemoresistance, rationalising its use in combination with existing drug regimens for the treatment of neuroblastoma<sup>140</sup> or PCa<sup>141</sup>.

DSF is a highly reactive thiol-containing compound first discovered for its alcohol dehydrogenase inhibiting properties. Dehydrogenases represent a class of oxidizing enzymes which perform a variety of roles. They are mainly detoxifying enzymes, such as alcohol and aldehyde dehydrogenases, or metabolic enzymes, such as pyruvate or glucose-6-phosphate dehydrogenases. Dehydrogenases oxidise a substrate and transfer an electron to an acceptor, usually a molecule of NAD<sup>+</sup> or a functionally similar coenzyme. Dehydrogenases have various effects on xenobiotics such as chemotherapeutic agents. The oxidation can either convert the chemical into an active (e.g. etoposide) or an inactive form (e.g. cyclophosphamide).

Etoposide damages DNA through the formation of a cleavable complex with topoisomerase II and the formation of DNA-binding metabolites<sup>142</sup>. It was reported that etoposide cytotoxicity was inhibited by DSF *in vitro*<sup>143</sup>. Furthermore, other inhibitors of ALDH inhibited etoposide-induced cytotoxicity. The authors concluded that ALDH was required for the activation of etoposide<sup>143</sup>. Clearly, the combination of the ALDH-inhibitor DSF with etoposide is antagonistic and does not represent an efficient treatment modality worth pursuing.

On the other hand, cyclophosphamide requires a succession of metabolic transformations in order to be activated *in vivo*<sup>144</sup>. The active metabolite of cyclophosphamide, 4-hydroxycyclophosphamide, exists in equilibrium with aldophosphamide. ALDH is responsible for a decrease in active 4-hydroxycyclophosphamide by converting aldophosphamide into the non-toxic alcohosphamide. Therefore the benefit from ALDH inhibition in combination with cyclophosphamide has been suggested<sup>145</sup>. It has been shown that DSF was able to increase the oncolytic activity of cyclophosphamide in mice in a schedule-dependent manner<sup>146</sup>. Moreover, DSF could reduce cyclophosphamide-induced urologic toxicity to the bladder. However haematopoietic toxicity induced by cyclophosphamide was slightly increased by DSF<sup>146</sup>.

Furthermore, it has been shown that DSF prevents cisplatin-induced myelosuppression and nephrotoxicity without affecting anti-tumour activity<sup>147</sup>. While still controversial, the mechanism of DSF-mediated protection against cisplatin toxicity is thought to be due to chelation of platinum<sup>148</sup>, myeloprotection or through the shift of platinum excretion to the bile, thereby sparing the kidneys<sup>149</sup>.

Cisplatin and cyclophosphamide are used as first line chemotherapy of neuroblastoma. This regimen might be improved by the inclusion of DSF. On the other hand, combination with etoposide is likely to be antagonistic. Due to the inhibition of P-gp-mediated chemoresistance, DSF may still increase the retention of a wide range of chemotherapeutic drugs. However, the example of the antagonistic combination of DSF with etoposide illustrates the need for pre-clinical evaluation of the combinations of DSF with chemotherapeutic agents.

### **1.2.7 Cancer stem cells and ALDH**

Besides its role in alcohol metabolism, ALDH was also shown to be overexpressed in stem cells, both normal and malignant<sup>150</sup>. The cancer stem cell (CSC) hypothesis implicates normal stem cells as the origin of a tumour. CSC are capable of asymmetric division producing another CSC and a more differentiated tumour cell. It is thought that CSC are responsible for driving metastasis and for tumour relapse after therapy<sup>151</sup>. CSC escape treatment due to their limited number within a tumour, their location in hypoxic niches distant from blood vessels, and their chemoresistance and radioresistance. For instance, it has been shown that transgenic mice over-expressing ALDH were protected from alcohol-mediated enhancement of the pro-apoptotic machinery, indicating that aldehydes are pro-apoptotic and ALDH anti-apoptotic<sup>152</sup>. It has been suggested that ALDH inhibition by DSF

could re-establish CSC sensitivity to apoptosis<sup>150</sup>. Recently, it has been shown that glioblastoma neurospheres have increased ALDH levels compared with their monolayers counterparts<sup>153</sup>. Glioblastoma cells grown as neurospheres are thought to be enriched in glioblastoma stem-like cells. Interestingly, it has been found that the ability of the glioblastoma cells to form neurospheres could be inhibited by DSF in a Cu-dependent manner<sup>153</sup>. This study suggested that DSF has cytotoxic properties against glioblastoma CSC via the inhibition of ALDH. Since metastasis and relapse after treatment are the two leading causes of death from cancer, the targeting of CSC via the ALDH-inhibitory properties of DSF may be a useful new therapeutic strategy.

### **1.2.8 Angiogenesis**

Angiogenesis, the formation of blood vessels, is required to provide oxygen and nutrients to tumour cells in order to sustain growth. Therefore, anti-angiogenic chemotherapy has been devised for the treatment of cancer. Tumour-associated angiogenesis, like normal angiogenesis, requires Cu as a co-factor<sup>154</sup>. Although, there is no consensus mechanism to explain Cu requirement in blood vessel formation, angiogenic growth factors, such as vascular endothelial growth factor (VEGF) and fibroblast growth factor (FGF), require Cu binding for their secretion and activity. Cu chelators, such as penicillamine, have been shown to have anti-angiogenic properties<sup>155</sup>. It has been hypothesised that DSF may have similar properties. Indeed, DSF has been shown to inhibit metalloproteinases (MMP-9 and MMP-4)<sup>156</sup>, key enzymes in the angiogenic process that require zinc as a co-factor. DSF may inhibit MMPs via zinc chelation. However, it has been reported that DSF-induced inhibition of MMPs may be mediated by the activation of “reversion-inducing-cysteine-rich protein with kazal motifs” (RECK)<sup>157</sup> ENREF\_116, an inhibitor of metalloproteinases associated with favourable prognosis in colorectal cancer<sup>158</sup>. Therefore, DSF inhibits angiogenesis and may disrupt tumour homeostasis at the vascular stage of tumour development.

### **1.2.9 DSF targets cancer cells**

The specific targeting of malignant lesions rather than normal tissue by anti-cancer therapies diminishes the occurrence of side-effects. Cancer cells have a higher proliferation rate than normal cells, thus cancer cells are more susceptible to therapies targeting dividing cells, such as DNA damaging agents and radiotherapy. As a consequence of their higher metabolic rate, tumour cells have increased oxidative stress compared with normal cells, thus they are more susceptible to therapy designed to elevate oxidative stress beyond a threshold that will trigger cell death. It has also been shown that numerous components of

the proteasomal degradation pathway are overexpressed in tumour cell lines and in tumour biopsies<sup>159,160</sup>. Finally, cancer cells have a higher Cu content than normal cells. Elevated Cu levels, increased oxidative stress, elevated proteasome activity and faster proliferative rate of tumour cells compared with non-malignant cells are differences that can be exploited for the targeting of cancer cells over non-malignant cells. DSF has emerged as an anti-cancer agent due to its ability to interact with multiple components overexpressed in tumour cells and necessary for their survival:

- Inhibition of the proteasome
- Induction of oxidative stress via Cu deposition and inhibition of antioxidants such as glutathione and SOD
- Inhibition of angiogenesis
- Inhibition of resistance to therapy by inactivation of ALDH, NF- $\kappa$ B and P-gp
- Inhibition of ALDH and the targeting of CSC

#### **1.2.10 Pharmacology and toxicity of DSF**

From the pioneering work on the alcohol deterrent properties of DSF and its broader use in anti-addictive therapies to its anti-cancer properties, DSF targets a variety of cellular pathways which suggest the possibility of an unfavourable toxicity profile. A summary of the pharmacology and the toxicity of DSF is provided in the following paragraphs.

DSF is unstable *in vivo* and is rapidly metabolised. It has been shown that the peak plasma concentration of DSF in humans (0.35  $\mu$ g/ml; 1.18 $\mu$ M) is reached 10 h following a single oral dose of 250 mg and that the DSF plasma concentration is zero 72 h after administration<sup>161</sup>. DSF is reduced to DETC by GSH primarily in erythrocytes<sup>162</sup>. The reactivity of the free thiol of DETC confers upon itself the ability to form disulphide bridges with cellular thiols. Accordingly, it has been shown that approximately 20% of the drug remains bound to tissues in the body for 1 to 2 weeks after ingestion<sup>163</sup>. Alternatively, DETC can be chemically modified by liver enzymes through methylation and sulfoxidation or by conjugation to glucuronic acid for rapid excretion in urine<sup>164</sup>. Non-enzymatic breakdown of DETC may also occur, yielding carbon disulphide and diethylamine<sup>165</sup>.

Carbon disulphide is thought to be the most toxic metabolite of DSF, particularly to nerve cells<sup>166</sup>. The side-effects of DSF include hepatotoxicity<sup>167</sup>, optic neuritis<sup>168</sup>, encephalopathies and neuropathies<sup>166,169-172</sup>, malaise, nausea, diarrhoea, endocrine and cardiovascular abnormalities<sup>173</sup>. However, three case reports have described the reversible

nature of the side-effects after cessation of DSF or reduction of the dose<sup>109,169,170</sup>. The typical oral dose of DSF given to patients is 250-500 mg daily. In this regimen, the most severe side-effects (neurotoxicity) appear after several months of therapy<sup>173</sup>. Despite case reports of DSF-induced toxicity, millions of alcoholic patients have been treated safely with DSF since it was approved by the FDA in 1948<sup>174</sup>.

### **1.2.11 Old drugs, new tricks**

It is a long and expensive process to develop new and effective anti-cancer agents. It takes on average 13.5 years from discovery to marketing. It usually involves validation of a target, validation of targeting compounds, pre-clinical evaluation and Phase I, II and III clinical trials. However, the rate of drugs entering clinical trials and failing to demonstrate therapeutic efficacy is 70% in Phase II and 59% in Phase III<sup>175</sup> ENREF 131. These high failure rates are coupled with the high development cost of new compounds<sup>176</sup>. DSF was approved by the FDA in 1948 and has been in clinical use ever since for alcohol aversion therapy. Therefore the clinical practice, toxicity and other pharmacological data related to DSF, normally determined in lengthy and expensive clinical trials, are already well known.

Moreover, the cost of cancer treatment is escalating for the patient and societies. For instance, more than 90% of FDA-approved anti-cancer compounds in the last 4 years cost more than \$20,000 for a treatment lasting 12 weeks<sup>177</sup> ENREF 133. An alternative approach has been proposed: the use of non-profit drugs such as DSF<sup>178</sup> ENREF 134. This involves using off-target effects of cheap and available old drugs. One year's treatment with DSF costs £550 per patient<sup>178</sup>. DSF has recently been described as an anti-cancer agent for its Cu-dependent cytotoxicity. This is an off-target effect, i.e. unrelated to ALDH inhibition which is responsible for alcohol aversion. In a financial climate where investments are at risk, it is not surprising to see many studies and clinical trials investigating DSF as an anti-cancer therapy<sup>179</sup> ENREF 135.

### **1.2.12 Clinical trials involving DSF**

There are five clinical trials listed by the US National Institute of Health, which aim to determine the feasibility of DSF treatment in cancer patients (Table 3). Several scientific approaches have been chosen in these clinical trials. Whereas two clinical trials are investigating the effect of DSF alone in prostate cancer and melanoma, three are investigating the effect of DSF in combination with Cu, cisplatin or standard radio-chemotherapy. The Cu-dependency of DSF cytotoxicity is well known; therefore it is important to test whether Cu supplementation is required to enhance the tumour control by

DSF in humans. Secondly, the clinical trials investigating the combinations of DSF with cisplatin in non-small cell lung cancer or with standard radio-chemotherapy of glioblastoma multiform are testing the hypothesis that DSF is an effective adjuvant therapeutic option. The ability of DSF to enhance chemotherapy with cisplatin via inhibition of side-effects or the ability of DSF to inhibit P-gp-mediated chemoresistance was discussed previously (Section 1.2.6).

Principal investigator	Cancer	Comment	Phase	Dose	ID
Nechustan H	Non-small cell lung cancer	Combination with cisplatin	II - III		NCT00312819
Grossmann K	Solid tumour metastasis to the liver	Combination with Cu gluconate	I	250 mg DSF + 2 mg Cu gluconate daily	NCT00742911
Fruehauf JP	Metastatic melanoma		I - II	250 mg twice daily	NCT00256230
Karamanakos PN	Glioblastoma multiform	DSF as an adjuvant therapy prior to standard radio-chemotherapy	II		NCT01777919
Carducci MA	Prostate cancer			250 or 500 mg daily	NCT01118741

**Table 3 Clinical trials investigating DSF as an anti-cancer therapeutic**

### 1.2.13 DSF, a radiation modifier

A consideration of the biological effects of DSF also provides a rationale for the investigation of DSF in combination with radiation. The activation of NF- $\kappa$ B results in the expression of anti-apoptotic and antioxidant genes which confers upon cells radioresistant properties (Section 1.2.4.2). Thus, the inhibition of the proteasome/NF- $\kappa$ B pathway by DSF could explain radiosensitising properties of DSF. On the other hand, the pro- and anti-oxidative properties of DSF led to the hypotheses that DSF was a radiosensitiser and a radioprotector, respectively. The conflicting literature describing the radiomodifying properties of DSF is presented in Table 4 and is described below.

Author	In vivo	In vitro	Chemical	Schedule	Radiomodification	Endpoint
Van Bekkum DW (1956) <sup>180</sup>	Yes	No	DSF 4800 mg/kg	Simultaneous	No effect	30-days survival
Nemavarkar P et al. (2004) <sup>181</sup>	No	Yes	DSF 100-200 $\mu$ M	DSF 20 min post IR	No effect	Yeast survival
Nemavarkar P et al. (2004) <sup>181</sup>	No	Yes	DSF 100-200 $\mu$ M	DSF 20 min pre IR - wash	No effect	Yeast survival
Taylor RD et al. (1986) <sup>182</sup>	No	Yes	DSF 0.337 $\mu$ M	DSF 24 h prior IR - no wash	No effect	Surviving fraction
Evans RG et al. (1982) <sup>183</sup>	No	Yes	DETC 1 mM	DETC 1 h prior to IR - no wash	Radioprotection	Surviving fraction
Evans RG et al. (1983)	Yes	No	DETC 1000 mg/kg	DETC 0.5 h prior to IR	Radioprotection	Survival
Van Bekkum DW (1956) <sup>180</sup>	Yes	No	DETC 360 mg/kg	Simultaneous	Radioprotection	30-days survival
Rencova J et al. (1997) <sup>184</sup>	Yes	No	DETC 120 mg/kg	Simultaneous	Radioprotection	Survival
Nemavarkar P et al. (2004) <sup>181</sup>	No	Yes	DSF 100-200 $\mu$ M	Simultaneous	Radioprotection	Yeast survival
Gandhi NM et al. (2003) <sup>185</sup>	Yes	No	DSF 50 mg/kg	DSF 1 h prior to IR	Radioprotection	Lipid peroxidation and DNA damage
Kent et al. (1988) <sup>186</sup>	Yes	No	DETC 50 mg/kg	DETC 2 to 4 h prior to IR	Radiosensitisation	Tumour growth delay
Lin PS et al. (1979) <sup>187</sup>	No	Yes	DETC 0.1 $\mu$ M	DETC 1 h prior to IR - no wash	Radiosensitisation	Surviving fraction
Evans RG et al. (1982) <sup>183</sup>	No	Yes	DETC 1 mM	Simultaneous	Radiosensitisation	Surviving fraction
Stone D et al. (1978) <sup>188</sup>	No	Yes	DETC 2.4 mM	DETC 1 h after IR	Radiosensitisation	Haemolysis
Stone D et al. (1978) <sup>188</sup>	No	Yes	DETC 2.4 mM	DETC 1 h prior to IR - no wash	Radiosensitisation	Haemolysis
Westman G et al. (1980) <sup>189</sup>	No	Yes	DETC 3 mM	DETC 1 h prior to IR - wash	Radiosensitisation	Surviving fraction

**Table 4 The conflicting literature on the modification of the radiation effect by DSF and DETC**

### 1.2.13.1 The mixed disulphide theory

Thiol groups are major constituents of cellular proteins. They are readily oxidised to form disulphide bridges. According to the mixed disulphide theory, thiol-containing compounds (R1-SH) exist in a mixed disulphide state with the target cellular thiol (R2-SH):



Being already oxidised, the mixed disulphide confers radioprotection to the target cellular thiol from the oxidising effect of IR<sup>190</sup>. Many thiol-containing compounds, including DSF and its metabolite DETC, have been studied for their radioprotective properties in the search for a compound that would protect workers in the radiation industry and the armed forces<sup>180,191</sup>. The mixed disulphide must be a transient and reversible complex in order to avoid toxicity in case of the target cellular thiol being involved in vital cellular processes. Thus, the timing and scheduling of administration of the thiol-containing compound simultaneously with or around the time of irradiation is critical in order to achieve optimal radioprotection.

The mixed disulphide theory also offers an explanation for the radiosensitising effect of thiol-containing compounds. The glutathione system is responsible for the redox homeostasis of the cell by cycling between GSH and GSSG. Therefore, thiol-containing compounds may form a mixed disulphide with GSH:



In this context, the GSH pool would be diminished, making the cell more susceptible to oxidative stress from IR. The mixed disulphide theory offers an explanation for both the radiosensitisation and radioprotection conferred by DSF and its derivatives (Table 4).

### 1.2.13.2 Radioprotection

DSF and its metabolic derivatives, including DETC, were screened for their ability to alter the lethal effect of X-rays in mice<sup>180</sup>. It has been found that all tested compounds, but not DSF, had radioprotective properties. This is surprising because DSF is metabolised to two DETC molecules and DETC was found to be radioprotective. However, unlike the other

compounds, the administration of DSF was intraorally in arachis oil, which, according to the author, caused diarrhoea thus limiting absorption of DSF into the body<sup>180</sup>.

Another study reported that Sprague-Dawley rats died within 14 to 44 days after a tail vein injection of 1.45 MBq/kg of <sup>210</sup>Po whereas they died within 36 to 93 days after the same <sup>210</sup>Po treatment but co-administered with 120 mg/kg of DETC<sup>184</sup>. DETC also partially restored blood and bone marrow cell count. The radioprotective mechanism of DETC was argued to be due to chelation of <sup>210</sup>Po to facilitate its excretion<sup>184</sup>.

Other mechanisms of radioprotection by DSF or its derivatives have been demonstrated in two studies. The yeast *Saccharomyces cerevisiae* was investigated, cultured either in its aerobic or anaerobic state. Radioprotective properties of DSF were observed in the aerobic cultures but not in the anaerobic ones, suggesting that scavenging of radiation-induced ROS is the mechanism by which DSF protects from the lethal effect of radiation<sup>181</sup>. By extrapolation, one can consider anaerobic cultures to resemble hypoxic tumours, which rely on glycolysis for energy production, and aerobic cultures to mimic non-malignant cells. If oxygen level is lower in the tumour than in normal tissue, radioprotection by DSF could only be achieved in healthy non-malignant tissues.

Interestingly, others have reported the reduction of radiation-induced lipid peroxidation and DNA damage *in vivo* by DSF<sup>185</sup> and the protection of bone marrow colony forming units *in vivo* following irradiation<sup>192</sup>.

### **1.2.13.3 Radiosensitisation**

In a study involving erythrocytes, DETC was shown to enhance radiation-induced haemolysis which was likely due to inhibition of SOD and subsequent elevation of ROS levels<sup>188</sup>. This result have been supported by two subsequent reports<sup>187,189</sup>. These data are in striking opposition to radioprotection due to scavenging of ROS by DSF<sup>181</sup>.

Interestingly, a study reported that, when non-cancerous cells in the plateau phase of growth were irradiated and immediately thereafter exposed to 1 mM of DETC, an enhanced kill compared with radiation alone was detected<sup>183</sup>. This effect was not observed when the same scheduling and dosing of DETC and radiation were applied to cells maintained in Hank's balanced salt solution (HBSS) as opposed to Eagle's minimum essential medium complemented with foetal calf serum (FCS)<sup>183</sup>. One may conclude that

complemented medium contains an agent that confers upon DETC the ability to enhance radiation-induced cell kill.

#### **1.2.13.4 All about scheduling?**

In the study comparing the radiomodifying effect of DETC in cells maintained in complemented culture medium compared with cells maintained in HBSS<sup>183</sup>, DETC was shown to have radioprotective properties if the cells were exposed to DETC for 1 hour prior to irradiation and a radiosensitising effect if the cells were exposed to DETC at the same time as irradiation<sup>183</sup>, suggesting that scheduling was critical. However, in a separate study, it has also been shown that cells exposed to DETC 1 h prior to irradiation or 1 h after irradiation were both radiosensitised<sup>188</sup>. One possible explanation for these contradictory results is that non-dividing Chinese Hamster HA-1 fibroblasts were used in the first study whereas human erythrocytes were used in the second. Erythrocytes transport oxygen and thus rely to a greater extent on ROS detoxifying enzymes, such as SOD, than the HA-1 cells to protect themselves from the oxidising effect of radiation. This would make erythrocytes more susceptible to SOD inhibition due to DETC and explain the potent radiosensitising effect of both schedules. In the first study, the radioprotective effect of DETC (the cells were exposed to DETC 1 h prior to irradiation) was in line with the theory that constituents of the cells are protected from the oxidative effect of radiation by mixed disulphide formation. In the simultaneous treatment, DETC may not have had time to bind cellular thiols therefore failing to protect against radiation. Pre-incubation with DETC was required for radioprotection whereas radiosensitisation occurred instantly (the simultaneous exposure to radiation and DETC was radiosensitising). This implies that the radioprotective mechanism of DETC is a slower mechanism than its radiosensitising effect.

Among the *in vivo* studies listed in Table 4, DETC given 0.5 to 1 h prior to irradiation provided radioprotection<sup>185,186,193</sup> whereas DETC given 2 to 4 h prior to irradiation afforded radiosensitisation<sup>186</sup>. The longer pre-incubation period before irradiation resulted in radiosensitisation whereas the shorter pre-incubation period resulted in radioprotection, which was contradictory to the *in vitro* findings described in the previous paragraph. These results demonstrated the added complication of *in vivo* scheduling of radiosensitisers with radiation. For optimal combination therapy, the time taken for the radiosensitiser to penetrate the tumour must be taken into account in order to achieve maximal intratumoural activation/inhibition of the radiosensitising target at the time of tumour irradiation.

Likewise, in the case of targeted radiotherapy, knowledge about the time taken for the radiopharmaceutical to reach the tumour must be taken in account. The effect of DETC on the survival of rats following injection of the radionuclide  $^{210}\text{Po}$  (1.45 MBq/kg) has been evaluated<sup>184</sup>. The schedule for optimal DETC-induced radioprotection is dependent on  $^{210}\text{Po}$  pharmacodynamics. For example, absorbed  $^{210}\text{Po}$  remains in the body with a half-time of over 100 days<sup>194</sup>. Thus, in the study evaluating the effect of DETC on the survival of rat following administration of  $^{210}\text{Po}$ , tissues were exposed to  $^{210}\text{Po}$  irradiation for over 100 days. DETC peak plasma concentration occurs 10 h after a single oral dose<sup>161</sup>. DETC was given ten times over 2 weeks after  $^{210}\text{Po}$  administration. Therefore, DETC was bound to tissues during at least the first two weeks during which tissues were exposed to irradiation from  $^{210}\text{Po}$ , conferring radioprotection during this period.

#### **1.2.14 Conclusion**

Despite its use as an alcohol deterrent for the past 60 years, the biological effects of DSF are still not completely understood. The multiplicity of targets inhibited by DSF and overexpressed in cancer cells (Section 1.2.9) makes DSF an attractive anti-cancer option. The scavenging of ROS and the reduction of peroxidised lipids were shown to confer upon DSF and its derivatives antioxidant properties whereas the reduction of the glutathione pool, the inhibition of SOD-mediated removal of ROS, the inhibition of NF- $\kappa$ B activation and the deposition of Cu were shown to confer upon DSF and its derivatives oxidising properties (Table 2). Of the studies listed in Table 4, DETC was shown to be a radioprotector and a radiosensitiser whereas DSF was shown to have no effect or to be radioprotective. There was no association between pro-oxidative or anti-oxidative properties of DSF or DETC with radiosensitisation or radioprotection, respectively. Strikingly, the demonstration of radioprotection by DSF via scavenging of ROS<sup>181</sup> was in sharp contrast to the radiosensitisation by DETC via inhibition of SOD and subsequent rise of ROS<sup>188</sup>. The studies listed in Table 4 are heterogeneous with respect to the dose range of DSF or DETC used (0.1  $\mu\text{M}$  to 2.4 mM), the use of different schedules of combination treatment with radiation and the endpoint investigated. There was no trend found between these parameters and the observation of radiosensitisation or radioprotection. This indicated the existence of other determinants of the radiomodifying property of DSF and its derivatives, such as the amount of Cu present, the status of NF- $\kappa$ B, P-gp expression, SOD activity or glutathione levels.

## 2 Thesis aims

- to investigate the dependence on Cu of DSF toxicity
- to investigate alternative determinants of the radiomodifying properties of DSF
- to quantify the radiomodifying properties of DSF in cellular monolayers following external beam irradiation
- to quantify the radiomodifying properties of DSF in multicellular tumour spheroids following exposure to [<sup>131</sup>I]mIBG or [<sup>131</sup>I]MIP-1095
- to determine a mechanism explaining the radiomodifying properties of DSF

### 3 The Cu-dependent toxicity of DSF to tumour cells grown as monolayers.

#### 3.1 Introduction

##### 3.1.1 The cytotoxic activity of DSF is imperfectly understood

DSF targets multiple molecular entities that are essential for the survival and the proliferation of cancer cells, notably the proteasome and NF- $\kappa$ B<sup>121,129,195</sup>. The proteasome is involved in many biological pathways including antigen presentation<sup>196</sup>, survival, progression through the cell cycle and apoptosis<sup>197,198</sup>. NF- $\kappa$ B is a stress sensor which, upon activation, drives the transcription of antioxidant and of anti-apoptotic genes<sup>199,200</sup>. The inhibition of the proteasome/NF- $\kappa$ B axis was hypothesised to confer upon DSF pro-oxidative and pro-apoptotic properties<sup>201-203</sup>. Another cancer-related target of DSF is superoxide dismutase (SOD) whose inhibition also results in increased oxidative stress<sup>117,204</sup>. By virtue of its disulphide bridge, DSF interacts with the glutathione system, thereby altering the antioxidant defences of the tumour cell<sup>120</sup>. The pro-oxidative effect of DSF is mediated by the inhibition of multiple targets (the glutathione system, SOD, NF- $\kappa$ B) resulting in the reduction of cell viability and cell death<sup>205</sup>. However, the concentration-dependent cytotoxicity of DSF is not well understood. It has been demonstrated that DSF-induced cell kill follows a reverse N-shape relationship with increasing concentration *in vitro*<sup>206</sup>. Explicitly, DSF induced cell kill at low concentration followed by a reversal of cytotoxicity at higher concentration and a further increase in DSF concentration resulted in a second phase of cell kill. This biphasic response profile cannot be explained by conventional pharmacological laws stipulating that a particular effect follows a linear, hyperbolic or sigmoidal relationship with increasing dose.

It has been hypothesised that the biphasic response profile might be due to the multiplicity of disulfiram targets but this hypothesis was not tested<sup>206</sup>. According to this hypothesis, the inhibition of one particular molecular target (target 1) by DSF would lead to cell kill at low concentrations and the inhibition of a second particular target (target 2) would lead to a second cell kill at high concentrations. The  $IC_{50}$  value of mechanism 1 ( $IC_{50-1}$ ) should be lower than the  $IC_{50}$  value of mechanism 2 ( $IC_{50-2}$ ). Furthermore, in order to explain the reversal of cytotoxicity observed at intermediate concentrations of DSF, mechanism 2 and mechanism 1 should be antagonistic. As the DSF concentration increases beyond  $IC_{50-1}$  but has not yet reached  $IC_{50-2}$ , mechanism 2 inhibits mechanism 1 resulting in a reversal of cytotoxicity. A further increase in DSF concentration results in cytotoxicity due to mechanism 2 only (Figure 7).

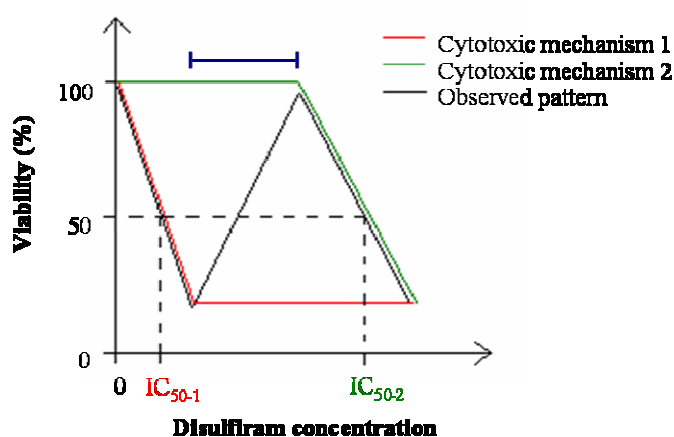


**Figure 7 The two-mechanisms hypothesis of the particular concentration-effect of DSF**

The inhibition of target 1 results in the loss of viability in the low concentration range of DSF which is defined by  $IC_{50-1}$ . Similarly, the inhibition of target 2 results in the loss of viability in the high concentration range of DSF which is defined by  $IC_{50-2}$ . The range of DSF concentrations indicated by the blue segment defines the concentration range of DSF at which mechanism 2 is not yet cytotoxic but antagonises mechanism 1 resulting in reversal of cytotoxicity.

The DSF metabolite diethyldithiocarbamate (DETC) may be produced by the chemical or enzymatic reduction of the disulphide bridge of DSF. DETC could then have cytotoxic effects of its own but with potency ( $IC_{50}$ ) different from that of DSF. Therefore, it was hypothesised that the biphasic response profile may be due to the alternative chemical form of DSF. However, DETC was shown to have similar proteasome-inhibitory effects to DSF<sup>121,207</sup>, suggesting that DETC is not responsible for the biphasic response profile.

*In vivo* experiments have demonstrated that DSF can delay the growth of melanoma as well as breast and prostate carcinoma xenografts in mice<sup>109,121,208,209</sup>. The biphasic response profile has never been reported *in vivo*. However, these studies investigated the xenograft growth delay after a single dose of DSF (30, 50 or 200 mg/kg). The  $LD_{50}$  dose of DSF given orally is 1,980 mg/kg in mice<sup>210</sup>. Thus, the DSF doses administered to animals in these studies (30, 50 or 200 mg/kg) are an order of magnitude lower than what can be used safely in mice. However, the routine regimen of DSF therapy in alcoholic patients is daily oral intake of 250 or 500 mg<sup>161</sup>. In an average man weighing 75 kg, this dose corresponds to 3.33 or 6.66 mg/kg in men. Within the methodological limits of extrapolating from mice to humans, the doses used in the animal experiments stated above are in excess compared to what is routinely used in men. The effect of a wide dose range of DSF on the growth of xenografts remains to be investigated and the existence of a biphasic response profile *in vivo* has yet to be resolved.

Finally, the biphasic response profile may represent an artefact of the experimental setup. For instance, one property of DSF is chelation of Cu<sup>205</sup>. Similarly to DSF, the majority of Cu-binding proteins in the human body contain thiol-rich domains that form the Cu-binding site<sup>211</sup>. DSF chelates Cu through the interaction of its four sulphur atoms and has been shown to increase dramatically the cytotoxic<sup>205</sup> and the proteasome-inhibitory effects of DSF<sup>121</sup>. Notably, Cu is present in the serum used to complement cell culture medium<sup>212</sup>. It has been demonstrated that the cytotoxicity of PDTC, a member of the dithiocarbamate family, increased with the serum content of the culture medium<sup>213</sup>. Since PDTC-mediated cytotoxicity was prevented when dialysed serum was used, the authors concluded that cytotoxicity was due to a protein. However, since Cu binds to proteins and is rarely in its free ionic form in biological systems, dialysis may also have eliminated Cu from the serum. Since Cu increases DSF-induced cytotoxicity, the Cu concentration must be carefully monitored in all experiments involving DSF. Accordingly, serum-free culture medium was used in the ensuing investigation of the cytotoxicity of DSF in Cu-controlled conditions.

### **3.1.2 The importance of defining the concentration-effect relationship of DSF on the basis of pharmacological laws.**

The work in the following chapters will focus on the cytotoxic effect of the combination of DSF with  $\gamma$ -radiation. In order to analyse the effect of a combination treatment, one has to understand the interaction between the single agents used in the combination. Combination analyses are more extensively explained in the next chapters. For now, suffice to say that the analysis of a combination treatment depends on the application of a mathematical model, the median effect principle, which is built from pharmacological laws that describe the concentration-effect relationship of the single agents<sup>214</sup>. Particularly, the dose-effect relationship is described by two parameters: the concentration reducing the effect by 50% (IC<sub>50</sub>) and the coefficient of sigmoidicity *m* of the concentration-effect relationship. DSF-induced cytotoxicity does not follow a classical concentration-effect relationship, as indicated by the biphasic response profile. Therefore the evaluation of the interaction between DSF and radiation is not amenable to combination analyses which require a monotonic response to dose escalation. The experimental work of this chapter will determine the effect of equimolar concentrations of DSF and Cu (DSF:Cu). It will be also be shown that the median effect principle can describe DSF:Cu-induced cytotoxicity.

## 3.2 Aims

The aims of this chapter are:

- determination of the involvement of Cu in the biphasic response profile of DSF.
- determination *in vitro* of the parameters  $IC_{50}$  and  $m$  of the concentration-effect relationship of DSF and DSF:Cu in SK-N-BE(2c) and UVW/NAT cells

## 3.3 Materials and methods

### 3.3.1 Cell culture

The cell lines SK-N-BE(2c) (neuroblastoma) and LNCaP (prostate carcinoma) were purchased from the American Tissue Culture Collection (ATCC). SK-N-BE(2c) cells were grown in Dulbecco's modified essential medium (DMEM) media supplemented with 15% (v/v) FCS (Autogen Bioclear), 2 mM L-glutamine and 1% (v/v) non-essential amino acids. LNCaP cells were grown in Roswell Park Memorial Institute (RPMI) media supplemented with 10% (v/v) FCS (Hyclone, Fisher Scientific, UK), 4 mM L-glutamine, 10 mM HEPES, 2.52 g/l D-glucose and 1 mM sodium pyruvate. The UVW/NAT cell line was derived from a human glioblastoma and obtained from the Medical Oncology Department, Beatson Laboratories, Glasgow<sup>215</sup>. It was previously transfected to express the NAT gene (UVW/NAT)<sup>92</sup>. UVW/NAT cells were grown in Modified Essential Medium (MEM) supplemented with 10% (v/v) FCS (Autogen Bioclear), 2 mM L-glutamine and 1 mg/ml geneticin for the selection of the NAT-expressing cells. All media and supplements were obtained from Invitrogen (Paisley, UK).

SK-N-BE(2c), UVW/NAT and LNCaP monolayers were passaged twice weekly at 1:10, 1:10 and 1:3 dilutions, respectively. Fresh cultures were thawed from liquid nitrogen stock at passage 30. The monolayers were incubated at 37°C in a 5% CO<sub>2</sub> atmosphere.

### 3.3.2 Drugs and drugs treatments

The following nomenclature for DSF and Cu complexes will be adopted in this thesis:

- DSF refers to the molecule of DSF without addition of copper
- DETC refers to the molecule of dithiocarbamate obtained by reduction of the disulphide bridge of DSF
- DSF:Cu refers to the Cu-chelated form of DSF obtained by mixing equimolar concentrations of DSF and Cu
- DETC<sub>2</sub>:Cu refers to the Cu-chelated form of DETC obtained by mixing DETC and Cu in a 2 to 1 molar ratio of DETC to Cu
- Cu[DETC]<sub>2</sub> is the commercial form of Cu-chelated DSF.

It is important to note that the chemical formulae of DSF:Cu, DETC<sub>2</sub>:Cu and Cu[DETC]<sub>2</sub> are similar.

All treatments were carried out using cells in exponential growth. DSF and DETC were dissolved in 100% dimethyl sulfoxide (DMSO). DSF, DETC and DSF:Cu treatments were carried out in culture media for 24 h at 37°C and 5% CO<sub>2</sub>. The concentration of DMSO was kept constant at 0.1% (v/v) in all treatments. When indicated, the Cu chelator bathocuproine disulfonate (BCPD) or the radical mop NAC were added along with DSF. Cu, in the form of chloride salt, was dissolved in water before addition to the culture medium. Serum-free culture medium was used in the cases where the concentration of Cu required to be controlled. Untreated controls with serum-free culture medium were always included. After 24 h of treatment, the cells were washed three times in phosphate-buffered saline (PBS) in order to remove the drugs. DMSO, DSF, DETC, Cu, BCPD and NAC were obtained from Sigma-Aldrich (Dorset, UK). The DSF tablets Antabuse were obtained from Actavis, Denmark, and Cu[DETC]<sub>2</sub> was obtained from Tokyo Chemical Industry.

### **3.3.3 Viability assay**

The reduction of 3-(4,5-Dimethylthiazol-2-yl)-2,5-diphenyltetrazolium (MTT) to formazan by mitochondrial reductases was assessed as described previously<sup>216</sup>. Cells were seeded in 96-well plates (Iwaki, Japan) at 37°C and 5% CO<sub>2</sub>. Once in exponential growth, 200 µl of fresh medium containing drugs was added. After 24 h incubation, the drug-containing medium was removed and replaced by fresh, drug-free medium. Then 50 µl of a 5 mg/ml MTT solution (Sigma-Aldrich, Dorset, UK) was added for 4 h in the dark and at 37°C. The medium containing MTT was then removed and formazan was solubilised with DMSO. Cell viability is proportional to the absorbance of formazan at 570 nm. The spectrophotometer Emax precision microplate reader (Molecular devices, US) was used to measure formazan absorbance at 570 nm.

### **3.3.4 Clonogenic assay**

After drug treatments, the cells were trypsinised and counted using a haemocytometer. For every treatment, cells were seeded in triplicate dishes (Nunclon, Roskilde, Denmark) in 4 ml fresh medium. Preliminary experiments indicated that the appropriate cell number to seed per dish was 250 for UVW/NAT and 600 for SK-N-BE(2c). The number of cells to seed per dish was chosen experimentally to yield the maximal number colonies without overlapping. The plating efficiencies were  $70.55 \pm 4.64\%$  and  $32.98 \pm 2.40\%$  for

UVW/NAT and SK-N-BE(2c), respectively. The colonies were allowed to grow for up to 14 days at 37°C and 5% CO<sub>2</sub>. The medium was then removed; the colonies were washed in PBS and fixed in 50% (v/v) methanol in PBS. Methanol was removed after 10 min and the dishes were allowed to dry. The colonies were stained with a 0.1% (v/v) crystal violet (Sigma-Aldrich, Dorset, UK) for 10 min and rinsed with tap water. Colonies containing more than 50 cells were then counted by eye. The surviving fractions were calculated for each treatment by dividing the number of colonies derived from treated cultures by the number of colonies of the untreated control. Three independent experiments were performed for every cell line.

### 3.3.5 The median effect principle

The median effect principle<sup>217</sup> is a mathematical model describing the relationship between a dose D of an agent and its associated effect fa/fu:

$$fa/fu = (D / IC_{50})^m \quad (3)$$

where fa is the fraction affected by the dose D, fu is the fraction unaffected by a dose D (fu = 1 – fa), IC<sub>50</sub> is the dose which inhibits 50% of the effect and m is the coefficient describing the shape of the dose-effect relationship, where m = 1, m > 1, and m < 1 indicate hyperbolic, sigmoidal, and flat sigmoidal dose-effect curves, respectively<sup>214</sup>.

The logarithmic form of equation (3) converts it into a linear form “y = mx + b”:

$$\log fa/fu = m \log D - m \log IC_{50} \quad (4)$$

A linear regression using the method of least squares applied to equation (4) allows the determination of the slope m and of the y-intercept b (b = - m log IC<sub>50</sub>). The IC<sub>50</sub> can then be calculated using:

$$IC_{50} = 10^{-b/m} \quad (5)$$

The accuracy of the calculation of the IC<sub>50</sub> and m depends on the degree of fitness of the linear transformation of the data obtained after the method of least squares has been applied to equation (4). The degree of fitness is measured by the coefficient of determination R<sup>2</sup>. R<sup>2</sup> values higher than 0.9 were accepted<sup>214</sup>.

### 3.3.6 Absorbance measurement

The absorbance profiles of DSF, DETC, Cu, DSF:Cu and Cu[DETC]<sub>2</sub> were obtained using a UV/VIS spectrophotometer Lambda 25 (Perkin Elmer). Each compound or mixture was dissolved in 1 ml DMSO and the absorbance profiles were obtained for wavelengths ranging from 200 to 600 nm.

In subsequent experiments, the absorbance at 438 nm was measured in 200 µl DMSO using an Emax precision microplate reader (Molecular devices, US). When the absorbance of DSF:Cu was measured intracellularly, 100% (v/v) DMSO was added onto the cells in order to solubilise DSF:Cu. For the experiments carried out in the presence of a reducing agent, ascorbic acid (Asc ac) was also dissolved in DMSO.

### 3.3.7 Proteasome assay

Chymotrypsin-like proteasomal activity was measured using Proteasome-Glo™ Chymotrypsin-Like, Trypsin-Like and Caspase-Like Cell-based Assay kit (Promega, US). Exponentially growing cells were treated in 96-well plates with equimolar concentrations of DSF and Cu for 8 h at 37°C and 5% CO<sub>2</sub>. The known proteasome inhibitor bortezomib was used as a positive control. Exponentially growing cells were treated in 96-well plates with bortezomib for 2 h at 37°C and 5% CO<sub>2</sub>. The cells were washed with PBS and resuspended in 100 µl of PBS. One hundred µl of the manufacturer's buffer containing luciferase and the proteasome substrate Suc-LLVY-luciferin was then added to the cells. Proteasomal cleavage released aminoluciferin which can then be used as a substrate by luciferase. Luciferase released a luminescent signal which was a measure of proteasomal activity. Luminescence was measured using a Lmax luminometer (Molecular Devices, US).

### 3.3.8 Fluorescence-activated cell sorting (FACS) analysis of the cell cycle

Proliferating cells can be categorised by virtue of their DNA content. Cells that have undergone mitosis but have not yet started to replicate their DNA contain N amount of DNA. This is the G<sub>0</sub>/G<sub>1</sub> population. Cells that have replicated their DNA but not yet undergone mitosis contain 2N amount of DNA. This is the G<sub>2</sub>/M population. Cells containing between N and 2N amount of DNA are in the DNA replicating phase called S. The fluorescent DNA-binding molecule propidium iodide (PI) can be used to determine the cell cycle profile of a population of cells based on DNA content<sup>218</sup>. The cells were treated with DSF:Cu and harvested by trypsinisation after 1, 2, 4, 8, 12 and 24 h. The cells were

washed and fixed in a dH<sub>2</sub>O solution containing 70% (v/v) ethanol for at least 24 h at -20°C. Ethanol was washed off and the cells were suspended in PBS containing 20 µg/ml of PI and 200 µg/ml of RNase A for 2 h at room temperature in the dark. The cell cycle profile was obtained by FACS analysis using FACSCalibur (BD Biosciences, Mountain View, CA). The data were acquired using BD CellQuest™ Pro software (BD Biosciences, Mountain View, CA). A minimum of 10,000 cells was acquired for each sample. The percentage of cells in each phase of the cell cycle (G0/G1, S and G2/M) was obtained using the analysis software FlowJo (BD Biosciences, Mountain View, CA). An example of the analysis and gating on cell populations of interest using FlowJo is shown in the appendix (Figure 80).

### **3.3.9 Statistical analysis**

The independent samples t-test was used to compare the means of two groups. The assumption of equal variance was tested using Levene's test. All statistical tests were carried out using SPSS v.19 (IBM). If the p-value was greater than 0.05, the difference was not considered statistically significant.

## **3.4 Results**

### **3.4.1 The biphasic response profile of DSF**

The biphasic response profile of DSF was compared with that of Antabuse (clinical version of DSF in the form of tablets) in SK-N-BE(2c) cells. Serum-complemented culture medium was used. DSF and Antabuse induced similar biphasic response profiles. The first clonogenic cell kill, ranging from 55% for DSF and 75% for Antabuse, was observed at 1.7 µM. The reversal of cytotoxicity peaked at 10 µM. A further increase in DSF or Antabuse concentrations yielded a 70% clonogenic cell kill at 16.9 µM (Figure 8a).

The clonogenic cell kill at low and high concentrations of DSF may represent two different mechanisms reflecting the multiple targets inhibited by DSF. BCPD, a Cu chelator, and the antioxidant NAC were used to assess the involvement of Cu and the involvement of oxidative stress in the DSF-induced clonogenic cell kill, respectively. BCPD (300 µM) prevented the clonogenic cell kill at DSF concentration less than 3.4 µM, implicating a Cu-dependent mechanism of cytotoxicity at these low DSF concentrations. On the other hand, NAC prevented the clonogenic cell kill at concentrations of DSF higher than 10.1 µM, implicating a pro-oxidative mechanism of cytotoxicity at the higher DSF concentrations (Figure 8b). These observations are consistent with Cu-dependent, DSF-induced

clonogenic cell kill at low DSF concentration whereas cytotoxicity at high concentrations of DSF was dependent on the generation of oxidative stress. These results were repeated in a second cell line, UVW/NAT, but were reported elsewhere<sup>219</sup>.

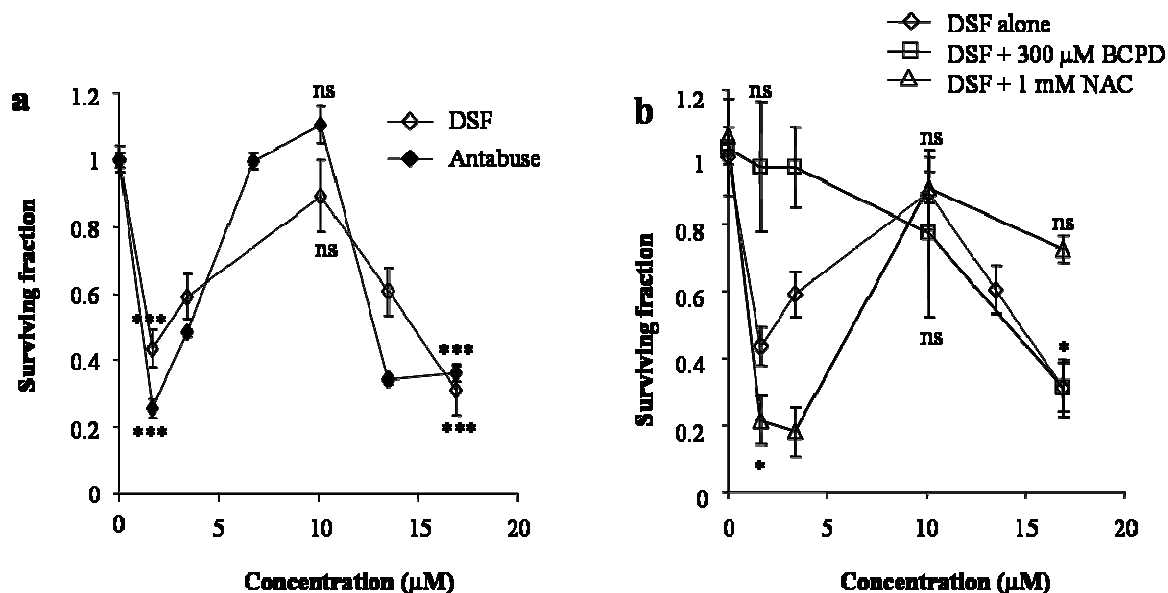


**Figure 8** The biphasic response of SK-N-BE(2c) clonogens to treatment with DSF

(a) Clonogenic assay was used to determine the surviving fraction of SK-N-BE(2c) cells following treatment with DSF or Antabuse alone. (b) The clonogenic survival of SK-N-BE(2c) was determined after treatment with DSF in the presence or in the absence of the Cu chelator bathocuproine disulfonate (BCPD) or the antioxidant N-acetylcysteine (NAC). Data are means  $\pm$  SEM;  $n=3$ . The independent samples t-test was used to compare the mean surviving fraction of the treated groups with that of untreated controls. One symbol (\*) indicates  $p < 0.05$  and three symbols indicate  $p < 0.001$ , respectively.

### 3.4.2 The effect of the molar ratio of DSF or DETC to Cu on the cytotoxicity of DSF and DETC

The MTT assay was used to assess viability of SK-N-BE(2c), LNCaP and UVW/NAT cells following exposure to various ratios of molar concentrations of DSF and Cu. The same investigation was carried out with the DSF metabolite DETC. DETC is formed after reduction of the disulphide bridge of DSF.

In the absence of Cu, DSF increased the viability of SK-N-BE(2c) cells by 20% up to 2  $\mu$ M but the difference was not statistically significant. Both 4 and 10  $\mu$ M of DSF induced less than 20% loss of viability. Again this was not significantly different from the viability of the control (Figure 9a). DSF alone, up to a concentration of 10  $\mu$ M, was not toxic to LNCaP cells (Figure 9b) whereas 10  $\mu$ M of DSF alone induced a 30% loss of viability in

UVW/NAT cells ( $p < 0.05$ ) (Figure 9c). When treatment consisted of equimolar concentrations of DSF and Cu, a statistically significant loss of viability was observed in all three cell lines (Figure 9a, Figure 9b and Figure 9c). Interestingly, there was a statistically significant reversal of the loss of viability when DSF was in molar excess relative to Cu. This effect applied to all three cell lines (Figure 9a, Figure 9b and Figure 9c).

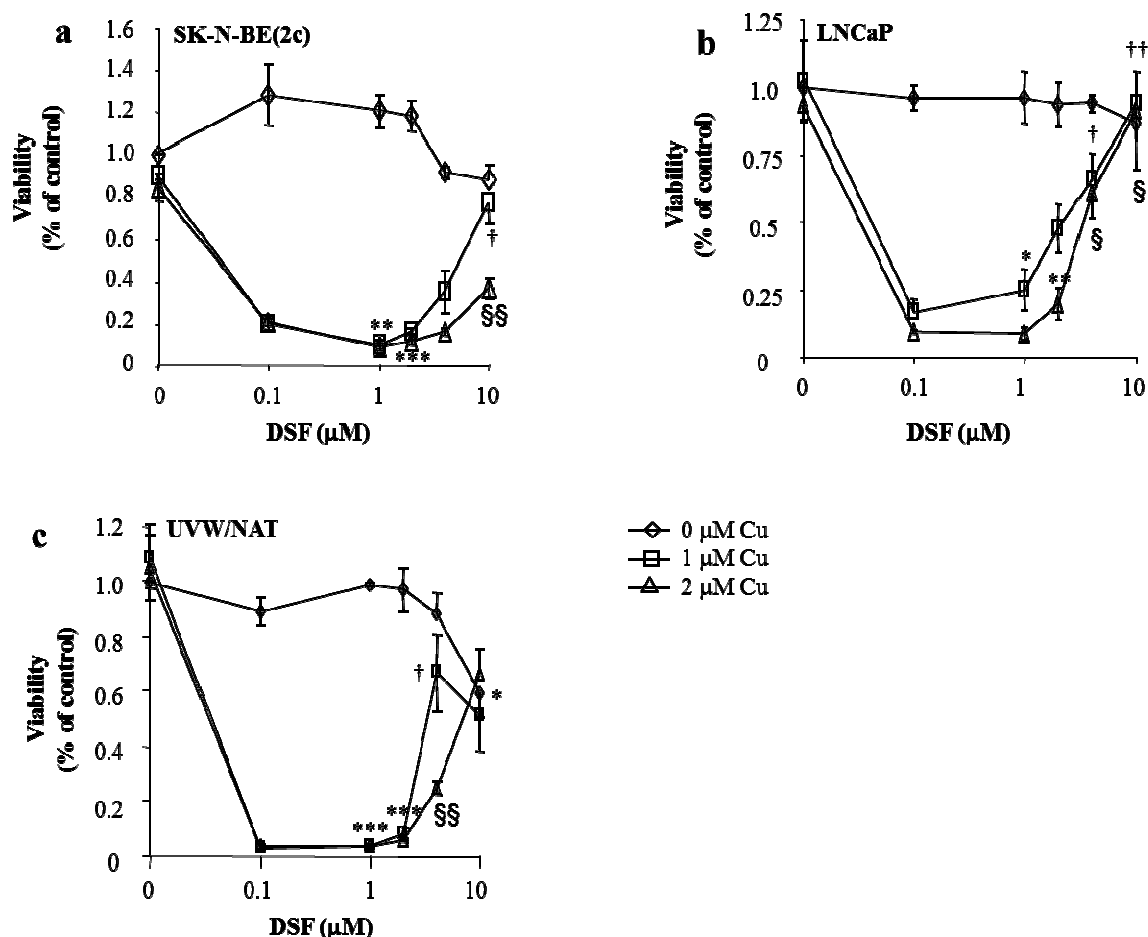


**Figure 9** The effect of ratios of DSF to Cu on the viability of SK-N-BE(2c), UVW/NAT and LNCaP cells

Cells were exposed to various ratios of DSF to Cu for 24 h in serum-free culture medium. DSF and Cu were then washed off and the cells exposed to a MTT solution for 4 h. The formazan absorbance was measured at 570 nm. Data are means  $\pm$  SEM;  $n=3$ . The independent samples t-test was used to determine the significance of difference between treatments. The p-values are indicated by the following symbols: \*, compared with the control group; †, compared with the group treated with 1  $\mu$ M DSF in the presence of 1  $\mu$ M Cu; §, compared with the group treated with 2  $\mu$ M DSF in the presence of 2  $\mu$ M Cu. One symbol indicates  $p < 0.05$ ; two symbols indicate  $p < 0.01$ ; three symbols indicate  $p < 0.001$ .

In the absence of Cu, DETC was not toxic to any cell line examined (Figure 10a, Figure 10b, Figure 10c). A concentration of 1  $\mu$ M DETC induced 85-95% loss of viability in the

presence of 1  $\mu\text{M}$  Cu in SK-N-BE(2c) ( $p < 0.01$ ), UVW/NAT ( $p < 0.001$ ) and LNCaP ( $p < 0.001$ ) cells (Figure 10a, Figure 10b and Figure 10c). Similarly to DSF, when DETC was in molar excess relative to Cu, there was a reversal of the loss of viability although this effect was not statistically significant in the case of SK-N-BE(2c) cells (Figure 10a, Figure 10b and Figure 10c).

These results confirmed the requirement of Cu for DETC- and DSF-induced cytotoxicity. More importantly, these results also demonstrated that cytotoxicity was dependent on the molar ratios of DSF or DETC to Cu. The dose response profile was characterised by increasing cytotoxicity with increasing concentrations of DSF or DETC to a nadir, followed by a reversal of cytotoxicity in response to treatments with excess molar of DSF or DETC relative to Cu. This pattern suggested that the Cu-chelated forms of DSF and DETC – i.e. DSF:Cu and DETC<sub>2</sub>:Cu - were the cytotoxic agents. Therefore, the chelation process was investigated to determine whether DSF:Cu and DETC<sub>2</sub>:Cu were formed in the experimental conditions after treatment of cells with equimolar concentrations of DSF or DETC with Cu.

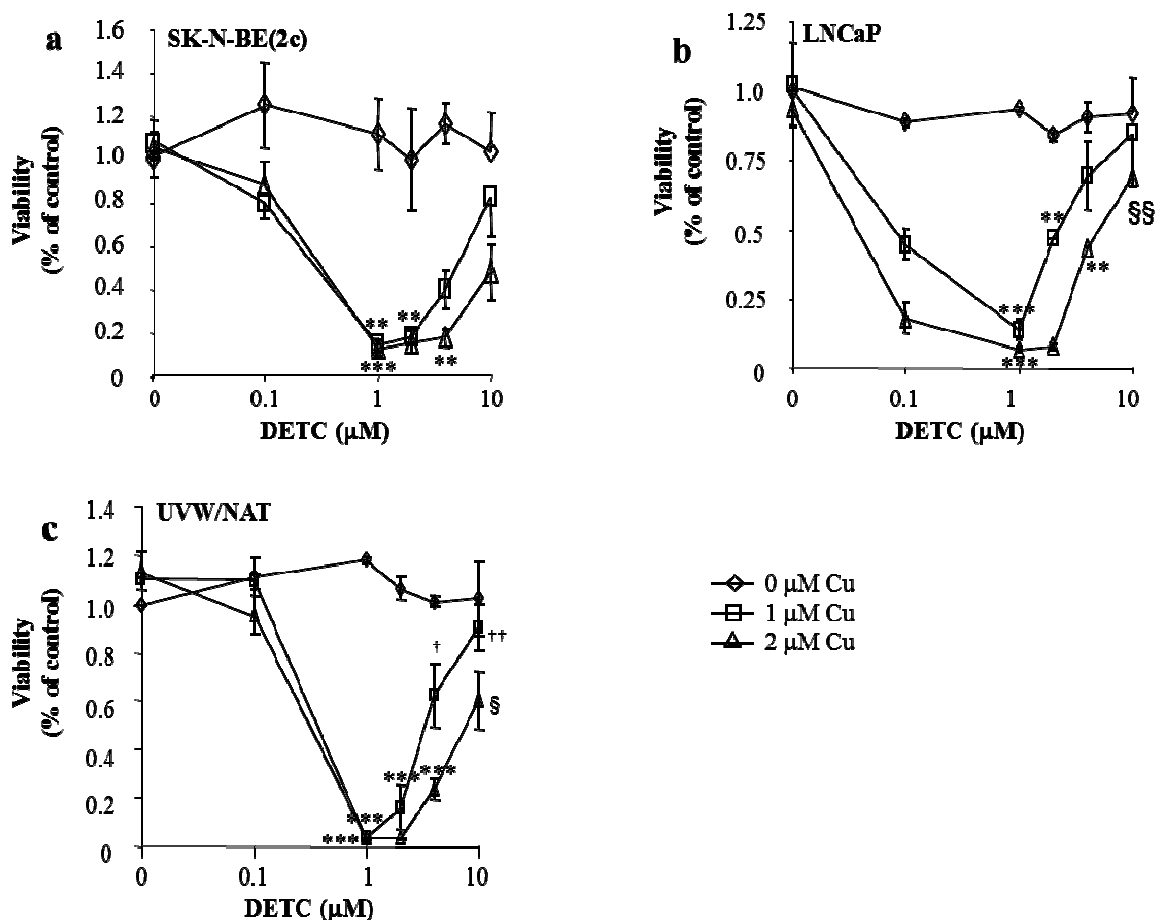


Figure 10 The effect of ratios of DETC to Cu on the viability of SK-N-BE(2c), UVW/NAT and LNCaP cells

Cells were exposed to various ratios of DETC to Cu for 24 h in serum-free culture medium. DETC was then washed off and the cells were exposed to a MTT solution for 4 h. The absorbance was measured at 570 nm. Data are mean  $\pm$  SEM (n=3). The independent samples t-test was used to determine the significance of difference between treatments. The p-values are indicated by the following symbols: \*, compared with the control group; †, compared to the group treated with 2  $\mu$ M DETC in the presence of 1  $\mu$ M Cu; §, compared to the group treated with 4  $\mu$ M DETC in the presence of 2  $\mu$ M Cu. One symbol indicates  $p < 0.05$ ; two symbols indicate  $p < 0.01$ ; three symbols indicate  $p < 0.001$ .

### 3.4.3 The chelation of Cu by DSF and DETC

The mixing of one mole of Cu ions with two moles of DETC or one mole of DSF results in the formation of DETC<sub>2</sub>:Cu and DSF:Cu, respectively. These chelations can be monitored spectrophotometrically<sup>110</sup>. The Cu-chelated form of DSF was also purchased from Tokyo Chemical Industry, Japan. The commercial form of the Cu-chelated form of DSF is denoted Cu[DETC]<sub>2</sub>. The peak absorbance of 100  $\mu$ M Cu[DETC]<sub>2</sub> was 437 nm (Figure 11a). The solvent in which Cu and DETC were dissolved was 100% DMSO (v/v). DMSO did not absorb light between 300 and 600 nm, indicative of the specificity of this wavelength range for Cu[DETC]<sub>2</sub> (Figure 11a).

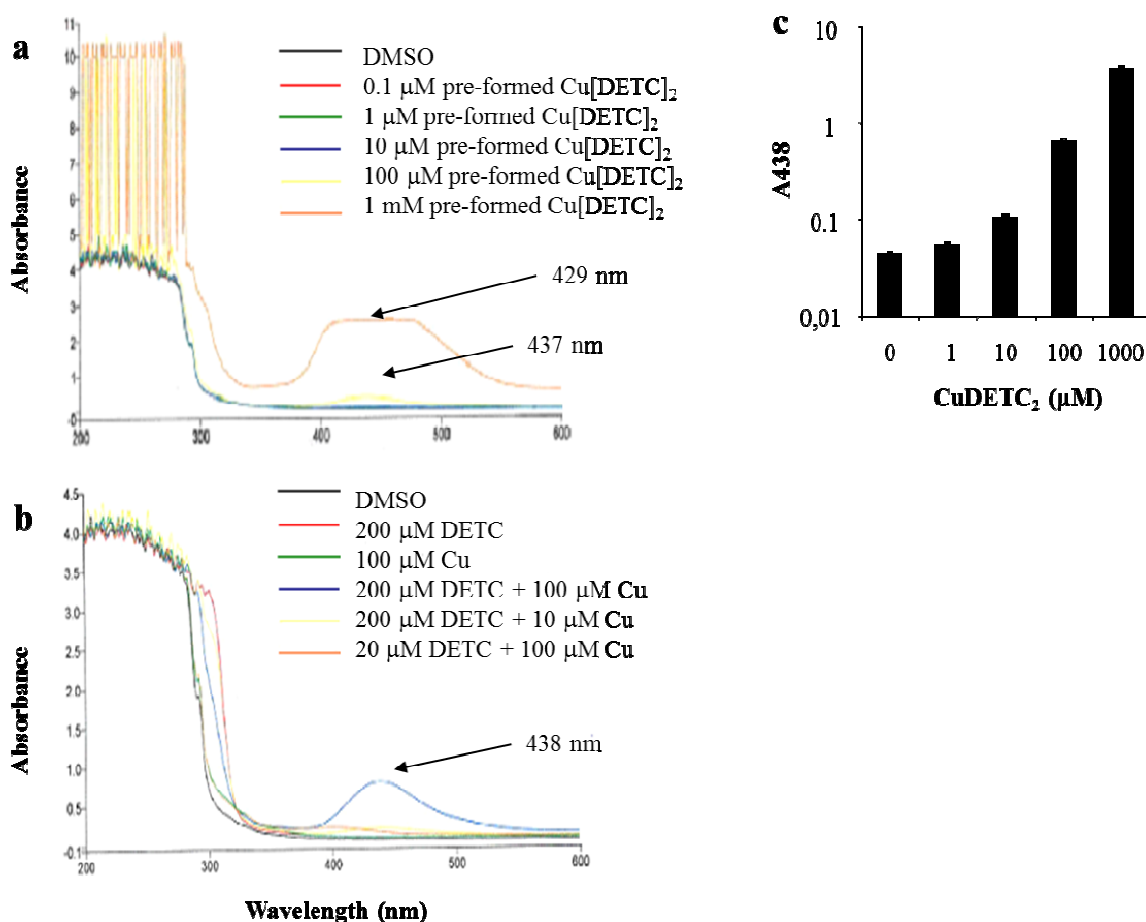


Figure 11 The absorption spectrum of DETC, Cu, DETC + Cu and Cu[DETC]<sub>2</sub>

The absorbance profiles of DMSO solutions containing Cu[DETC]<sub>2</sub> (a), DETC, Cu and DETC<sub>2</sub>:Cu (b) were analysed at wavelengths ranging from 200 to 600 nm. (c) The relationship between the absorbance and the molar concentration of Cu[DETC]<sub>2</sub> is shown.

When DETC was mixed with Cu in a 2:1 molar ratio, a single peak appeared at 438 nm. DMSO, DETC and Cu alone did not result in a peak absorbance at or near to 438 nm. The wavelength (438 nm) of the absorbance peak obtained after mixing 200 µM DETC with 100 µM Cu (Figure 11b) was similar to that obtained by 100 µM of the commercially available Cu-chelated form of DSF Cu[DETC]<sub>2</sub> (437 nm) (Figure 11a). This suggested the formation of DETC<sub>2</sub>:Cu after mixing DETC and Cu in DMSO (Figure 11b). Thus, it is possible to monitor the formation of the Cu-chelated form of DSF by measuring absorbance. The wavelength 438 nm was chosen in all subsequent experiments.

When equimolar concentrations of DSF and Cu were mixed in DMSO (100 µM), there was no absorbance measured at 438 nm, indicative of no formation of DSF:Cu. However, formation of DSF:Cu was observed in the presence of 10 mM of the reducing agent Asc ac ( $p < 0.001$ ) (Figure 12a). These data indicated that the disulphide bridge in the DSF molecule needs to be reduced into two DETC molecules in order to be able to chelate Cu and form DSF:Cu. Importantly, commercial Cu[DETC]<sub>2</sub> was not affected by Asc ac (Figure 12b).

Since the cytotoxicity of DSF and DETC depends on ratios of DSF or DETC to the relative concentration of Cu, the stoichiometry of the formation of DSF:Cu and DETC<sub>2</sub>:Cu was investigated. Two molecules of DETC or one molecule of DSF and one molecule of Cu were required for the maximal formation of DETC<sub>2</sub>:Cu and DSF:Cu, respectively (Figure 13a). No significant increase in the formation of DETC<sub>2</sub>:Cu was achieved by increasing the molar ratio of DETC relative to Cu beyond 2:1 (Figure 13a). In the case of the mixture of DSF and Cu, one mole of DSF and one mole of Cu were required for the maximal formation of DSF:Cu. The DSF:Cu absorbance was not significantly modified by further increase, beyond equimolarity, in the concentration of DSF relative to that of Cu (Figure 13b). Formation of DSF:Cu was increased by Asc ac (Figure 13b). This experiment demonstrated that a molar excess of DSF and DETC relative to Cu did not alter the structure of the compound formed. Therefore, the reversal of cytotoxicity observed by MTT assay in the presence of an excess molar concentration of DSF or DETC relative to Cu (Figure 9 and Figure 10) could not be explained by alteration of the Cu-chelation process.

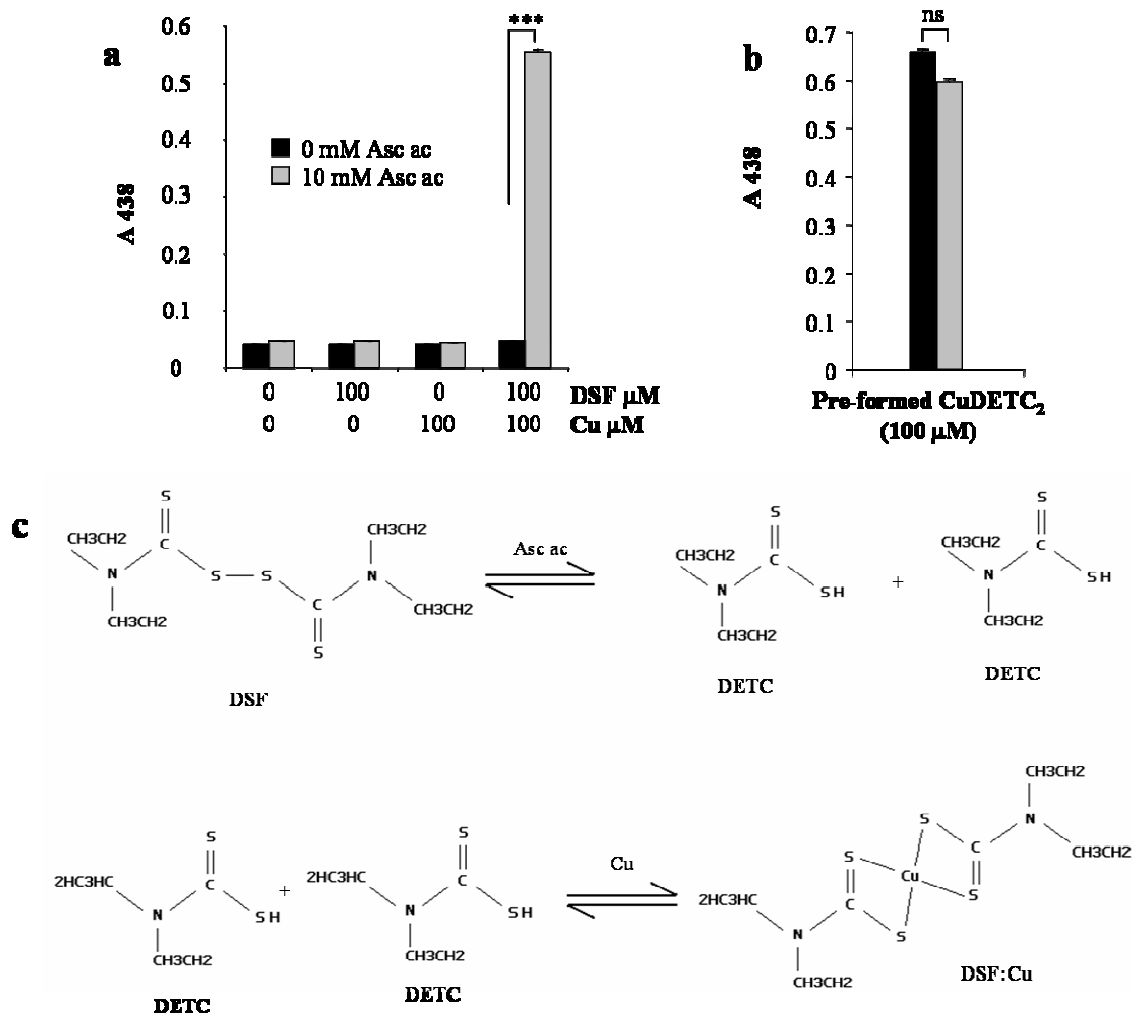


**Figure 12** The requirement of a reducing agent for the formation of the Cu-chelated form of DSF (DSF:Cu)

DSF alone, Cu alone or their combination (a) and Cu[DETC]<sub>2</sub> (b) were dissolved in DMSO at the indicated concentrations. The absorbance of the Cu-chelated form of disulfiram was measured instantly at 438 nm in the presence or in the absence of 10 mM of the reducing agent ascorbic acid (Asc ac). Data are means  $\pm$  SEM; n=3. The independent samples t-test was used to compare the mean absorbance values as indicated by the bars. One symbol indicates  $p < 0.05$  and three symbols indicate  $p < 0.001$ . (c) Relationship between DSF, DETC and DSF:Cu. C, carbon; H, hydrogen; S, sulphur; N, nitrogen.

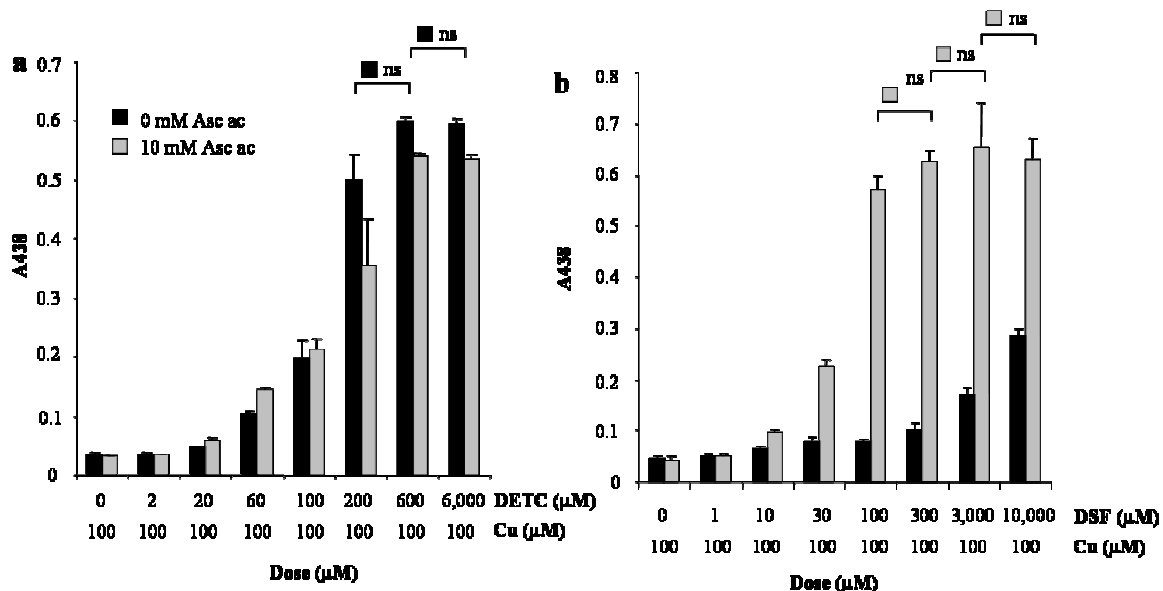


**Figure 13** The effect of excess DETC or DSF relative to Cu on the formation of DETC<sub>2</sub>:Cu or DSF:Cu. DETC (a) or DSF (b) were mixed with Cu at various molar ratios. The absorbance values of the resulting DETC<sub>2</sub>:Cu or DSF:Cu, respectively, were measured at 438 nm in the presence or in the absence of 10 mM of ascorbic acid (Asc ac). Data are mean ± SEM (n=3). The independent samples t-test was used to compare the mean absorbance values. ns indicates non-significance (p > 0.05).

The formation of DSF:Cu in the cytosol of UVW/NAT and SK-N-BE(2c) cells was investigated after incubation for 30 min with DSF and Cu. It was anticipated that the cytosolic concentration of DSF:Cu would be lower than the concentration of DSF:Cu present in the culture medium. Moreover, the lower detection limit of DSF:Cu absorbance is 10 μM (Figure 11c). Therefore, a high concentration of DSF and Cu (1 mM) were used in these experiments. When monolayers were exposed to equimolar concentrations of DSF and Cu, DSF:Cu was formed in the cytosol (Figure 14a, Figure 14b). The formation was significant only in UVW/NAT compared with the untreated control (p < 0.05). If no cell was present, there was no formation of DSF:Cu, indicating that DSF and Cu were efficiently washed off from the flasks before solubilising DSF:Cu. The Cu chelator BCPD was used as a negative control. The  $K_d$  value of BCPD was estimated to be  $10^{-19.8} \text{ M}^{220}$ . Due to the low  $K_d$  value of BCPD it was anticipated that equimolar concentrations of BCPD would compete with DSF for the binding to Cu. BCPD inhibited the formation of DSF:Cu in the cytosol, demonstrating the competition for Cu binding between equimolar concentrations of BCPD and DSF (Figure 14a and Figure 14b). BCPD does not penetrate into the cytosol. Thus the inhibition of DSF:Cu formation by BCPD occurred in the culture medium. It further suggested that there is a reducing agent in the culture medium allowing the chelation of Cu by DSF. Indeed, it was shown that DSF required Asc ac in order to chelate Cu and form DSF:Cu (Figure 12a).

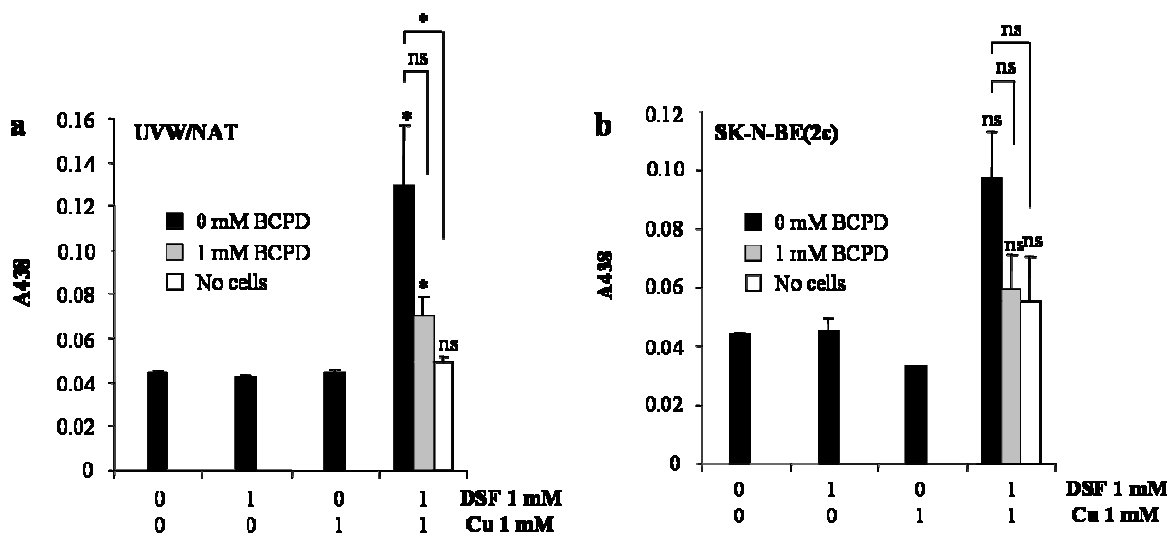


**Figure 14 DSF:Cu is present in cells exposed to DSF and Cu**

UVW/NAT (a) and SK-N-BE(2c) (b) monolayers were exposed to 1 mM of DSF with 1 mM of Cu in serum-free culture medium in the presence or in the absence of 1 mM of the Cu chelator BCPD for 30 min. After 30 min, the monolayers were washed to remove DSF, Cu or BCPD remaining in the culture medium. The cell pellets were then dissolved in 100 ml of DMSO. The absorbance was measured at 438 nm. Data are mean  $\pm$  SEM; n=3. The independent samples t-test was used to compare the mean absorbance values to that of the control unless otherwise indicated. ns indicates non-significant ( $p > 0.05$ ) and one symbol (\*) indicates  $p < 0.05$  compared to untreated control.

#### 3.4.4 The determination of the dose-response relationship of DSF in the presence or in the absence of Cu

A decrease in MTT absorbance signal may be due to cell death, lower proliferation rate or increased senescence. The MTT assay is an approximate measurement of cellular viability. On the other hand, the clonogenic assay assesses the ability of a single cell, a clonogen, to form a colony comprising more than 50 cells, i.e. the ability to proliferate indefinitely. Since it was shown that equimolar concentrations of DSF and Cu form the cytotoxic compound DSF:Cu (Figure 12a), the concentration-effect relationship of DSF:Cu was investigated using the clonogenic assay. UVW/NAT and SK-N-BE(2c) cell lines were used to measure the parameters  $m$  and  $IC_{50}$  using the median effect principle describing the behaviour of DSF:Cu as indicated in Section 3.3.5. LNCaP cells did not form colonies and were therefore excluded from this analysis. In the presence of equimolar concentrations of DSF and Cu, the  $IC_{50}$  was 0.32  $\mu$ M in SK-N-BE(2c) cells (Figure 15a) and 0.28  $\mu$ M in UVW/NAT cells (Figure 15b). The parameters of the concentration-effect relationship of DSF:Cu were calculated based on the median effect plots (Figure 15c and Figure 15d). In the absence of Cu, the  $IC_{50}$  for DSF was 16.50  $\mu$ M in SK-N-BE(2c) cells (Figure 16a) and 23.61  $\mu$ M in UVW/NAT cells (Figure 16b). The parameters of the concentration-effect

relationship of DSF were calculated based on the median effect plots (Figure 16c and Figure 16d).

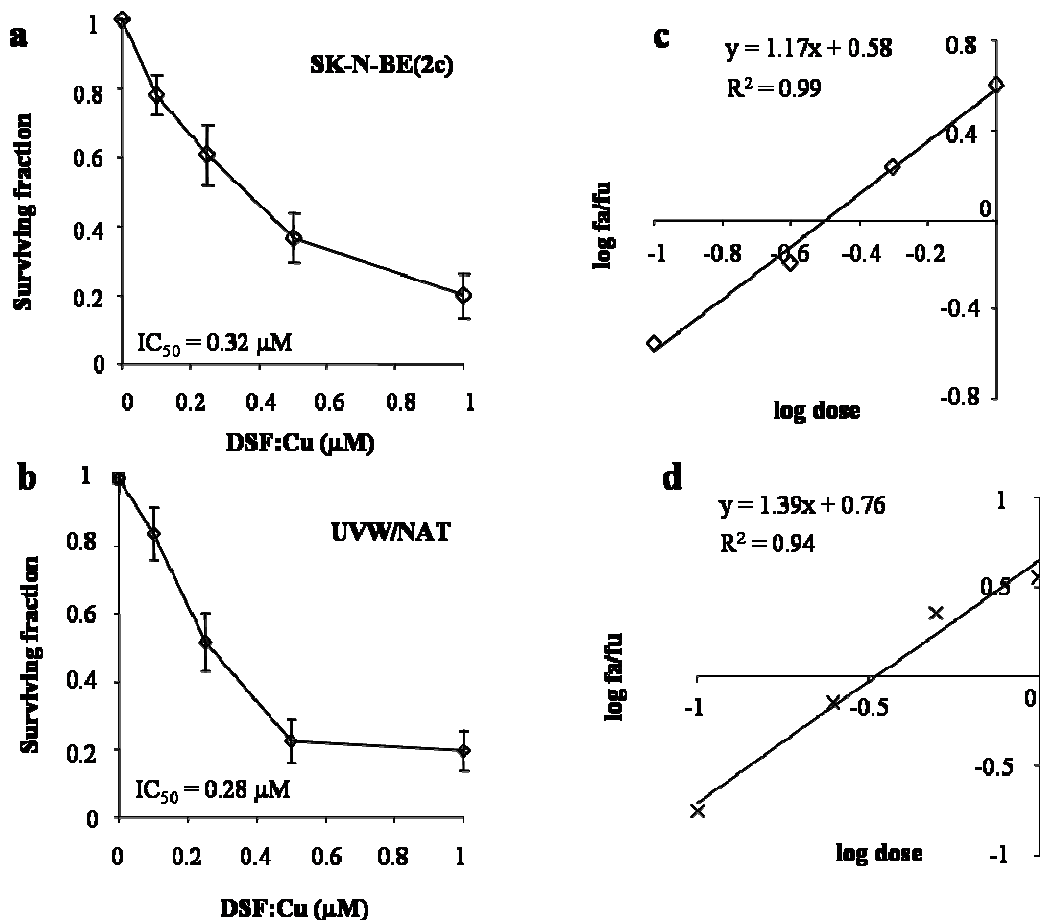


**Figure 15** The effect of equimolar concentrations of DSF and Cu (DSF:Cu) on the clonogenic capacity of SK-N-BE(2c) and UVW/NAT cells

SK-N-BE(2c) (a, c) and UVW/NAT (b, d) cells were exposed to equimolar concentrations of DSF and Cu for 24 h in serum-free culture medium. The cells were washed with PBS and clonogenic assay was performed. Data are mean  $\pm$  SEM; n=3. (c, d) The median effect plots were constructed using  $\log fa/ fu = m \log D - m \log \text{IC}_{50}$  where fa is the fraction of clonogens affected by the treatment, fu is the unaffected fraction of clonogens, and m is the coefficient of the sigmoidicity of the concentration-effect curve. Linear regression was performed to calculate m (the slope) and  $\text{IC}_{50} = 10^{-\text{intercept}/m}$ .

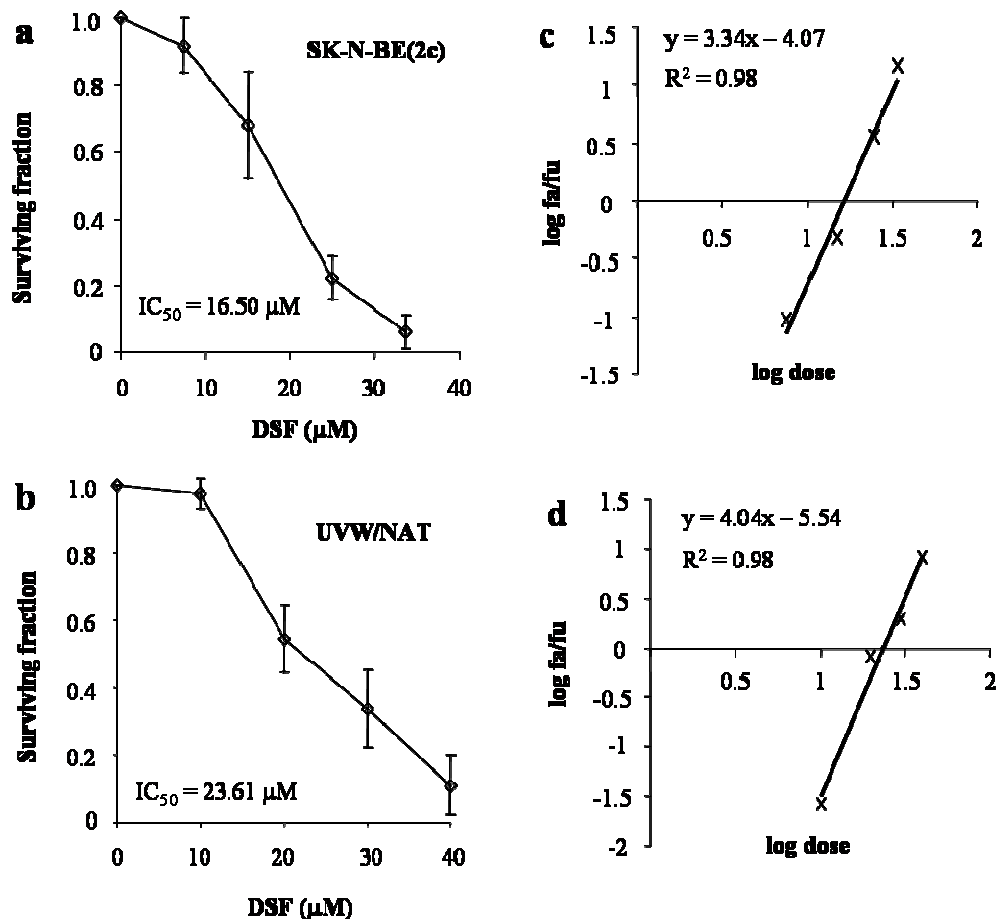


**Figure 16** The effect of DSF alone on the clonogenic capacity of SK-N-BE(2c) and UVW/NAT SK-N-BE(2c) (a, c) and UVW/NAT cells (b, d) cells were exposed to various concentrations of DSF without Cu for 24 h in serum-free culture medium. The cells were washed with PBS and clonogenic assay was performed. Data are mean  $\pm$  SEM; n=3. (c, d) The median effect plots were constructed using  $\log fa/ fu = m \log D - m \log \text{IC}_{50}$  where fa is the affected fraction, fu is the unaffected fraction, and m is the coefficient of the sigmoidicity of the concentration-effect curve. Linear regression was performed to calculate m (the slope) and  $\text{IC}_{50} = 10^{-\text{intercept}/m}$ .

### 3.4.5 Proteasome activity

The proteasome inhibitory activity of DSF:Cu in vitro requires concentrations in excess of  $1 \mu\text{M}^{121,221}$ . Since it was shown that DSF:Cu is cytotoxic at concentrations  $< 1 \mu\text{M}$  (Figure 15), the proteasome inhibitory property of DSF:Cu was investigated at these concentrations in LNCaP, SK-N-BE(2c) and UVW/NAT cells to determine the contribution of proteasome inhibition to cell kill (Figure 17a). The concentrations of DSF:Cu inhibiting 50% of the proteasome activity of the untreated control were 1.42, 4.99 and  $7.48 \mu\text{M}$  in LNCaP, SK-N-BE(2c) and UVW/NAT cells, respectively (Figure 17c). It is noteworthy that  $1 \mu\text{M}$  DSF:Cu induced 75-90% kill in the three cell lines examined (Figure 9) but inhibited only 0.02-36.1% of the proteasome activity (Figure 17c). This indicated that the mechanism responsible for cell kill, at DSF:Cu concentrations lower than  $1 \mu\text{M}$ , is unlikely

to be proteasome inhibition. The well-established proteasome inhibitor bortezomib was included as a positive control for proteasome inhibition (Figure 18). The bortezomib concentrations inhibiting 50% of the proteasome activity were 10.81, 3.11 and 3.43  $\mu\text{M}$  in LNCaP, SK-N-BE(2c) and UVW/NAT, respectively (Figure 18c). Significantly, these values are within the range of the average bortezomib concentration which inhibited cell growth by 50% (7 nM) in a panel of sixty cancer cell lines<sup>222</sup>. Therefore, bortezomib-induced cytotoxicity may be explained by inhibition of the proteasome whereas this mechanism of action made no more than a minor contribution to DSF:Cu-induced cytotoxicity.

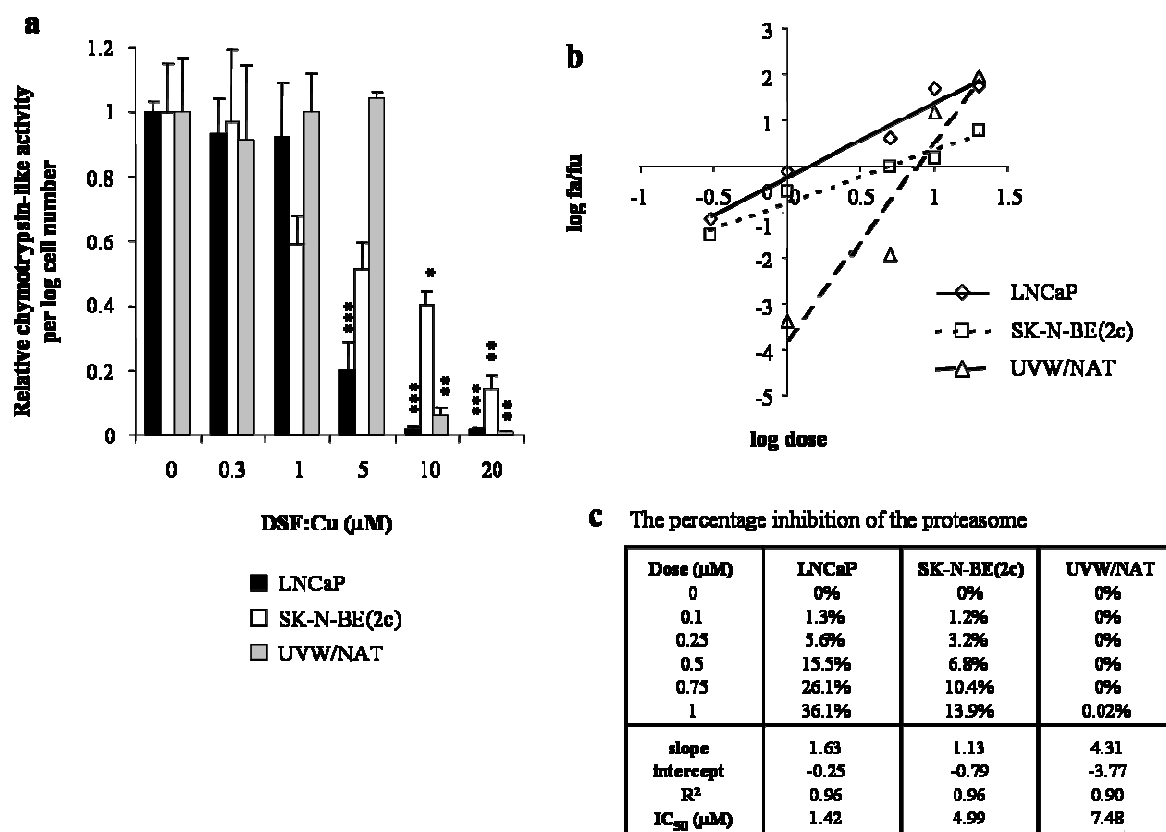


**Figure 17** The effect of DSF:Cu on the chymotrypsin-like catalytic activity of the proteasome in LNCaP, SK-N-BE(2c) and UVW/NAT cells

(a) The cells were exposed to various equimolar concentrations of DSF and Cu for 8 h in serum-free culture medium. After washing, a buffer containing luciferase and the aminoluciferin substrate were applied to the cells and luminescence was measured. Data are mean  $\pm$  SEM; n=3. The independent samples t-test was used to compare the mean absorbance value of the DSF:Cu-treated groups with the respective untreated control for every cell line. One symbol indicates  $p < 0.05$ ; two symbols indicate  $p < 0.01$  and three symbols indicate  $p < 0.001$ . (b) The median effect plot of proteasome inhibition. (c) The concentration-effect parameters (m, IC<sub>50</sub>, R<sup>2</sup> and the y-intercept) and the calculated percentage inhibition of the proteasome based on the median effect equation are shown.

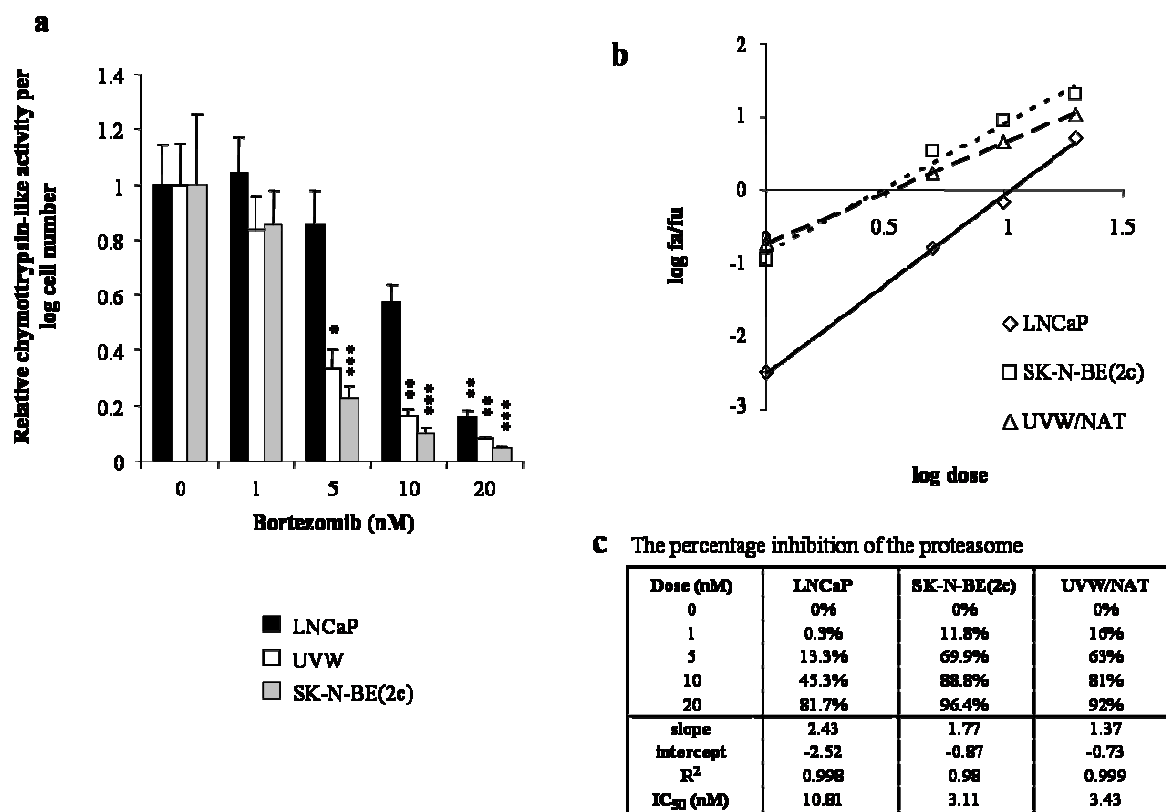


**Figure 18** The effect of bortezomib on the chymotrypsin-like catalytic activity of the proteasome in LNCaP, SK-N-BE(2c) and UVW/NAT cells

(a) The cells were exposed to various concentrations of bortezomib for 2 h in serum-free culture medium. After washing, a buffer containing luciferase and the aminoluciferin substrate were applied to the cells and luminescence was measured. Data are mean  $\pm$  SEM; n=3. The independent samples t-test was used to compare the mean absorbance value of the bortezomib-treated groups with their respective untreated control for every cell line. One symbol indicates  $p < 0.05$ ; two symbols indicate  $p < 0.01$ ; three symbols indicate  $p < 0.001$ . (b) The median effect plot of proteasome inhibition is presented. (c) The concentration-effect parameters (m, IC<sub>50</sub>, R<sup>2</sup> and the y-intercept) and the calculated percentage inhibition of the proteasome based on the median effect equation are shown.

### 3.4.6 Cell cycle

The effect of 5  $\mu$ M DSF on the cell cycle has previously been investigated<sup>109</sup>. The results showed that DSF induced a decrease in the G0/G1 population, an increase in the S population and an increase of the Sub-G1 population indicative of apoptosis<sup>109</sup>. Proteasome activity is an important modulator of cell cycle progression<sup>223</sup>. Since the proteasome was found not to be the major target for DSF:Cu cytotoxicity at concentrations less than 1  $\mu$ M (Figure 17), it was hypothesised that concentrations up to 1  $\mu$ M would not affect the cell cycle profile. To determine the legitimacy of this conjecture, the cell cycle profiles of LNCaP, SK-N-BE(2c) and UVW/NAT were acquired 1, 2, 4, 8, 12 and 24 h following treatment with 0.3 and 1  $\mu$ M DSF:Cu.

There was no significant change in the distribution of LNCaP, SK-N-BE(2c) or UVW/NAT cells throughout the phases of the cell cycle after 12 h exposure to 0.3 or 1  $\mu\text{M}$  of DSF:Cu (Figure 19a, Figure 19b and Figure 19c). Furthermore, there was no significant change in the distribution of LNCaP, SK-N-BE(2c) or UVW/NAT cells throughout the phases of the cell cycle up to 24 h (Figure 19a, Figure 19b and Figure 19c). All LNCaP cells were killed by 12 h of exposure to equimolar concentrations of DSF and Cu. Therefore the investigation of the cell cycle in LNCaP cells 24 h following exposure to DSF:Cu was impossible because no adherent cell was recovered.

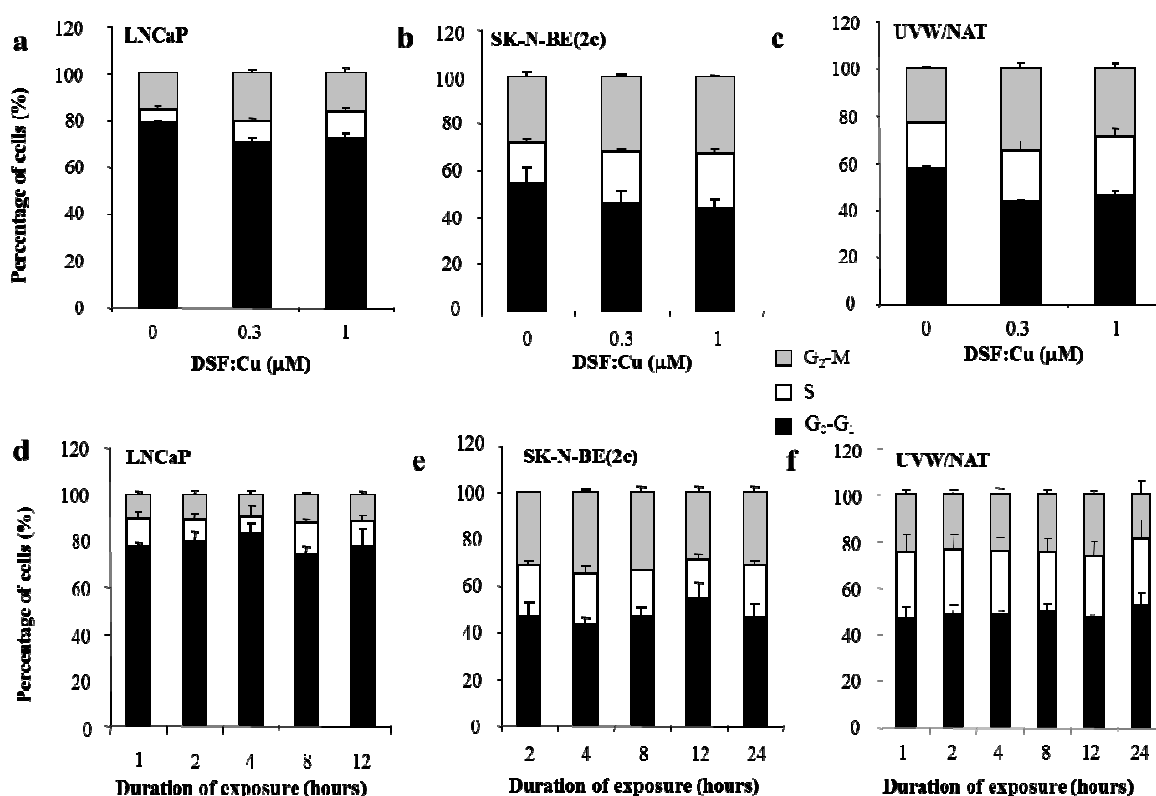


**Figure 19** The effect of DSF:Cu on the distribution of cells throughout the phases of the cell cycle (a, b and c) The cells were exposed to equimolar concentrations of DSF and Cu (0.3 or 1  $\mu\text{M}$ ) in serum-free medium for 12 h. (d, e and f) The cells were exposed to equimolar concentrations of DSF and Cu (1  $\mu\text{M}$ ) for 1, 2, 4, 8, 12 and 24 h in serum-free culture medium. Cell cycle profiles were obtained by FACS analysis of 10000 propidium iodide-stained cells. The assignment of a cell into a phase of the cell cycle was based on the amount of DNA [N (G<sub>0</sub>/G<sub>1</sub>), 2N (G<sub>2</sub>/M) or more than N but less than 2N (S)]. The proportions of cells in G<sub>0</sub>/G<sub>1</sub>, S and G<sub>2</sub>/M were measured using the software FlowJo (BD Biosciences, Mountain View, CA). Data are mean  $\pm$  SEM; n=3.

### 3.5 Discussion and summary of the results

For most drugs, the relationship between concentration and effect is linear, hyperbolic or sigmoidal. In contrast, the response of several cancer cell lines to treatment with a range of doses of DSF has been described by a biphasic response profile<sup>206</sup>, for which the present

results offer an explanation. Clonogenic cell kill resulting from exposure to DSF concentrations less than or equal to 3.4  $\mu\text{M}$  in serum-complemented medium was inhibited by the Cu chelator BCPD (Figure 8b), demonstrating the dependency on Cu for DSF-mediated cytotoxicity at low dosage. The cell culture media DMEM, MEM and RPMI contain no Cu supplementation. However, the FCS used to complement the culture media contained approximately 15  $\mu\text{M}$  of  $\text{Cu}^{212,224-226}$ . Therefore, the Cu concentration in the medium used for the culture of SK-N-BE(2c) cells, which comprised 15% serum, was 2.25  $\mu\text{M}$ . This was close to the concentration of DSF (1.6  $\mu\text{M}$ ) which induced maximal, Cu-dependent, clonogenic cell kill.

The investigation of the Cu-dependence of the cytotoxicity of DSF in serum-free culture medium revealed that Cu reduced the  $\text{IC}_{50}$  concentration of DSF 80-fold and 50-fold in UVW/NAT and SK-N-BE(2c) cell lines, respectively (Figure 15 and Figure 16). Moreover, DSF-induced cytotoxicity was dependent on the ratio of DSF to Cu. The clonogenic survival nadir was observed when DSF and Cu were present in equimolar amounts. This was a reflection of the 1:1 ratio of DSF and Cu required for chelation to generate DSF:Cu. Similarly, significant cytotoxicity occurred when DETC (two molecules of which produce DSF under oxidising conditions) and Cu were mixed in a 2:1 molar ratio. Two molecules of DETC plus one molecule of Cu yielded one molecule of  $\text{DETC}_2\text{:Cu}$ . Therefore it was the Cu-chelated form of DETC and the Cu-chelated form of DSF that were cytotoxic at concentrations less than or equal to 3.4  $\mu\text{M}$  in serum-complemented culture medium. However, it has to be acknowledged that in the investigation of the dependency on the ratio of DETC to Cu for cytotoxicity in LNCaP and UVW/NAT cells, the cytotoxicity was greater when equimolar concentrations of DETC and Cu were mixed together (Figure 10b). This suggested that  $\text{DETC:Cu}$  is also formed and is as cytotoxic as  $\text{DETC}_2\text{:Cu}$ .

A hypothesis that explained the biphasic response profile of DSF in serum-complemented culture medium was shown in Figure 7. It was hypothesised that DSF was cytotoxic via two independent and antagonistic mechanisms (1 and 2) with two distinct potencies ( $\text{IC}_{50-1}$  and  $\text{IC}_{50-2}$ ) (Figure 7). Since DSF-cytotoxicity at low dosage was inhibited by the Cu chelator BCPD and DSF-cytotoxicity at higher dosage was inhibited by the antioxidant NAC, the two mechanisms hypothesis seemed plausible. The results presented in this chapter suggested that mechanism 1 is mediated by Cu (Figure 8b), which conferred upon DSF the ability to inhibit a cellular target more potently than DSF alone. The addition of

Cu reduced the IC<sub>50</sub> value of DSF 80-fold and 50-fold in UVW/NAT and SK-N-BE(2c) cells lines, respectively (Figure 15 and Figure 16). The Cu atom may confer a planar structure upon DSF<sup>132</sup> thereby facilitating intercalation between planar molecules (such as aromatic side-chains of amino acids [phenylalanine, tyrosine and tryptophan]) in a manner analogous to the integration of carcinogenic acridine dyes in DNA<sup>227</sup>. An analogy may be drawn with the anti-cancer drug elesclomol that induces apoptosis in cancer cells by elevating the levels of intracellular reactive oxygen species (ROS)<sup>228</sup>. The chelation of Cu by elesclomol is necessary for its pro-oxidative and pro-apoptotic effects. It has been shown that the target of the elesclomol-Cu complex is the mitochondria, in which the redox cycling of Cu(II) to Cu(I) results in ROS production<sup>113</sup>. Interestingly, the chelation of Cu by elesclomol created a compound characterised by tetra-coordinated trapezoid planar geometry (Figure 20)<sup>229</sup>. In the light of the effect of Cu on the structure of elesclomol, the results presented in this chapter suggested that Cu may induce similar conformational constraints on the DSF molecule resulting in a planar structure. In turn, the Cu-dependent planar structure of DSF could confer increased affinity for a particular target, thus leading to greater cytotoxic potency of DSF:Cu compared with DSF as indicated by the 50- to 80-fold decrease in the IC<sub>50</sub> concentration of DSF:Cu compared to DSF (Figure 15 and Figure 16).

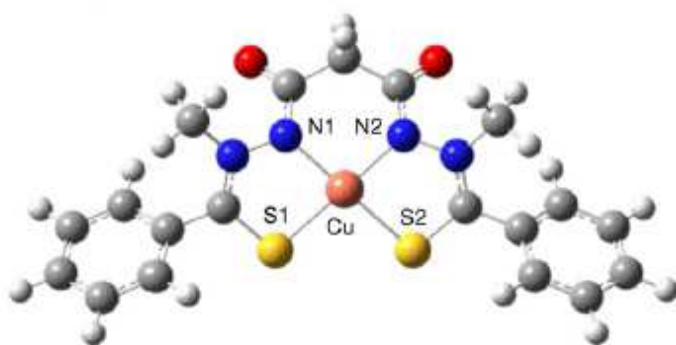


**Figure 20** The planar structure of the elesclomol:Cu complex, adapted from Lianming Wu et al. (2011)<sup>229</sup>

Blue, nitrogen (N) atoms; yellow, sulphur (S) atoms; pink, copper (Cu) atom; red, oxygen atoms; grey, carbon atoms; white, hydrogen atoms.

Secondly, the ratios of DSF or DETC to Cu influenced the cytotoxicity. There was a progressive reversal of cytotoxicity when DSF or DETC was present in molar excess relative to Cu (Figure 9 and Figure 10). This phenomenon suggested competition between DSF and DSF:Cu for an intracellular site whose integrity is necessary for cell survival. The hypothesis that Cu confers upon DSF a conformational change in its chemical structure

thereby leading to higher potency offered an explanation for the competitive nature of the reversal of DSF:Cu-mediated cytotoxicity by DSF. The concentration of DSF must be greater than the concentration of DSF:Cu in order to displace DSF:Cu from its cellular targets because DSF:Cu has more affinity for the target than DSF. Importantly, excess concentration of DSF or DETC to Cu did not reduce the chelation of Cu by DSF (Figure 13b) nor DETC (Figure 13a), discounting the possibility that prevention of kill by excess molar ratio of DSF to Cu was due to the reduced formation of DSF:Cu. Thus, the results suggested that competition of DSF with DSF:Cu explained the recovery phase of the biphasic response profile of DSF shown in Figure 8a.

Finally, in SK-N-BE(2c) cells, the last phase of the biphasic response profile at DSF concentrations greater than 10  $\mu\text{M}$  was explained by a second cytotoxic mechanism, for which the  $\text{IC}_{50}$  was 16.50  $\mu\text{M}$  (Figure 16a). The inhibition of DSF cytotoxicity by the antioxidant NAC suggested that DSF was cytotoxic at these doses via the generation of an oxidative stress. Therefore, these results are not entirely consistent with the hypothesis stated in Figure 7. The more potent mechanism 1 is brought about by the conformational change conferred upon DSF by Cu. The mechanism 2 is the generation of oxidative stress by DSF alone. However, the hypothesis stated that mechanism 2 (the generation of an oxidative stress) must antagonise mechanism 1 (Cu-mediated) resulting in a reversal of cytotoxicity. The question whether the generation of an oxidative stress inhibits the Cu-mediated cytotoxicity of mechanism 1 remains unanswered and constitutes a follow-up project. Instead, it was speculated that the reversal of cytotoxicity was triggered by the competition between DSF and DSF:Cu for the binding to an intracellular target.

Cu-dependent DSF cytotoxicity, as opposed to the cell kill mediated by oxidative stress (Figure 8), is of therapeutic interest for two reasons. Firstly, it has been determined that an oral dose of 250 mg of DSF results in a peak plasma concentration of 1  $\mu\text{M}$  (0.3  $\mu\text{g/ml}$  or 1  $\mu\text{M}$ )<sup>161</sup>. A daily oral dose of 250 mg is a routine regimen in the treatment of alcoholics. The  $\text{IC}_{50}$  concentrations of DSF:Cu in SK-N-BE(2c) and UVW/NAT cells are 0.32 and 0.28  $\mu\text{M}$  (Figure 15 and Figure 16), respectively. These values are within the range of the low dose kill observed in many other cancer cell lines<sup>206</sup> and are lower than the peak plasma concentration of DSF in patients<sup>161</sup>. For the future use of DSF in the treatment of cancer, firstly it is important to demonstrate efficacy at plasma concentrations that can be achieved in patients. Secondly, DSF has side effects such as vomiting, drowsiness, loss of coordination and loss of consciousness. Therefore it is important to use the lowest possible

therapeutic dose, especially if administered in combination with other therapeutic modalities.

An alternative theory for the mode of action of DSF may be as a Cu ionophore<sup>114,205</sup>. It has been argued that the resulting Cu overload in the cytosol is responsible for the inhibition of multiple targets, including the proteasome<sup>121</sup>. Under appropriate intracellular redox conditions, Cu could be released by DSF resulting in various cytotoxic effects. Similarly, elesclomol has been shown to chelate Cu in the extracellular space, transport Cu into the cytosol as an elesclomol-Cu complex, deposit Cu inside the mitochondria, then efflux from the cytosol into the extracellular space in order to chelate more Cu and start another cycle of transmembrane Cu transport<sup>113</sup>. However, the detection of DSF:Cu in lysed cells (Figure 14) suggests that DSF acts not solely as a Cu ionophore. DSF:Cu may also exist in its complexed form in the cytosol and have a cytotoxic effect in its own right. The reversal of cytotoxicity observed when DSF is in molar excess relative to DSF:Cu suggests competition between the two entities. The competition for the same target implies that DSF:Cu has an effect of its own and does not act merely as a Cu ionophore. Therefore both Cu on its own and the complex formed with DSF may play a role in DSF:Cu-induced cytotoxicity.

The cytotoxicity of DSF:Cu was compared with that of DSF. The coefficient of sigmoidicity  $m$  was approximately 1 for DSF:Cu (Figure 15) and 4 for DSF (Figure 16), indicative of hyperbolic and sigmoidal dose-response relationships, respectively. A hyperbolic curve indicates a steeper increase in cytotoxicity at low concentrations whereas the increase in the effect slows down at higher concentrations. On the other hand, a sigmoidal curve indicates a slow increase in cytotoxicity at low and high concentrations (shoulders in the curve) whereas there is a steep increase in cytotoxicity at intermediate concentrations. For instance, a 10% kill is achieved at lower concentrations of a drug with a hyperbolic concentration-effect relationship than a drug with a sigmoidal concentration-effect relationship. This is consistent with the hypothesis that Cu stabilises the 3-D structure of DSF in a fixed plan, making the DSF molecule less free to rotate around its disulphide bridge. Therefore, the stabilised DSF:Cu molecule has more affinity for its target and is more cytotoxic, consistent with the observations that Cu lowers the  $IC_{50}$  of DSF and switches the shape of the curve from sigmoidal to hyperbolic.

A wide range of DSF concentrations ( $10^{-2}$  to  $10^2$   $\mu$ M) has been shown to inhibit the proteasome in several cell lines<sup>195,221</sup>. However, in SK-N-BE(2c), UVW/NAT and LNCaP

cells, DSF:Cu did not inhibit the proteasome at concentrations that are therapeutically relevant (0.3 µg/ml – equivalent to 1 µM) (Figure 17). Furthermore, the distribution of cells through the different phases of the cell cycle was unaffected by DSF:Cu. In contrast, the proteasome inhibitory properties of bortezomib can explain its toxicity in cells (Figure 18) and it was shown that bortezomib induced a cell cycle arrest at the transition between the G2 phase and mitosis<sup>230</sup>. Therefore, it was concluded that DSF:Cu-induced cytotoxicity at concentrations less than 1 µM was not due to inhibition of the proteasome in SK-N-BE(2c), UVW/NAT and LNCaP cells. The cytotoxic mechanism of DSF:Cu remains not well understood.

The fact that DSF competes with DSF:Cu for intracellular targets means that if DSF is in molar excess relative to Cu in the tumour, a tumouricidal effect may not be achieved. The plasma concentration of Cu is in the range 10 to 20 µM<sup>224,226,231,232</sup> and Cu is mostly bound to proteins such as ceruloplasmin and albumin. The  $K_d$  values characterising the binding of Cu to ceruloplasmin and albumin are  $10^{-17}$  and  $10^{-11}$  M, respectively<sup>233</sup>. It has been shown that a concentration of 5 µM of DSF alone had little effect on the cell cycle but DSF in combination with ceruloplasmin, added as a source of Cu, was able to induce dramatic changes in the distribution of cells through the cell cycle<sup>109</sup>. It has also been shown that DSF and DETC bind to albumin in the plasma<sup>234</sup>. These reports suggest that DSF may bind Cu in the plasma through direct binding to albumin and, perhaps, ceruloplasmin. Furthermore, Cu is a co-factor of many cellular enzymes. Therefore tumours are enriched in Cu due to their high metabolic demand<sup>84</sup>. The affinity of DSF for Cu may represent a tumour-targeting mechanism by which DSF:Cu may form preferentially in the tumour so that DSF:Cu may always be in excess compared with DSF in the tumour.

The biphasic response profile of DSF was explained and classical hyperbolic concentration-effect curves of DSF:Cu were obtained for SK-N-BE(2c) (Figure 15) and UVW/NAT cells (Figure 16). The  $IC_{50}$  and  $m$  parameters were determined, allowing the analysis of the interaction between DSF:Cu and radiation in the next chapter.

## 4 The radiosensitising effect of DSF:Cu

### 4.1 Introduction

DSF and its metabolite DETC are known radiation modifiers (Table 4). Both enhancement<sup>183,186-189</sup> of and protection from the effect of radiation<sup>180,181,184,185,193</sup> have been reported using a variety of endpoints. The demonstration of radiosensitisation by DETC in serum-complemented culture medium but not in Hank's Balanced Salt Solution (HBSS)<sup>183</sup> (Section 1.2.13.3) is significant because DETC requires Cu for cytotoxicity (Figure 10). HBSS contains salts such as magnesium, sodium, potassium and chloride but does not contain Cu. Conversely, the serum used to complement culture medium contains approximately 15  $\mu\text{M}$  Cu<sup>212,224-226</sup>. Since the presence of Cu is important for the DETC-mediated cytotoxicity (Figure 10), it is hypothesized that the lack of Cu in HBSS was the reason for the absence of a radiosensitising effect. Therefore, the first aim of this chapter is to investigate the effect of Cu on the putative radiosensitising effect DSF.

The IC<sub>50</sub> concentrations of DSF:Cu in SK-N-BE(2c) and UVW/NAT cells are 0.32 and 0.28  $\mu\text{M}$ , respectively (Figure 15). These concentrations are clinically relevant. The peak plasma concentration of DSF achieved after ingestion of 250 mg dose is 1  $\mu\text{M}$ <sup>161</sup>. Among the ten studies, listed in Table 4, which have investigated the radiomodifying effect of DSF or DETC *in vitro*, only two have examined clinically relevant concentrations - 0.1  $\mu\text{M}$  DETC<sup>187</sup> and 0.337  $\mu\text{M}$  DSF<sup>182</sup>. Therefore, the second aim of this chapter is to investigate the putative radiosensitising effect of DSF:Cu in the human neuroblastoma cell line SK-N-BE(2c) and the human glioma cell line UVW/NAT at clinically applicable levels. The concentrations of DSF:Cu or DSF used in combination with  $\gamma$ -radiation are based on the results depicted previously showing the dependency of clonogenic cell kill on dose of DSF:Cu and DSF administered as single agents (Figure 15 and Figure 16).

#### 4.1.1 Assessing the efficacy of the combination of drugs with radiation

There are several ways of analysing the effect of a combination of a drug with radiation. One method uses the linear-quadratic model to assess the effect of a range of radiation doses on cultured cells in the presence of the radiomodifier compared with the effect of radiation alone<sup>235</sup>. Secondly, the nature of the interaction of two agents in combination can be assessed by either the isobologram method<sup>98</sup> or the combination index method of synergy analysis<sup>217</sup>.

### 4.1.2 The linear-quadratic model

A radiosensitiser is defined *in vitro* as a drug which enhances the cell killing of radiation alone<sup>82</sup>. Radiosensitisation may occur by the targeting of critical cellular components required for cell survival after irradiation, increased formation of radicals or inhibition of DNA repair<sup>82</sup>. All of these mechanisms result in a leftward shift of the radiation survival curve (Figure 21).

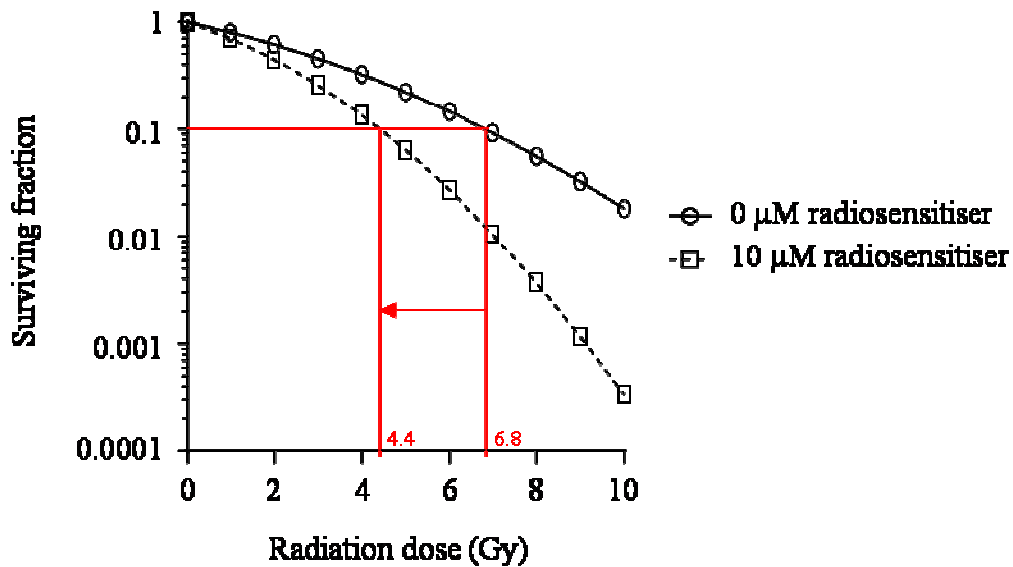


**Figure 21 The effect of a radiosensitiser on the survival of clonogens following radiation treatment**

The surviving fraction is the fraction of clonogens able to grow a colony following treatment compared with the number of clonogens forming colonies in the unirradiated control. In this example, 6.8 Gy radiation alone induced a 90% clonogenic cell kill whereas only 4.4 Gy was required to induce a similar kill in the presence of 10 μM of a radiosensitiser. The leftward shift demonstrating radiosensitisation at the 90% level of clonogenic cell kill is indicated by the red arrow. The dose enhancement factor (DEF) was  $6.8/4.4 = 1.55$ .

The linear-quadratic model describes the effect of radiation on the survival of cells<sup>235</sup>. The mathematical relationship between radiation dose and cell survival defines two components of cell killing. The linear component, defined by the initial slope  $\alpha$  of the radiation survival curve, is the result of readily repairable SSB in DNA induced by sub-lethal doses of radiation. As the radiation dose increases, the likelihood of DSB in DNA, which occur as a result of two separate ionisations, also increases. DSB are more likely to be lethal than single strand breaks. This is manifest as a greater decrease in clonogenic survival per unit dose at high radiation dose. The latter phenomenon is the quadratic component of radiation kill<sup>235</sup>. Using the linear-quadratic equation, it is possible to quantify the leftward shift of the radiation survival curve in the presence of a radiomodifier. The dose enhancement factor (DEF) measures the percentage reduction in a

radiation dose that can be delivered in the presence of a radiosensitiser that results in the same clonogenic kill as radiation alone (Figure 21).

#### **4.1.3 Isobologram and combination index methods of synergy analysis**

The use of the linear-quadratic model enables the designation of a drug as a radiosensitiser if it enhances radiation kill compared with that achieved by radiation alone. Therefore, the dose enhancement factor, calculated according to the linear-quadratic model, only measures the effect of one component (e.g. a radiomodifier) of the combination on the other agent (i.e. radiation). However, the effect of a combination treatment results from the effect of agent A on the cytotoxicity induced by agent B and from the effect of agent B on the cytotoxicity induced by agent A. The dose enhancement factor is not a measure of the interaction of two agents in a combination. Several methods have been used to analyse the response of cells to combination treatment<sup>214</sup>. The most widely used are the isobologram<sup>98</sup> and the combination index<sup>217</sup> methods of synergy analysis. Both methods define the concept of additivity and compare the effect of the combination to a theoretical additive interaction between the two agents of the combination. The theoretical additive effect is calculated based on the concentration-effect relationships of each single agent. A combination treatment may be infra-additive, additive or supra-additive if the combined effect is less than, equal to or greater than the expected addition of the effects of each agent, respectively. The quantification of radiosensitisation using the dose enhancement factor calculated from the leftward shift of the radiation survival curve does not give information concerning the nature of the radiosensitising effect (additive versus supra-additive). There is not a defined threshold value of the dose enhancement factor beyond which radiosensitisation no longer results from a simple additive effect but results from a supra-additive effect.

A synergistic combination has therapeutic advantages over an additive combination. Synergism means that the doses of both components of the combination can be reduced and still be as (or more) cytotoxic in combination with each other. Consequently, the reduction of the doses of each agent will reduce side-effects, leading to an improvement of the patient's quality of life. A purely additive combination may still be of therapeutic interest due to the increase in tumour cell toxicity compared to each agent alone, especially if the combination does not increase toxicity in normal tissue<sup>98</sup>. Therefore, the *in vitro* determination of the additive or the supra-additive nature of the radiosensitising effect allows the prediction of a combination treatment which could induce less clinical side-effects while retaining its efficacy.

This chapter is concerned with the determination of the nature of the interaction between DSF:Cu or DSF and  $\gamma$ -radiation using the clonogenic assay. It will be shown that DSF:Cu and DSF are both radiosensitisers. The interactions between DSF:Cu or DSF and  $\gamma$ -radiation were synergistic, additive or antagonistic depending on the level of toxicity induced by the combined treatments.

## **4.2 Aims**

- determination of the requirement of Cu for the radiomodifying properties of DSF
- determination of the radiomodifying effects of DSF:Cu and DSF in the human cell lines SK-N-BE(2c) (neuroblastoma) and UVW/NAT (glioma) at clinically relevant concentrations
- analysis of the interaction between DSF:Cu or DSF and  $\gamma$ -radiation

## **4.3 Materials and methods**

### **4.3.1 Tissue culture**

See Section 3.3.1.

### **4.3.2 $\gamma$ -radiation treatment**

The cells were irradiated using an external beam irradiator containing a  $^{60}\text{Co}$  source (Alcyon II Teletherapy Unit). The flasks containing the cells were covered using a 0.8 cm perspex plate to ensure maximal energy deposition. The dose rate was approximately 1 Gy/min.

### **4.3.3 Clonogenic assay**

See section 3.3.4.

### **4.3.4 The linear-quadratic model**

#### **4.3.4.1 The linear-quadratic equation**

The linear-quadratic model describes the effect of radiation on the survival of cells. The cell survival curve follows the mathematical equation:

$$\text{SF} = \exp(-\alpha D - \beta D^2) \quad (4)$$

in which SF is the fraction of clonogens surviving a dose D of radiation. The linear-quadratic model assumes two components of clonogenic kill, one that is proportional to the dose D of  $\gamma$ -radiation with a coefficient  $\alpha$  and one that is proportional to the square of D with a coefficient  $\beta$ <sup>235</sup>. GraphdPadPrism version 6.01 was used to fit clonogenic survival data to the linear-quadratic model and to calculate  $\alpha$  and  $\beta$  values.

#### 4.3.4.2 Calculation of the IC<sub>50</sub>

Equations (5) and (6) are two versions of the logarithmic transformation of equation (1):

$$\ln SF = -\alpha D - \beta D^2 \quad (5)$$

$$0 = -\alpha D - \beta D^2 - \ln SF \quad (6)$$

The resolution of a quadratic equation is based on the calculation of its determinant  $\Delta$ <sup>236</sup>:

$$\Delta = \alpha^2 - 4\beta \ln SF \quad (7)$$

If  $\Delta < 0$ , there is no solution to equation (6), if  $\Delta \geq 0$ , the two solutions  $D_1$  and  $D_2$  to equation (6) are given by:

$$D_1 = (-\alpha + \sqrt{\Delta}) / 2\beta \quad (8) \text{ and}$$

$$D_2 = (-\alpha - \sqrt{\Delta}) / 2\beta \quad (9)$$

As the surviving fraction cannot increase with increasing radiation dose, the values  $\alpha$  and  $\beta$  are positive values according to equation (4). Furthermore, the surviving fraction is always a value between 0 and 1. Therefore  $\ln SF$  is negative. From these observations, it follows that  $4\beta \ln SF$  is always a negative value. Therefore, for all possible surviving fraction values,  $\Delta$  is always greater than 0 according to equation (7). Because  $\Delta > 0$  and a dose cannot be negative, the unique solution of equation (6) is given by:

$$D = [-\alpha + \sqrt{(\alpha^2 - 4\beta \ln SF)}] / 2\beta \quad (10)$$

It follows that:

$$IC_{50} = [-\alpha + \sqrt{(\alpha^2 - 4\beta \ln 0.5)}] / 2\beta \quad (11)$$

#### 4.3.4.3 Calculation of DEF

DEF is the factor by which the dose of radiation may be reduced in the presence of a drug to achieve the same clonogenic cell kill as would radiation treatment alone. Three levels of clonogenic cell kill were assessed: 25%, 50% and 75%.  $IC_{25}$ ,  $IC_{50}$  and  $IC_{75}$  were calculated using equation (10), by replacing SF by 0.75, 0.5 and 0.25, respectively. For each level of clonogenic cell kill,  $DEF_{25}$ ,  $DEF_{50}$  and  $DEF_{75}$  were calculated using:

$$DEF_x = IC_x \text{ radiation alone} / IC_x \text{ of radiation in the presence of a drug} \quad (12)$$

The greater the  $DEF_x$  value, the smaller the radiation dose needed in the presence of a drug in order to induce the same clonogenic cell kill as radiation alone.

#### 4.3.4.4 Drug treatment

SK-N-BE(2c) and UVW/NAT cells were exposed to various doses of  $\gamma$ -radiation in the absence or in the presence of various concentrations of DSF:Cu or DSF in serum-free medium. The doses of  $\gamma$ -radiation and the concentrations of DSF:Cu and DSF were chosen so that the maximal combination treatment intensity corresponded to a mixture of the  $IC_{50}$  values of each agent. The cells were exposed to DSF:Cu or DSF and irradiated immediately afterward. Clonogenic assays were performed 24 h after treatment of the cells with DSF:Cu or DSF.

#### 4.3.5 The median effect principle

The median effect principle is described in Section 3.3.5. The mathematical equation relating the dose of an agent to its effect is:

$$fa/fu = (D / IC_{50})^m \quad (3)$$

where  $fa$  is the fraction of clonogens affected by the dose  $D$ ;  $fu$  is the fraction of clonogens unaffected by dose  $D$  (hence  $fu = 1 - fa$ );  $IC_{50}$  is the dose which inhibits 50% of the effect ( $IC_{50}$ ) and  $m$  is the coefficient of sigmoidicity describing the shape of the dose-effect relationship, where  $m = 1$ ,  $m > 1$ , and  $m < 1$  indicate hyperbolic, sigmoidal, and flat sigmoidal dose-effect curves, respectively<sup>214</sup>. The parameters  $m$  and the  $IC_{50}$  value can be calculated as described in Section 3.3.5. Equation (3) can be rearranged in order to calculate the concentration producing a given effect:

$$D = IC_{50} \times (fa/fu)^{1/m} \quad (12)$$

#### 4.3.6 Isobologram analysis

Isobologram analysis was performed in order to determine the nature of the interaction between DSF:Cu or DSF with  $\gamma$ -radiation according to the method of Steel and Peckham<sup>98</sup>. The concept of additive interaction between two agents in a combination is based on their dose-response curves as single agents. There are two ways of defining additivity by the isobologram method: mode I and mode II. In the mode I determination of additivity, it is considered that there is a linear relationship between concentration of each agent and the effect produced, i.e. the clonogenic cell kill for any increment in concentration is constant for all parts of the survival curve. In the mode II determination of additivity, it is considered that there is a non-linear relationship between the concentration of each agent and the effect produced, i.e. the clonogenic cell kill for any increment in concentration varies throughout the survival curve<sup>98</sup>.

##### 4.3.6.1 Mode I isobologram analysis

In mode I, both agents reduce the surviving fraction in a linear fashion. Therefore, as the concentration increases by a constant increment, the reduction of the surviving fraction is constant. In order to obtain mode I in an isobologram constructed at the 50% level of cytotoxicity, a series of concentrations of agent A that produce an effect up to 50% as a single agent are calculated using the median effect principle. The effects were 0%, 10%, 20%, 30%, 40% and 50%. Then, concentrations of agent B are calculated so that, when added to the effect of agent A, they produce an overall 50% reduction in clonogenicity. For example, the concentration of agent A producing a 30% effect is 3 AU and the concentration of agent B producing a 20% effect is 0.8 AU (Figure 22a). Finally, mode I is constructed by plotting the pairs of concentrations of agents A and B whose combined effect adds up to 50% (Figure 22d). The circled diamond corresponds to the pair IC<sub>30</sub> of agent A (3 AU) combined with the IC<sub>20</sub> of agent B (0.8 AU) as calculated in Figure 22a.

##### 4.3.6.2 Mode II isobologram analysis

In mode II, both agents reduce the surviving fraction in a non-linear fashion. Therefore, as the concentration increases by a constant increment, the reduction of the surviving fraction varies. Modes IIa and IIb assume non-linearity of the effect of agents A and B with increasing concentration, respectively. In order to obtain mode IIa in an isobologram constructed at the 50% level of effect, a series of concentrations of agent B that produces a

series of levels of toxicity up to 50% (0%, 10%, 20%, 30%, 40% and 50%) is calculated. This series of effects is then used as the initial level of cytotoxicity from which the increment of the concentration of agent A that produces a total level of toxicity of 50% is calculated (Figure 22b). For example, the concentration of agent B that produces a 20% cell kill is 2.2 AU and the increment concentration of agent A that allows the overall toxicity to increase from 20% to 50% is 1.2 AU (8 - 6.8) (Figure 22b). Finally, mode IIa is constructed by plotting the concentration of agent B against the increment concentration of agent A whose combined effect adds up to 50% (Figure 22e). The circled triangle (Figure 22e) corresponds to the pair  $IC_{50} - IC_{20}$  of agent A (1.2 AU) combined with the  $IC_{20}$  of agent B (2.2 AU) as calculated in Figure 1b.

In order to obtain mode IIb in an isobologram constructed at the 50% level of effect, a series of concentrations of agent A that produces a series of levels of toxicity up to 50% (0%, 10%, 20%, 30%, 40% and 50%) is calculated. This series of effects is then used as the initial level of cytotoxicity from which the increment of the concentration of agent B that produces a 50% effect is calculated (Figure 22c). For example, the concentration of agent A that produces a 20% effect is 6.8 AU and the increment concentration of agent B that allows the overall toxicity to increase from 20% to 50% is 1.4 AU (3.6 - 2.2) (Figure 22c). Finally, mode IIb is constructed by plotting the increment concentration of agent B against the concentration of agent A whose combined effect adds up to 50% (Figure 22e). The circled square (Figure 22e) corresponds to the pair  $IC_{20}$  of agent A (6.8 AU) combined with the  $IC_{50} - IC_{20}$  of agent B (1.4 AU) as calculated in Figure 1c.

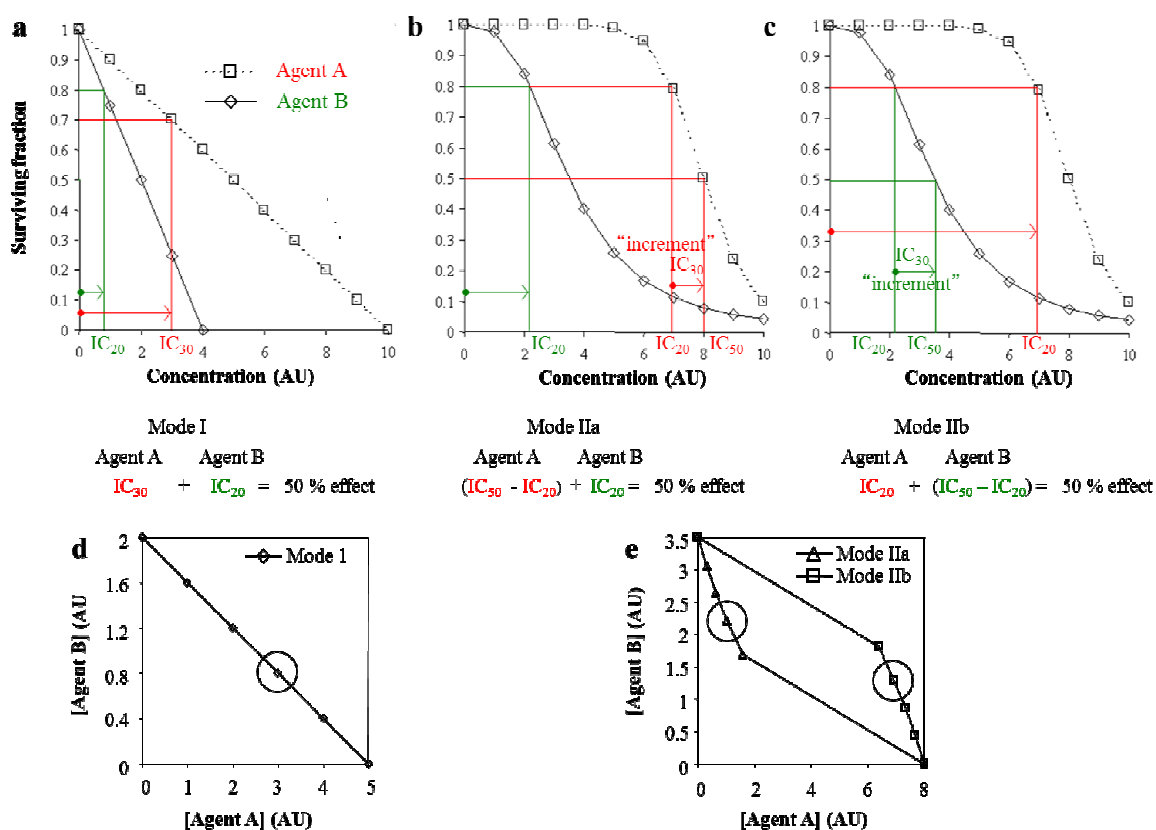


**Figure 22** The determination of additivity by mode I, IIa and IIb in the construction of an isobologram at the 50% level of cytotoxicity

The example given for the construction of modes I (a), IIa (b) and IIb (c) is a combination of the concentration of one agent that produce a 20% effect with the concentration of the second agent producing a 30% effect. (d) Mode I defines the line of additivity. (e) Modes IIa and IIb define the envelope of additivity.

#### 4.3.6.3 Determination and interpretation of the isoeffect points

The following method describes the determination of the isoeffect points at the 50% level of toxicity. Firstly, the surviving fractions are plotted against the concentrations of agent A in the absence and in the presence of 4 different concentrations of agent B. The concentrations of agent A producing a 50% effect ( $IC_{50}$ ) in the presence of 2, 4, 6 and 8 AU of agent B are calculated using the median effect principle (Figure 23a). In this example, they are 6.34, 4.85, 3.83 and 2.68 AU, respectively (Figure 23a). Therefore, 6.34 AU of agent A in combination with 2 AU of agent B produces a 50% reduction in clonogenicity. The pairs of AU values (6.34, 2), (4.85, 4), (3.83, 6) and (2.68, 8) are the coordinates of four isoeffect points at the 50% level of cytotoxicity (Figure 23a). Secondly, the analogous procedure is performed to determine the effect of agent B on the survival fraction in the absence and in the presence of 4 different concentrations of agent A (Figure 23b). The concentrations of agent B producing a 50% effect ( $IC_{50}$ ) in the presence of 3, 5, 7 and 9 AU of agent A are calculated using the median effect principle (Figure 23b). The

pairs of AU values (3, 12.68), (5, 9.69), (7, 7.66) and (9, 5.36) are the coordinates of four isoeffect points at the 50% level of cytotoxicity (Figure 23b).

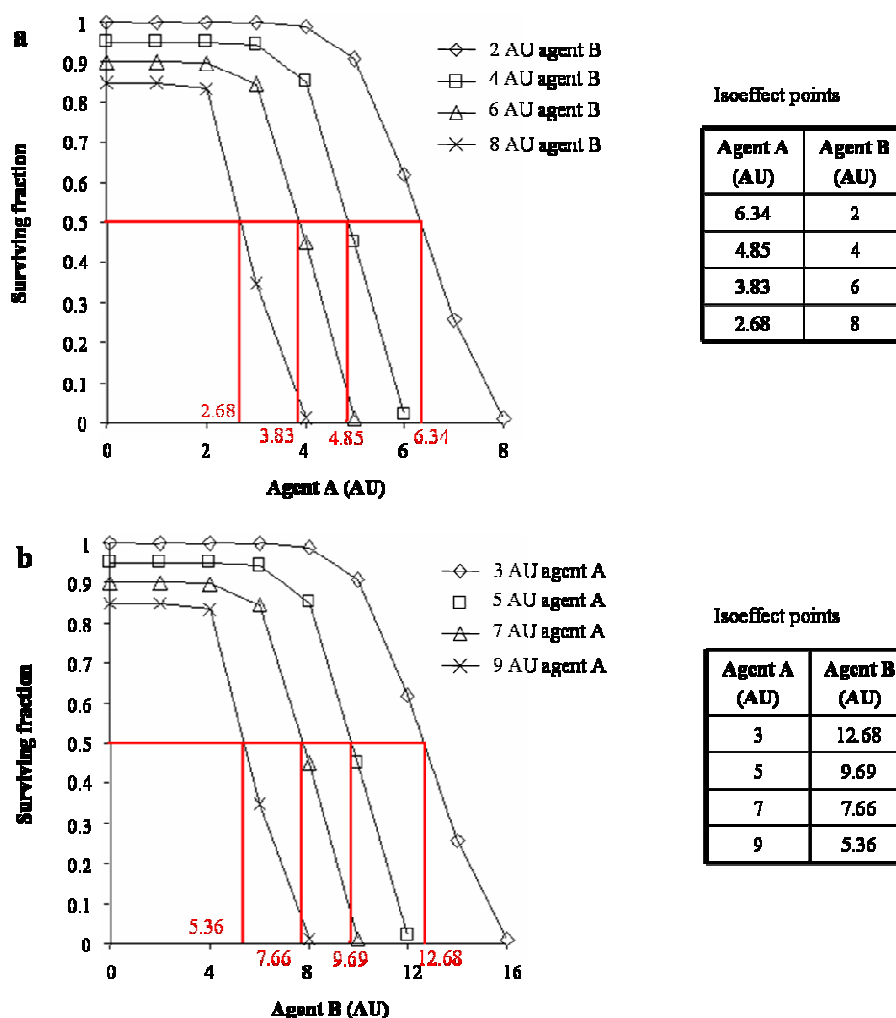


**Figure 23 Determination of isoeffect points**

(a) The effect of agent A on the survival fraction in the absence and in the presence of 4 concentrations of agent B. (b) The effect of agent B on the survival fraction in the absence and in the presence of 4 concentrations of agent A. The median effect principle is used to calculate the concentration producing a particular effect of agent A in the presence of various concentrations of agent B, and, *vice versa*, of agent B in the presence of various concentrations of agent A. The effect of 50% is chosen in the case of an isobologram constructed at the 50% level of cytotoxicity.

The isoeffect points generated from the combinations of agent A and B are then plotted onto the isobologram chart, as shown in Figure 24. If the isoeffect points lie to the left of the envelope of additivity, the response is supra-additive. If the isoeffect points lie within the envelope of additivity, the response is additive. If the isoeffect points lie to the right of the envelope of additivity but within the square of the doses of the single agents producing the same effect, the response is infra-additive. If the isoeffect points lie outside that square, the response is protective (Figure 24).

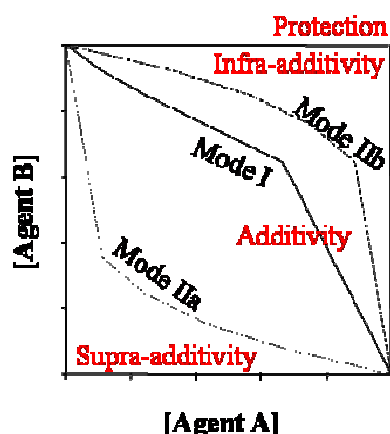


Figure 24 The significance of plotted isoeffect points relative to the envelope of additivity

#### 4.3.6.4 Drug treatment

Isobologram analysis was performed on the data set obtained for the evaluation of the combination of DSF:Cu or DSF with  $\gamma$ -radiation using the linear-quadratic model. Methodology is described in Section 4.3.4.4.

#### 4.3.7 Combination index analysis

##### 4.3.7.1 Combination index analysis

Combination index analysis was performed according to the method of Chou and Talalay<sup>217</sup>. In this method, the doses of each agent within the combination that produce a given level of cytotoxicity are compared with those producing the same level of cytotoxicity as single agents. The median effect equation is used to calculate the parameters  $m$  and  $IC_{50}$  of the single agents and the combinations as described in Section 3.3.5. Knowing  $m$  and  $IC_{50}$ , the median effect equation could be rearranged to calculate a dose  $D$  corresponding to a given effect using equation (12):

$$D = IC_{50} \times (fa/fu)^{1/m} \quad (12)$$

in which  $fa$  is the fraction of clonogens affected by a dose  $D$ ,  $fu$  is the unaffected fraction of clonogens,  $IC_{50}$  is the dose required to reduce the effect by 50% and  $m$  is the coefficient of sigmoidicity describing the shape of the dose-effect relationship, where  $m = 1$ ,  $m > 1$ , and  $m < 1$  indicate hyperbolic, sigmoidal, and flat sigmoidal dose-effect curves, respectively<sup>214</sup>.

For combination treatments, the calculated dose  $D$  is the sum of the doses of each agent. The contribution of each agent to the combination is calculated using a constant ratio ( $P/Q$ ) of the doses of each agent. For instance, the dose  $D$  of the combination is split into the concentration of agent A ( $D_A$ ) and the dose of agent B ( $D_B$ ).  $P$  is the proportion of the total dose  $D$  of the combination which corresponds to the concentration of agent 1, whereas  $Q$  is the proportion of the total dose  $D$  of the combination which corresponds to the dose of agent B:

$$D_A = D \times P/(P+Q) \quad (13)$$

$$D_B = D \times Q/(P+Q) \quad (14)$$

The dose reduction index (DRI) was then calculated for each agent of the combination by dividing the dose within the combination by the dose as a single agent that induced the same kill:

$$\text{DRI} = D \text{ within the combination} / D \text{ as single agent} \quad (15)$$

The combination index (CI) was the sum of the DRI of each agent of the combination:

$$\text{CI} = \text{DRI}_{\text{agent1}} + \text{DRI}_{\text{agent2}} \quad (16)$$

The interpretation of the CI value for the determination of infra-additivity, additivity or supra-additivity is given in Table 5.

Range of Combination Index	Description	Graded Symbols
<0.1	Very strong synergism	+++++
0.1–0.3	Strong synergism	++++
0.3–0.7	Synergism	+++
0.7–0.85	Moderate synergism	++
0.85–0.90	Slight synergism	+
0.90–1.10	Nearly additive	±
1.10–1.20	Slight antagonism	–
1.20–1.45	Moderate antagonism	--
1.45–3.3	Antagonism	---
3.3–10	Strong antagonism	----
>10	Very strong antagonism	-----

**Table 5 The interpretation of the combination index (CI) according to Chou<sup>214</sup>**

Supra-additivity (synergy) is defined by CI values lower than 0.90, additivity is defined by CI values comprised between 0.90 and 1.10 and infra-additivity (antagonism) is defined by CI values greater than 1.10.

#### 4.3.7.2 Drug treatment

The combination index method of synergy analysis was applied to a data set different from the one used for the analysis of radiosensitisation by the linear-quadratic method and analysis of synergy by the isobologram method. SK-N-BE(2c) and UVW/NAT cells were treated with DSF:Cu, DSF and  $\gamma$ -radiation as single agents and with combinations of DSF:Cu or DSF with  $\gamma$ -radiation. DSF:Cu and DSF treatments were carried out in serum-free medium for 24 h. DSF:Cu and DSF were combined with  $\gamma$ -radiation in a constant ratio based on the IC<sub>50</sub> concentrations of each agent. The selected combination treatment of highest intensity was a mixture of the 50% inhibitory concentrations of each agent (IC<sub>50</sub>). The altered combination treatments consisted of one-half, one-quarter and one-eighth of the maximum combination treatment dose<sup>214</sup> (Table 6).

Toxicity level	Agent A (M)	Agent B (M)
IC <sub>0</sub>	0	0
IC <sub>50/8</sub>	IC <sub>50-A/8</sub>	IC <sub>50-B/8</sub>
IC <sub>50/4</sub>	IC <sub>50-A/4</sub>	IC <sub>50-B/4</sub>
IC <sub>50/2</sub>	IC <sub>50-A/2</sub>	IC <sub>50-B/2</sub>
IC <sub>50</sub>	IC <sub>50-A</sub>	IC <sub>50-B</sub>

**Table 6 Experimental design of the combination treatment intensities in combination index analysis**

The IC<sub>50</sub> values of DSF:Cu and DSF were determined previously (Figure 15 and Figure 16). The IC<sub>50</sub> values of  $\gamma$ -radiation will be described in Figure 25. SK-N-BE(2c) cells were treated with a ratio of 3 Gy  $\gamma$ -radiation to 0.3  $\mu$ M DSF:Cu or 3 Gy  $\gamma$ -radiation to 15  $\mu$ M DSF. UVW/NAT cells were treated with a ratio of 3 Gy  $\gamma$ -radiation to 0.3  $\mu$ M DSF:Cu or 3

Gy  $\gamma$ -radiation to 24  $\mu$ M DSF. For the combinations, the cells were treated with the drugs and irradiated immediately afterward. Clonogenic assay was performed immediately after the 24 h incubation period in the presence of drugs.

#### 4.4 Results

##### 4.4.1 Mathematical modelling of the effect of $\gamma$ -radiation as a single agent using the linear-quadratic model

The effect of  $\gamma$ -radiation as a single agent in SK-N-BE(2c) and UVW/NAT cells was firstly investigated in order to determine the radiation dose range to use in combination with DSF:Cu or DSF. SK-N-BE(2c) and UVW/NAT cells were exposed to various doses of  $\gamma$ -radiation and clonogenic assay was performed 24 h later. The doses of  $\gamma$ -radiation which killed 50% of clonogens ( $IC_{50}$ ) were 2.82 and 2.77 Gy for SK-N-BE(2c) and UVW/NAT cells, respectively (Figure 25). The smaller  $\beta$  value in UVW/NAT cells than SK-N-BE(2c) cells indicated that UVW/NAT cells were more resistant to  $\gamma$ -radiation treatment than SK-N-BE(2c) cells (Figure 25). Based on this result, the  $\gamma$ -radiation dose range of 0-3 Gy was employed for the study of the combination of  $\gamma$ -radiation with DSF:Cu or DSF.

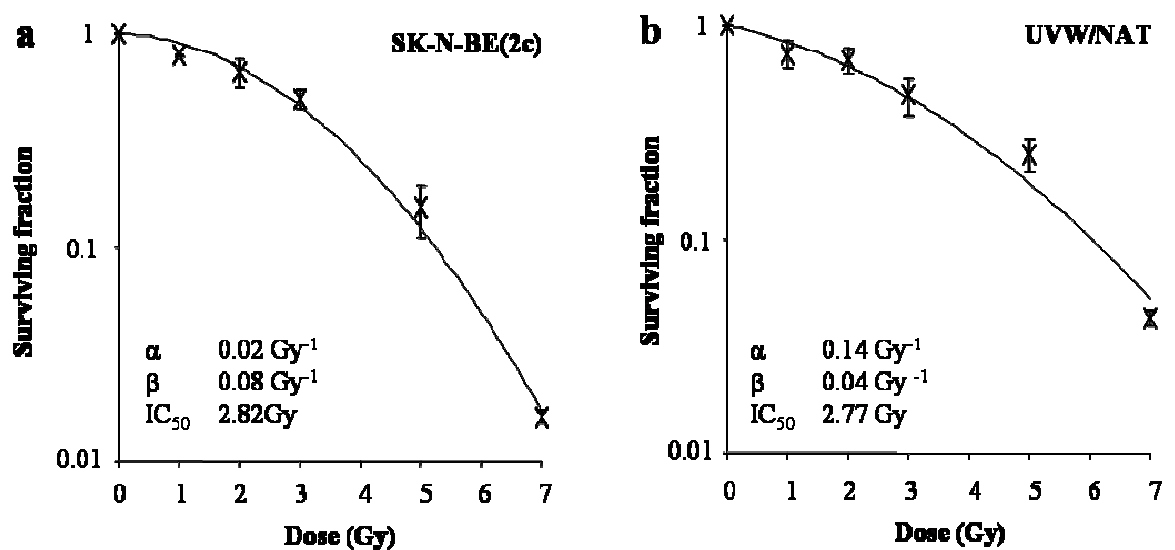


**Figure 25** The effect of  $\gamma$ -radiation on the clonogenic survival of SK-N-BE(2c) and UVW/NAT cells

The clonogenic survival of SK-N-BE(2c) (a) and UVW/NAT (b) cells was determined 24 h after  $\gamma$ -radiation treatment using a cobalt-60 external beam irradiator. Data are means  $\pm$  SEM; n=5.

##### 4.4.2 Determination of the radiosensitising effect of disulfiram using the linear-quadratic model

The effect of DSF:Cu and DSF on radiation cell kill was assessed using the clonogenic assay. SK-N-BE(2c) and UVW/NAT cells were irradiated with various  $\gamma$ -radiation doses in

the presence and in the absence of various concentrations of DSF:Cu and DSF. The concentrations of DSF:Cu and DSF and the doses of  $\gamma$ -radiation were selected so that the maximum treatment intensity corresponded to the  $IC_{50}$  value of each modality. The linear-quadratic equation was fitted to the data in order to calculate  $\alpha$ ,  $\beta$ ,  $IC_{50}$  and DEF values at the 25%, 50% and 75% cytotoxicity levels. These values were then used to characterise the radiosensitising potency of DSF:Cu and DSF.

#### **4.4.2.1 The effect of DSF:Cu on the survival of $\gamma$ -irradiated SK-N-BE(2c) clonogens**

DSF:Cu enhanced the  $\gamma$ -radiation-induced kill of SK-N-BE(2c) cells (Figure 26a). The  $IC_{50}$  value decreased from 3.22 Gy in the absence of DSF:Cu to 0.76 Gy in the presence of 0.3  $\mu$ M DSF:Cu (Figure 26b). The DEF values of 0.3  $\mu$ M DSF:Cu were 5.42, 4.24 and 3.59 at 25, 50 and 75% cytotoxicity, respectively (Figure 26b). Moreover, the  $\alpha$  value increased with increasing concentrations of DSF:Cu (Figure 26b). This indicated that DSF:Cu increased the proportion of  $\gamma$ -radiation-induced cytotoxicity caused by breakage of single strands of DNA. Finally, the  $\beta$  value increased with increasing DSF:Cu concentrations, indicative of the increase by DSF:Cu of the proportion of  $\gamma$ -radiation-induced cytotoxicity caused by multi-event DNA damage (Figure 26b).

#### **4.4.2.2 The effect of DSF on the survival of SK-N-BE(2c) clonogens following $\gamma$ -radiation treatment**

Similarly, DSF enhanced the  $\gamma$ -radiation-induced kill of SK-N-BE(2c) cells (Figure 26c). The  $IC_{50}$  value decreased from 3.04 Gy in the absence of DSF to 0.82 Gy in the presence of 15  $\mu$ M DSF (Figure 26d). The DEF values of 15  $\mu$ M DSF were 5.03, 3.72 and 3.29 at 25, 50 and 75% clonogenic kill, respectively (Figure 26d). Moreover, the  $\alpha$  and  $\beta$  values increased in response to  $\gamma$ -radiation treatment with increasing concentrations of DSF (Figure 26d). This indicated that DSF increased the proportion of  $\gamma$ -radiation-induced cytotoxicity caused by both single and multi-event DNA damage (Figure 26d).

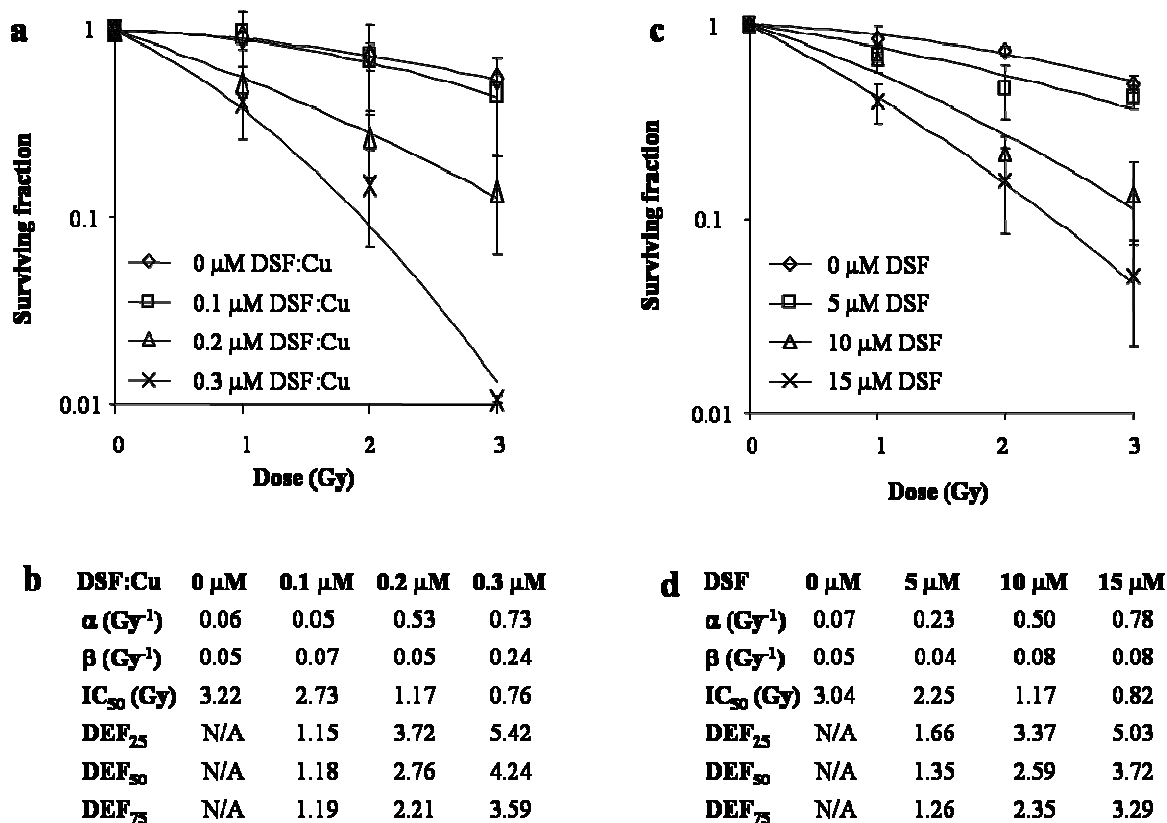


**Figure 26** The radiosensitising effect of DSF:Cu and DSF in SK-N-BE(2c) cells

The clonogenic survival of SK-N-BE(2c) cells was determined 24 h after  $\gamma$ -radiation treatment in the absence or in the presence of various concentrations of DSF:Cu (a) or DSF (c). The data were fitted to the linear-quadratic equation using GraphPad Prism version 6.0.1. Data are means  $\pm$  SEM; n=3. The values  $\alpha$ ,  $\beta$ ,  $\text{IC}_{50}$ ,  $\text{DEF}_{25}$ ,  $\text{DEF}_{50}$  and  $\text{DEF}_{75}$  were calculated for DSF:Cu (b) or DSF (d) as described in Section 4.3.4.

#### 4.4.2.3 The effect of DSF:Cu on the survival of UVW/NAT clonogens following $\gamma$ -radiation treatment

UVW/NAT cells were more resistant than SK-N-BE(2c) cells to the radiosensitising effect of DSF:Cu (Figure 27a). The  $\text{IC}_{50}$  value decreased from 3.75 Gy in the absence of DSF:Cu to 1.87 Gy in the presence of 0.3  $\mu\text{M}$  DSF:Cu (Figure 27b). The DEF values of 0.3  $\mu\text{M}$  DSF:Cu were 2.55, 2.00 and 1.62 at 25%, 50% and 75% cytotoxicity, respectively (Figure 27b). Moreover, the  $\alpha$  value increased with increasing concentrations of DSF:Cu (Figure 27b). This indicated that DSF:Cu increased the proportion of  $\gamma$ -radiation-induced cytotoxicity caused by single event DNA damage. Finally, the  $\beta$  value decreased from 0.03 to 0.01 in response to  $\gamma$ -radiation treatment with increasing concentrations of DSF:Cu, suggesting that the proportion of  $\gamma$ -radiation-induced cytotoxicity caused by DSB of DNA decreased (Figure 27b) in response to  $\gamma$ -radiation treatment with increasing concentrations of DSF:Cu. This may explain the reduced radiosensitising effect of DSF:Cu in UVW/NAT cells compared with SK-N-BE(2c) cells.

#### 4.4.2.4 The effect of DSF on the survival of UVW/NAT clonogens following $\gamma$ -radiation treatment

UVW/NAT cells were also more resistant than SK-N-BE(2c) to the radiosensitising effect of DSF (Figure 27c). The  $IC_{50}$  value decreased from 4.67 Gy in the absence of DSF to 2.16 Gy in the presence of 24  $\mu$ M DSF (Figure 27d). The DEF values of 24  $\mu$ M DSF were 2.48, 2.17 and 1.90 at 25%, 50% and 75% clonogenic kill, respectively (Figure 27d). Moreover, the  $\alpha$  values were increased with increasing DSF concentrations (Figure 27d). This indicated that DSF increased the proportion of  $\gamma$ -radiation-induced cytotoxicity caused by single event DNA damage. There was no change in the  $\beta$  value derived from this model, suggesting that  $\gamma$ -radiation-induced cytotoxicity caused by multi-event DNA damage was not affected (Figure 27d). Again, the absence of a modification of the  $\gamma$ -radiation-induced clonogenic cell kill due to multi-event DNA damage may explain the reduced radiosensitising effect of DSF in UVW/NAT compared with SK-N-BE(2c) cells.

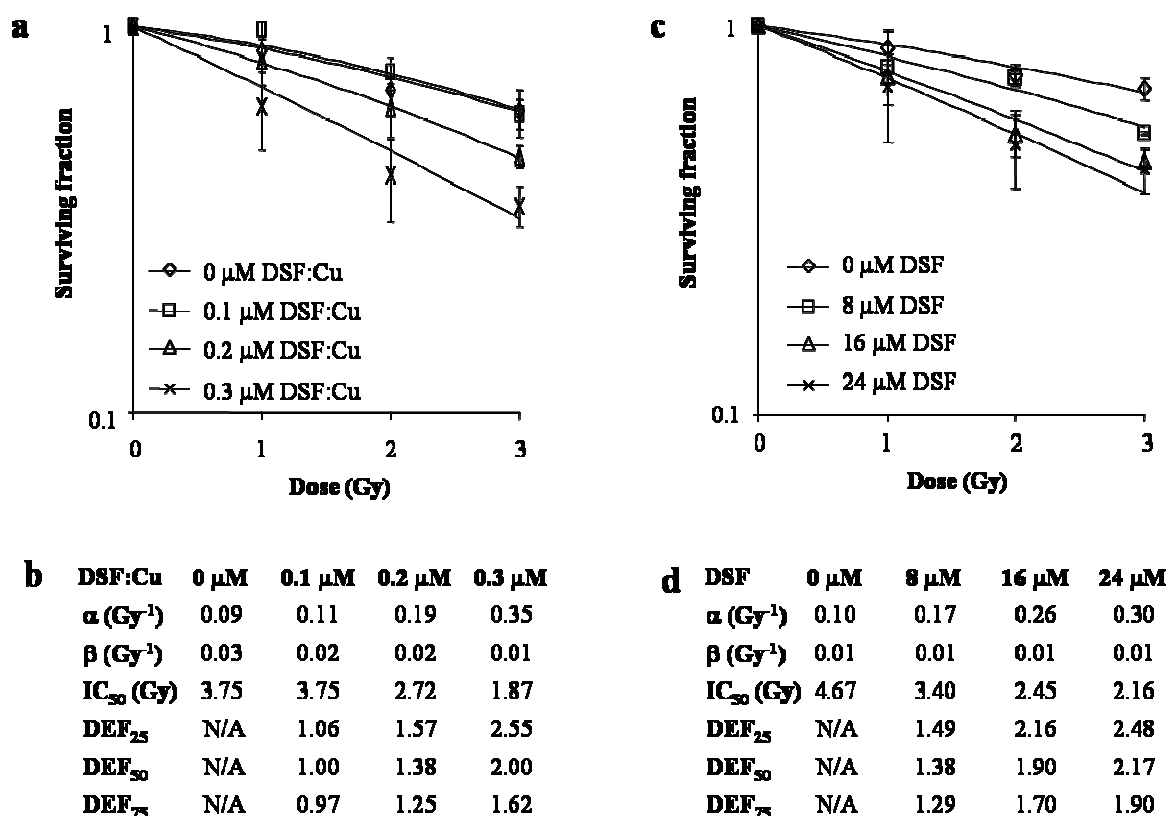


**Figure 27** The radiosensitising effect of DSF:Cu and DSF in UVW/NAT cells

The clonogenic survival of UVW/NAT cells was determined 24 h after  $\gamma$ -radiation treatments in the absence or in the presence of various concentrations of DSF:Cu (a) or DSF (c). The data were fitted with the linear-quadratic equation using GraphPad Prism version 6.0.1. The values  $\alpha$ ,  $\beta$ ,  $IC_{50}$ ,  $DEF_{25}$ ,  $DEF_{50}$  and  $DEF_{75}$  were calculated for DSF:Cu (b) or DSF (d) as explained in Section 4.3.4. Data are means  $\pm$  SEM; n=3.

#### 4.4.2.5 Conclusions

These data demonstrated that both DSF:Cu and DSF are radiosensitisers as indicated by the leftward shifts of their respective radiation survival curves. However, the peak plasma concentration after oral administration of a typical daily dose (250 mg) of DSF is  $1 \mu\text{M}^{161}$ . The radiosensitisation induced by DSF:Cu occurred at concentrations achievable in patients (0.1 to 0.3  $\mu\text{M}$ ) whereas the radiosensitisation induced by DSF occurred at concentrations greater than 5  $\mu\text{M}$ . Thus, only the radiosensitisation induced by DSF:Cu is expected to be clinically applicable.

The  $\alpha$  and  $\beta$  values measure the proportion of radiation kill due to SSB and DSB, respectively. The observed variations in  $\alpha$  and  $\beta$  values allow for the formulation of an hypothesis concerning the mechanism of radiosensitisation by DSF:Cu. The  $\alpha$  value of the radiation kill was increased 12.2-fold and 3.9-fold when SK-N-BE(2c) and UVW/NAT cells, respectively, were irradiated in the presence of 0.3  $\mu\text{M}$  DSF:Cu. This indicated that the radiosensitising mechanism of DSF:Cu is the increase of SSB incidence or the inhibition of repair of SSB. Furthermore, the proportion of SSB after radiation treatment in the presence of DSF:Cu was increased to a greater extent in SK-N-BE(2c) compared to UVW/NAT cells. The latter observation suggests that the SSB repair machinery was more efficient in UVW/NAT cells than in SK-N-BE(2c) cells.

Similarly, the  $\beta$  value of the radiation kill was increased 4.8-fold when SK-N-BE(2c) cells were irradiated in the presence of 0.3  $\mu\text{M}$  DSF:Cu compared with the 3-fold decrease of the  $\beta$  value observed in UVW/NAT cells. This indicates that UVW/NAT are also more efficient at repairing DSB than SK-N-BE(2c) cells. Furthermore, since UVW/NAT are more efficient at repairing SSB than SK-N-BE(2c) cells, as indicated by the smaller increase in the  $\alpha$  value, fewer SSB will be converted into DSB during DNA replication. This is consistent with the absence of an increase in the  $\beta$  value after treatment of UVW/NAT cells with radiation in the presence of DSF:Cu.

#### 4.4.3 Determination of the nature of the radiosensitising effect of DSF:Cu and DSF

The effect of a radiosensitiser on the response of cells to  $\gamma$ -radiation is the enhancement of  $\gamma$ -radiation kill compared with  $\gamma$ -radiation alone. DEF values are calculated as a measure of radiosensitisation. However, a comparison of DEF values does not enable the assignment of additive, supra-additive or infra-additive interactions between agents in a combination treatment. Moreover, the DEF values only quantify the potentiating effect of a drug on the

clonogenic cell kill of  $\gamma$ -radiation. The extent to which radiosensitisation results from an additive or a supra-additive interaction is investigated by isobologram and combination index methods of synergy analysis. These procedures enable the determination of the effect of DSF:Cu or DSF on radiation cell kill and the effect of  $\gamma$ -radiation on cytotoxicity induced by DSF:Cu or DSF.

#### **4.4.3.1 Isobologram analysis**

##### **4.4.3.1.1 Isobologram analysis of DSF:Cu or DSF in combination with $\gamma$ -radiation in SK-N-BE(2c) cells**

The effect of  $\gamma$ -radiation and DSF:Cu on the survival of SK-N-BE(2c) clonogens is shown in Figure 28a. The corresponding median effect plot and the parameters of the median effect equations are shown in Figure 28b and Figure 28c. Similarly, the effect of  $\gamma$ -radiation and DSF on the clonogenic survival of SK-N-BE(2c) is shown in Figure 28d. The corresponding median effect plot and the parameters of the median effect equations are shown in Figure 28e and Figure 28f. The isobologram analysis of the combination of DSF:Cu or DSF with  $\gamma$ -radiation at 25%, 50% and 75% toxicity levels are shown in Figure 29.

At the 25% level of toxicity, one isoeffect point plotted above the envelope of additivity whereas the second isoeffect point plotted below, indicating synergistic or antagonistic interactions between DSF:Cu and  $\gamma$ -radiation depending on the relative contribution of each agent (Figure 29a). That is, when  $\gamma$ -radiation made a minor contribution to kill of 25% of clonogens, the interaction with DSF:Cu was antagonistic whereas the interaction between DSF:Cu and  $\gamma$ -radiation was synergistic when DSF:Cu made a minor contribution to kill of 25% (Figure 29a). At the 50% and 75% levels of toxicity, the isoeffect points, with one exception (Figure 29b), plotted below or within the envelope of additivity, demonstrating respectively supra-additive and additive interactions between DSF:Cu and  $\gamma$ -radiation depending on the relative dose of each agent (Figure 29b and Figure 29c). The combination of a large dose of  $\gamma$ -radiation with a small dose of DSF:Cu resulted in additive interactions. Likewise, the same result was observed following combinations of a small dose of  $\gamma$ -radiation with a large dose of DSF:Cu.

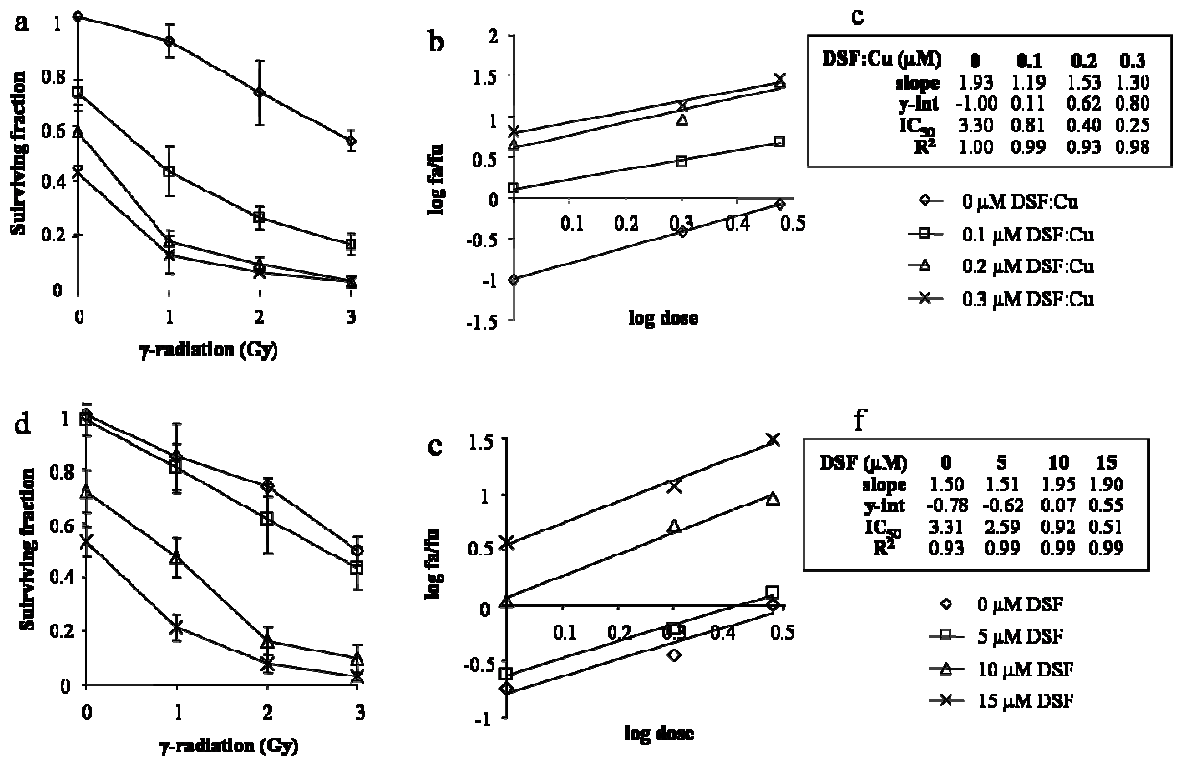


**Figure 28** Median effect analysis of the combination of DSF:Cu or DSF with  $\gamma$ -radiation in SK-N-BE(2c) cells

The clonogenic survival of SK-N-BE(2c) cells was determined 24 h after  $\gamma$ -radiation treatment in the absence or in the presence of various concentrations of DSF:Cu (a) or DSF (d). The corresponding median effect plots and parameters are shown in (b, c) and (e, f). A linear regression of the median effect equation was carried out as explained in Section 4.3.7 in order to calculate the parameters  $m$ , the y-axis intercept (y-int), the dose required to kill 50% of the clonogens (IC<sub>50</sub>) and the coefficient of determination R<sup>2</sup>. Data are means  $\pm$  SEM; n=3.

The isobologram analysis of the combination of DSF with  $\gamma$ -radiation in SK-N-BE(2c) cells demonstrated an additive effect at the 25% and 50% toxicity levels, as indicated by 6 out of 8 isoeffect points plotting within the envelope of additivity (Figure 29d, Figure 29e). At the 75% level of toxicity, 5 isoeffect points out of 6 plotted below the envelope of additivity, demonstrating synergism (Figure 29f). At the 75% level of toxicity, one isoeffect point corresponding to a high dose of  $\gamma$ -radiation combined with a low concentration of DSF, lay above the envelope of additivity, demonstrating antagonism in this particular condition.

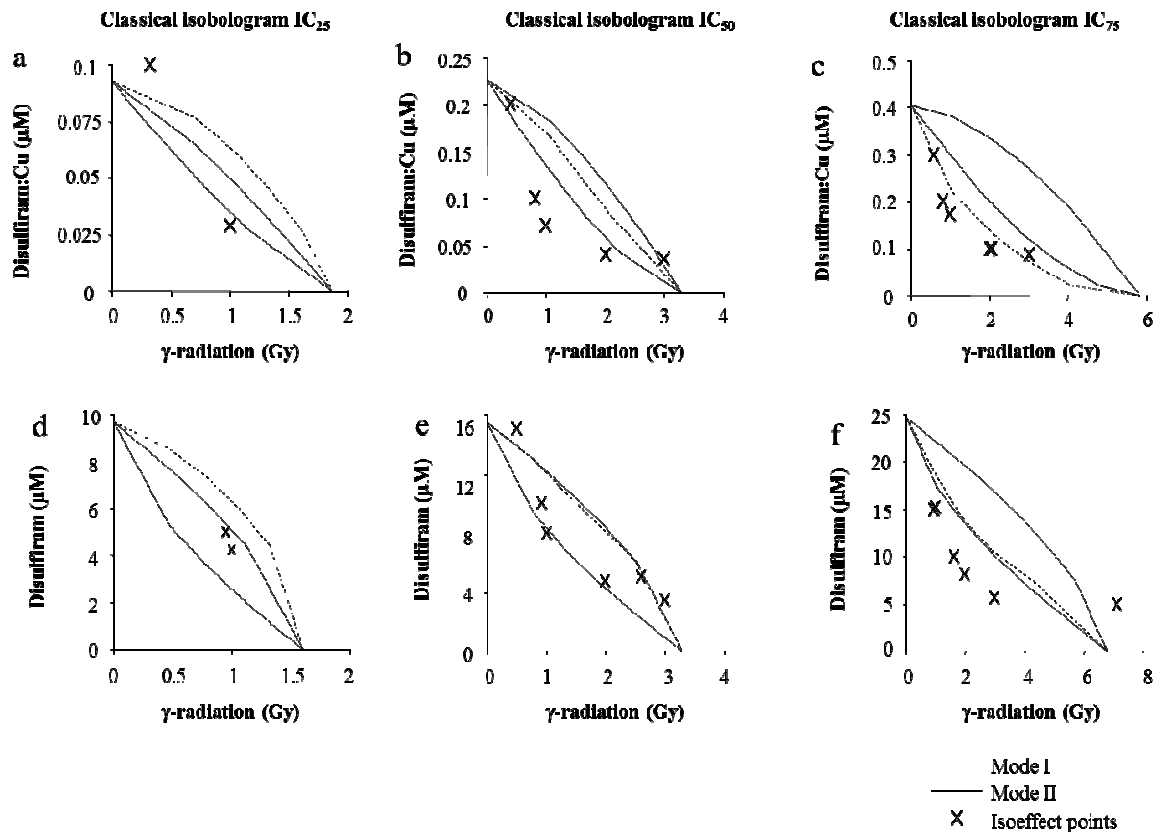


**Figure 29** Isobologram analysis of the combination of DSF:Cu or DSF with  $\gamma$ -radiation in SK-N-BE(2c) cells

The isobologram charts for the combination of DSF:Cu and  $\gamma$ -radiation are shown at the 25% (a), 50% (b) and 75% (c) levels of toxicity. Similarly, the isobologram charts for the combination of DSF and  $\gamma$ -radiation are shown at the 25% (d), 50% (e) and 75% (f) levels of toxicity. If the isoeffect points lie below and to the left of the envelope of additivity, the combination is synergistic; if the isoeffect points lie above and to the right of the envelope of additivity, the combination is antagonistic; and if the isoeffect points lie within the envelope of additivity, the combination is additive.

The trend toward decreased synergy following combination treatment comprising a small dose of one agent with a high dose of the second agent may be explained as follows. The example considers an isobologram constructed at the 50% toxicity level (Figure 30). In the design of such an experiment, the dose D1 of agent A may be selected so that the toxic effect of agent A alone is significantly less than 50%. In this case, there is a wide range of doses of agent B which could produce synergy as indicated by the red arrow (Figure 30). As the selected concentration of agent A is increased toward its  $IC_{50}$  value, the range of doses of agent B which could produce synergy in combination decreases as indicated by the blue arrow (Figure 30). There is less scope for synergy as the contribution of one agent markedly exceeds the contribution of the second agent in a combination treatment. This phenomenon may have biological relevance. As the concentration of one agent of the

combination increases, the dose of the second agent required to produce a combined 50% kill decreases.

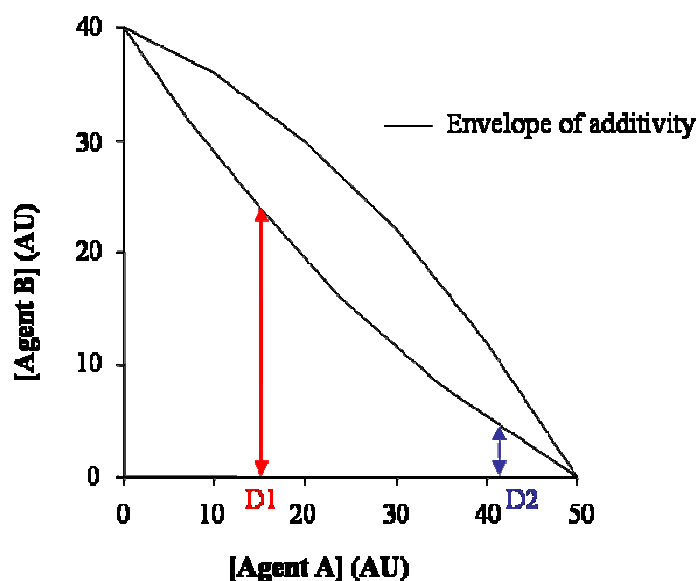


**Figure 30 The effect of imbalance in the contribution of two agents on synergistic interaction**

An idealised isobologram constructed at the 50% toxicity level is shown for the combination of agent A with agent B. Two hypothetical doses of agent A, D1 and D2, are selected such that  $D1 < D2 < IC_{50}$ . The red and blue arrows illustrate the range of doses of agent B which could produce synergy in combination with the doses D1 and D2 of agent A, respectively.

The doses of therapeutic agents in combination were selected so that the majority of the survival curves encompassed the 50% toxicity level. This design also provided satisfactory information for the determination of the corresponding combination effects at the 75% toxicity level. However, the selected doses were less informative at the 25% toxicity level. Only two or three of the resulting survival curves intersected the 25% toxicity level, resulting in the construction of  $IC_{25}$  isobologram charts with two or three isoeffect points only.

#### **4.4.3.1.2 Isobologram analysis of DSF:Cu and DSF in combination with $\gamma$ -radiation in UVW/NAT cells**

The effect of  $\gamma$ -radiation and DSF:Cu on the survival of UVW/NAT clonogens is shown in Figure 31a. The corresponding median effect plot and the parameters of the median effect equations are shown in Figure 31b and Figure 31c. Similarly, the effect of  $\gamma$ -radiation and DSF on the clonogenic survival of UVW/NAT is shown in Figure 31d. The corresponding median effect plot and the parameters of the median effect equations are shown in Figure

31e and Figure 31f. The isobologram analyses of the combination of DSF:Cu or DSF with  $\gamma$ -radiation at 25%, 50% and 75% toxicity levels are shown in Figure 32.

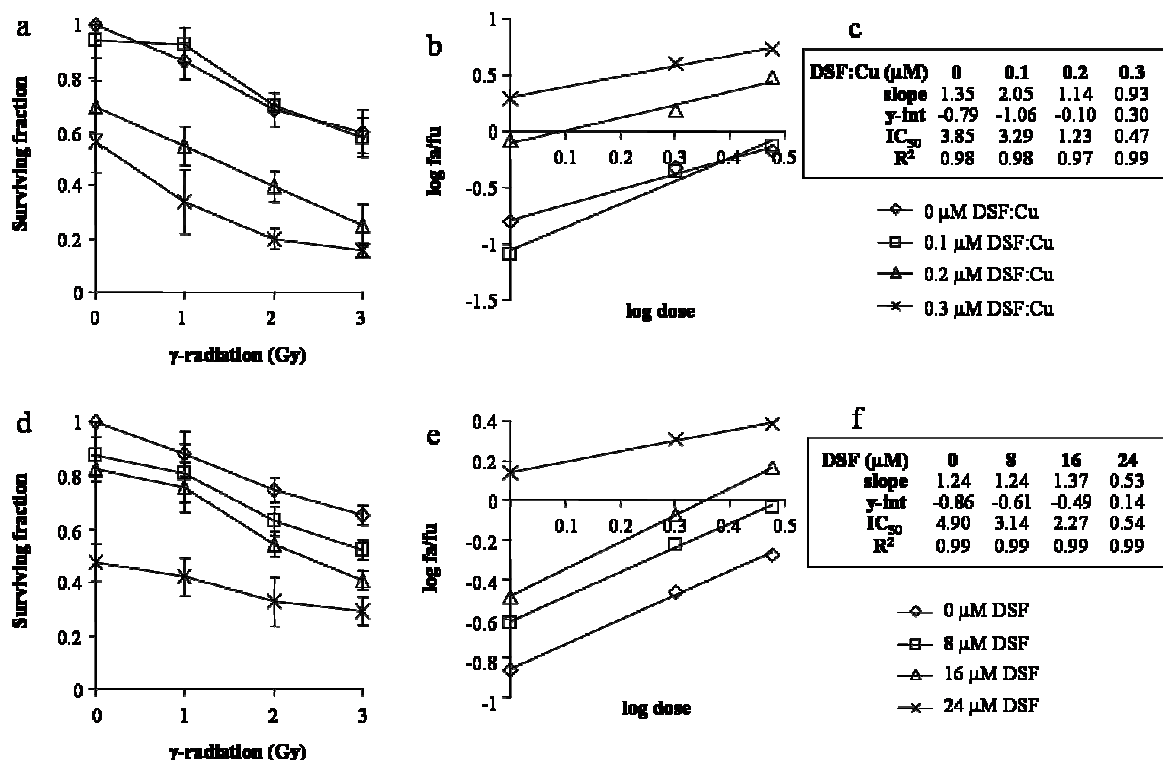


Fig 10.

Figure 31 Median effect analysis of the combination of DSF:Cu or DSF with  $\gamma$ -radiation in UVW/NAT cells

The clonogenic survival of UVW/NAT cells was determined 24 h after  $\gamma$ -radiation treatments in the absence or in the presence of various concentrations of DSF:Cu (a) or DSF (d). The corresponding median effect plots are shown in (b, c) and (e, f). A linear regression of the median effect equation was carried out as explained in Section 4.3.7 in order to calculate the parameters  $m$ , the y-axis intercept (y-int), the dose required to kill 50% of the clonogens (IC<sub>50</sub>) and the coefficient of determination R<sup>2</sup>. Data are means  $\pm$  SEM; n=3.

At the 25% level of toxicity, the isoeffect points lay above the envelope of additivity, demonstrating an antagonistic interaction between DSF:Cu and  $\gamma$ -radiation (Figure 32a). However, 11 isoeffect points out of 12 plotted within the envelope of additivity at the 50% and 75% levels of toxicity, demonstrating a predominantly additive interaction between DSF:Cu and  $\gamma$ -radiation (Figure 32b and Figure 32c).

The isobologram analysis of the combination of DSF and  $\gamma$ -radiation in UVW/NAT cells demonstrated antagonism at the 25% level of toxicity, as indicated by all isoeffect points lying above the envelope of additivity (Figure 32d). However, 9 out of 12 isoeffect points plotted below or within the envelope of additivity at 50% and 75% levels of toxicity,

demonstrating the mainly additive nature of the combination of DSF and  $\gamma$ -radiation in UVW/NAT cells.

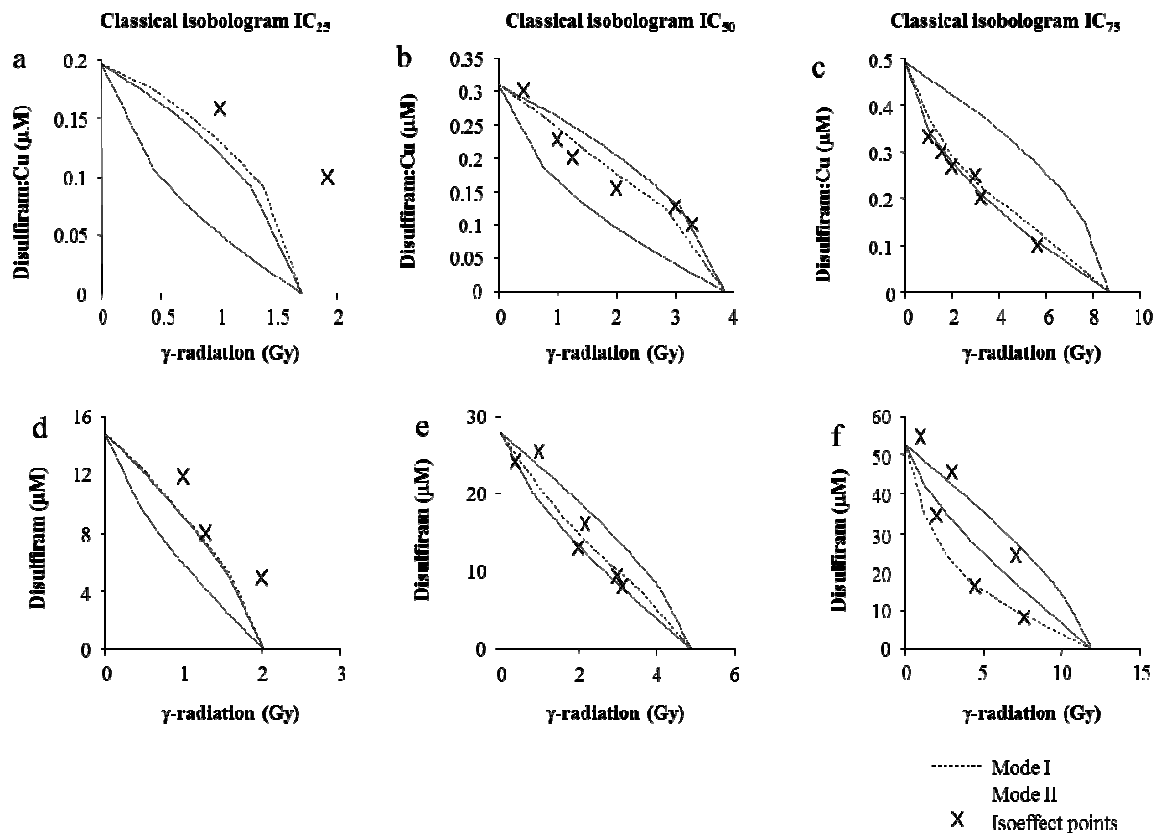


**Figure 32** Isobologram analysis of the combination of DSF:Cu or DSF with  $\gamma$ -radiation in UVW/NAT cells

The isobologram charts for the combination of DSF:Cu and  $\gamma$ -radiation are shown at the 25% (a), 50% (b) and 75% (c) level of toxicity. Similarly, the isobologram charts for the combination of DSF and  $\gamma$ -radiation are shown at the 25% (d), 50% (e) and 75% (f) level of toxicity. If the isoeffect points lie below and to the left of the envelope of additivity, the combination is synergistic; if the isoeffect points lie above and to the right of the envelope of additivity, the combination is antagonistic; and if the isoeffect points lie within the envelope of additivity, the combination is additive.

#### 4.4.3.2 Combination index analysis

##### 4.4.3.2.1 Combination index analysis of DSF:Cu in combination with $\gamma$ -radiation in SK-N-BE(2c) cells

The toxicity of DSF:Cu,  $\gamma$ -radiation or their combination to SK-N-BE(2c) cells is shown in Figure 33a, Figure 33b and Figure 33c, respectively. The resultant median effect plot is shown in Figure 33d and the parameters of the median effect equation are given in Figure 33e. The CI values are shown in Figure 33f. The CI values decreased from 1.07 at a 5% level of toxicity to 0.61 at 95% level of toxicity. Since a CI value comprised between 0.9 and 1.1 indicates additivity and a CI value less than 0.9 indicates synergism according to

the criteria of Chou and Talalay (Table 5)<sup>214</sup>, these data indicated an additive effect between DSF:Cu and  $\gamma$ -radiation at toxicity levels less than 15% and increasing supra-additivity at toxicity levels of 15% and higher (Figure 33f).

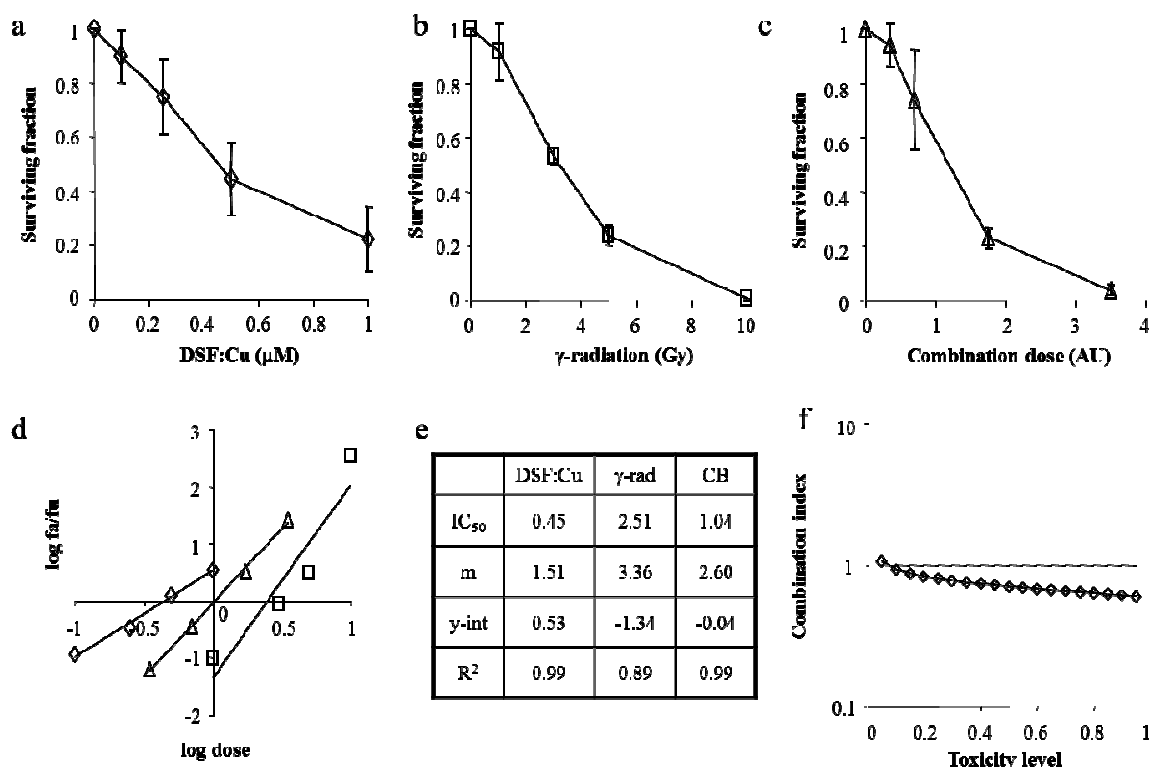


**Figure 33** The combination index analysis of the combination of DSF:Cu with  $\gamma$ -radiation in SK-N-BE(2c) cells

The clonogenic survival of SK-N-BE(2c) cells was determined 24 h after exposure to DSF:Cu (a), 24 h after  $\gamma$ -radiation treatment (b) or 24 h after treatment with various intensities of both agents in a constant ratio of 3 Gy to 0.3  $\mu$ M (c). Data are means  $\pm$  SEM; n=3. The median effect plot of the single agents and the combination is shown in (d) and the parameters m, the y-axis intercept (y-int), the dose required to kill 50% of the clonogens (IC<sub>50</sub>) and the coefficient of determination R<sup>2</sup> are shown in (e). The relationship between combination index (CI) and intensity of treatment (level of toxicity) is shown in (f). CI values less than 0.90 indicate synergism; CI values greater than 1.10 indicate antagonism; and CI values between 0.90 and 1.10 indicate additivity.

#### 4.4.3.2.2 The combination index analysis of DSF in combination with $\gamma$ -radiation in SK-N-BE(2c) cells

The toxicity of DSF,  $\gamma$ -radiation or their combination to SK-N-BE(2c) cells is shown in Figure 34a, Figure 34b and Figure 34c, respectively. The resultant median effect plot is shown in Figure 34d and the parameters of the median effect equations are given in Figure 34e. The CI values are shown in Figure 34f. The CI values decreased from 1.20 at 5% toxicity level to 0.76 at 95% toxicity level. These data indicated antagonism between DSF

and  $\gamma$ -radiation at toxicity levels less than 15%, additive effect at toxicity levels between 15% and 60% and increasing supra-additivity at toxicity levels of 60% and higher (Figure 34f).

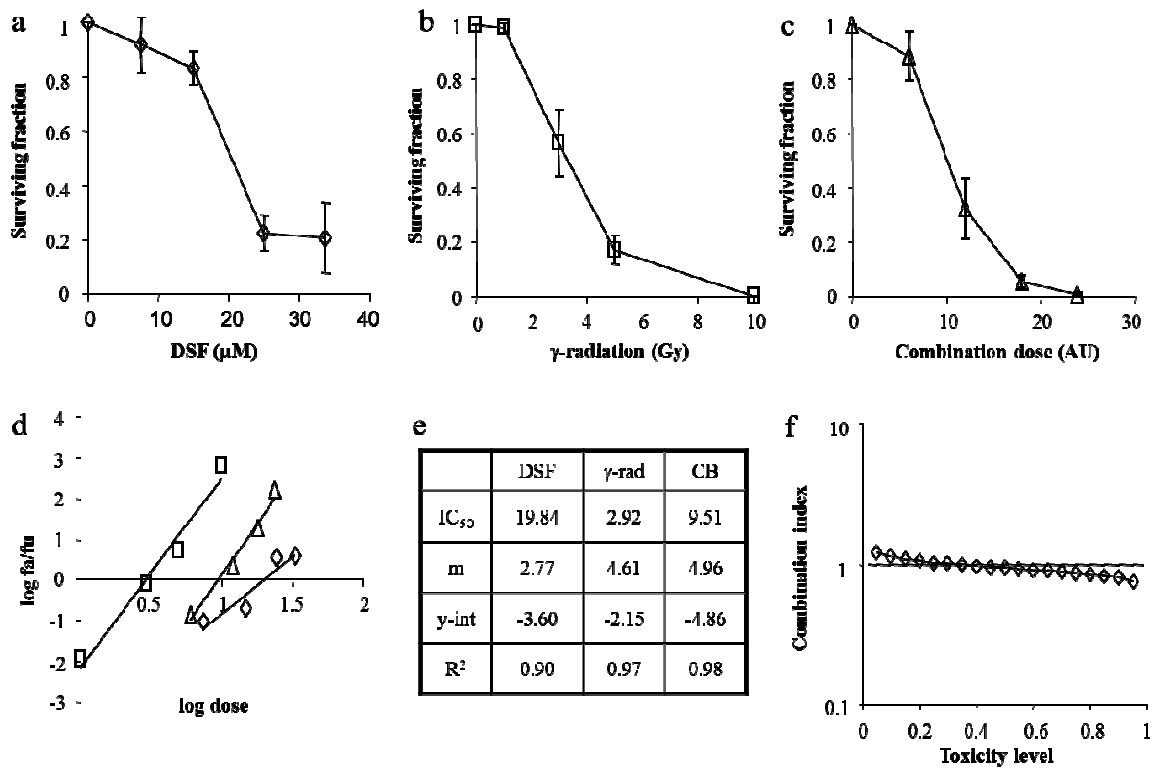


**Figure 34** The combination index analysis of the combination of DSF with  $\gamma$ -radiation in SK-N-BE(2c) cells

The clonogenic survival of SK-N-BE(2c) cells was determined 24 h after exposure to DSF (a), 24 h after  $\gamma$ -radiation treatment (b) or 24 h after treatment with various intensities of both modalities in a constant ratio of 3 Gy to 15  $\mu$ M (c). Data are means  $\pm$  SEM; n=3. The median effect plot of the single agents and the combination is shown in (d) and the parameters m, the y-axis intercept (y-int), the dose required to kill 50% of the clonogens ( $IC_{50}$ ) and the coefficient of determination  $R^2$  are shown in (e). The relationship between combination index (CI) and intensity of treatment (level of toxicity) is shown in (f). CI values less than 0.90 indicate synergism; CI values greater than 1.10 indicate antagonism; and CI values between 0.90 and 1.10 indicate additivity.

#### 4.4.3.2.3 The combination index analysis of DSF:Cu in combination with $\gamma$ -radiation in UVW/NAT cells

The toxicity of DSF:Cu,  $\gamma$ -radiation or their combination to UVW/NAT cells is shown in Figure 35a, Figure 35b and Figure 35c, respectively. The resultant median effect plot is shown in Figure 35d and the parameters of the median effect equations are given in Figure 35e. The CI values are shown in Figure 35f. The CI values decreased from 2.78 at 5% toxicity level to 0.27 at 95% toxicity level. These data indicated antagonism between

DSF:Cu and  $\gamma$ -radiation at toxicity levels less than 25%, additivity at toxicity levels between 25% and 35% and increasing supra-additivity at toxicity levels of 35% and higher (Figure 35f).

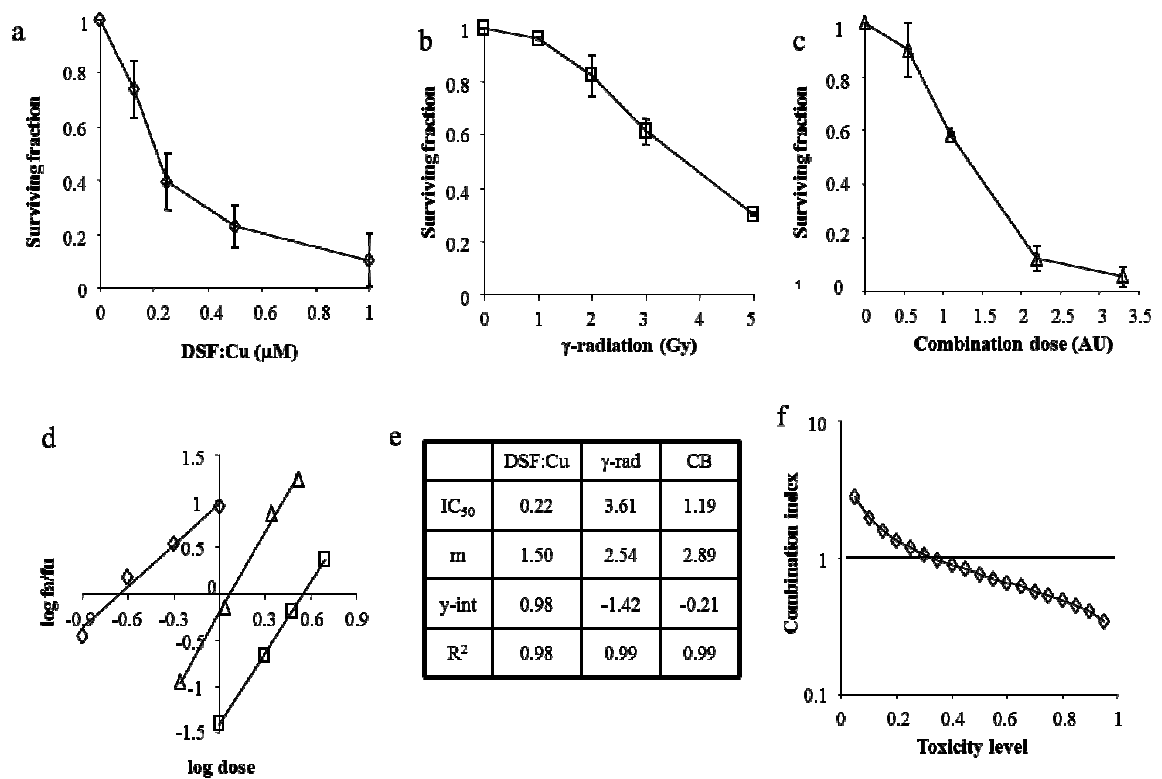


**Figure 35** The combination index analysis of the combination of DSF:Cu with  $\gamma$ -radiation in UVW/NAT cells

The clonogenic survival of UVW/NAT cells was determined 24 h after exposure to DSF:Cu (a), 24 h after  $\gamma$ -radiation treatment (b) or 24 h after treatment with various intensities of both modalities in a constant ratio of 3 Gy to 0.3  $\mu\text{M}$  (c). Data are means  $\pm$  SEM; n=3. The median effect plot of the single agents and the combination is shown in (d) and the parameters m, the y-axis intercept (y-int), the dose required to kill 50% of the clonogens (IC<sub>50</sub>) and the coefficient of determination R<sup>2</sup> are shown in (e). The relationship between combination index (CI) and intensity of treatment (level of toxicity) is shown in (f). CI values less than 0.90 indicate synergism; CI values greater than 1.10 indicate antagonism; and CI values between 0.90 and 1.10 indicate additivity.

#### 4.4.3.2.4 The combination index analysis of DSF in combination with $\gamma$ -radiation in UVW/NAT cells

The toxicity of DSF,  $\gamma$ -radiation or their combination to UVW/NAT cells is shown in Figure 36a, Figure 36b and Figure 36c, respectively. The median effect plot is shown in Figure 36d and the parameters of the median effect equations are given in Figure 36e. The CI values are shown in Figure 36f. The CI values decreased from 1.93 at 5% toxicity level to 0.93 at 95% toxicity level. These data indicated antagonism between DSF and  $\gamma$ -

radiation at toxicity levels less than 70% and an additive effect at toxicity levels of 70% and higher (Figure 36f).

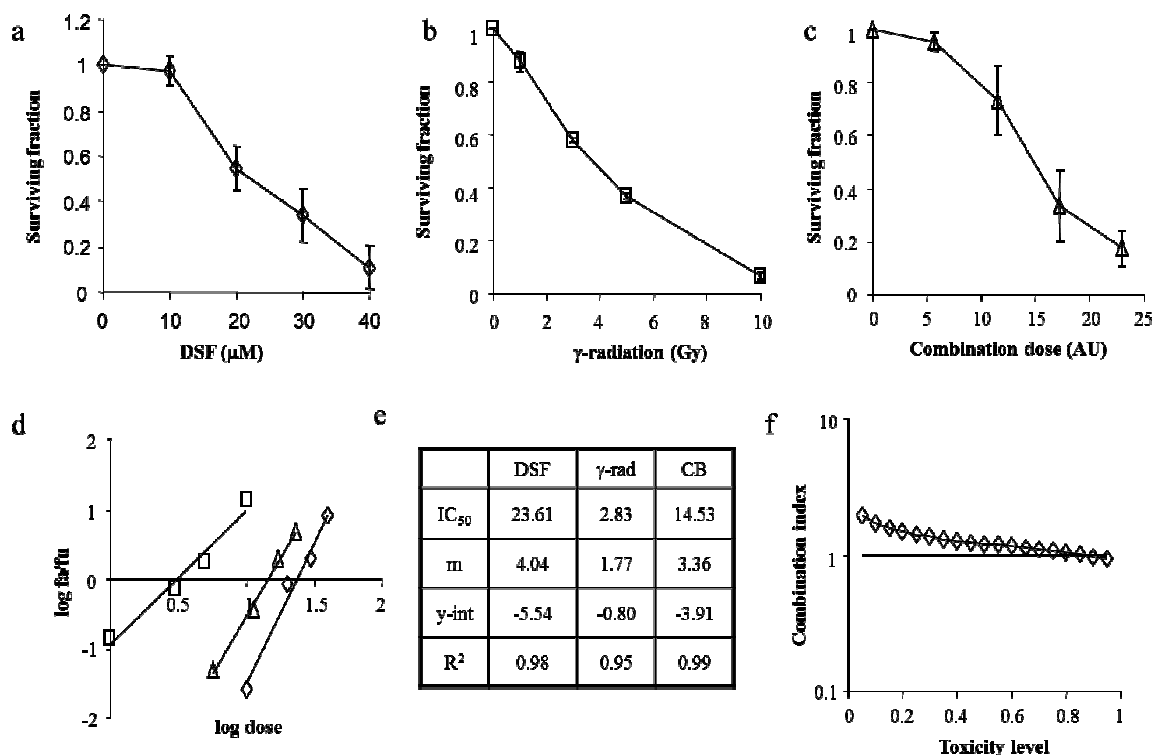


**Figure 36** The combination index analysis of the combination of DSF with  $\gamma$ -radiation in UVW/NAT cells

The clonogenic survival of UVW/NAT cells was determined 24 h after exposure to DSF (a), 24 h after  $\gamma$ -radiation treatment (b) or 24 h after treatment with various intensities of both modalities in a constant ratio of 3 Gy to 24  $\mu$ M ratio (c). The combination dose is the dimensionless sum of the dose of  $\gamma$ -radiation and the concentration of DSF. Data are means  $\pm$  SEM; n=3. The median effect plot of the single agents and the combination is shown in (d) and the parameters m, the y-axis intercept (y-int), the dose required to kill 50% of the clonogens (IC<sub>50</sub>) and the coefficient of determination R<sup>2</sup> are shown in (e). The relationship between combination index (CI) and intensity of treatment (level of toxicity) is shown in (f). CI values less than 0.90 indicate synergism; CI values greater than 1.10 indicate antagonism; and CI values between 0.90 and 1.10 indicate additivity.

#### 4.4.3.3 Conclusions

The data from the isobologram analyses demonstrate the supra-additive nature of the combination of DSF:Cu and  $\gamma$ -radiation in SK-N-BE(2c) cells at 50% and 75% toxicity levels. Similarly, DSF without Cu supplementation synergised with  $\gamma$ -radiation at the 75% toxicity levels. UVW/NAT cells were more resistant than SK-N-BE(2c) cells to the radiosensitising effect of DSF:Cu or DSF. In UVW/NAT cells, the combination of DSF:Cu or DSF with  $\gamma$ -radiation sterilised clonogens in an additive fashion at 50% and 75% toxicity levels.

The results from the combination index analyses demonstrated that supra-additivity between DSF:Cu and  $\gamma$ -radiation occurred at toxicity levels greater than 15% and 35% in SK-N-BE(2c) and UVW/NAT cells, respectively. Combinations of DSF with  $\gamma$ -radiation were less effective than those of DSF:Cu with  $\gamma$ -radiation, as indicated by CI values, in the presence of DSF, greater than those obtained in the presence of DSF:Cu at similar levels of toxicity. Overall, UVW/NAT cells were more resistant than SK-N-BE(2c) cells, manifest by greater CI values, to the combination of either DSF:Cu or DSF with  $\gamma$ -radiation.

#### 4.5 Discussion

It was demonstrated that DSF:Cu and DSF are both radiosensitisers, as indicated by the leftward shift of the radiation survival curve in the presence of DSF:Cu or DSF compared to the radiation curve after radiation treatment alone (Figure 26 and Figure 27). Moreover, DSF:Cu and DSF increased the cytotoxicity of  $\gamma$ -radiation in a dose-dependent manner. For instance, the DEF<sub>50</sub> values were 1.18, 2.76 and 4.24 following treatment of SK-N-BE(2c) with  $\gamma$ -radiation in the presence of 0.1, 0.2 and 0.3  $\mu$ M DSF:Cu, respectively (Figure 26b). Following treatment of SK-N-BE(2c) cells with  $\gamma$ -radiation in the presence of 5, 10 and 15  $\mu$ M DSF, the DEF<sub>50</sub> values were 1.35, 2.59 and 3.72, respectively (Figure 26d). Similarly, the DEF<sub>50</sub> values were 1.00, 1.38 and 2.00 following treatment of UVW/NAT with  $\gamma$ -radiation in the presence of 0.1, 0.2 and 0.3  $\mu$ M DSF:Cu, respectively (Figure 27b). Following treatment of UVW/NAT cells with  $\gamma$ -radiation in the presence of 8, 16 and 24  $\mu$ M DSF, the DEF<sub>50</sub> values were 1.38, 1.90 and 2.17, respectively (Figure 27d). Similar increases in the DEF values were obtained at the 25% and 75% kill in both cell lines and for both DSF:Cu and DSF (Figure 26 and Figure 27). The classical method of displaying the effect of radiation modifiers (linear-quadratic evaluation of  $\gamma$ -radiation survival curves in the absence and in the presence of a drug) is not complete because it only measures the effect of a drug on the radiation survival curve. The reciprocal effect, the effect of radiation on the cytotoxicity of the drug, is ignored. The cytotoxic effect of a combination results from the mutual interaction of both agents which may be infra-additive, additive or supra-additive. The interaction of two agents in combination is more thoroughly examined by the isobologram and combination index methods of synergy analysis rather than by the quantification of the leftward shift of the radiation survival curve. With respect to therapeutic application, the demonstration of supra-additivity over additivity has implications for the control of side-effects and normal tissue toxicity. The administration of DSF has been associated with vomiting, drowsiness, loss of coordination and loss of

consciousness<sup>173</sup> whereas radiotherapy may have side effects such as fatigue, skin changes, diarrhoea, xerostomia and haematotoxicity. Therefore, synergistic interaction between DSF and radiotherapy is expected to result in the delivery of reduced dose with concomitant improvement of the quality of life of cancer patients.

The isobologram and combination index methods of synergy analyses have been developed to determine supra- or infra-additivity when both agents of the combination have an effect of their own<sup>214</sup>. In these methods, the effect (potency and the shape of the dose-response curve) of each single agent is measured and taken into account in order to construct the theoretical additive effect of the combination (the envelope of additivity in the case of the isobologram and  $CI = 1$  in the case of the combination index analysis). The observed experimental effect of the combination is then compared with the theoretical additive effect. Both methods were used to analyse the interaction between DSF:Cu or DSF with  $\gamma$ -radiation. There was an overall agreement between the two methods: both demonstrated greater synergism between  $\gamma$ -radiation and DSF:Cu or DSF at increasing intensity of treatment. Specifically, the CI values decreased with increasing levels of toxicity and the isobologram showed a trend from infra-additive or additive interaction at the 25% level of toxicity to additive or supra-additive interaction at the 75% level of toxicity (Table 7). Furthermore, both the isobologram and the combination index analyses indicated that the combinations of DSF:Cu or DSF with  $\gamma$ -radiation were more effective in SK-N-BE(2c) than UVW/NAT cells. The CI values were on average higher for UVW/NAT than for SK-N-BE(2c) cell and the isobologram analysis demonstrated that either DSF:Cu or DSF in combination with  $\gamma$ -radiation induced additive responses in UVW/NAT cells at toxicity levels which corresponded to supra-additivity in SK-N-BE(2c) cells (Table 7).

<b>a</b> SK-N-BE(2c)				<b>c</b> UVW/NAT			
DSF:Cu	25%	50%	75%	DSF:Cu	25%	50%	75%
DEF	5.42	4.24	3.59	DEF	2.55	2.00	1.62
Isobologram	N/A	Supra-additive	Supra-additive	Isobologram	Infra-additive	Additive	Additive
CI	0.80 ± 0.12	0.71 ± 0.11	0.65 ± 0.10	CI	1.17 ± 0.44	0.76 ± 0.13	0.53 ± 0.08

<b>b</b> SK-N-BE(2c)				<b>d</b> UVW/NAT			
DSF	25%	50%	75%	DSF	25%	50%	75%
DEF	5.03	3.72	3.29	DEF	2.48	2.17	1.90
Isobologram	Additive	Additive	Supra-additive	Isobologram	Infra-additive	Additive	Additive
CI	1.02 ± 0.12	0.94 ± 0.09	0.86 ± 0.09	CI	1.40 ± 0.18	1.21 ± 0.10	1.07 ± 0.09

**Table 7 Comparison between DEF, isobologram analysis and combination index analysis for the evaluation of the interaction between DSF:Cu or DSF with  $\gamma$ -radiation**

This table summarises the data from Figure 26 to Figure 36. The DEF values signify the fold decrease of the  $\gamma$ -radiation dose that can be applied, in the presence of 0.3  $\mu$ M DSF:Cu, to achieve the same kill as  $\gamma$ -radiation alone. In the case of isobologram analysis, if the majority of isoeffect points lay within the envelope of additivity, the combination was considered additive. Similarly, if the majority of isoeffect points lay to the left and below or to the right and above the envelope of additivity, the combination was considered supra- or infra-additive, respectively. The combination index (CI) is reported as mean  $\pm$  SEM; n=3.

The linear-quadratic evaluation of the effect of DSF:Cu or DSF on the radiation survival curve suggested that UVW/NAT cells were also more resistant to the combination treatment due to the less appreciable increase of the quadratic component ( $\beta$ ) of radiation cell kill than observed in the case of SK-N-BE(2c) cells. An increase in the  $\beta$  value of the radiation kill induced by a radiosensitiser may be due to the increase in the incidence of DSB or to the inhibition of their repair. The ability of SK-N-BE(2c) and UVW/NAT cells to repair DSB has previously been investigated by comet assay after treatment with the radiopharmaceutical [ $^{131}$ I]mIBG alone or in combination with the topoisomerase I inhibitor topotecan<sup>92</sup>. It was shown that more DSB were produced by topotecan alone, [ $^{131}$ I]mIBG alone or the combination of both in UVW/NAT cells compared with SK-N-BE(2c) immediately after the treatment<sup>92</sup>. However, UVW/NAT cells repaired 100% of the DSB 24 h after treatments with topotecan alone, [ $^{131}$ I]mIBG alone or the simultaneous combination of both agents compared with only 70-90% of DSB repaired in SK-N-BE(2c) cells<sup>92</sup>. This study demonstrated the greater ability of UVW/NAT cells to repair DSB compared to SK-N-BE(2c) cells, which was consistent with the increase in the  $\beta$  value in SK-N-BE(2c) cells but not in UVW/NAT cells after irradiation in the presence of DSF:Cu.

Although both the isobologram and the combination methods of synergy analysis indicated a more synergistic interaction between  $\gamma$ -radiation and DSF:Cu or DSF at increasing levels of toxicity, the DEF values decreased with increasing levels of toxicity (Table 7). This contradictory result may be explained as follows. The DEF values are calculated based on the linear-quadratic equation which describes the leftward shift of the radiation curve provoked by the addition of a radiosensitiser. The effect of a radiosensitiser is likely to be due to an increase in the linear ( $\alpha$ ) or quadratic ( $\beta$ ) components of radiation cell killing or both.

Firstly, we consider that the effect of a radiosensitiser is solely to increase the linear component of the radiation cell killing while the quadratic component remains constant (Figure 37a). Treatment with such a radiosensitiser would increase and straighten the initial slope of the radiation survival curve, with resulting higher DEF values at the initial levels of kill. Since the contribution of the quadratic component is greater than the linear component in response to radiation alone than in response to combination treatment, it follows that, with increasing radiation dose, the survival curve of radiation treatment alone starts bending at lower radiation dose than in the survival curve of the combination. This results in lower DEF values at higher levels of kill. An increase in the  $\alpha$  value, with a constant  $\beta$  value, resulted in radiosensitisation, manifest by the DEF values greater than 1 (Figure 37a). Furthermore, DEF values decreased with increasing toxicity levels (Figure 37a). For instance, in the radiation survival curve obtained in the presence of a radiosensitiser characterised by  $\alpha = 0.95$  and  $\beta = 0.04$ , the DEF values were 7.12, 5.06 and 3.84 at the 25%, 50% and 75% level of toxicity, respectively (Figure 37a).

Secondly, we consider that the effect of an alternative radiosensitiser is solely an increase of the quadratic component of radiation cell killing, while the linear component remains constant (Figure 37b). Treatment with such a radiosensitiser increases the curvature of the radiation survival curve. The result is that the radiosensitiser plus radiation curve departs more from the radiation alone curve with increasing radiation dose. Therefore the DEF values increase with increasing toxicity levels. The increase of the  $\beta$  value, with a constant  $\alpha$  value, showed a radiosensitising effect as indicated by DEF values greater than 1 (Figure 37b). Moreover, DEF values increased with increasing toxicity levels (Figure 37b). For instance, in the radiation survival curve obtained in the presence of a radiosensitiser characterised by  $\alpha = 0.05$  and  $\beta = 0.24$ , the DEF values were 2.14, 2.24 and 2.30 at the 25%, 50% and 75% level of toxicity, respectively (Figure 37b).

The linear component of the radiation cell kill was increased by DSF:Cu and DSF to a greater extent than the quadratic component (Figure 26 and Figure 27). For instance, 0.3  $\mu\text{M}$  DSF:Cu induced a 12.2- and 3.9-fold increase in the  $\alpha$  value in SK-N-BE(2c) (Figure 26b) and UVW/NAT cells (Figure 27b), respectively. In contrast, the  $\beta$  values were only increased 4.8-fold in SK-N-BE(2c) cells (Figure 26b) and decreased 3-fold in UVW/NAT cells (Figure 27b). The greater increase in the  $\alpha$  values compared to the  $\beta$  values by DSF:Cu may account for the decreasing DEF values at increasing toxicity levels despite the demonstration of increased additivity at greater toxicity levels, as demonstrated by the isobologram and the combination index methods of synergy analysis. This discrepancy was explained by the strong reliance of the calculations of the DEF values on the shape of the linear-quadratic curve. The relative contributions of the linear ( $\alpha$ ) and quadratic ( $\beta$ ) components of radiation cell kill, which may be differentially affected by different radiosensitisers, introduced a bias for the determination of radiosensitising potentials at different toxicity levels. These data demonstrated that the degree of radiosensitisation (additivity or supra-additivity) cannot be reliably assessed by the calculation of DEF values. Instead, the isobologram and the combination index methods of synergy analysis are particularly suited to this purpose.

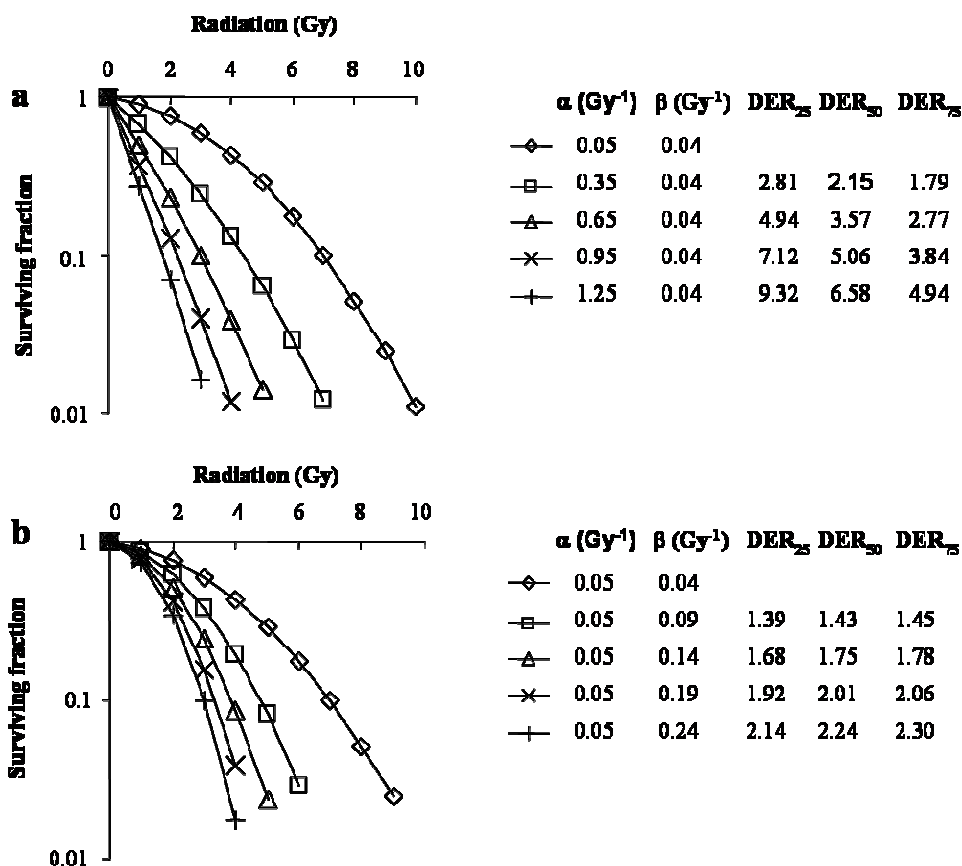


**Figure 37** The effect of the modification of the linear ( $\alpha$ ) or the quadratic ( $\beta$ ) component of radiation cell killing on the survival curve

The surviving fraction SF of radiation survival curves were calculated by computing radiation doses (D),  $\alpha$  and  $\beta$  values into the linear-quadratic equation  $\text{SF} = e^{-(\alpha D + \beta D^2)}$ . (a) The linear component ( $\alpha$ ) of radiation cell kill was increased from 0.05 to 1.25  $\text{Gy}^{-1}$  by 0.3 increments. The quadratic component ( $\beta$ ) of radiation cell kill was kept constant at 0.04  $\text{Gy}^{-1}$ . The  $\text{DER}_{25}$ ,  $\text{DER}_{50}$  and  $\text{DER}_{75}$  values were calculated at the 25, 50 and 75% kill, respectively. (b) The quadratic component ( $\beta$ ) of radiation cell kill was increased from 0.04 to 0.24  $\text{Gy}^{-1}$  by 0.05 increments. The linear component ( $\alpha$ ) of radiation cell kill was kept constant at 0.05  $\text{Gy}^{-1}$ . The  $\text{DER}_{25}$ ,  $\text{DER}_{50}$  and  $\text{DER}_{75}$  values were calculated at the 25, 50 and 75% kill, respectively.

The dataset also showed a discrepancy between the isobologram and the combination index analysis for the UVW/NAT cell line. The isobologram method indicated an additive interaction between DSF:Cu and  $\gamma$ -radiation at the 50% and 75% levels of toxicity whereas combination index analysis indicated synergism at these levels of toxicity (Table 7c). However, the isoeffect points corresponding to the combination of DSF:Cu with  $\gamma$ -radiation at the 75% level of toxicity plotted at the border between additivity and supra-additivity (Fig. 12). Moreover, in the case of combinations of DSF and  $\gamma$ -radiation, isobologram analysis revealed additivity at the 50% level of toxicity whereas combination index analysis disclosed an infra-additive interaction (Table 7d). The observed discrepancy between the isobologram and the combination index analyses may derive from the differences in drug treatment used in the two methods. In combination index analysis, a

fixed ratio of drug concentration to  $\gamma$ -radiation dose was used. In contrast, for isobologram analysis, the doses of drug and  $\gamma$ -radiation were both variable. Therefore, it is possible that the incongruities observed between the isobologram and combination index analyses may be due to differences in the relative contributions of each agent to the effectiveness of the combination. That is, variable ratios of dose of the two modalities are applied in the isobologram procedure whereas a fixed ratio of dose of the two treatments is used in the combination index analysis.

DSF without Cu was also found to be a radiosensitiser, as indicated by DEF values greater than 1 (Table 7b and Table 7d). However, the concentrations of DSF between 5 and 24  $\mu\text{M}$  examined in this study cannot be achieved in human plasma. It was shown that the peak plasma concentration measured after oral administration of a 250 mg DSF tablet was 1  $\mu\text{M}$ <sup>161</sup>. Therefore, radiosensitisation of a tumour using DSF is impossible. These results demonstrated that DSF-induced enhancement of  $\gamma$ -radiation treatment only occurred when the DSF concentration was high enough to induce cytotoxic effects as a single agent.

Since it has been argued that DSF acts as a Cu ionophore, and that Cu alone exerts cytotoxic effects<sup>114</sup>, it could be hypothesised that Cu itself is a radiosensitiser. The results demonstrating radiosensitisation of SK-N-BE(2c) and UVW/NAT cells were obtained in physiological conditions, namely 5% CO<sub>2</sub>, 20% O<sub>2</sub> and 75% N<sub>2</sub>. It has previously been shown that CuCl<sub>2</sub> radiosensitises the bacterial strain *Shigella Flexneri Y6R* in hypoxic conditions but not in aerated cultures<sup>237</sup>. Furthermore, it has been hypothesised that the radiosensitising effect of Cu is due to the radiation-induced conversion of Cu<sup>2+</sup> into the highly toxic Cu<sup>+</sup> in hypoxia. In aerated cultures, O<sub>2</sub> was able to convert Cu<sup>+</sup> back to the less toxic Cu<sup>2+</sup> resulting in the loss of the radiosensitising effect<sup>238</sup>. These two reports suggest that Cu is not a radiosensitiser in aerobic conditions. Therefore, the hypothetical radiosensitising effect of Cu alone in the experiments carried out in aerobic conditions in this chapter is unlikely.

Isobologram analysis demonstrated that combination treatment was less effective when the contribution of one agent became greater than the contribution of the second agent (Figure 29 and Figure 32). In patients, the distribution of a drug within the tumour is uneven because all parts of the tumour are not homogeneously vascularised<sup>239,240</sup>. Therefore differential distribution of DSF:Cu within a tumour due to uneven vascularisation may result in sub-optimal additive or supra-additive effects. Preclinical evaluation should be

conducted to determine the optimal doses of DSF:Cu which must be administered in order to avoid this complication.

Together, these data demonstrated the benefit of using the isobologram and the combination index methods of synergy analysis over the calculation of the leftward shift of radiation curves for the determination of the degree and type of interaction (additivity or supra-additivity) between therapeutic modalities. These data also demonstrated that DSF:Cu sensitised monolayers of cancer cells to external beam  $\gamma$ -radiation treatment in a supra-additive fashion at toxicity levels greater than 50%. The evaluation of the radiosensitising effect of DSF:Cu using the linear-quadratic model unearthed an hypothesis regarding the mechanism of radiosensitisation. That is the greater increase of  $\alpha$  values compared with the increase in  $\beta$  value following irradiation in the presence of DSF:Cu suggested that DSF:Cu increased the amount of SSB following radiation treatment. The DSF:Cu-mediated increase in SSB following radiation treatment might be due to the abrogation of the cell cycle delay by DSF:Cu or to the inhibition of the SSB DNA repair machinery. In the next chapter, the former hypothesis will be tested.

## **5 A hypothesised mechanism for the radiosensitisation induced by DSF:Cu**

### **5.1 Introduction**

The study described in chapter 4 has demonstrated the radiosensitising capacity of DSF:Cu. However, its mechanism of radiosensitisation remains unknown. The results of the analysis of the radiosensitising effect of DSF:Cu by the linear-quadratic model predict that DSF:Cu may increase the proportion of SSB to a greater extent than DSB after radiation treatment, as indicated by the greater increase in the  $\alpha$  than the  $\beta$  values (Section 4.4.2). The increase in SSB and DSB following irradiation in the presence of DSF:Cu could be due to the inhibition of DNA repair by DSF:Cu or to the abrogation of cell cycle checkpoints which does not allow enough time for the repair of SSB and DSB. Since cell cycle arrest at the G2 checkpoint, which controls entry to mitosis, is considered a hallmark of the cellular response to  $\gamma$ -radiation<sup>241</sup>, it is hypothesised that DSF:Cu may inhibit G2 arrest following irradiation.

Serum starvation has been shown to arrest cancer cells in the G1 phase of the cell cycle<sup>242</sup>. It has also been reported that serum starvation arrests the cell cycle in G2, especially in the case of a deficient G1 checkpoint<sup>243</sup>. In such studies cells were serum-starved for at least 24 h before the observation of cell cycle arrest<sup>242-245</sup>. The treatment of cells with DSF:Cu requires serum-free conditions in order to study the effect of Cu. It was anticipated that serum starvation may influence the cell cycle response to radiation at a timepoint earlier than 24 h - used for the determination of clonogenic cell kill (Figure 26).

The accumulation of cells in G2 following  $\gamma$ -radiation treatment in the presence and in the absence of DSF:Cu will be carried out in this chapter by FACS analysis of PI-stained cells. It will be shown that DSF:Cu abrogates the  $\gamma$ -radiation-induced G2 arrest in LNCaP, SK-N-BE(2c), UVW/NAT, HCT116 p53+/+ and HCT116 p53-/- cells.

### **5.2 Aims**

The aims of this chapter were:

- determination of the time after radiation treatment required for maximal cell cycle arrest in G2
- determination of the effect of serum starvation on the distribution of cells throughout the phases of the cell cycle

- determination of the effect of DSF:Cu on cell cycle arrest in G2 following radiation treatment

### **5.3 Materials and methods**

#### **5.3.1 Tissue culture**

LNCaP, SK-N-BE(2c) and UVW/NAT cells were maintained in culture as described in Section 3.3.1. HCT116 p53<sup>+/+</sup> (parent) and HCT116 p53<sup>-/-</sup> cells were generously gifted by Dr Jane Plumb. The two alleles of the p53 gene were sequentially disrupted in the parent HCT116 cell line by homologous recombination. The p53 sequence was replaced by a geneticin resistance sequence<sup>246</sup>. Both cell lines were grown in Dulbecco's modified essential medium (MEM) supplemented with 10% (v/v) FCS (Autogen Bioclear) and 2 mM L-glutamine. All media and supplements were obtained from Invitrogen (Paisley, UK). HCT116 p53<sup>-/-</sup> cells were maintained in culture medium containing 1 mg/ml geneticin for the selection of p53<sup>-/-</sup> mutants<sup>246</sup>.

#### **5.3.2 $\gamma$ -radiation treatment**

Section 4.3.2.

#### **5.3.3 Serum starvation**

SK-N-BE(2c) and UVW/NAT cells were washed in PBS three times and incubated in fresh serum-complemented culture medium or serum-free culture medium for 2, 4, 8, 12 and 24 h. At the end of the incubation period, the cells were washed in PBS and fixed in 70% ethanol at -20°C.

#### **5.3.4 DSF:Cu treatment in combination with $\gamma$ -radiation**

LNCaP, SK-N-BE(2c) and UVW/NAT cells were exposed to 0.3 or 1  $\mu$ M DSF:Cu in serum-free culture medium. The cells were irradiated with 5 Gy  $\gamma$ -radiation immediately after exposure to DSF:Cu. All treatments were carried out in serum-free conditions (untreated controls, radiation, DSF:Cu and the combination of both). The cells were fixed in 70% ethanol at -20°C, 12 h after irradiation. The choice of this timepoint was based on results presented in Section 5.4.2.

#### **5.3.5 Cell cycle analysis**

See Section 3.3.8.

### **5.3.6 Statistical analysis**

See Section 3.3.9.

## **5.4 Results**

### **5.4.1 The effect of serum starvation on cell cycle distribution**

SK-N-BE(2c) and UVW/NAT cells were cultured in serum-free culture medium for 2, 4, 8, 12 or 24 h. In UVW/NAT cells, there was no accumulation of cells in the G2/M nor in the G0/G1 phase of the cell cycle up to 24 h exposure to serum-complemented culture medium (Figure 38a). Similarly, there was no redistribution of cells throughout the phases of the cell cycle after exposure to serum-free conditions for 24 h (Figure 38b).

In SK-N-BE(2c) cells, there was no accumulation of cells in the G2/M nor in the G0/G1 phase of the cell cycle after exposure to serum-complemented culture medium for 24 h (Figure 38c). Although serum starvation appeared to reduce the percentage of cells in the S phase of the cell cycle with a concomitant increase in the proportion of cells in the G2/M phase of the cell cycle, these modifications were not statistically significant ( $p > 0.05$ ) (Figure 38d). A true G2/M arrest would result in an increased G2/M associated with a decreased G0/G1 population. These features were not observed in Figure 38d. Therefore, these data indicated that serum-starvation for up to 24 h did not influence the distribution of UVW/NAT or SK-N-BE(2c) cells throughout the phases of the cell cycle. Nevertheless, in the following experiments, all treatments (untreated controls, radiation, DSF:Cu and combination treatments) were conducted in serum-free conditions whether DSF:Cu was present or not.

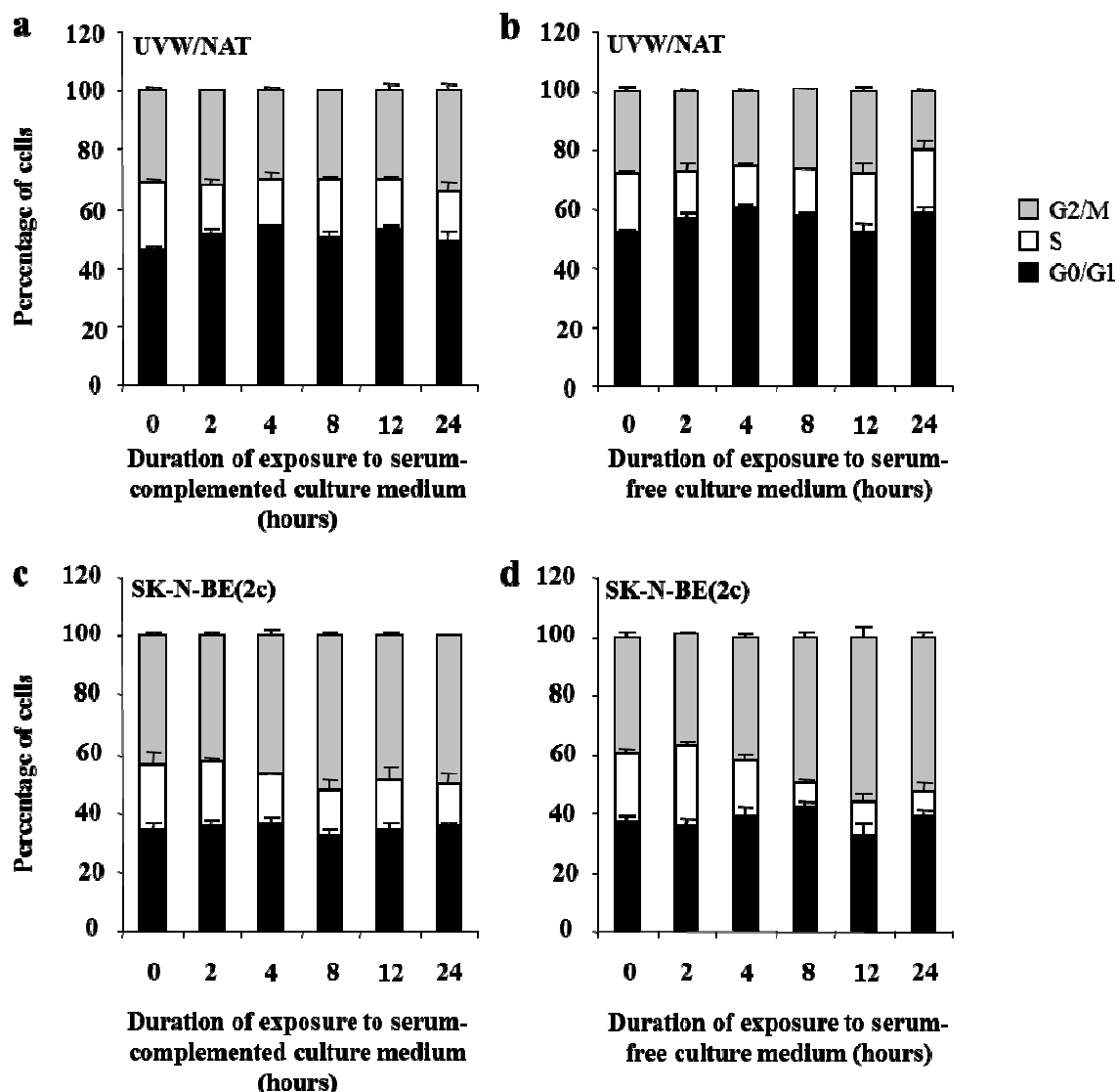


**Figure 38** Absence of an effect of serum starvation on the distribution of SK-N-BE(2c) and UVW/NAT cells throughout the phases of the cell cycle

UVW/NAT (a and b) and SK-N-BE(2c) (c and d) were exposed to serum-complemented culture medium (a and c) or to serum-free culture medium (b and d) for 2, 4, 8, 12 and 24 h. At the indicated timepoint after the start of the exposure to the different culture media, the cells were trypsinised and fixed in 70% ethanol at -20°C. FACS analysis of PI-stained cells was then carried out to determine the distribution of cells throughout the phases of the cell cycle. The software FlowJo was used to quantify the proportion cells in each phase of the cell cycle. Data are mean  $\pm$  SEM; n=3.

#### 5.4.2 Cell cycle arrest in response to $\gamma$ -radiation treatment

In all three cell lines, there was a time-dependent increase in the G2/M population 12 h after irradiation, followed by a decrease of the G2/M population from 12 to 24 h after irradiation (Figure 39). The accumulation of cells in G2/M at 12 h after irradiation was statistically significant in all three cell lines compared with non-irradiated controls (Figure 39). The accumulation of cells in the G2/M phase of the cell cycle was accompanied by a

decrease in the proportion of cells in G1, demonstrating that irradiated cells were unable to exit G2, progress through mitosis and enter the G1 phase of the cell cycle.

These data indicated that LNCaP, SK-N-BE(2c) and UVW/NAT cells were all able to arrest in G2 following irradiation. The maximal G2/M proportion of cells was observed 12 h after irradiation (Figure 39). Accordingly this timepoint was selected for the investigation of the effect of DSF:Cu on radiation-induced cell cycle arrest. Furthermore, the impact of the p53 status on the effect of DSF:Cu on radiation-induced cell cycle arrest was investigated by comparison of the HCT116 p53<sup>+/+</sup> cells with the HCT116 p53<sup>-/-</sup> cells.

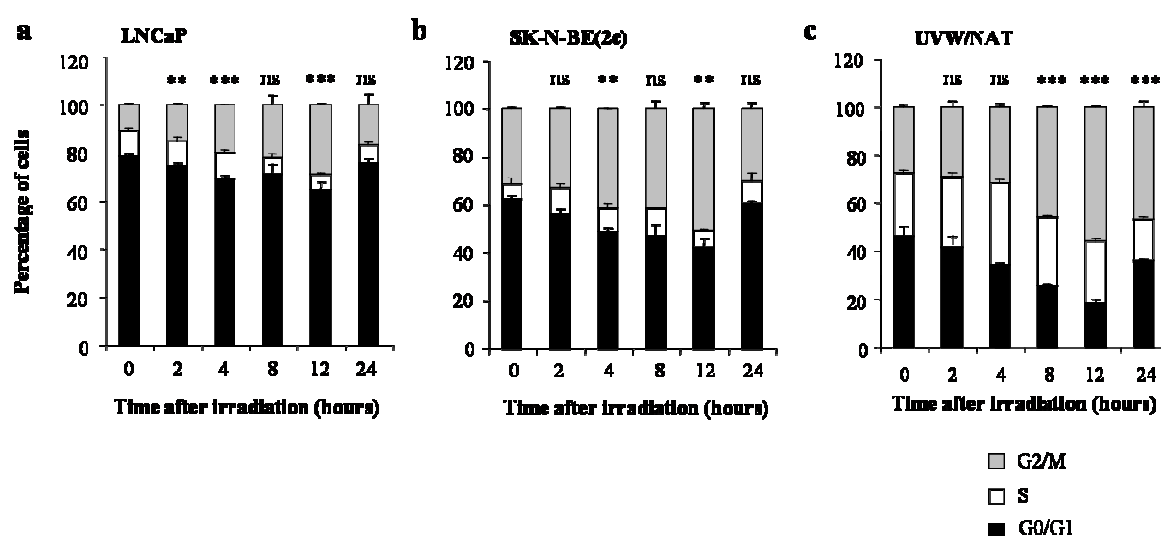


**Figure 39 Time-dependency of G2 arrest after  $\gamma$ -radiation treatment**

LNCaP (a), SK-N-BE(2c) (b) and UVW/NAT cells (c) were fixed in 70% ethanol at  $-20^{\circ}\text{C}$  at various timepoints after  $\gamma$ -radiation treatment. The cell cycle profiles were obtained by FACS analysis of PI-stained cells. The quantification of the percentage of cells in each phase of the cell cycle (G0/G1, S, G2/M) was carried out using FlowJo software (BD Biosciences, Mountain View, CA). Data are means  $\pm$  SEM; n=3. Independent samples t-test was used to compare the mean percentage of irradiated cultures with that of unirradiated controls. One symbol indicates  $p < 0.05$ , two symbols indicate  $p < 0.01$  and three symbols indicate  $p < 0.001$ .

#### 5.4.3 The effect of DSF:Cu on G2 arrest following $\gamma$ -radiation treatment

The effect of DSF:Cu on the cell cycle response of SK-N-BE(2c) cells to  $\gamma$ -radiation treatment is shown in Figure 40. In these experiments, there was a statistically significant increase in the G2/M population after  $\gamma$ -radiation treatment compared with untreated controls ( $p < 0.05$ ) (Figure 40a). There was a statistically significant reduction in the G2/M population following  $\gamma$ -radiation treatment in the presence of  $1 \mu\text{M}$  DSF:Cu, but not  $0.3$

$\mu\text{M}$  DSF:Cu, compared with the G2/M population after  $\gamma$ -radiation treatment alone ( $p < 0.05$ ). The percentages of cells in G2/M were 53.7% and 23.1% following  $\gamma$ -radiation treatment alone and after  $\gamma$ -radiation treatment in the presence of 1  $\mu\text{M}$  DSF:Cu, respectively (Figure 40b).

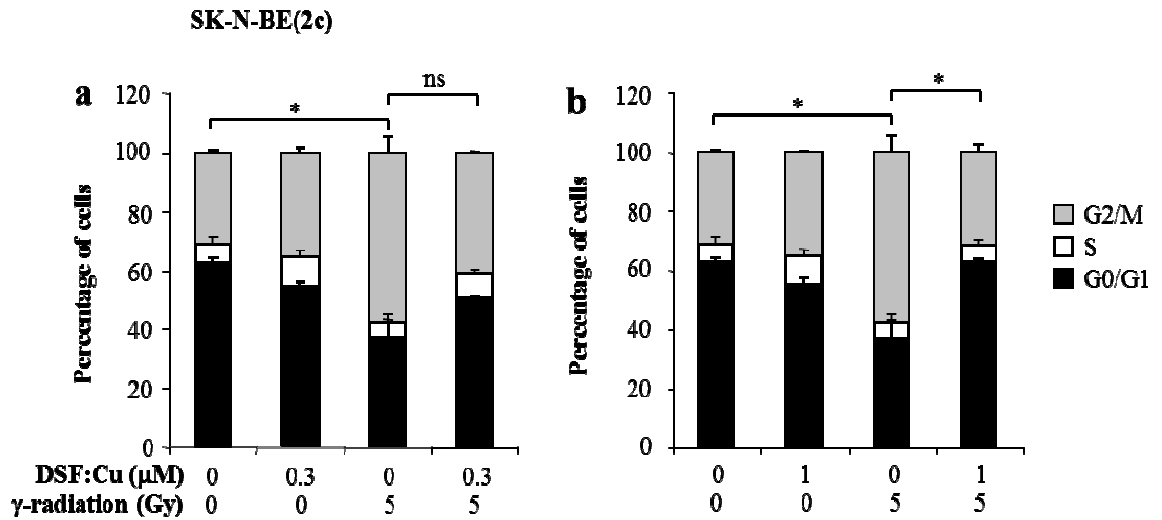


**Figure 40** The effect of DSF:Cu on the redistribution of SK-N-BE(2c) cells throughout the phases of the cell cycle following  $\gamma$ -radiation treatment

SK-N-BE(2c) cells were fixed in 70% ethanol at  $-20^{\circ}\text{C}$ , 12 h after  $\gamma$ -radiation treatment in the absence or in the presence of 0.3 (a) or 1  $\mu\text{M}$  DSF:Cu (b). The cell cycle profile was obtained by FACS analysis of PI-stained cells. The quantification of the percentage of cells in each phase of the cell cycle (G0/G1, S, G2/M) was carried out using FlowJo software (BD Biosciences, Mountain View, CA). Data are mean  $\pm$  SEM;  $n=3$ . One symbol indicates  $p < 0.05$ .

The effect of DSF:Cu on the cell cycle response of UVW/NAT cells to  $\gamma$ -radiation is shown in Figure 41. There was a statistically significant increase in the G2/M population after  $\gamma$ -radiation treatment compared with untreated controls ( $p < 0.001$ ) (Figure 41a). There was a statistically significant reduction in the G2/M population following  $\gamma$ -radiation treatment in the presence of 0.3 or 1  $\mu\text{M}$  DSF:Cu compared with the G2/M population after  $\gamma$ -radiation treatment alone ( $p < 0.01$ ). The percentages of cells in G2/M were 56.2% and 38.3% after  $\gamma$ -radiation treatment alone and  $\gamma$ -radiation treatment in the presence of 1  $\mu\text{M}$  DSF:Cu, respectively (Figure 41b).

The effect of DSF:Cu on the cell cycle response of LNCaP cells to  $\gamma$ -radiation is shown in Figure 42. There was a statistically significant increase in the G2/M population after  $\gamma$ -radiation treatment compared with untreated controls ( $p < 0.01$ ) (Figure 42a). There was a statistically significant reduction of the G2/M population following  $\gamma$ -radiation treatment in

the presence of 1  $\mu\text{M}$  DSF:Cu ( $p < 0.01$ ) (Figure 42b), but not 0.3  $\mu\text{M}$  DSF:Cu (Figure 42a), compared with the G2/M population after  $\gamma$ -radiation treatment alone. The percentages of cells in G2/M were 25.7% and 18.67% after  $\gamma$ -radiation treatment alone and  $\gamma$ -radiation treatment in the presence of 1  $\mu\text{M}$  DSF:Cu, respectively (Figure 42b).

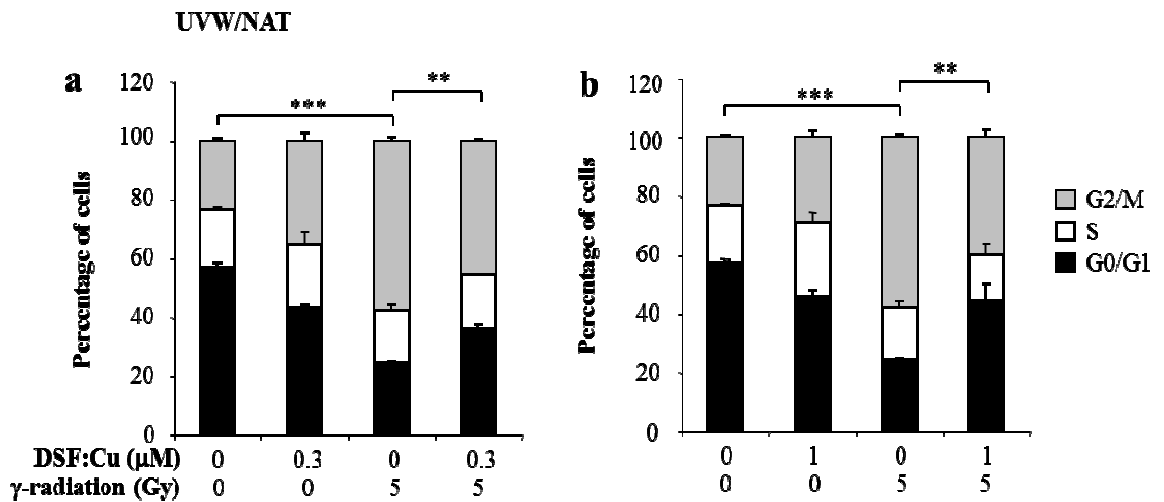


**Figure 41** The effect of DSF:Cu on the redistribution of UVW/NAT cells throughout the phases of the cell cycle following  $\gamma$ -radiation treatment

UVW/NAT cells were fixed in 70% ethanol at  $-20^{\circ}\text{C}$ , 12 h after  $\gamma$ -radiation treatment in the absence or in the presence of 0.3 (a) or 1  $\mu\text{M}$  DSF:Cu (b). The cell cycle profile was obtained by FACS analysis of PI-stained cells. The quantification of the percentage of cells in each phase of the cell cycle (G0/G1, S, G2/M) was carried out using FlowJo software (BD Biosciences, Mountain View, CA). Data are mean  $\pm$  SEM;  $n=3$ . Two symbols indicate  $p < 0.01$  and three symbols indicate  $p < 0.001$ .

The effect of DSF:Cu on the cell cycle response of HCT116 p53+/+ cells to  $\gamma$ -radiation is shown in Figure 43. There was a statistically significant increase in the G2/M population after  $\gamma$ -radiation treatment compared with untreated controls ( $p < 0.001$ ) (Figure 43a).

There was a statistically significant reduction in the G2/M population following  $\gamma$ -radiation treatment in the presence of 0.3 ( $p < 0.01$ ) or 1  $\mu\text{M}$  DSF:Cu ( $p < 0.001$ ), compared with the G2/M population after  $\gamma$ -radiation treatment alone. The percentages of cells in G2/M were 57.27% and 41.87% after  $\gamma$ -radiation treatment alone and  $\gamma$ -radiation treatment in the presence of 1  $\mu\text{M}$  DSF:Cu, respectively (Figure 43b).

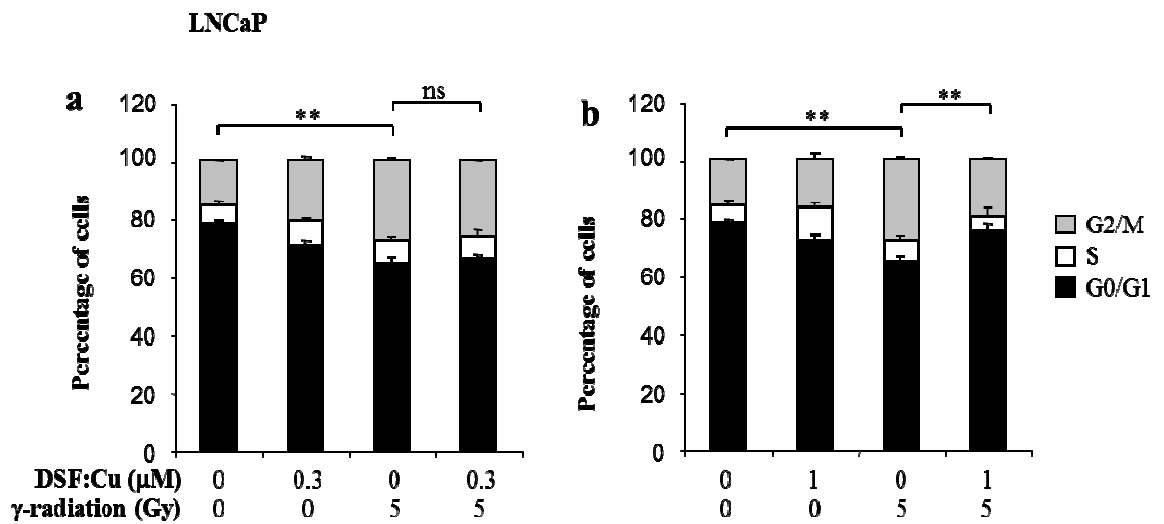


**Figure 42** The effect of DSF:Cu on the redistribution of LNCaP cells throughout the phases of the cell cycle following  $\gamma$ -radiation treatment

LNCaP cells were fixed in 70% ethanol at  $-20^{\circ}\text{C}$ , 12 h after  $\gamma$ -radiation treatment in the absence or in the presence of 0.3 (a) or 1  $\mu\text{M}$  DSF:Cu (b). The cell cycle profile was obtained by FACS analysis of PI-stained cells. The quantification of the percentage of cells in each phase of the cell cycle (G0/G1, S, G2/M) was carried out using FlowJo software (BD Biosciences, Mountain View, CA). Data are mean  $\pm$  SEM;  $n=3$ . Two symbols indicate  $p < 0.01$ .

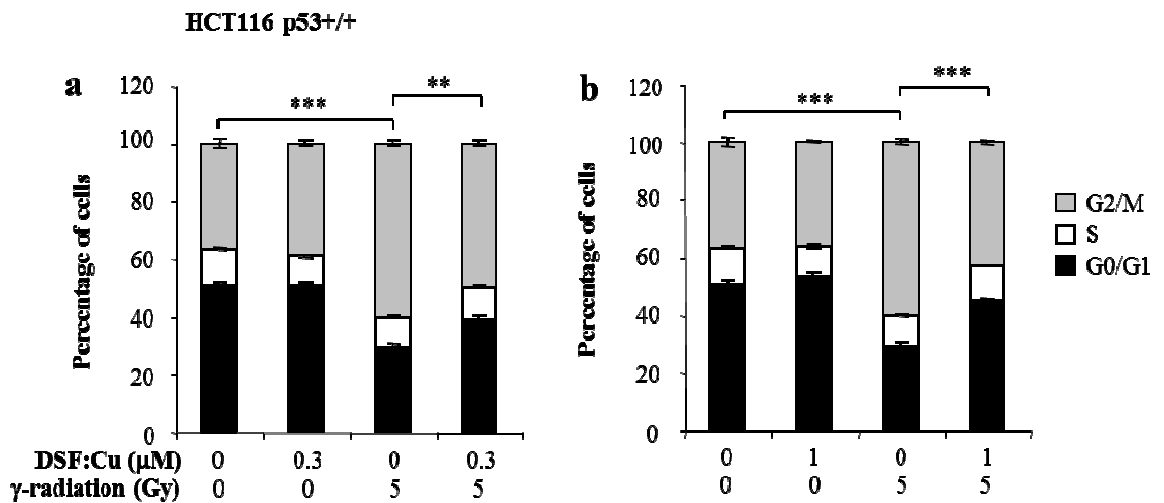


**Figure 43** The effect of DSF:Cu on the redistribution of HCT116 p53+/+ cells throughout the phases of the cell cycle following  $\gamma$ -radiation treatment

HCT116 p53+/+ cells were fixed in 70% ethanol at  $-20^{\circ}\text{C}$ , 12 h after  $\gamma$ -radiation treatment in the absence or in the presence of 0.3 (a) or 1  $\mu\text{M}$  DSF:Cu (b). The cell cycle profile was obtained by FACS analysis of PI-stained cells. The quantification of the percentage of cells in each phase of the cell cycle (G0/G1, S, G2/M) was carried out using FlowJo software (BD Biosciences, Mountain View, CA). Data are mean  $\pm$  SEM;  $n=3$ . Two symbols indicate  $p < 0.01$  and three symbols indicate  $p < 0.001$ .

The effect of DSF:Cu on the cell cycle response of HCT116 p53-/- cells to  $\gamma$ -radiation is shown in Figure 44. There was a statistically significant increase in the G2/M population

after  $\gamma$ -radiation treatment compared with untreated controls ( $p < 0.01$ ) (Figure 44a). There was a statistically significant reduction in the G2/M population following  $\gamma$ -radiation treatment in the presence of 1  $\mu\text{M}$  DSF:Cu ( $p < 0.01$ ) (Figure 44b), but not in the presence of 0.3  $\mu\text{M}$  DSF:Cu (Figure 44a), compared with the G2/M population after  $\gamma$ -radiation treatment alone. The percentages of cells in G2/M were 55.60% and 35.13% after  $\gamma$ -radiation treatment alone and  $\gamma$ -radiation treatment in the presence of 1  $\mu\text{M}$  DSF:Cu, respectively (Figure 44b).

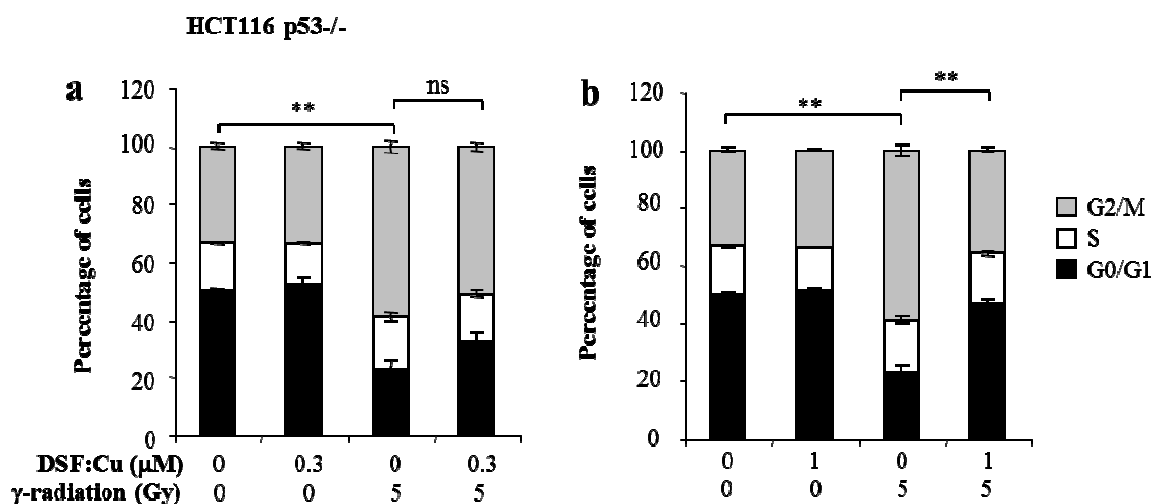


**Figure 44** The effect of DSF:Cu on the redistribution of HCT116 p53<sup>-/-</sup> cells throughout the phases of the cell cycle following  $\gamma$ -radiation treatment

HCT116 p53<sup>-/-</sup> cells were fixed in 70% ethanol at  $-20^{\circ}\text{C}$ , 12 h after  $\gamma$ -radiation treatment in the absence or in the presence of 0.3 (a) or 1  $\mu\text{M}$  DSF:Cu (b). The cell cycle profile was obtained by FACS analysis of PI-stained cells. The quantification of the percentage of cells in each phase of the cell cycle (G0/G1, S, G2/M) was carried out using FlowJo software (BD Biosciences, Mountain View, CA). Data are mean  $\pm$  SEM;  $n=3$ . Two symbols indicate  $p < 0.01$ .

These data demonstrated that DSF:Cu prevented the G2 arrest following  $\gamma$ -radiation treatment in LNCaP, SK-N-BE(2c) and UVW/NAT cells. Furthermore, the presence or the absence of functional p53 did not affect the inhibition of the G2 arrest by DSF:Cu in HCT116 cells, as indicated by the comparable abrogation of the  $\gamma$ -radiation-induced G2 arrest by DSF:Cu in HCT116 p53<sup>+/+</sup> and HCT116 p53<sup>-/-</sup> cells.

## 5.5 Discussion

Cell cycle checkpoints at the G1/S and G2/M transitions are activated in response to  $\gamma$ -radiation treatment. The resulting delay in progression into the S phase and mitosis allows for the repair of radiation-induced DNA damage<sup>247</sup>. If SSB are not efficiently repaired,

they are converted into DSB during DNA replication in the S phase. DSB are strong signals for apoptosis<sup>248</sup>. The inappropriate entry of cells into mitosis in the presence of DNA damage leads to mitotic catastrophe. Mitotic catastrophe is not clearly defined. It is a cell death mechanism which results from aberrant mitotic activity of cells which have been damaged by chemotherapeutic drugs or radiation treatment<sup>249</sup>. Therefore, cells must undergo cell cycle arrest in order to avoid entry to mitosis (G2 arrest) or to the S phase (G1 arrest) if their DNA has been damaged. In the experiments presented in this chapter, DSF:Cu inhibited  $\gamma$ -radiation-induced G2/M arrest in a variety of cell lines (Figure 40 to Figure 44), resulting in progression to mitosis in the presence of DNA damage. Therefore the suggested radiosensitising mechanism of DSF:Cu is increased cell death, through mitotic catastrophe, following exit from the G2/M phase of the cell cycle after the inefficient repair of  $\gamma$ -radiation-induced damage of DNA.

Radiosensitisation by DSF:Cu in combination with  $\gamma$ -radiation treatment was demonstrated in SK-N-BE(2c) and UVW/NAT cells (Section 4.4.2). In these experiments, the cells were irradiated and then incubated with DSF:Cu for 24 h before clonogenic assay. At 24 h after irradiation, all SK-N-BE(2c) cells had undergone G2 arrest, progressed to mitosis and entered G1 (Figure 39b). This indicated that 24 h after irradiation, the majority of cells had re-entered the cell cycle following G2 arrest. In the radiosensitisation experiments using SK-N-BE(2c) cells (Section 4.4.2), DSF:Cu was present in the culture medium for 24 h following irradiation. Thus, the majority of cells which would otherwise have arrested in G2 in order to repair their DNA, were prevented from doing so by DSF:Cu. These cells then entered mitosis carrying the burden of unrepaired DNA resulting in mitotic catastrophe.

However, the percentage of UVW/NAT cells in G2/M 24 h after irradiation was 45% versus 25% for the control, indicating the presence of a population of UVW/NAT cells still arrested in G2 24 h after irradiation (Figure 39c). This observation was consistent with the finding that the  $\beta$  value was lower in UVW/NAT cells following treatment with  $\gamma$ -radiation compared with SK-N-BE(2c) cells. The greater ability of UVW/NAT cells than SK-N-BE(2c) cells to repair DSB, indicated by the lower  $\beta$  value (Section 4.4.2), may be a result of the longer cell cycle delay in G2. UVW/NAT cells benefit from more time to repair DNA damage following radiation. This could explain lower radiosensitivity of UVW/NAT cells compared with SK-N-BE(2c) cells.

The inhibition of G2 arrest following  $\gamma$ -radiation treatment occurred regardless of the p53 status of the cell line, as indicated by the comparable abrogation of G2 arrest in HCT116 p53<sup>+/+</sup> cells (Figure 43) and HCT116 p53<sup>-/-</sup> cells (Figure 44). Also, the inhibition of G2 arrest following  $\gamma$ -radiation treatment occurred regardless of the duration of the G2 arrest produced by  $\gamma$ -radiation treatment. For instance, all SK-N-BE(2c) cells had re-entered the cell cycle 24 h after irradiation (Figure 39b) whereas 20% of UVW/NAT (Figure 39c) cells were still arrested in G2 24 h following irradiation. For instance, DSF:Cu abrogated G2 arrest following  $\gamma$ -radiation treatment in both SK-N-BE(2c) and UVW/NAT cells. These observations may indicate the generality of the inhibitory effect of DSF:Cu on G2 arrest after irradiation. Thus it may be hypothesised that the mechanism by which DSF:Cu inhibits G2 arrest is not through the specific regulation of the phosphorylation of key effectors of the G2 arrest. Instead, it may be due to a more general effect on the level of expression of proteins involved in cell cycle regulation. Experiments are currently being performed to elucidate the mechanism of DSF:Cu radiosensitisation via inhibition of the G2 arrest machinery. Furthermore, the consequence of the abrogation of the cell cycle arrest in G2 by DSF:Cu following irradiation should be an increase in SSB and DSB, as indicated by the increase in  $\alpha$  and  $\beta$  values. Such conjectures are currently being tested.

This series of experiments demonstrated the abrogation of G2 arrest following external beam radiation treatment by DSF:Cu which resulted in radiosensitisation of cells cultured as monolayers. However, two-dimensional monolayers are inadequately representative of tumours. The ensuing chapters will describe the characterisation of multicellular tumour spheroids as models for the study of the sensitisation of avascular metastases to targeted radiotherapy by DSF:Cu.

## **6 Characterisation of multicellular tumour spheroids (MTS) for the study of combination treatments**

### **6.1 Introduction**

#### **6.1.1 Spheroids**

For the purpose of cancer research, malignant cells may be kept in their proliferating state attached to plastic surfaces as two-dimensional monolayers. Alternatively, they may be grown as multicellular tumour spheroids. These are spherical multicellular aggregates of malignant cells proliferating freely in suspension in culture medium. A range of spheroid models have been described to study many types of cancers such as breast cancer<sup>250</sup>, prostate cancer<sup>251</sup>, glioma<sup>252</sup>, colon cancer<sup>252</sup> and lung cancer<sup>253</sup>. Spheroids bear greater similarity to tumours than monolayers because of their 3-dimensional morphology. For instance, the 3-D organisation of spheroids enables the investigation of the ability of a chemotherapeutic agent to penetrate the spheroid and target deeply located cells. Compounds with a high molecular weight or with low lipophilicity will penetrate less deeply inside a tumour than small lipophilic molecules thus resulting in lower toxicity to tumours. Such dependency cannot be evaluated in monolayers.

Culture medium contains oxygen and nutrients essential for spheroid cells' survival and proliferation. Upon attaining a diameter of approximately 300  $\mu\text{m}$ , a decreasing gradient of nutrient and oxygen forms from the outer layer to the inner core<sup>254</sup>. The core of spheroids is accordingly hypoxic and exhibits low pH<sup>255,256</sup>. The cells in the outer layer of a spheroid are in a proliferating state because they are more adequately supplied with oxygen and nutrients. Although drug penetrability accounts for chemoresistance of spheroids, it has also been demonstrated that the proliferating status and the microenvironment (nutrient availability, hypoxia and pH) of the various layers within the spheroid influence sensitivity to treatment<sup>257</sup>. For instance, the proliferating outer layer is more sensitive to antimetabolites such as doxorubicin or FUra<sup>258</sup>. Moreover, the alkylating agent mitomycin is known to be more cytotoxic in hypoxic cells<sup>259</sup>. It was shown that mitomycin was more toxic to cells located within the core of spheroids, consistent with the hypoxia-specific cytotoxicity of mitomycin<sup>258</sup>.

Furthermore, the indirect effect of radiation treatment was described in Section 1.1.5.1. ROS, formed by ionisation of oxygen-containing compounds, can damage DNA in the same way as its direct irradiation. The indirect effect of radiation relies on the presence of oxygen in the irradiated milieu. It follows that hypoxic regions are more resistant to

radiation than normoxic tissue<sup>260</sup>. This is supported by the demonstration that large spheroids are more resistant to radiation treatment than small spheroids due to the presence of a hypoxic core<sup>261,262</sup>.

Tumour microenvironment plays an important role in the sensitivity to therapy. Therefore spheroids allow for a more accurate prediction of the outcome of chemotherapy and radiotherapy than monolayers. It was demonstrated that a human ovarian carcinoma cell line grown as xenografts and spheroids resembled tumours with respect to growth rate, necrotic region, hypoxia and radiation sensitivity<sup>263</sup>. However, there are differences between spheroids and tumours. For instance, decreasing gradients of nutrients and oxygen exist from the outside to the innermost regions of spheroids in a concentric layer fashion. This is in contrast to tumours where gradients of nutrients and oxygen form according to the blood supply within the tumour. Tumours could be represented by a “mosaic” of microenvironments whereas a spheroid could be represented as concentric circles of microenvironments. Furthermore, spheroids fail to represent the complete microenvironment in which the tumour is confined. Fibroblasts, endothelium and components of the immune system communicate with the tumour through secretion of growth factors and cytokines. Although spheroids lack these features, they do represent a useful alternative to xenografts in experimental animals by recreating *in vitro* the heterogeneity of microenvironments observed in a tumour<sup>264</sup>.

### **6.1.2 Considerations for targeted radiotherapy**

Radiopharmaceuticals exert their cytotoxic effect by direct deposition of energy in targeted cells and by cross-fire to neighbouring cells. Thus, 3-D aggregates of cells such as spheroids, in which cross-fire occurs to a greater extent than in monolayers, constitute a better model to study therapeutic radiopharmaceuticals.

Targeted radiotherapy is able to reach all malignant lesions expressing the specific molecular target regardless of the size or morphology of the target tissue. Spheroids are models of avascular micrometastases and have been used as models for the investigation of the effect of drugs or the penetration of agents within avascular malignant tissues<sup>265-268</sup>. Spheroids are perfectly suited for the investigation of radiopharmaceuticals in the context of targeted radiotherapy.

### **6.1.3 A mathematical approach to the quantification of spheroid growth delay**

One index of treatment-induced growth delay of spheroids is the time required for an  $x$ -fold increase in volume ( $\tau_x$ )<sup>269,270</sup>. Alternatively, the incorporation of fluorescent dyes may be used to measure cellular viability at a particular timepoint after treatment. However, the effect of a treatment may be the reduction of the growth rate of the spheroid or the increase of the growth delay before the proliferating phase of the spheroid. Thus, the measurement of cellular viability at a particular timepoint is not the optimal method of determining the effect of experimental therapy of spheroids. Instead, the kinetics of growth were measured over a period of 3 to 4 weeks which corresponded to the phase of exponential growth of LNCaP spheroids<sup>271</sup>.

The mathematical equation for the dose-response relationship is given by the median effect principle. The median effect principle is based on the determination of a surviving fraction (unaffected by the treatment) and an affected fraction. Thus, in order to apply the median effect principle to the investigation of spheroid growth, it is necessary to derive the surviving fraction from growth delay experiments. In this chapter, the most appropriate index of the effect of a treatment that enables the calculation of surviving fraction - area under the volume-time curve or the time required for an  $x$ -fold increase in spheroid volume - will be evaluated. Furthermore, it will be assessed whether the median effect principle can be applied to spheroid growth delay experiments to determine the nature of the interaction between two agents in combination.

## **6.2 Aims**

- investigation of the morphology of the spheroids during treatment and during their growth
- determination of the growth characteristics of spheroids
- the establishment of an analytical method to determine the dose-response relationship in spheroid growth delay experiments

## **6.3 Materials and methods**

### **6.3.1 Spheroid initiation**

The prostate carcinoma cell line LNCaP, the glioma cell line UVW/NAT and the neuroblastoma cell line SK-N-BE(2c) were cultured as spheroids using the liquid overlay technique<sup>272</sup>. The monolayers were trypsinized and  $3 \times 10^6$  cells were seeded into a 25cm<sup>2</sup> plastic flask coated with 1% agar. The agar solution was prepared by dissolving 1g of agar powder (Melford Laboratories Ltd, Ipswich) into 20 ml of distilled water and heated in a

microwave before the addition of 80 ml culture medium at 50°C. The cells were incubated for a period of 3 to 4 days in 95% air and 5% CO<sub>2</sub> at 37°C. At the end of this period, spheroids had formed and were used for treatment.

### 6.3.2 DSF:Cu treatment

After 3 to 4 days of incubation in 95% air and 5% CO<sub>2</sub> at 37°C, the spheroids were centrifuged at 300 rpm for 3 min and resuspended in 2 ml fresh serum-free culture medium containing DSF:Cu in universal tubes. Universal tubes were used in preference to agar-coated flask used for initiation because it was anticipated that agar may interfere with the availability of drugs. Spheroids did not attach to the sides of the universal tube. At the end of the treatment period, the spheroids were washed three times in PBS.

### 6.3.3 Spheroid volume measurement

At the end of the treatment period, spheroids of approximately 100 µm in diameter were manually selected under a magnifying lamp and individually transferred into agar-coated wells of a 24-well plate (Fisher Scientific UK Ltd, Loughborough). The growth of individual spheroids was monitored twice per week using an inverted phase-contrast microscope connected to an image acquisition system. Two orthogonal diameters,  $d_{\max}$  and  $d_{\min}$  (µm), were measured using the image analysis software ImageJ and the volume,  $V$  ( $10^6 \mu\text{m}^3$ ), was calculated using the formula<sup>272</sup>:

$$V = \pi \times d_{\max} \times d_{\min}^2 / 6,000,000 \quad (17)$$

Alternatively, the volume,  $V$ , of a single spheroid was divided by its initial volume  $V_0$  ( $V/V_0$ ), to enable comparison between treatments.

### 6.3.4 Calculation of the growth delay ( $\tau_2$ ) and the doubling time (DT)

Linear regression analysis between the logarithm of the fold increase of individual spheroid volume ( $\log V/V_0$ ) and time  $t$  was performed using the method of least squares. The linear regression equation was fitted to the exponential part of the spheroid growth curve. The slope,  $b$ , and the y-intercept,  $a$ , of the linear regression equation  $\log V/V_0 = bt + a$  were used to calculate the time,  $\tau_2$ , required for an 2-fold increase in spheroid volume from day 0:

$$\tau_2 = (\log 2 - a) / b \quad (18)$$

Alternatively, DT was defined as the time required for a 2-fold increase in volume in the exponential part of the spheroid growth curve. DT was calculated using equation (20):

$$DT = \log 2 / b \quad (20)$$

The  $\tau_2$  values represent a measure of the growth delay while the DT values represent a measure of the growth rate. Indeed, the effect of a treatment may be the delay of the start of the proliferating phase with an ensuing proliferating phase parallel to that of the untreated control. Alternatively, the effect of a treatment may be the reduction of the growth rate (i.e. reduction of the slope of the log-transformed growth curve). Figure 45 shows the growth curves of an untreated spheroid (Figure 45a) and that of a spheroid treated with 3.7 MBq/ml of the radiopharmaceutical [<sup>131</sup>I]MIP-1095 (Figure 45b). The untreated spheroid is characterised by a  $\tau_2 = 3.50$  days and DT = 2.82 days (Figure 45a). Note that, in this particular example, the proliferating phase of the untreated spheroid starts from day 0 without a lag phase (Figure 45a). On the other hand, the spheroid treated with 3.7 MBq/ml [<sup>131</sup>I]MIP-1095 is characterised by an increased  $\tau_2$  (8.77 days) but a similar DT value (3.31 days) (Figure 45b). This indicates that this radioactivity concentration of [<sup>131</sup>I]MIP-1095 delays the start of the proliferating phase but does not alter the growth rate. This is consistent with a proportion of cells being killed by the treatment and the remaining cells able to proliferate at the same rate as the control. This example demonstrates the need to report both values in order to assess the effect of treatment on the growth of spheroids.

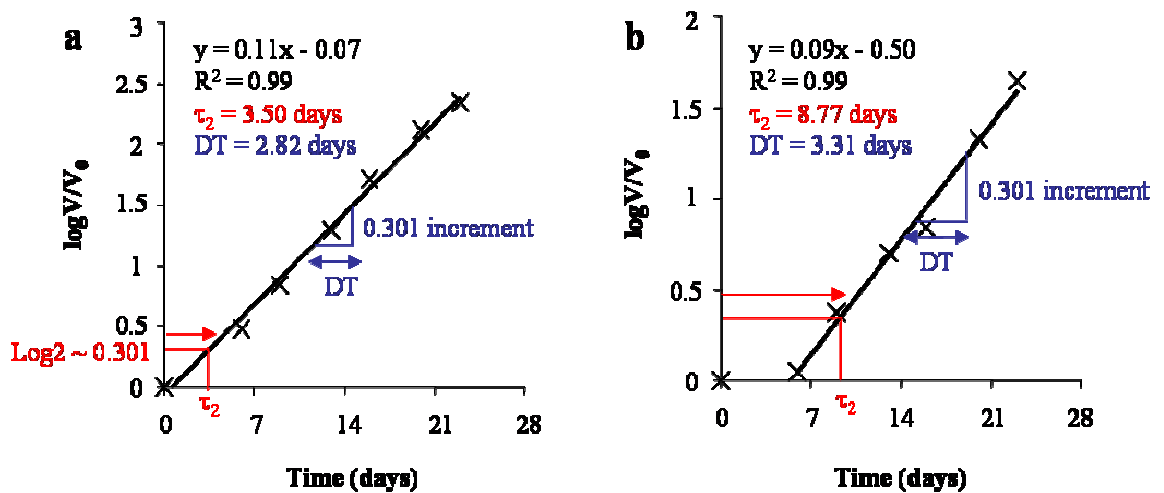


**Figure 45 Comparison between  $\tau_2$  and DT values for the measure of spheroid growth**

Two spheroids were evaluated: one untreated (a) and one treated with 3.7 MBq/ml [<sup>131</sup>I]MIP-1095 (b). The logarithm of the  $V/V_0$  values was calculated in order to obtain a linear relationship between  $\log V/V_0$  and time. The volume against time data were fitted by linear regression using the method of least squares. The  $\tau_2$

value was defined as the time required to achieve a 2-fold increase in spheroid volume from day 0 and the DT value was defined as the time required to achieve a 2-fold increase in spheroid volume during the exponential growth of the spheroid. The  $\tau_2$  values are represented graphically by the red arrows whereas the DT values are represented graphically by the blue arrows. In both panels, the equation of the linear regression, the coefficient of determination  $R^2$ , the  $\tau_2$  and the DT values are reported.

### **6.3.5 Calculation of the area under the curve (AUC)**

The area under the  $V/V_0$  versus time curve ( $AUC_{\text{linear}}$ ) was calculated for individual spheroids using trapezoidal approximation. Similarly, the area under the  $\log V/V_0$  versus time curve ( $AUC_{\text{log}}$ ) was also calculated for individual spheroids using trapezoidal approximation.

### **6.3.6 Statistical analysis**

The logarithmic transformation of the  $V/V_0$  values ( $\log V/V_0$ ) linearises the growth curve, i.e. each timepoint is equally weighed in the calculation of  $AUC_{\text{log}}$ . In contrast, the  $AUC_{\text{linear}}$  value is relatively more dependent on the  $V/V_0$  values at the later timepoints than at the earlier timepoints because of the exponential increase in volume. Therefore, the  $AUC_{\text{log}}$  values were chosen over the  $AUC_{\text{linear}}$  values for the statistical analyses.

The distributions of  $\tau_2$ , DT or  $AUC_{\text{log}}$  values were not normal therefore non-parametric testing was performed using the statistical analysis software SPSS v.19 (IBM). The Kruskal-Wallis test was used to determine whether experimental data indicated a significant level of difference between the medians of the groups. If the p-value of the Kruskal-Wallis test was less than 0.05, the Mann-Whitney test was used for pairwise comparisons. The statistical analysis of the effect of increasing doses of a treatment was performed as follows. First, the median of the group treated with the highest concentration was compared with that of the control. If the p-value returned by the Mann-Whitney test was less than 0.05, the difference between the two groups was considered significant and the median of the group treated with the next highest concentration was then compared with that of the control. This stepwise procedure was applied to each drug concentration with 0.05 as the significance level until the median of a group was not significantly different from that of the control. When a comparison returned a p-value greater than 0.05, the effects of treatment with lower concentrations were considered not statistically significant. The assumption was made that increasing dose increases the effect, thus an observation of a more significant effect at a lower concentration was considered to be due to random variation.

### **6.3.7 Regression analysis**

The significance of the correlation between the parameters  $\tau_2$ , DT or  $AUC_{\log}$  and the initial spheroid volume at day 0 was determined using the statistical analysis software SPSS v.19 (IBM). A linear regression equation was calculated by the software and an analysis of variance (ANOVA) was performed to determine whether the correlation was statistically significant.

### **6.3.8 Immunocytochemistry**

Spheroids were stored at 4°C overnight in formalin and delicately processed into a wax block. Wax sections 4 µm thick were cut using a microtome (ThermoFisher Scientific, Hemel Hempstead, UK). These sections were placed onto poly-lysine coated slides and baked in an oven at 60°C for at least 1 h. Immunohistochemistry was performed using an automated staining platform. The sections were de-waxed in xylene and re-hydrated by successive immersions in 100% (v/v) alcohol, 75% (v/v) alcohol and distilled water. Endogenous peroxidase activity was quenched by incubation in 0.3% (v/v) H<sub>2</sub>O<sub>2</sub> solution in methanol for 30 min. For epitopic exposure, heat-induced retrieval was performed in a 10 mM sodium citrate, 0.05% (v/v) Tween 20, pH6 buffer using a pre-treatment module (DAKO, Cambridge, UK) set to 98°C for 25 minutes. The sections were then washed using Tris-buffered Tween before being exposed to anti-Ki67 (Thermo, 1:100) or anti-phosphorylated caspase 3 (pCASP3) (Cell Signalling, 1:50). The anti-rabbit EnVision™ system (DAKO, Cambridge, UK) was used in conjunction with the 3, 3'-diaminobenzidine (DAB) substrate kit for peroxidase (Vector Laboratories, Burlingame, CA) to visualise epitope positivity. The spheroid sections were then counterstained with haematoxylin and immersed in Scotts tap water for 1 min in order to improve the contrast with eosin staining. Finally, the sections were dehydrated and rewaxed by successive immersions in 75% (v/v) ethanol, 100% (v/v) ethanol and xylene before application of DPX mountant (VWR, UK) and a glass coverslip.

### **6.3.9 Pimonidazole treatment**

The hypoxic status of spheroids was determined using the hypoxyprobe™ kit (Hypoxyprobe Inc, Burlington, MA). Live spheroids were treated for 24 h with 200 µM pimonidazole in culture medium. Pimonidazole binds to thiol groups of proteins in the absence of or in the presence of low levels of oxygen<sup>273</sup>. Therefore, pimonidazole adducts

are markers of anoxia and hypoxia. After treatment with pimonidazole, the spheroids were fixed in formalin for 24 h before processing.

### **6.3.10 Staining of pimonidazole adducts**

Spheroid sections were de-waxed and rehydrated by successive immersions in xylene, 100% (v/v) ethanol, 75% (v/v) ethanol and distilled water. Firstly, endogenous peroxidase activity was quenched by incubation in 0.3% (v/v) H<sub>2</sub>O<sub>2</sub> solution in methanol for 30 min. The sections were then blocked in 10% (v/v) goat serum in Tris-buffered EDTA (TBE) for 30 min. Secondly, the sections were incubated in 10% (v/v) goat serum in TBE containing monoclonal mouse anti-pimonidazole adducts antibody (Hypoxyprobe, Inc, Burlington, MA, 1:5,000 or 1:1,000 dilutions as indicated) for 1 h. The spheroid sections were then incubated in 10% (v/v) goat serum in TBE containing a rabbit biotinylated polyclonal anti-mouse secondary antibody (DAKO, Cambrifge, UK, 1:100) for 45 min. For visualisation of the pimonidazole adducts, the spheroid sections were incubated in TBE containing avidin and biotinylated horseradish peroxidase macromolecular complex (Vectastatin Elite ABC kit, Vector Laboratories, Burlingame, CA) for 30 min at room temperature followed by incubation in distilled water containing DAB (Vector Laboratories, Burlingame, CA) for 10 min at room temperature according to the manufacturer's protocol. The spheroid sections were then counterstained with haematoxylin and immersed in Scotts tap water for 1 min in order to improve the contrast with eosin staining. Finally, the sections were dehydrated and rewaxed by successive immersions in 75% (v/v) ethanol, 100% (v/v) ethanol and xylene before application of DPX mountant (VWR, UK) and a glass coverslip.

### **6.3.11 Heamatoxylin and eosin**

Firstly, the sections were de-waxed in xylene and re-hydrated by successive immersions in 100% (v/v) alcohol, 75% (v/v) alcohol and water. The staining procedure involved successive immersions in haematoxylin (Cell Path, UK, 7 min), 1% (v/v) acid alcohol, Scott's tap water (1 min) and eosin (made in-house, 5 min) with intermediate washes in water. Finally, the stained sections were dehydrated in 75% (v/v) and 100% (v/v) alcohol solutions and immersed in xylene before application of DPX mountant (VWR, UK) and a glass coverslip.

## **6.4 Results**

### **6.4.1 The morphology of spheroids is dependent on their size**

Spheroids were initiated using the liquid overlay technique for 3-4 days. Single spheroids were transferred into individual wells for monitoring of their size. The timepoint at which

the first spheroid image was captured was designated day 0. At day 0, spheroids were on average 100  $\mu\text{m}$  in diameter whereas they were on average 500  $\mu\text{m}$  at day 21. The H&E staining of spheroid sections was used to reveal their internal morphology. Day 0 LNCaP spheroids stained homogeneously for H&E. Many purple nuclei surrounded by a pink cytoplasm demonstrated a dense and homogeneous population of viable cells (Figure 46). On the other hand, 21 days old LNCaP spheroids stained heterogeneously for H&E. The outer layer was constituted of densely located nuclei surrounded by a cytoplasm reminiscent of the morphology of day 0 spheroids. The inner core was composed of areas of cells staining predominantly pink and possessing nuclei smaller than those in the outer layers. Both of these features were consistent with cell death in the core and an area of proliferating cells in the outer layer (Figure 46)<sup>274</sup>.

LNCaP spheroids were also stained for markers of proliferation (Ki67) and hypoxia (pimonidazole adducts). Day 0 LNCaP spheroids contained a sub-population of Ki67-positive, proliferating cells scattered randomly throughout the spheroid (Figure 46). Moreover, hypoxia was not evident (Figure 46). In contrast, 21 days old LNCaP spheroids showed heterogeneous staining for Ki67 and hypoxia. There was an outer layer of Ki67-positive proliferating cells and an inner population of hypoxic cells (Figure 46).

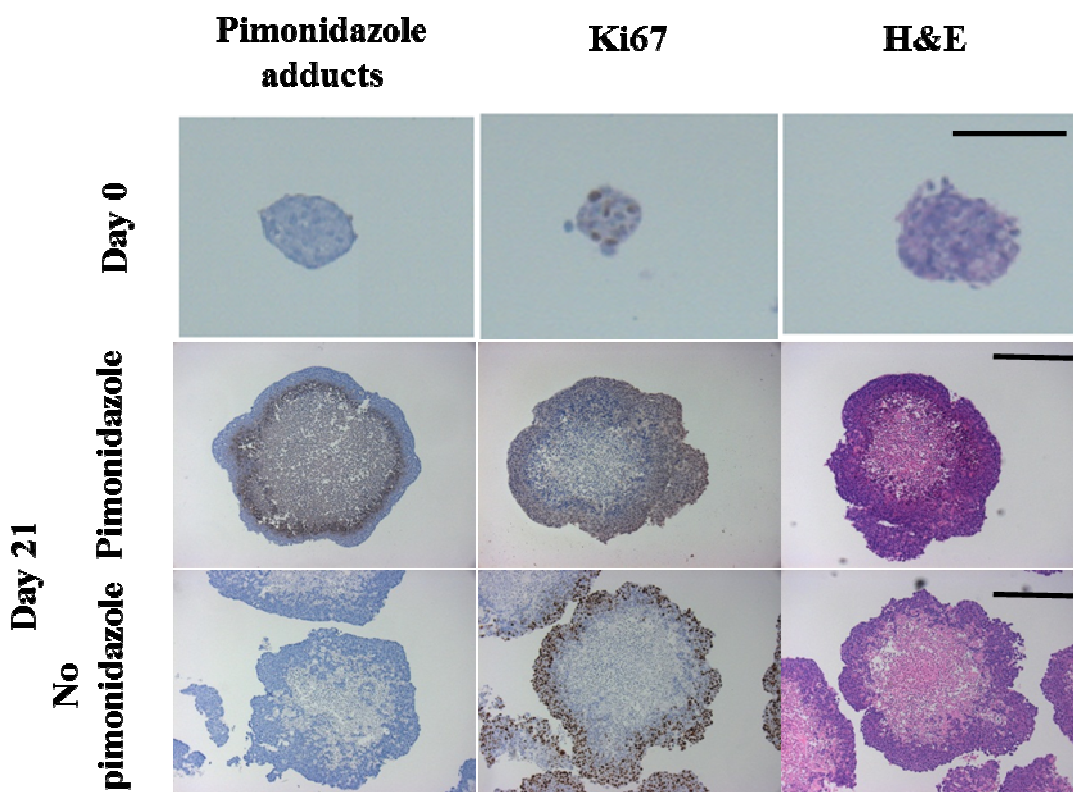


Figure 46 Hypoxic core and proliferative outer layer in LNCaP spheroids

LNcaP spheroids of diameter 100-150  $\mu\text{m}$  (day 0) or 500  $\mu\text{m}$  (day 21) were exposed to 200  $\mu\text{M}$  of pimonidazole for 24 h then fixed in formalin and stained with an anti-pimonidazole adduct antibody (Hypoxiprobe™, 1:5,000) as described in Section 6.3.10. Ki67 staining was used to reveal proliferating regions within spheroids. Hematoxylin and eosin (H&E) staining was used to reveal the internal morphology of the spheroids. The bars indicate 150  $\mu\text{m}$ .

Day 0 SK-N-BE(2c) spheroids contained a homogeneous population of normoxic and proliferative cells (Figure 47). On the other hand, day 21 SK-N-BE(2c) spheroids consisted of a heterogeneous population of cells: a hypoxic core surrounded by a Ki67-positive proliferating outer layer (Figure 47). H&E staining revealed an outer layer comprising numerous densely organised nuclei whereas the inner core contained fewer nuclei of chaotic morphology, indicative of a healthy outer layer surrounding a dying core (Figure 47).

Day 0 UVW/NAT spheroids showed a homogeneous, non-hypoxic and proliferative population of cells (Figure 48). On the other hand, day 21 UVW/NAT spheroids showed a heterogeneous population of cells: there was a hypoxic core surrounded by an outer layer of Ki67-positive proliferating cells (Figure 48). The hypoxic core stained positively for pCASP3, signifying apoptosis (Figure 48).

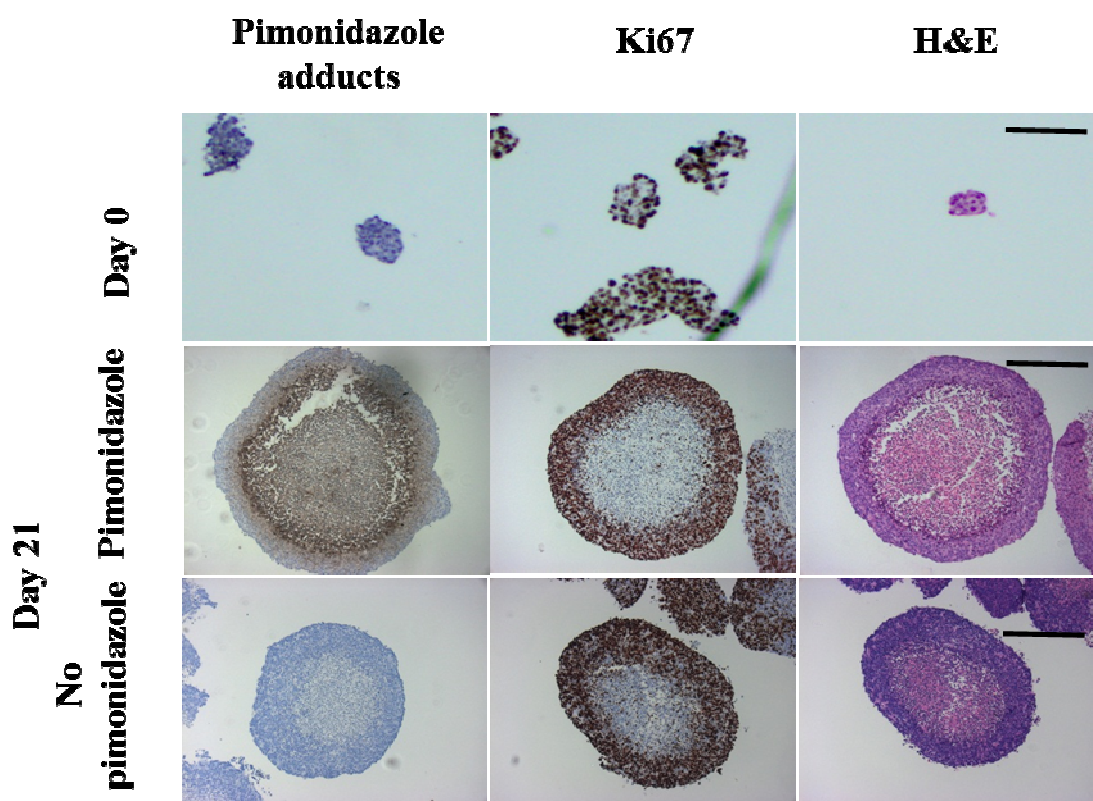
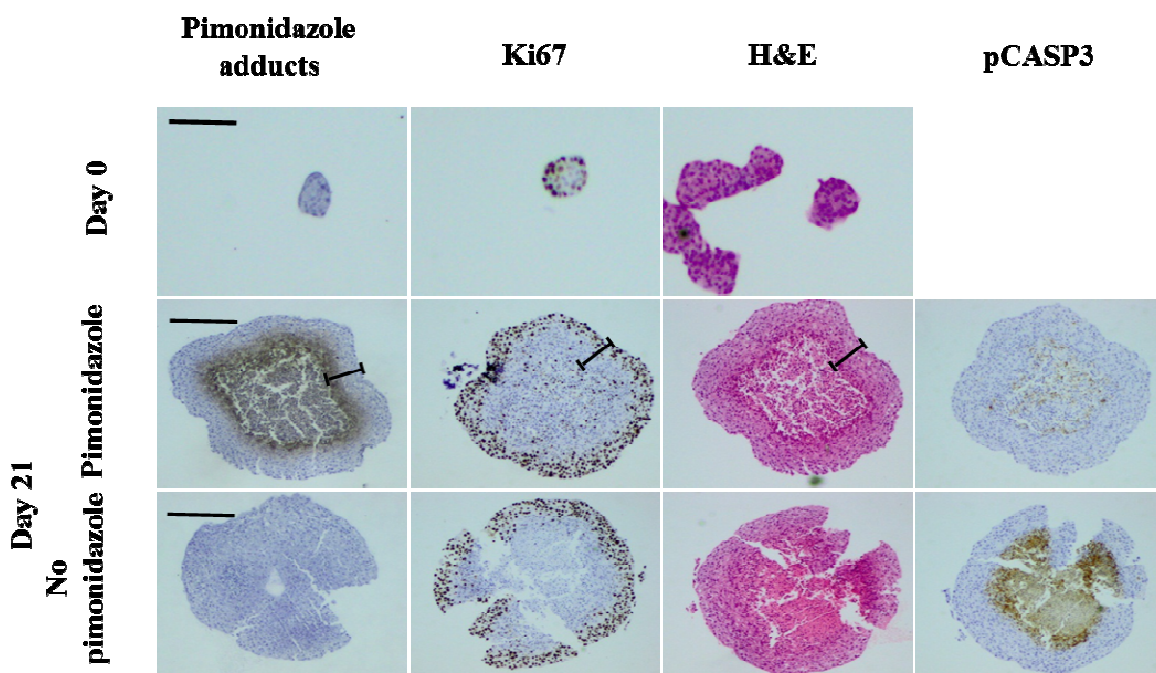


Figure 47 Hypoxic core and proliferative outer layer in SK-N-BE(2c) spheroids

SK-N-BE(2c) spheroids with a diameter of approximately 100  $\mu\text{m}$  (day 0) or 500  $\mu\text{m}$  (day 21) were exposed to 200  $\mu\text{M}$  of pimonidazole for 24 h, then fixed in formalin and stained with anti-pimonidazole adduct (Hypoxiprobe™, 1:5,000) as described in Section 6.3.10. Ki67 staining was used to reveal the proliferative status of the spheroids. Hematoxylin and eosin (H&E) were used to reveal the internal morphology of the spheroids. The bars indicate 150  $\mu\text{m}$ .

A significant observation was the presence of a hypoxic ring of greater staining intensity located at the periphery of the hypoxic core and on the internal edge of the outer layer. This feature was present in LNCaP (Figure 46), SK-N-BE(2c) (Figure 47) and UVW/NAT spheroids (Figure 48). The greater intensity of staining for pimonidazole adducts at this location could not be due to lower oxygen tension since this would be contrary to the depth-dependent oxygen gradient. A proportion of cells located on the internal edge of the outer layer which was defined by the H&E staining as a densely organised viable population of cells also stained positive for pimonidazole adducts. The illusion of greater intensity arose from the pimonidazole adduct staining of the more densely packed population of the outer layer compared with that of the dying core. This suggested there was a population of cells deemed viable according to the H&E staining which was also hypoxic. Finally, the width of the Ki67-positive proliferating ring was thinner than that of the H&E-stained viable outer layer (Figure 48). The Ki67-positive proliferating ring did not overlap with the hypoxic ring on the internal edge of the H&E-stained viable outer layer (Figure 48). These observations suggested the presence of a non-dividing or quiescent population of live cells located within the spheroids. The latter conclusion is speculative because a similarly hypoxic yet viable region was less apparent in LNCaP (Figure 46) or SK-N-BE(2c) spheroids (Figure 47).



**Figure 48 Hypoxic core and proliferative outer layer in UVW/NAT spheroids**

UVW/NAT spheroids with a diameter of approximately 100  $\mu\text{m}$  (day 0) or 500  $\mu\text{m}$  (day 21) were exposed to 200  $\mu\text{M}$  of pimonidazole for 24 h, then fixed in formalin and stained with anti-pimonidazole adduct (Hypoxiprobe™, 1:1,000) as described in Section 6.3.10. Ki67 staining was used to reveal the proliferative status of the spheroids. Hematoxylin and eosin (H&E) were used to reveal the morphology of the spheroids. Apoptosis was detected using an antibody directed against the phosphorylated form of caspase 3 (pCASP3). The segments determine the width of the outer layer of viable cells as defined by the H&E staining. The bars indicate 150  $\mu\text{m}$ .

## 6.4.2 Spheroid growth rate is dependent on initial size

The  $\tau_2$ , DT and  $\text{AUC}_{\log}$  values of untreated LNCaP, UVW/NAT and SK-N-BE(2c) spheroids were compared with their initial diameter. The correlation between each of these parameters and initial volume was investigated by regression analysis.

### 6.4.2.1 LNCaP

Growth curves were constructed for three size classes of LNCaP spheroids: those of diameter  $\leq 200$   $\mu\text{m}$ , those of diameter 200 to 300  $\mu\text{m}$  and those of diameter  $\geq 300$   $\mu\text{m}$  (Figure 49). Analysis of the growth curves indicated that the bigger the initial volume, the slower the growth (Figure 49a and Figure 49b). A regression analysis of the correlation between  $\tau_2$ , DT,  $\text{AUC}_{\log}$  and initial volume ( $V_0$ ) was carried out. According to the data displayed in Figure 49c,  $\tau_2$  values can be defined as follows:

$$\tau_2 = 0.04 V_0 + 3.10$$

The growth delay increased by 0.04 days for every  $1 \times 10^6 \mu\text{m}^3$  increase of  $V_0$  ( $p = 0.008$ ). The  $R^2$  value was 10%, indicating that 10% of the variability of  $\tau_2$  was explained by the variability of  $V_0$  ( $n = 66$ ) (Figure 49c). Similarly, according to the data displayed in Figure 49d, DT values can be defined as follows:

$$DT = 0.08 V_0 + 3.54$$

The doubling time increased by 0.08 days for every  $1 \times 10^6 \mu\text{m}^3$  increase of  $V_0$  ( $p < 0.001$ ). The  $R^2$  value was 37%, indicating that 37% of the variability of DT was explained by the variability of  $V_0$  ( $n = 66$ ) (Figure 49d). Finally, according to the data displayed in Figure 49e,  $AUC_{\log}$  values can be defined as follows:

$$AUC_{\log} = -0.03 V_0 + 2.70$$

The area under the  $\log V/V_0$  versus time curve decreased by 0.03 AU (AU = time \* volume) for every  $1 \times 10^6 \mu\text{m}^3$  increase of  $V_0$  ( $p < 0.001$ ). The  $R^2$  value was 75%, indicating that 75% of the variability of  $AUC_{\log}$  values was explained by the variability of  $V_0$  ( $n = 27$ ) (Figure 49e).

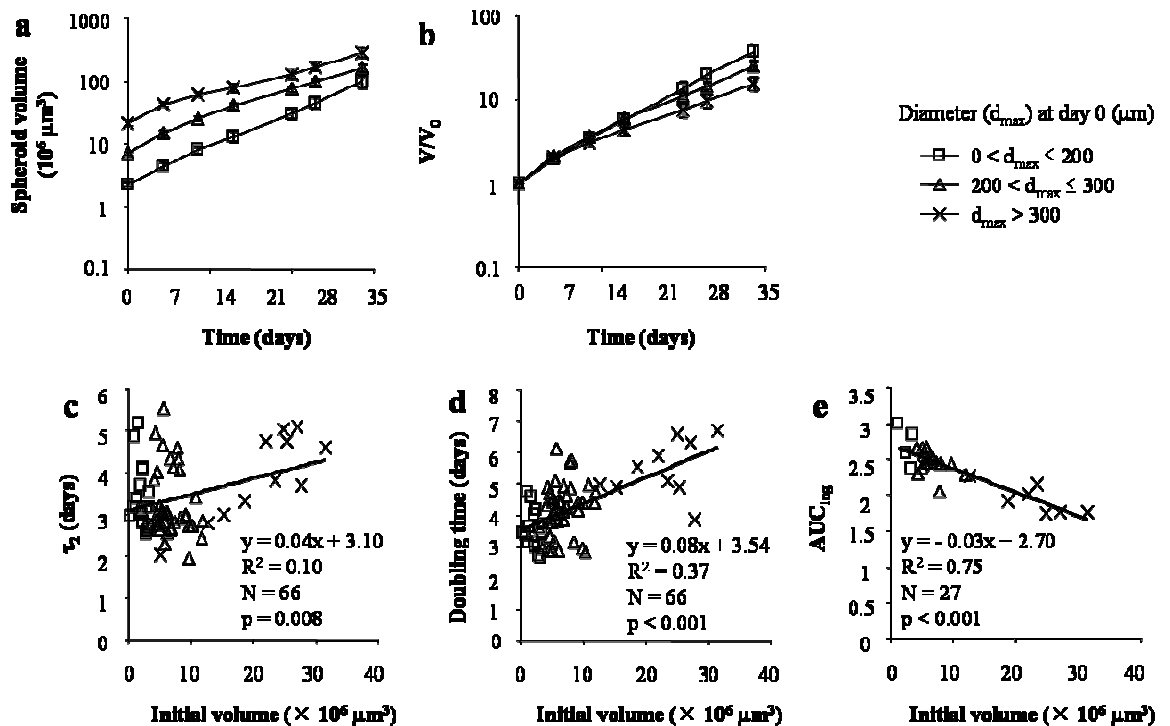


**Figure 49** The effect of the initial volume ( $V_0$ ) on the growth rate of LNCaP spheroids

Spheroids were sorted according to their initial diameter  $d_{\max}$  at day 0. Spheroid volumes are plotted in order to demonstrate the difference between the initial volumes (a). The  $V/V_0$  values are plotted to demonstrate the

inverse correlation between initial volume and growth rate (b).  $\tau_2$  values are plotted against initial volume (c). DT values are plotted against initial volume (d).  $AUC_{\log}$  values are plotted against initial volume (e). The correlations between  $\tau_2$ , DT,  $AUC_{\log}$  and the initial volume were statistically evaluated using SPSS; the regression equation, the coefficient of determination  $R^2$ , the number of spheroid N and the p-value are given for each parameter.

#### 6.4.2.2 SK-N-BE(2c)

Growth curves were constructed for three size classes of SK-N-BE(2c) spheroids: those of diameter  $\leq 100 \mu\text{m}$ , those of diameter 100 to  $200 \mu\text{m}$  and those of diameter  $\geq 200 \mu\text{m}$  (Figure 50). Analysis of the growth curves indicated that the bigger the initial volume, the slower the growth (Figure 50a and Figure 50b). A regression analysis of the correlation between  $\tau_2$ , DT,  $AUC_{\log}$  and  $V_0$  was carried out. According to the data displayed in Figure 50c,  $\tau_2$  values can be defined as follows:

$$\tau_2 = 0.17 V_0 + 1.96$$

The growth delay increased by 0.17 days for every  $1 \times 10^6 \mu\text{m}^3$  increase of  $V_0$  but the correlation was not statistically significant ( $p = 0.162$ ) (Figure 50c). Similarly, according to the data displayed in Figure 50d, DT values can be defined as follows:

$$DT = 0.19 V_0 + 1.96$$

The growth rate increased by 0.19 days for every  $1 \times 10^6 \mu\text{m}^3$  increase of  $V_0$  ( $p < 0.001$ ). The  $R^2$  value was 71%, indicating that 71% of the variability of DT was explained by the variability of  $V_0$  ( $n = 21$ ) (Figure 50d). Finally, according to the data displayed in Figure 50e,  $AUC_{\log}$  values can be defined as follows:

$$AUC_{\log} = - 0.39 V_0 + 5.46$$

The area under the  $\log V/V_0$  versus time curve decreased by 0.39 AU (AU = time \* volume) for every  $1 \times 10^6 \mu\text{m}^3$  increase of  $V_0$  ( $p < 0.001$ ). The  $R^2$  value was 67%, indicating that 67% of the variability of  $AUC_{\log}$  was explained by the variability of  $V_0$  ( $n = 21$ ) (Figure 50e).

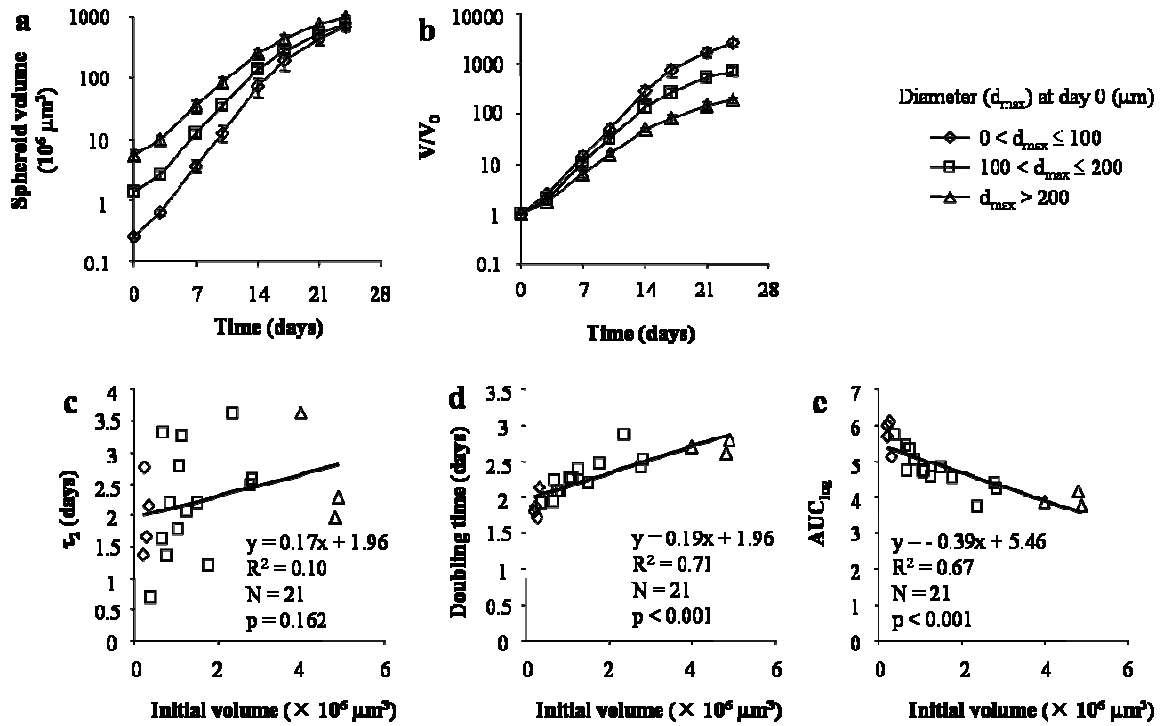


**Figure 50** The effect of the initial volume ( $V_0$ ) on the growth rate of SK-N-BE(2c) spheroids

Spheroids were sorted according to their initial diameter  $d_{max}$  at day 0. Spheroid volumes are plotted in order to demonstrate the difference between the initial volumes (a). The  $V/V_0$  values are plotted to demonstrate the inverse correlation between initial volume and growth rate (b). The  $\tau_2$  values are plotted against initial volume (c). DT values are plotted against initial volume (d).  $AUC_{log}$  values are plotted against initial volume (e). The correlation between  $\tau_2$ , DT,  $AUC_{log}$  and the initial volume was statistically evaluated using SPSS; the regression equation, the coefficient of determination  $R^2$ , the number of spheroid  $N$  and the  $p$ -value are given for each parameter.

### 6.4.2.3 UVW/NAT

Growth curves were constructed for three size classes of UVW/NAT spheroids (i) those of diameter  $\leq 100 \mu\text{m}$ , (ii) those of diameter 100 and 200  $\mu\text{m}$  and (iii) those of diameter  $\geq 200 \mu\text{m}$  (Figure 51). Analysis of the growth curves indicated that the bigger the initial volume, the slower the growth (Figure 51a and Figure 51b). The analysis of the correlation between  $\tau_2$ , DT,  $AUC_{log}$  and  $V_0$  was carried out. According to the growth delay data displayed in Figure 51c,  $\tau_2$  values can be defined as follows:

$$\tau_2 = 0.48 V_0 + 0.87$$

The growth delay increased by 0.48 days for every  $1 \times 10^6 \mu\text{m}^3$  increase of  $V_0$  ( $p < 0.001$ ). The  $R^2$  value was 60%, indicating that 60% of the variability of  $\tau_2$  was explained by the variability of  $V_0$  ( $n = 40$ ) (Figure 51c). Similarly, according to the doubling time data displayed in Figure 51d, DT values can be defined as follows:

$$DT = 0.26 V_0 + 2.17$$

The growth rate increased by 0.26 days for every  $1 \times 10^6 \mu\text{m}^3$  increase of  $V_0$  ( $p < 0.001$ ). The  $R^2$  value was 51%, indicating that 51% of the variability of DT was explained by the variability of  $V_0$  ( $n = 40$ ) (Figure 51d). Finally, according to the area under the curve data displayed in Figure 51e,  $AUC_{\log}$  values can be defined as follows:

$$AUC_{\log} = -0.33 V_0 + 3.99$$

The area under the  $\log V/V_0$  versus time curve decreased by 0.33 AU (AU = time \* volume) for every  $1 \times 10^6 \mu\text{m}^3$  increase of  $V_0$  ( $p < 0.001$ ). The  $R^2$  value was 40%, indicating that 40% of the variability of  $AUC_{\log}$  was explained by the variability of  $V_0$  ( $n = 35$ ) (Figure 51e).

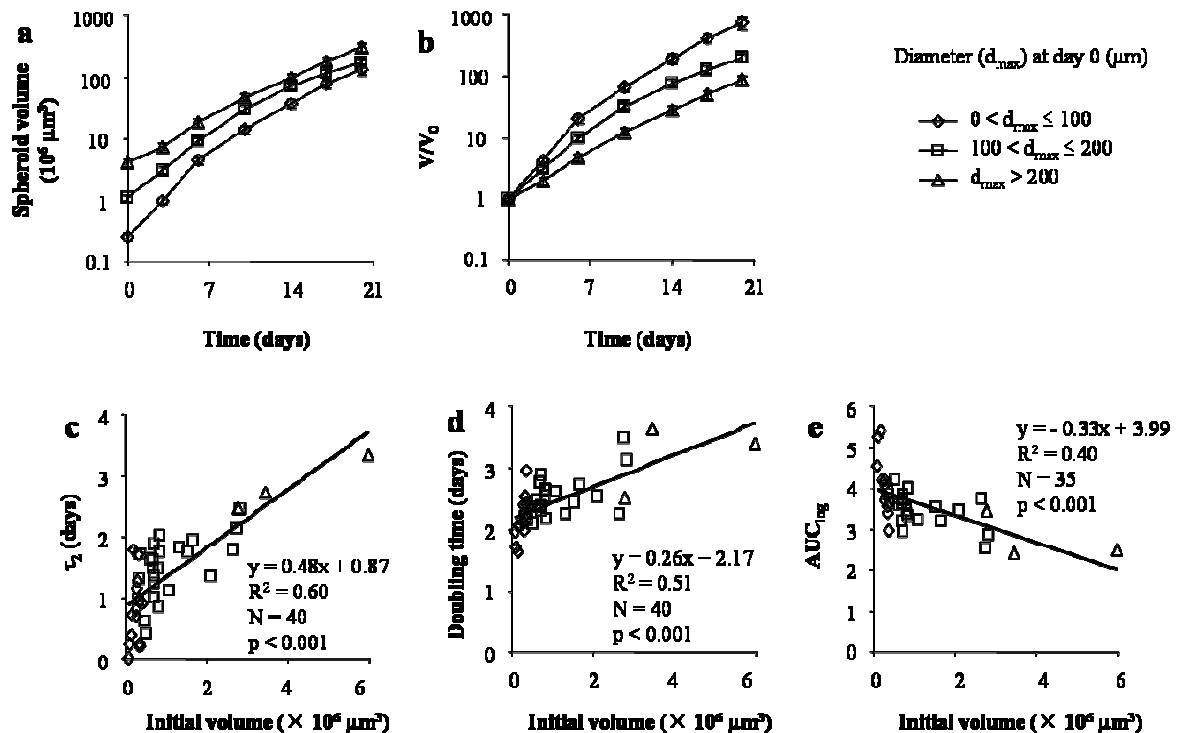


**Figure 51** The effect of the initial volume ( $V_0$ ) on the growth rate UVW/NAT spheroids.

Spheroids were sorted according to their initial diameter  $d_{\max}$  at day 0. Spheroid volumes are plotted in order to demonstrate the difference between the initial volumes (a). The  $V/V_0$  values are plotted to demonstrate the inverse correlation between initial volume and growth rate (b).  $\tau_2$  values are plotted against initial volume (c). DT values are plotted against initial volume (d).  $AUC_{\log}$  values are plotted against initial volume (e). The correlation between  $\tau_2$ , DT,  $AUC_{\log}$  and the initial volume was statistically evaluated using SPSS; the regression equation, the coefficient of determination  $R^2$ , the number of spheroid  $N$  and the  $p$ -value are given for each parameter.

These data demonstrate the statistically significant correlation between the three parameters  $\tau_2$ , DT and  $AUC_{\log}$  and the initial volume of LNCaP, SK-N-BE(2c) and UVW/NAT spheroids. Based on these results, all subsequent growth delay experiments have been carried out with spheroids of similar initial sizes in order to minimise the variation of the growth rate due to variation in initial size.

#### **6.4.3 Determination of the dose-response relationship using the spheroid model**

Our goal is to evaluate the radiosensitising potential of a drug in combination with targeted radiotherapy. For this purpose, spheroid growth curves must be analysed to determine the dose-response relationship. Furthermore, the dose-response relationship must conform to the median effect principle in order to calculate a combination index for the determination of supra- or infra-additive kill.

In order to transform spheroid growth delay data into a dose-response relationship, the growth curve of a particular treatment must be reduced to a single value, which would represent the measure of the effect of a particular treatment. Several parameters have been described previously:  $\tau_2$ , DT,  $AUC_{\log}$  and  $AUC_{\text{linear}}$ . Alternatively, the  $V/V_0$  value at a particular timepoint could be used as a measure of the effect of a treatment.

The median effect principle requires the surviving fraction to decrease with increasing doses. Thus,  $\tau_2$  and DT values, which both increase with increasing treatment dose, are not suitable for the application of the median effect principle. On the other hand, the  $AUC_{\log}$ ,  $AUC_{\text{linear}}$  or the  $V/V_0$  values at a particular timepoint decrease with increasing doses. Thus these three parameters were considered for the application of the median effect principle.

An example will be used for the determination of the best parameter for the application of the median effect principle (Figure 52). The effect of various concentrations of the radiopharmaceutical [ $^{131}\text{I}$ ]MIP-1095 on the growth of LNCaP spheroids is shown on a linear scale (Figure 52a) and on a log scale (Figure 52b). The effect of a drug may be defined as the fractional reduction of the spheroid volume compared with that of the control, i.e. the affected fraction. The unaffected fraction, or surviving fraction, is given by 1 minus this effect. The surviving fractions (1 minus the fractional reduction in  $V/V_0$ ) were calculated by dividing the  $V/V_0$  value after treatment by that of the untreated control at each timepoint. The resultant DSF:Cu dose-response relationship at each timepoint

demonstrated the variability of the surviving fractions among the timepoints (Figure 52c). The corresponding median effect plots are shown in Figure 52d. The median effect plots demonstrate the applicability of the median effect equation at 23 and 27 days, as indicated by the  $R^2$  values greater than 0.9 (Figure 52d). However, the variability of the  $IC_{50}$  values confirmed the unreliability of the arbitrary choice of a particular timepoint for the application of the median effect principle (Figure 52d).

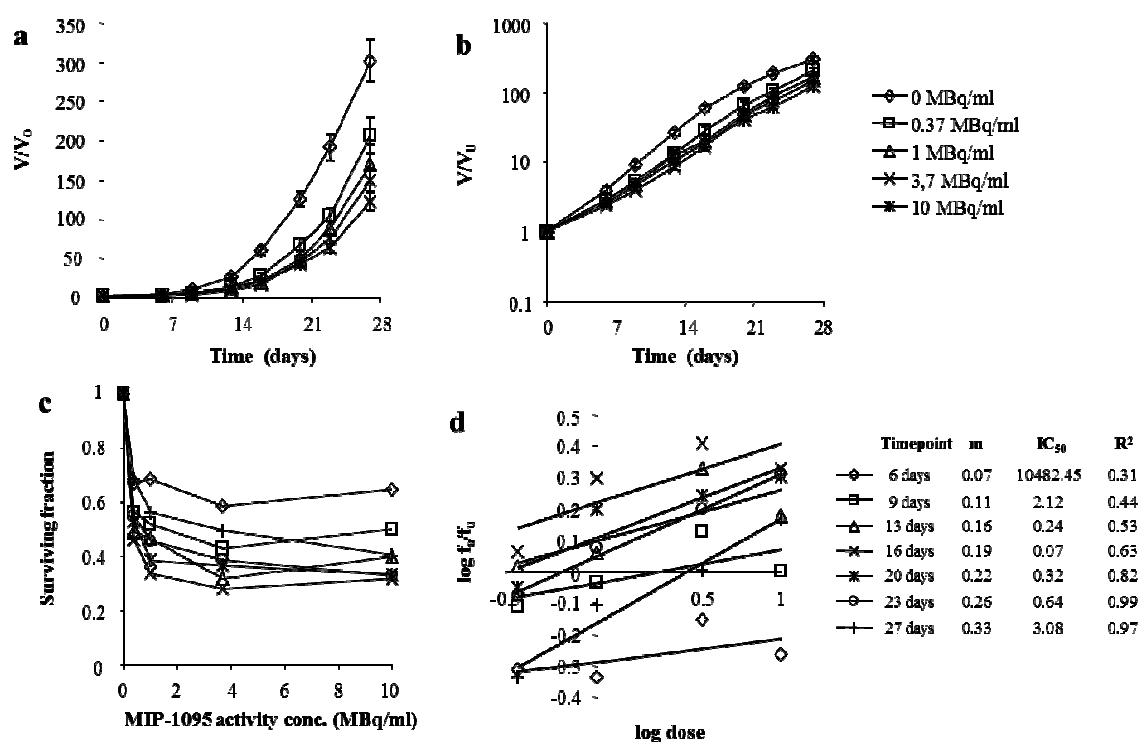


**Figure 52** The effect of the arbitrary choice of a timepoint on the variability of the surviving fractions. The effect of  $[^{131}\text{I}]\text{MIP-1095}$  on the growth of LNCaP spheroids is shown on a linear scale (a) or on a log scale (b). At each timepoint, the  $V/V_0$  value of the group treated with a particular  $[^{131}\text{I}]\text{MIP-1095}$  radioactivity concentration was divided by that of the untreated control in order to obtain a surviving fraction (c). The respective median effect plots were constructed using the data from panel (c) according to Section 3.3.5.

The area under the curve is the average of the  $V/V_0$  values of all timepoints multiplied by the time, i.e. the area under the curve is proportional to  $V/V_0$ . Thus, the definition of the surviving fraction at one timepoint (1 minus the fractional reduction of the  $V/V_0$  value as compared with that of the control) can be extrapolated to 1 minus the fractional reduction of the area under the curve compared with that of the untreated control.

The comparison of the use of  $AUC_{\text{linear}}$  with  $AUC_{\text{log}}$  was performed to determine whether the logarithmic transformation of the  $V/V_0$  values was needed for the application of the median effect principle (Figure 53). Since the surviving fraction was defined as “1 minus

the fractional reduction of the area under the  $V/V_0$  versus time curve” but not the area under the  $\log V/V_0$  versus time curve, it was anticipated that  $AUC_{\text{linear}}$ , but not  $AUC_{\text{log}}$ , would fit the median effect principle.

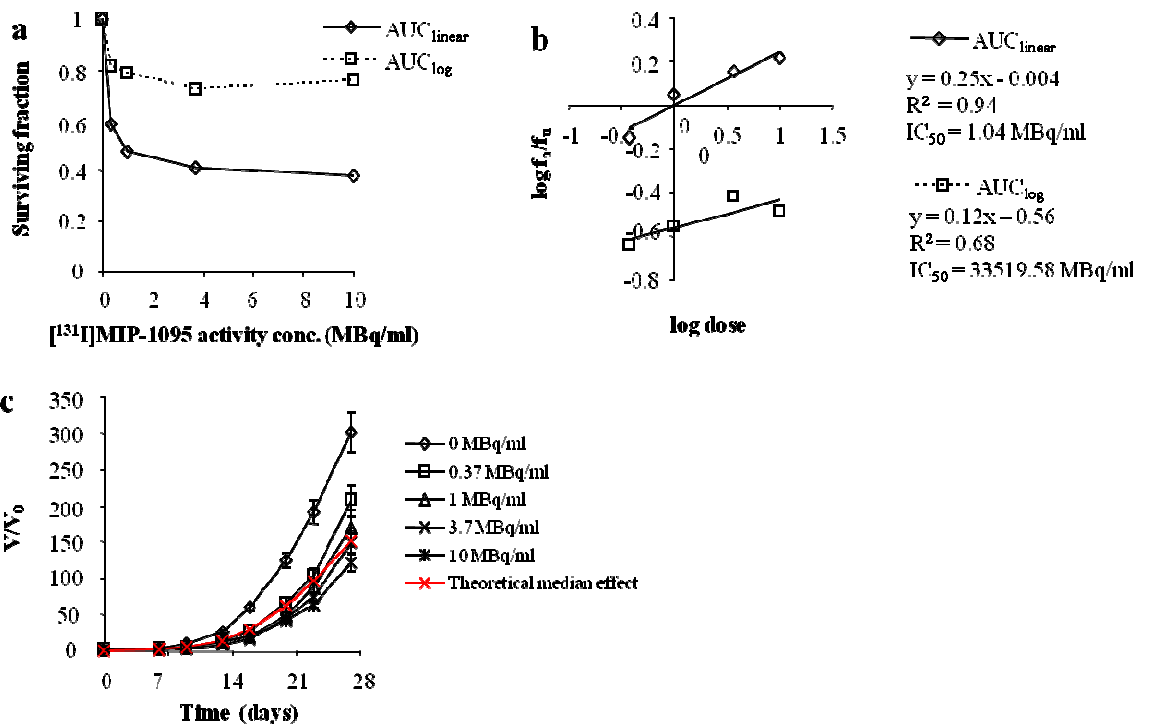


**Figure 53** The calculation of  $IC_{50}$  based on  $AUC_{\text{linear}}$  or  $AUC_{\text{log}}$  values

The surviving fractions were obtained by dividing the AUC values of the groups treated with a particular  $^{131}\text{I}$ MIP-1095 concentration by that of the control (a). The respective median effect plot was constructed according to Section 3.3.5 (b). The effect of  $^{131}\text{I}$ MIP-1095 on the growth of LNCaP spheroids is shown on a linear scale (c). The growth curve representing the theoretical median effect, i.e. obtained in response to treatment with the  $IC_{50}$  dose of  $^{131}\text{I}$ MIP-1095, was constructed by plotting the  $V/V_0$  values calculated as follows:  $V/V_{0\text{IC}50} = (V/V_{0\text{control}} - 1) / 2$ .

The  $AUC_{\text{linear}}$  and  $AUC_{\text{log}}$  values were divided by those of the control in order to obtain surviving fractions (Figure 53a). The surviving fractions calculated from  $AUC_{\text{linear}}$  values, but not those calculated from the  $AUC_{\text{log}}$  values, fitted the median effect equation as indicated by  $R^2$  values of 0.94 and 0.68, respectively (Figure 53b). The  $AUC_{\text{linear}}$  values returned an  $IC_{50}$  of 1.04 MBq/ml  $^{131}\text{I}$ MIP-1095 whereas  $AUC_{\text{log}}$  returned an  $IC_{50}$  of 33519.58 MBq/ml, demonstrating a discrepancy between the two modes of analysis (Figure 53b).

The maximal effect of a treatment results in a flat line in a spheroid growth delay experiment, i.e. the spheroids are sterilised hence fail to grow. The  $IC_{50}$  dose of the effect of  $^{131}\text{I}$ MIP-1095 should be equivalent to a concentration that induces half the maximal

effect, i.e. the growth curve resulting from such an effect should be equidistant between the growth curve of the untreated control and that of the maximal effect. Sterilisation is manifest by a growth curve defined by  $V/V_0$  values of 1. Therefore, the theoretical growth curve obtained in response to treatment with the  $IC_{50}$  dose of [ $^{131}$ I]MIP-1095 can be obtained by plotting the volumes at each timepoint according to:

$$V/V_{0\ IC_{50}} = (V/V_{0\ control} - 1) / 2 \quad (20)$$

The growth curve of the theoretical median effect is shown in Figure 53c. It plotted between the growth curves resulting from treatment with 0.37 and 1 MBq/ml [ $^{131}$ I]MIP-1095, indicating an  $IC_{50}$  value situated within this range (Figure 53c). Since the  $IC_{50}$  concentration calculated using the  $AUC_{linear}$  values was 1.04 MBq/ml, it was concluded that the  $AUC_{linear}$  values were more suited than  $AUC_{log}$  values for the application of the median effect principle. This observation was made in several other experiments not reported here.

#### 6.4.4 The influence of spheroid size on DSF:Cu cytotoxicity

It has previously been shown that the size of spheroids as well as the presence of a non-dividing and hypoxic population within spheroids influenced the response to drug treatment<sup>258</sup>. Therefore, the effect of spheroid size on the cytotoxicity of DSF:Cu was investigated (Figure 54). Non-hypoxic spheroids (average of 111  $\mu$ m in diameter) were exposed to various concentrations of DSF:Cu. A concentration-effect relationship was observed for the growth delay but not for the doubling time. The  $\tau_2$  values were  $3.66 \pm 0.45$ ,  $4.21 \pm 0.48$ ,  $6.43 \pm 1.28$  ( $p < 0.05$ ) and  $11.95 \pm 1.55$  ( $p < 0.001$ ) days for the untreated controls, 1  $\mu$ M, 3.37  $\mu$ M and 10  $\mu$ M DSF:Cu respectively. LNCaP spheroids were sterilised after exposure to 33.7  $\mu$ M as indicated by the sub-zero  $AUC_{log}$  value ( $p < 0.001$ ) (Figure 54a and Table 8a). Interestingly, the DT values did not significantly increase with DSF:Cu concentrations up to 10  $\mu$ M (Table 8a). This indicated that DSF:Cu killed a sub-population of cells within the spheroid, the affected fraction, whereas the unaffected fraction was responsible for the subsequent growth at the same rate as the untreated controls (Table 8a).

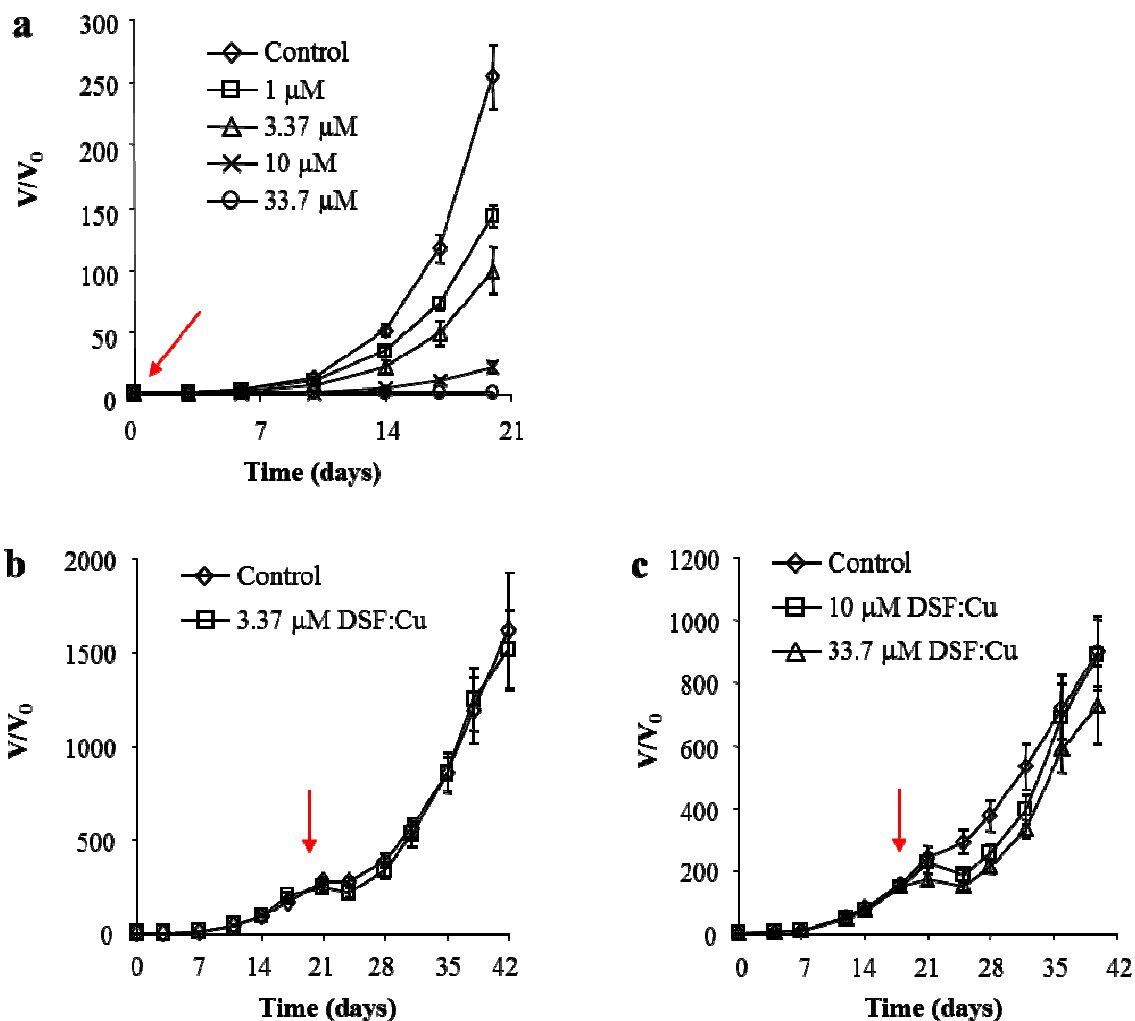


**Figure 54 The effect of spheroid size on DSF:Cu-induced growth delay**

LNCaP spheroids, with an average diameter of 111  $\mu\text{m}$  ( $0.57 \times 10^6 \mu\text{m}^3$ ), and lacking a hypoxic core were exposed to a range of equimolar concentrations of disulfiram and copper (DSF:Cu) for 24 h (a). The first image at day 0 was obtained at the end of the exposure period. LNCaP spheroids were allowed to grow for 20 days in order to form a hypoxic core and an outer proliferative layer. At day 20, LNCaP spheroids - on average 692  $\mu\text{m}$  in diameter ( $V = 136.68 \times 10^6 \mu\text{m}^3$ ) - were exposed to 3.37  $\mu\text{M}$  DSF:Cu for 24 h. Images were captured immediately after treatment at day 21 (b). Alternatively, at day 20, LNCaP spheroids - on average 652  $\mu\text{m}$  in diameter ( $V = 121.37 \times 10^6 \mu\text{m}^3$ ) - were exposed to 10 or 33.7  $\mu\text{M}$  DSF:Cu for 24 h. Images were captured immediately after treatment at day 21 (c). Data points are mean  $\pm$  SEM.

LNCaP spheroids were treated with 3.37, 10 or 33.7  $\mu\text{M}$  DSF:Cu 21 days after initiation. At this timepoint, spheroids were on average 652  $\mu\text{m}$  in diameter and displayed an organised internal morphology defined by an apoptotic and hypoxic core and a proliferative outer layer (Figure 46). The three parameters  $\tau_2$ , DT and  $\text{AUC}_{\log}$  were not significantly different from the untreated controls when hypoxic spheroids were treated with 3.37, 10 or 33.7  $\mu\text{M}$  DSF:Cu (Figure 54b and Figure 54c, Table 8b and Table 8c). Therefore, the hypoxic status, the proliferation status of the cells within the spheroid, the

acidic pH in the core of the spheroid and/or penetration within the spheroid may influence DSF:Cu cytotoxicity.

<b>a</b>	$\tau_2$	<b>DT</b>	<b>AUC<sub>log</sub></b>
<b>Control</b>	3.66 ± 0.45	2.34 ± 0.26	22.37 ± 2.55
<b>1 <math>\mu</math>M</b>	4.21 ± 0.48	2.53 ± 0.15	19.83 ± 1.33**
<b>3.37 <math>\mu</math>M</b>	6.43 ± 1.28*	2.44 ± 0.32	12.93 ± 2.27***
<b>10 <math>\mu</math>M</b>	11.95 ± 1.55***	2.19 ± 0.26	3.14 ± 0.85***
<b>33.7 <math>\mu</math>M</b>	N/A	N/A	-1.97 ± 0.43***

<b>b</b>	$\tau_2$	<b>DT</b>	<b>AUC<sub>log</sub></b>
<b>Control</b>	10.16 ± 1.60	7.62 ± 1.17	6.82 ± 1.14
<b>3.37 <math>\mu</math>M DSF:Cu</b>	9.30 ± 0.82	6.75 ± 0.60	5.29 ± 1.96

<b>c</b>	$\tau_2$	<b>DT</b>	<b>AUC<sub>log</sub></b>
<b>Control</b>	10.74 ± 0.99	10.04 ± 0.87	5.22 ± 0.49
<b>10 <math>\mu</math>M DSF:Cu</b>	12.65 ± 1.76	9.50 ± 1.34	4.35 ± 0.69
<b>33.7 <math>\mu</math>M DSF:Cu</b>	11.82 ± 0.56	9.04 ± 0.54	4.50 ± 0.59

**Table 8** The  $\tau_2$ , DT and AUC<sub>log</sub> values of the effect of spheroid size on the DSF:Cu-induced spheroid growth delay

$\tau_2$ , DT and AUC<sub>log</sub> values were calculated according to Section 6.3.4 and 6.3.5. Data are means ± SEM.

#### 6.4.5 The effect of confluency on DSF:Cu cytotoxicity

Day 21 LNCaP spheroids, on average 652  $\mu$ m in diameter, are more resistant to DSF:Cu treatment than day 0 LNCaP spheroids, on average 111  $\mu$ m in diameter (Figure 54, Table 8). The size-dependent resistance of LNCaP spheroids to DSF:Cu treatment may be due to inefficient penetration by DSF:Cu or to changes associated with the increase in spheroid size, namely acidic pH, hypoxia and reduction of the proliferating rate. It was first hypothesised that the resistance to DSF:Cu treatments encountered in day 21 spheroids was due to the presence of a non-dividing population of cells.

The growth rate of monolayers attached to a plastic surface decreases to 0-10% of the maximal growth rate once confluence has been attained<sup>275</sup>. The resulting plateau phase is a state defined as a balance between cell growth and cell death. Thereafter, late plateau-phase cells are defined as a non-dividing population of cells without cell loss<sup>276</sup>. At

confluence, density limitation is a signal for cessation or reduction of proliferation. In non-perfused cell cultures, the lack of nutrients, the accumulation of harmful waste and the acidification of the culture medium also cause cessation or reduction of the growth fraction<sup>275</sup>. Cellular monolayers in the plateau phase of their growth have been used as an *in vitro* model for the investigation of the effect of chemotherapeutic drugs in conditions found in the core of tumours, but without the penetration problems encountered in 3-D aggregates such as spheroids<sup>277,278</sup>. LNCaP cells in the plateau phase of their growth are used to determine whether proliferating status influences DSF:Cu cytotoxicity.

The MTT assay was used to assess the viability of LNCaP cells in various phases of growth. LNCaP cells seeded at 2,500 cells/cm<sup>2</sup> grew at a constant rate over 10 days, as indicated by the increase in A<sub>570</sub> (Figure 55a). In contrast, LNCaP cells seeded at 6,500 or 13,000 cells/cm<sup>2</sup> attained maximal formazan formation at day 7 and day 5 after seeding, respectively (Figure 55a). The maximal A<sub>570</sub> value was 0.85, which was indicative of a plateau phase rather than the upper detection limit of formazan. Indeed, formazan absorbance increased linearly with cell number up to an A<sub>570</sub> value of 1.2 (Figure 55b). Furthermore, daily microscopic examination of the monolayers confirmed that cell numbers increased until the cultures became confluent.

Three days after initiating LNCaP monolayers, the cells seeded at 2,500, 6,500 or 13,000 cells/cm<sup>2</sup> started to proliferate (Figure 55a). Treatment of the cultures at this time point with 1 µM DSF:Cu significantly reduced the viability of LNCaP cells by 80-95% regardless of the number of cells seeded (Figure 55c). At day 5, LNCaP cells seeded at 2,500 or 6,500 cells/cm<sup>2</sup> were proliferating and 1 µM DSF:Cu significantly reduced their viability by 80-95% (Figure 55d). In contrast, LNCaP cells seeded at 13,000 cells/cm<sup>2</sup> reached the plateau phase at day 5. In this case, the viability was reduced by only 30% following treatment with 1 µM DSF:Cu (Figure 55d). This indicated that DSF:Cu was more toxic to proliferating cells. At day 7, LNCaP cells seeded at 2,500 cells/cm<sup>2</sup> were proliferating, whereas those seeded at 6,500 or 13,000 cells/cm<sup>2</sup> reached the plateau phase (Figure 55a). At this timepoint, treatment with 1 µM DSF:Cu reduced the viability of LNCaP cells by 20-40%, regardless of the proliferative status of the cells (Figure 55e). This indicated that the proliferating state of LNCaP cells was not the sole determinant of DSF:Cu cytotoxicity since LNCaP cells seeded at 2,500 cells/cm<sup>2</sup> were proliferating at day 7 but those seeded at 6,500 and 13,000 cells/cm<sup>2</sup> were not (Figure 55a). The culture medium of LNCaP cells was deliberately not replaced by fresh medium over the course of

the experiment in order to recreate the accumulation of harmful waste and the acidification of the culture medium encountered in the core of hypoxic spheroids or in non-vascularised regions of tumours. Therefore, it was hypothesised that acidification of the culture medium could also be a determinant responsible for the loss of sensitivity to DSF:Cu treatments encountered after 7 days in culture (Figure 55e).

Most cells grow well at pH 7.4, though some cell types have shown preferences for pH in the range 5.5 – 7.7<sup>275</sup>. In an investigation of the effect of pH (range 6 to 7.2) on the cytotoxicity of 1-(2-chloroethyl)3-cyclohexyl-1-nitrosourea (CCNU), it has been observed that pH 6 reduced the plating efficiency of mouse mammary cells EMT6 by 70%<sup>278</sup>. The pH of the culture medium used for LNCaP cells is 7.2. Hydrochloric acid was added until pH 6.0 was reached. Alternatively, sodium hydroxide was added until pH 8.1 was obtained. Firstly, LNCaP cells seeded at 2,500, 6,500 or 13,000 cells/cm<sup>2</sup> were exposed to culture media at pH 6.0, 7.2 or 8.1 and the viability was measured (Figure 56a). Secondly, LNCaP cells seeded at 2,500, 6,500 or 13,000 cells/cm<sup>2</sup> were used for the investigation of the effect of pH on DSF:Cu cytotoxicity (Figure 56b, Figure 56c and Figure 56d). Exposure to DSF:Cu was carried out 5 days after seeding so that the results were comparable to those presented in Figure 56d.

The decrease of pH from 7.2 to 6.0 reduced the viability of LNCaP cells seeded at 2,500, 6,500 or 13,000 cells/cm<sup>2</sup> by 75% ( $p < 0.001$ ), 60% ( $p < 0.001$ ) or 40% ( $p < 0.01$ ), respectively (Figure 56a). There was a statistically significant correlation between increasing cell density and decreased toxicity at pH 6.0 ( $r = 0.97$ ,  $p < 0.001$ ), indicating that increasing seeding density conferred upon LNCaP monolayers resistance to acidic pH. After 5 days in culture, LNCaP cells seeded at 2,500 or 6,500 cells/cm<sup>2</sup> were proliferating whereas those seeded at 13,000 cells/cm<sup>2</sup> were in plateau phase (Figure 55a). Thus, it could be hypothesised that a slower proliferating rate conferred upon LNCaP cells resistance to acidic pH.

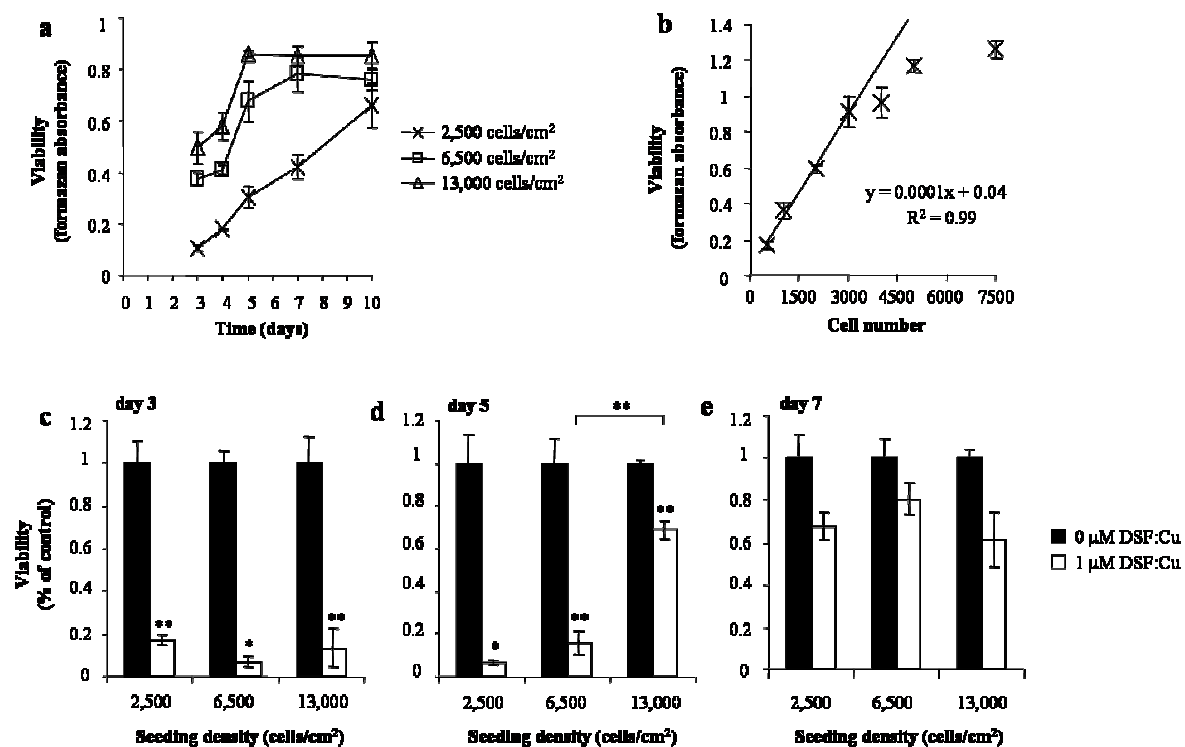


**Figure 55** The effect of confluency on DSF:Cu-induced toxicity to LNCaP cell monolayers

(a) LNCaP cells were seeded in 96-well plates at 2,500, 6,500 or 13,000 cells/cm<sup>2</sup>. The viability of untreated LNCaP cells was assessed by formazan absorbance (at 570 nm) measurements 3, 4, 5, 7 and 10 days after seeding. The culture medium was not replaced by fresh culture medium at any time throughout the course of the experiment. (b) The relationship between cell number and formazan absorbance was assessed. Regression analysis was applied to the linear part of the curve (up to 3,000 cells) using the method of least squares. The equation of the linear regression and the coefficient of determination ( $R^2$ ) are reported. (c, d and e) The viability of LNCaP cells seeded at 2,500, 6,500 or 13,000 cells/cm<sup>2</sup> following treatment with 1 μM DSF:Cu was assessed by formazan absorbance measurements 3, 5 and 7 days after seeding. The  $A_{570}$  values of DSF:Cu-treated groups were normalised to the mean absorbance value of the untreated groups for each seeding density. Data are mean  $\pm$  SEM; n=3. The independent sample t-test was used to compare the mean formazan absorbance values of the DSF:Cu treated groups with that of their respective controls at every seeding density. One symbol indicates  $p < 0.05$  and two symbols indicate  $p < 0.01$ .

Secondly, the increase of pH from 7.2 to 8.1 reduced the viability of LNCaP cells seeded at 2,500 and 6,500 cells/cm<sup>2</sup> by 50% ( $p < 0.01$ ) and 40% ( $p < 0.01$ ), respectively, whereas LNCaP cells seeded at 13,000 cells/cm<sup>2</sup> were not affected by an alkaline pH (Figure 56a). There was a statistically significant correlation between increasing cell density and decreased toxicity at pH 8.1 ( $r = 0.88$ ,  $p = 0.002$ ), indicating that increasing seeding density conferred upon LNCaP monolayers resistance to alkaline pH. These results indicated that pH variation within the range 6.0 - 8.1 reduced the viability of LNCaP cells and that an acidic culture medium was more cytotoxic than an alkaline one. Furthermore, it was suggested that increased seeding density or a decreased growth rate conferred upon LNCaP cells resistance to pH variation within the range 6.0 - 8.1.

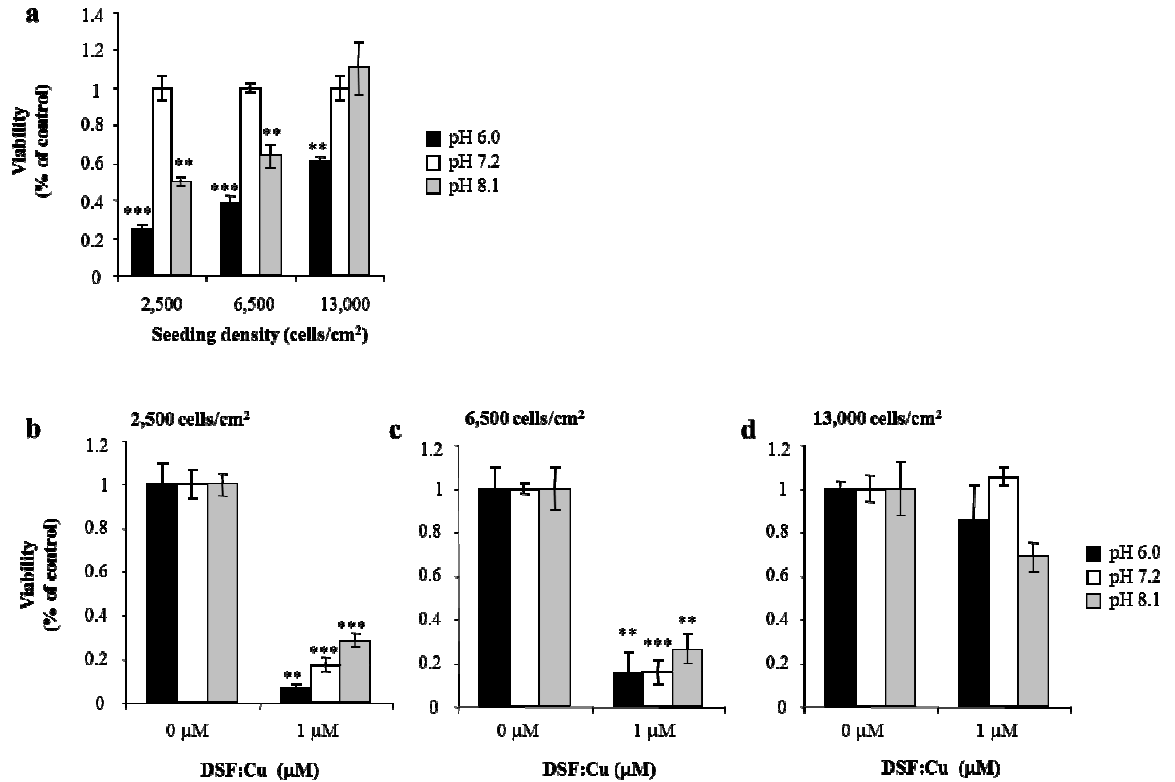


**Figure 56 The effect of pH on DSF:Cu cytotoxicity in LNCaP monolayers**

LNCaP cells were seeded in 96-well plates at 2,500, 6,500 or 13,000 cells/cm<sup>2</sup>. The viability of LNCaP cells was assessed by formazan absorbance measurements 5 days after seeding. The pH of the culture medium was adjusted to 6.0 by incremental additions of hydrochloric acid or to 8.1 by incremental addition of sodium hydroxide. (a) The effect of pH on untreated LNCaP cells was assessed by formazan absorbance measurements. Data are mean  $\pm$  SEM; n=3. (b, c and d) The effect of pH on the viability of LNCaP cells seeded at 2,500, 6,500 and 13,000 cells/cm<sup>2</sup> following treatment with 1  $\mu$ M DSF:Cu was assessed by formazan absorbance measurements 5 days after seeding. For every pH and seeding density, the mean formazan absorbance value of the DSF:Cu-treated groups were normalised to the mean absorbance value of the untreated control. Data are mean  $\pm$  SEM; n=3. For every pH and seeding density condition, the independent sample t-test was used to compare the mean formazan absorbance value of the DSF:Cu-treated groups with that of the untreated control. Two symbols indicate  $p < 0.01$  and three symbols indicate  $p < 0.001$ .

Next, the effect of pH variation within the range 6.0 - 8.1 on DSF:Cu cytotoxicity was studied in LNCaP cells seeded at 2,500, 6,500 or 13,000 cells/cm<sup>2</sup>. The viability of LNCaP cells seeded at 2,500 cells/cm<sup>2</sup> was significantly reduced by 90% ( $p < 0.01$ ), 80% ( $p < 0.001$ ) or 70% ( $p < 0.001$ ) after treatment with 1  $\mu$ M DSF:Cu at pH 6.0, 7.2 or 8.1, respectively (Figure 56b). There was no significant difference in the cytotoxicity of DSF:Cu resulting from altered pH ( $p > 0.05$ ). Secondly, the viability of LNCaP cells seeded at 6,500 cells/cm<sup>2</sup> was significantly reduced by 85% ( $p < 0.01$ ), 85% ( $p < 0.001$ ) or 75% ( $p < 0.01$ ) after treatment with 1  $\mu$ M DSF:Cu at pH 6.0, 7.2 or 8.1, respectively

(Figure 56c). Again, there was no significant difference in the cytotoxicity of DSF:Cu resulting from altered pH ( $p > 0.05$ ). Finally, although statistical significance was not reached, the viability of LNCaP cells seeded at 13,000 cells/cm<sup>2</sup> was reduced by 15% or 30% after treatment with 1  $\mu$ M DSF:Cu at pH 6.0 or 8.1, respectively (Figure 56d). These results indicated that DSF:Cu cytotoxicity was not dependent on the pH of the culture medium.

These results suggest that DSF:Cu is more efficient at killing cells within small spheroids which have not developed an organised internal morphology (Figure 54, Table 8). Studies using plateau phase cells have indicated that non-dividing cells or cells dividing at a slower rate than those in the proliferating phase were more resistant to DSF:Cu treatments (Figure 55). Since plateau phase cells did not receive fresh medium in the course of these experiments, it was possible that the accumulation of harmful waste, such as lactic acid, which also causes acidification of the culture medium, conferred upon LNCaP cells resistance to DSF:Cu treatments. However, pH variations within the range 6.0 to 8.1 did not affect DSF:Cu cytotoxicity. This suggested that the proliferating state of the cells but not the pH of the culture medium affected DSF:Cu cytotoxicity. That is, fast growing cells are more sensitive to DSF:Cu treatment than slow-growing cells.

The effect of the hypoxic status on DSF:Cu cytotoxicity and the capacity of DSF:Cu to penetrate large spheroids are discussed in Section 6.5.

## **6.5 Discussion/summary of the results**

Firstly, this chapter was concerned with the characterisation of the cellular aggregates obtained after seeding single cells onto agar-coated surfaces with respect to their morphology at a juvenile and at a more advanced stage of their growth. It has long been known that these cellular aggregates differentiate from a homogeneous to a heterogeneous mass of cells comprising a hypoxic and apoptotic core surrounded by a layer of proliferating cells<sup>254</sup>. These are called spheroids. The finding that these morphological changes occurred with increasing size (Table 9) demonstrated that the small cellular aggregates were indeed spheroids, the cell culture tool previously described as an *in vitro* model of avascular micrometastases<sup>265-268</sup>.

	Marker	Staining	
		Inner core	Outer layer
Day 0 spheroids (100-150 µm in diameter)	Ki67 (proliferation)	yes	
	Pimonidazole adducts (hypoxia)	yes	
Day 21 spheroids (500-600 µm in diameter)	Ki67 (proliferation)	no	yes
	Pimonidazole adducts (hypoxia)	yes	no
	pCASP3 (apoptosis)	yes	no

**Table 9 Summary of the metabolic characteristics of spheroids at day 0 and at day 21**

Spheroid initiation involves the seeding of single cells onto an agar-coated surface. The doubling time of LNCaP cells *in vitro* is approximately 60 h<sup>279</sup>, thus the clonal expansion from a single cell could only form an aggregate comprising between 2 and 4 cells after the initiation period which lasted 3 to 4 days. Therefore, it is likely that the majority of the spheroids were formed by aggregation rather than by clonal expansion.

In conditions designed to keep constant the nutrient and oxygen concentrations in the culture medium, the depth to which each molecule of the culture medium can penetrate into the spheroid is dependent on its physico-chemical properties such as lipophilicity and the molecular weight<sup>280</sup>. The result is the formation of gradients of pH, oxygen and nutrients within spheroids<sup>254</sup>. As the spheroids grow, the oxygen, nutrients and pH gradients are responsible for the increase in acidity and the decrease in concentrations of oxygen and nutrients at the deepest locations within the spheroid. Thus, a layer forms at the surface of the spheroid within which the pH and the concentrations of oxygen and nutrients are suitable to sustain cellular growth (Figure 46, Figure 47 and Figure 48). The depth of this layer is directly dependent on the concentration of nutrients and oxygen in the culture medium but also on their penetrability. It follows that, in conditions designed to keep constant the nutrient and oxygen concentrations in the culture medium, the depth of the layer capable of sustaining cellular proliferation remains constant. Therefore, the relative proportion of proliferative cells within the whole of the spheroid decreases as the spheroid grows in size, leading to an apparent decreasing growth rate. This phenomenon was particularly prominent in SK-N-BE(2c) (Figure 50) and UVW/NAT spheroids (Figure 51). It also explains why bigger spheroids grow more slowly than smaller spheroids (Figure 49, Figure 50 and Figure 51).

The demonstration that DSF:Cu was more cytotoxic in day 0 spheroids (100-150  $\mu\text{m}$  in diameter) than in day 21 spheroids (500-600  $\mu\text{m}$  in diameter) may be due to penetration issues, the presence of hypoxic region, the presence of a non-dividing population of cells or the presence of a region with acidic pH. It is improbable that resistance of LNCaP spheroids to DSF:Cu treatment (Figure 54, Table 8) was due to a poor penetrability because of the very small size (360 g/mol) and the lipophilic character of the DSF:Cu complex. Furthermore, it was previously demonstrated in Section 3.4.3 of this thesis that DSF:Cu entered the intracellular space without the assistance of a permeabilising agent (Figure 14). Therefore it was more likely that the oxygen status, the pH or the proliferative status of the cells within day 21 spheroids influenced DSF:Cu cytotoxicity. The effect of hypoxia on DSF:Cu cytotoxicity was assessed in monolayers but the results were inconclusive and not reported in this thesis. Indeed, as a positive control, monolayers were irradiated in hypoxic conditions and the clonogenic kill compared with that of cells irradiated in normoxic conditions. There was no prevention of the clonogenic kill in hypoxia compared with normoxia. The results of this experiment were not conclusive since hypoxic conditions were not achieved.

The use of plateau phase monolayers suggested that DSF:Cu was more cytotoxic to fast-growing cells compared with slow-growing cells or quiescent cells (Figure 55). The response to DSF:Cu treatment of plateau phase cells indicated that the pH did not affect the cytotoxicity of DSF:Cu (Figure 56). The demonstration of the increased DSF:Cu cytotoxicity in proliferating compared with non-proliferating LNCaP cells suggested that a quiescent sub-population of cells within day 21 spheroids which had undergone morphological reorganisation resisted DSF:Cu treatment and was able to recover and grow at a rate similar to that of untreated controls (Figure 54). Evidence of such a sub-population was found in UVW/NAT spheroids (Figure 48), but was not as obvious in LNCaP (Figure 46) or SK-N-BE(2c) spheroids (Figure 47). Indeed, within UVW/NAT spheroids, there was a hypoxic ring of cells deemed viable by H&E staining yet not proliferating as indicated by the absence of Ki-67 staining (Figure 48). These results suggested that, in patients, DSF:Cu may be more cytotoxic to proliferating tumour cells than to non-proliferating healthy tissues.

The resistance to DSF:Cu treatment of day 21 spheroids which have undergone internal morphological changes has implications for the optimal application of this compound for

the treatment of cancer. It suggested that DSF:Cu should be especially effective for the elimination of undetectable, micrometastatic malignant deposits which have not developed oxidic heterogeneity. It is unlikely that DSF:Cu as a single agent treatment will eliminate larger metastases which have undergone internal morphological changes since a concentration of more than 33.7  $\mu\text{M}$  would be required (Figure 54). This concentration is 100 times greater than the peak plasma concentration of DSF resulting from the administration of a 250 mg oral dose<sup>161</sup>.

The assessment of the interaction between the agents of a combination treatment (additive, supra- or infra-additive) requires the use of the combination index or the isobologram method of synergy analysis. Synergy analysis is based on the median effect principle which mathematically relates the surviving fraction to the dose. In order to apply such an analysis to a spheroid growth delay experiment, the growth curves must be converted into a single parameter describing the effect of the treatment in terms of a surviving fraction. The results of this chapter showed that  $\text{AUC}_{\text{linear}}$  values were amenable to the calculation of a surviving fraction. The surviving fraction after a particular treatment was defined as 1 minus the fractional reduction of the  $\text{AUC}_{\text{linear}}$  value compared with that of the control. This analytical method will be used in chapter 5 for the assessment of the effect of the combination of DSF:Cu with  $\gamma$ -radiation or with radiopharmaceuticals in spheroids which have not yet undergone internal morphological changes.

## 7 The enhancement of the effect of radiopharmaceuticals by DSF:Cu

### 7.1 Introduction

Targeted radiotherapy was introduced in Section 1.1.3. Targeted radiotherapy uses tumour-seeking radiopharmaceuticals for the systemic delivery of radiation specifically to malignant lesions while limiting the toxicity to normal tissues. It has been used successfully for the palliation of bone metastases (Section 1.1.4.2) and is a curative treatment of thyroid carcinoma (Section 1.1.4.1)<sup>281,282</sup>. However, the treatment of other diseases such as neuroblastoma by targeted radiotherapy as a single modality is limited by haematological toxicity and cure rates remain low (Section 1.1.4).

The results of Section 4.4.3 demonstrated the synergistic interaction between DSF:Cu and  $\gamma$ -radiation treatments which resulted in radiosensitisation. Thus, the putative synergistic interaction between radiopharmaceuticals and DSF:Cu could increase the tumouricidal effect of targeted radiotherapy, and improve patient outcome, without increasing radiation doses to levels detrimental to the patient. Furthermore, since a radiation dose is delivered specifically to the malignant lesions, the putative synergistic effect would only occur in the tumour while sparing normal tissue. The combination of DSF:Cu with targeted radiotherapy is not expected to result in a synergistic increase in normal tissue toxicity. The combination of DSF:Cu with radiopharmaceuticals will be investigated in order to determine whether a synergistic interaction similar to that of the combination with external beam radiotherapy occurs between DSF:Cu and radiopharmaceuticals.

The radiopharmaceuticals [<sup>131</sup>I]mIBG and [<sup>131</sup>I]MIP-1095 were described previously in Sections 1.1.4.5 and 1.1.4.6. Briefly, mIBG is a radiopharmaceutical taken up by cells expressing the noradrenaline transporter (NAT). [<sup>123</sup>I]mIBG has been successfully used for the imaging of neuroblastoma. Clinical trials investigating the therapeutic potential of [<sup>131</sup>I]mIBG have yielded overall response rates between 30% and 58%<sup>33-40</sup>. [<sup>131</sup>I]MIP-1095 has been developed to target PSMA<sup>65</sup>, which is overexpressed in malignant metastatic PCa<sup>60</sup>. CRPC is associated with a poor prognosis despite intensive hormonal and chemotherapeutic treatments. The median survival of patients with metastatic CRPC is 1 to 2 years<sup>50-52</sup>. Thus alternative strategies need to be developed to improve the outcome of this subset of patients.

### 7.1.1 Study model

The enhancement of the radiation kill was defined as the rightward and/or downward displacement of the spheroid growth curve obtained by combination treatment compared with that achieved by radiation treatment alone.  $\tau_2$ , DT and  $AUC_{\log}$  were used to quantify potentiation of radiation kill.

The study of the combination of DSF:Cu with [ $^{131}\text{I}$ ]mIBG was carried out in spheroids derived from the neuroblastoma cell line SK-N-BE(2c), which endogenously expresses NAT, and in spheroids derived from the NAT-transfected glioma cell line UVW/NAT. The evaluation of the combination of DSF:Cu and [ $^{131}\text{I}$ ]MIP-1095 was performed in spheroids derived from the prostate carcinoma cell line LNCaP, which expresses the target PSMA. LNCaP cells do not form colonies so that the analysis of the combination of DSF:Cu with  $\gamma$ -radiation using the clonogenic assay could not be performed in chapter 4. Therefore, the evaluation of the effect of DSF:Cu in combination with  $\gamma$ -radiation in LNCaP cells was conducted using spheroids.

The term “radiosensitisation” will not be used to refer to the enhancement of the cytotoxic effect of radiopharmaceuticals for the following reason. A “true radiosensitiser” was defined previously as “[...] a chemical which increases the cell-killing effect of a given dose of radiation. This is achieved either by increased formation of longer-lived toxic radiation-induced radicals or modification of vulnerable, critical targets in cells, or by interference with mechanisms of repair of sublethal radiation damage”<sup>82</sup>. In assessing the effect of a combination of a drug with a radiopharmaceutical in spheroids, the enhancement of the effect of the radiopharmaceutical may be due to the increase in its penetrability within tissues or to the increased binding to its target, the increased expression of transporter genes, as well as radiosensitising properties *per se*. Such effects on penetrability and/or binding of a radiopharmaceutical are independent of the enhancement of the kill due to the absorption of a radiation dose by a cell. Therefore, the term “radiosensitisation” will be replaced by enhancement or potentiation of the growth delay induced by radiopharmaceuticals.

## 7.2 Aims

- to evaluate the effect of DSF:Cu on the growth delay induced by  $\gamma$ -radiation in LNCaP spheroids

- to evaluate the effect of DSF:Cu on the growth delay induced by [<sup>131</sup>I]mIBG in SK-N-BE(2c) and UVW/NAT spheroids
- to evaluate the effect of DSF:Cu on the growth delay induced by [<sup>131</sup>I]MIP-1095 in LNCaP spheroids

### **7.3 Materials and methods**

#### **7.3.1 Spheroid initiation**

See Section 6.3.1.

#### **7.3.2 Spheroid treatments**

As a preliminary study, and in order to simplify analysis of treatment interaction with hypoxia, acidic pH and heterogeneous proliferation status, small spheroids, approximately 150 µm diameter, which had not yet undergone internal morphological changes were used to assess the toxicity of DSF :Cu in combination with radiopharmaceuticals. Such spheroids provide a 3-dimensionnal structure wherein cross-fire radiation from radiopharmaceutical-bound radionuclide will make a contribution to growth inhibition.

##### **7.3.2.1 DSF:Cu treatment**

See Section 6.3.2.

##### **7.3.2.2 γ-radiation treatment**

See Section 4.3.2.

##### **7.3.2.3 Radiopharmaceutical treatment**

After 3 to 4 days of incubation at 37°C and 5% CO<sub>2</sub>, spheroids were centrifuged at 300 rpm for 3 minutes and resuspended in 2 ml fresh culture medium. Based on previous studies demonstrating optimal [<sup>131</sup>I]mIBG uptake after 2 h of exposure<sup>283</sup>, spheroid growth delay experiments using spheroids grown from SK-N-BE(2c) and UVW/NAT cell lines were exposed to [<sup>131</sup>I]mIBG for 2 h at 37°C and 5% CO<sub>2</sub>. At the end of the incubation period, [<sup>131</sup>I]mIBG that had not been taken up by the cells was removed by washing three times in PBS.

Similarly, after 3 to 4 days of incubation at 37°C and 5% CO<sub>2</sub>, the spheroids were centrifuged at 300 rpm for 3 minutes and resuspended in 2 ml fresh culture medium. The optimal duration of exposure of LNCaP spheroids to [<sup>131</sup>I]MIP-1095 was determined

experimentally. This is described in Section 7.4.2. At the end of the incubation period, excess [<sup>131</sup>I]MIP-1095 that had not been taken up by the cells was removed by washing three times in culture medium. Culture medium was used for the washes instead of PBS because Molecular Insight Pharmaceuticals, Inc observed that PBS, but not culture medium, inhibited the binding of [<sup>131</sup>I]MIP-1095 to PSMA (Dr S. Hillier, personal communication).

#### **7.3.2.4 Combination treatment**

In the case of combination treatment consisting of DSF:Cu and  $\gamma$ -radiation, spheroids were exposed to DSF:Cu in serum-free culture medium immediately followed by irradiation. Spheroids were then incubated at 37°C and 5% CO<sub>2</sub> for 24 h before removal of excess DSF:Cu and the start of the monitoring of the size of individual spheroids. In the case of combination treatment consisting of DSF:Cu and a radiopharmaceutical, spheroids were treated with DSF:Cu and radiopharmaceutical simultaneously and incubated at 37°C and 5% CO<sub>2</sub> for 2 h. Thereafter excess radiopharmaceutical was washed off. The spheroids were re-incubated at 37°C and 5% CO<sub>2</sub> for 22 h in the presence of DSF:Cu before removal of the excess DSF:Cu by washing three times and the start of the monitoring of the size of individual spheroids.

#### **7.3.3 [<sup>131</sup>I]MIP-1095 uptake**

LNCaP spheroids were treated with various concentrations of [<sup>131</sup>I]MIP-1095 for 0.25, 0.5, 1, 2 and 8 h at 37°C and 5% CO<sub>2</sub>. Alternatively, LNCaP spheroids were equilibrated at 4°C for 30 min prior to treatment with [<sup>131</sup>I]MIP-1095 at 4°C and 5% CO<sub>2</sub>. At the end of the treatment, LNCaP spheroids were washed three times in culture medium, centrifuged and the pellets were resuspended in 1 ml fresh culture medium. A  $\gamma$ -counter (Canberra Packard, Berkshire) was used to measure the radioactivity (in count per minute [CPM]) retained in the pellet. The protein content of the pellet was measured according to Section 7.3.4 and the uptake value was expressed as CPM per mg of protein.

#### **7.3.4 Protein extraction and quantification**

Protein extracts of the spheroid pellets were obtained by incubation in 100  $\mu$ l lysis buffer [protease inhibitor (Calbiochem), 1.19 g HEPES, 1.46 g NaCl and 0.5 ml Nonidet P-40 in 100 ml distilled water, pH 7] for 45 min on ice. The extracts were centrifuged at 16,000 g for 5 min and the protein content of the supernatants was quantified using the Bradford assay<sup>284</sup>. Protein extracts and bovine serum albumin (BSA) standards (0, 0.2, 0.4, 0.6, 0.8,

1 mg/ml) were mixed in equal ratios with the Bradford reagent (Bio-Rad) in dH<sub>2</sub>O and the absorbance was measured at 595 nm ( $A_{595}$ ). The absorbance values ( $A_{595}$ ) and the protein concentrations of the BSA standards in mg/ml [BSA] were used to determine the relationship between absorbance and protein content according to equation (21):

$$A_{595} = b*[BSA] + a \quad (21)$$

Linear regression analysis of equation (21) by the method of the least squares allowed the calculation of the slope  $b$  and the y-intercept  $a$ . The amount of proteins in each spheroid pellet extract [extract] in mg was calculated using equation (22):

$$[\text{extract}] = 0.1 * (A_{595 \text{ extract}} - a) / b \quad (22)$$

### **7.3.5 Spheroid measurement**

See Section 6.3.3.

### **7.3.6 Calculation of $\tau_2$ and DT values**

See Section 6.3.4.

### **7.3.7 Calculation of AUC values**

See Section 6.3.5

### **7.3.8 Statistical analyses**

Because the distribution of  $\tau_2$ , DT and  $AUC_{\log}$  values were non-normally distributed, non-parametric testing (the Kruskal-Wallis test followed by the Mann-Whitney test) was carried out using SPSS (IBM).

#### **7.3.8.1 Statistical analysis of single agent dose-response effects**

This procedure was described in more details in Section 6.3.6. Briefly, the medians of  $\tau_2$ , DT and  $AUC_{\log}$  values of the group treated with the highest treatment intensity were compared with those of the untreated control by non-parametric testing (Kruskal-Wallis test followed by the Mann-Whitney test). If a significant difference was obtained ( $p < 0.05$ ), the medians of  $\tau_2$ , DT and  $AUC_{\log}$  values of the next highest treatment intensity were compared with those of the untreated controls. This procedure was carried out until a pairwise comparison returned a non-significant p-value (greater than 0.05).

### **7.3.8.2 Statistical analysis of the effect of 2-(phosphonomethyl)pentanedioic acid (PMPA) on the spheroid growth delay induced by [<sup>131</sup>I]MIP-1095**

The statistical analysis of the effect of the PSMA-specific binding inhibitor PMPA on the spheroid growth delay induced by [<sup>131</sup>I]MIP-1095 was carried out as follows. The groups treated with 0.37, 1, 3.7 or 10 MBq/ml [<sup>131</sup>I]MIP-1095 in the absence of PMPA, in the presence of 10 μM PMPA or in the presence of 100 μM PMPA were considered a family. Each family was analysed separately. Firstly, the medians of  $\tau_2$ , DT and AUC<sub>log</sub> values of the group treated with [<sup>131</sup>I]MIP-1095 in the presence of 100 μM PMPA was compared with that of the group treated with [<sup>131</sup>I]MIP-1095 alone. If the p-value returned by the Mann-Whitney test was higher than 0.05, there was no further testing of this family. Any significant difference between the medians of the group treated with [<sup>131</sup>I]MIP-1095 in the presence of 10 μM PMPA and that of the group treated with [<sup>131</sup>I]MIP-1095 alone was considered random variation if there was no significant difference between the medians of the group treated with [<sup>131</sup>I]MIP-1095 in the presence of 100 μM PMPA and that of the group treated with [<sup>131</sup>I]MIP-1095 alone.

On the other hand, if the p-value of the comparison between the medians of the group treated with [<sup>131</sup>I]MIP-1095 in the presence of 100 μl PMPA and that of the group treated with [<sup>131</sup>I]MIP-1095 alone was lower than 0.05, then the median of the group treated with [<sup>131</sup>I]MIP-1095 and 10 μM PMPA was compared with that of the group treated with [<sup>131</sup>I]MIP-1095 alone with a significance level of 0.05. This stepwise analysis was repeated independently for each family, i.e. for each radioactivity concentration of [<sup>131</sup>I]MIP-1095.

### **7.3.8.3 Statistical analysis of the potentiation of radiation kill**

In order to demonstrate the enhancement of the radiation-induced growth delay, the observed effect in response to a combination treatment of a drug with radiation must be greater than that induced by radiation alone. Moreover, the effect in response to the combination treatment must be greater than that of the drug alone. Even though the effect of the combination is greater than that induced by radiation alone, if there is no significant difference between the drug-induced effect and the combination-induced effect, then the effect of the combination could only be due to that of the drug alone. Secondly, the absence of the enhancement of radiation-induced growth delay could be due to either the intrinsic inability of the drug to potentiate the effect of radiation or to the use of a dose of the drug too low to have any effect at all. Therefore, the effect of the single agents

compared with the untreated control must also be examined. Thus, the determination of the presence or the absence of potentiation of the effect of radiation involves a family of four pairwise comparisons:

- 1- Drug versus untreated control
- 2- Radiation versus untreated control
- 3- Drug + radiation versus drug
- 4- Drug + radiation versus radiation

The multiple pairwise comparisons (four) required for the investigation of the enhancement of the growth delay induced by radiation are susceptible to the family-wise error. Indeed, the p-value is the probability to find a difference between two groups assuming there is none. If the significance level of a particular test is set at 5%, it follows from the definition of the p-value that in a family of comparisons, there is a 5% chance of finding a significant result assuming there is none. This is known as the family-wise error. The Bonferroni correction was used to overcome this issue. In order to keep the overall level of significance of 0.05, the level of significance of each pairwise comparison was set to 0.05 divided by the number of comparison, i.e. the significance level  $\alpha$  was set at 0.0125 ( $0.05/4 = 0.0125$ ).

### **7.3.9 Calculation of the combination index CI**

#### **7.3.9.1 Calculation of $IC_{50}$ and m parameters**

The surviving fraction of a treatment group was calculated as one minus the fractional reduction of the  $AUC_{linear}$  value compared with that of the control. The median effect principle was applied to the surviving fraction values in order to calculate the parameters m and  $IC_{50}$  as described in Sections 3.3.5.

#### **7.3.9.2 Calculation of the CI value**

Knowing the values of the  $IC_{50}$  and m parameters, the median effect principle allows the calculation of a dose D that produces a particular effect (fa/fu) as described in Section 4.3.5 by equation (12):

$$D = IC_{50} \times (fa/fu)^{1/m} \quad (12)$$

The calculation of the CI values was performed at the toxicity level obtained following combination treatment. For instance, if the combination treatment consisting of agent A and agent B produced 95% reduction of the control  $AUC_{linear}$  value, the CI value was

calculated at the 95% toxicity level. The doses of agent A and agent B within the combination were selected, hence known. The doses of agent A and agent B that would induce a 95% effect as single agents were calculated using equation (12).

Secondly, the dose reduction index DRI of one agent were calculated by dividing the dose of this agent within the combination by the dose of this agent that induced the same effect as a single treatment according to equation (15):

$$\text{DRI} = \text{dose within the combination} / \text{dose as single agent} \quad (15)$$

Finally, the CI value was calculated as the sum of the DRI values of each agent of the combination according to equation (16):

$$\text{CI} = \text{DRI}_{\text{agentA}} + \text{DRI}_{\text{agentB}} \quad (16)$$

## 7.4 Results

### 7.4.1 The radiosensitising effect of DSF:Cu in combination with $\gamma$ -radiation treatment in LNCaP spheroids

Prior to the study of the combination of DSF:Cu and  $\gamma$ -radiation treatment, the effect of  $\gamma$ -radiation as single agent on the growth of LNCaP spheroids was investigated. The effect of DSF:Cu on the growth of LNCaP spheroids was described in Section 6.4.4. To summarise, the  $\text{IC}_{50}$  value of DSF:Cu was  $1.82 \mu\text{M}$  (Figure 57d).

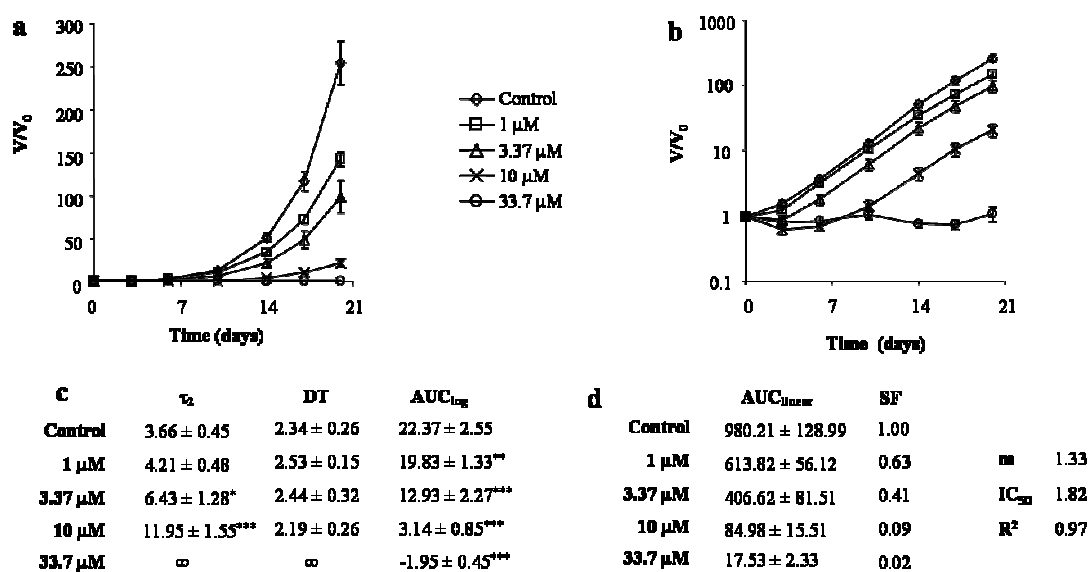


Figure 57 The effect of DSF:Cu on the growth of LNCaP spheroids

LNCaP spheroids were treated with various concentrations of DSF:Cu for 24 h. The  $V/V_0$  values are displayed on a linear scale (a) and on a logarithmic scale (b). Data are mean  $\pm$  SEM. (c)  $\tau_2$ , DT and  $AUC_{\log}$  values were calculated according to Section 6.3.4 and 6.3.5.  $\infty$  indicates that there was not a 2-fold increase in spheroid volume. Data are mean  $\pm$  SEM. The statistical significance of the differences in  $\tau_2$ , DT and  $AUC_{\log}$  values between groups was determined by non-parametric testing (Kruskal-Wallis followed by Mann-Whitney tests) using SPSS. The medians of  $\tau_2$ , DT and  $AUC_{\log}$  values of DSF:Cu-treated groups were compared with those of the untreated control (\*). One symbol indicates  $p < 0.05$ , two symbols indicate  $p < 0.01$  and three symbols indicate  $p < 0.001$ . (d) The surviving fraction (SF) was calculated using the  $AUC_{\text{linear}}$  values. The median effect principle was applied to the SF values in order to calculate  $m$  and the  $IC_{50}$  of the effect of DSF:Cu according to Section 3.3.5. The coefficient of determination ( $R^2$ ) is a measure of the goodness of the fit of the linear regression of the median effect plot.

Treatment with  $\gamma$ -radiation alone increased both the growth delay and the doubling time of the spheroids in a dose-dependent manner (Figure 58). The  $\tau_2$  values were  $3.06 \pm 0.18$ ,  $4.21 \pm 0.57$  ( $p < 0.001$ ),  $5.34 \pm 0.28$  ( $p < 0.001$ ),  $8.36 \pm 0.65$  ( $p < 0.001$ ) and  $11.55 \pm 0.85$  ( $p < 0.001$ ) days for untreated controls and the groups treated with 2, 4, 6 and 10 Gy, respectively (Figure 58c). The DT values were  $2.80 \pm 0.12$ ,  $3.41 \pm 0.47$  ( $p < 0.001$ ),  $5.37 \pm 0.25$  ( $p < 0.001$ ),  $11.40 \pm 0.98$  ( $p < 0.001$ ) and  $15.24 \pm 0.95$  ( $p < 0.001$ ) days for untreated controls and the groups treated with 2, 4, 6 and 10 Gy, respectively (Figure 58c). The  $IC_{50}$  value for  $\gamma$ -radiation was 1.69 Gy (Figure 58d). The growth delay after  $\gamma$ -radiation treatment was due to a reduction in the growth rate. This effect is consistent with all the cells within the spheroids being affected by  $\gamma$ -radiation. If only a sub-population was affected by  $\gamma$ -radiation, the unaffected population would grow at the same rate as the untreated controls, thus showing a growth delay followed by a parallel growth curve to that of the untreated control at the later timepoints. The lack of a growth delay (Figure 58b) indicated that all cells were affected by  $\gamma$ -radiation treatment.

Knowing the effects of DSF:Cu and  $\gamma$ -radiation as single agents, the investigation of the combination of both was carried out in order to determine whether DSF:Cu also radiosensitised LNCaP spheroids (Figure 59). The statistically significant increase in  $\tau_2$  and DT values and the statistically significant decrease in  $AUC_{\log}$  values following treatment with the combination of DSF:Cu and  $\gamma$ -radiation compared with either DSF:Cu or  $\gamma$ -radiation alone demonstrated the enhancement of  $\gamma$ -radiation kill by DSF:Cu. For instance, the  $\tau_2$  values were  $3.21 \pm 0.14$ ,  $5.21 \pm 0.43$  ( $p < 0.001$ ),  $4.44 \pm 0.28$  ( $p < 0.001$ ) and  $5.47 \pm 0.51$  ( $p < 0.001$ ) days for the untreated controls and the groups treated with 3 Gy, 1  $\mu$ M DSF:Cu and 3.37  $\mu$ M DSF:Cu, respectively (Figure 59c). In comparison, the  $\tau_2$  values were  $8.02 \pm 0.78$  ( $p < 0.01$ ) days for the combination of 1  $\mu$ M DSF:Cu with 3 Gy

and  $14.12 \pm 1.59$  ( $p < 0.001$ ) days for the combination of  $3.37 \mu\text{M}$  DSF:Cu with 3 Gy (Figure 59c). However, the increase in  $\gamma$ -radiation kill by  $1 \mu\text{M}$  DSF:Cu did not reach statistical significance according to both the DT and  $\text{AUC}_{\log}$  values (Figure 59c). This indicated that  $1 \mu\text{M}$  DSF:Cu enhanced  $\gamma$ -radiation kill transiently in the first week after treatment ( $\tau_2 = 8.02 \pm 0.78$  days) whereas the spheroids grew at a similar rate as that of the  $\gamma$ -radiation-treated group thereafter. All three parameters  $\tau_2$ , DT and  $\text{AUC}_{\log}$  showed a significant enhancement of  $\gamma$ -radiation kill by  $3.37 \mu\text{M}$  DSF:Cu (Figure 59c). The combination indices were 1.21 and 0.56 for the combinations of 3 Gy with  $1 \mu\text{M}$  and  $3.37 \mu\text{M}$  DSF:Cu, respectively (Figure 59d), indicative of a supra-additive interaction between DSF:Cu and  $\gamma$ -radiation treatment only in response to  $3.37 \mu\text{M}$  DSF:Cu.

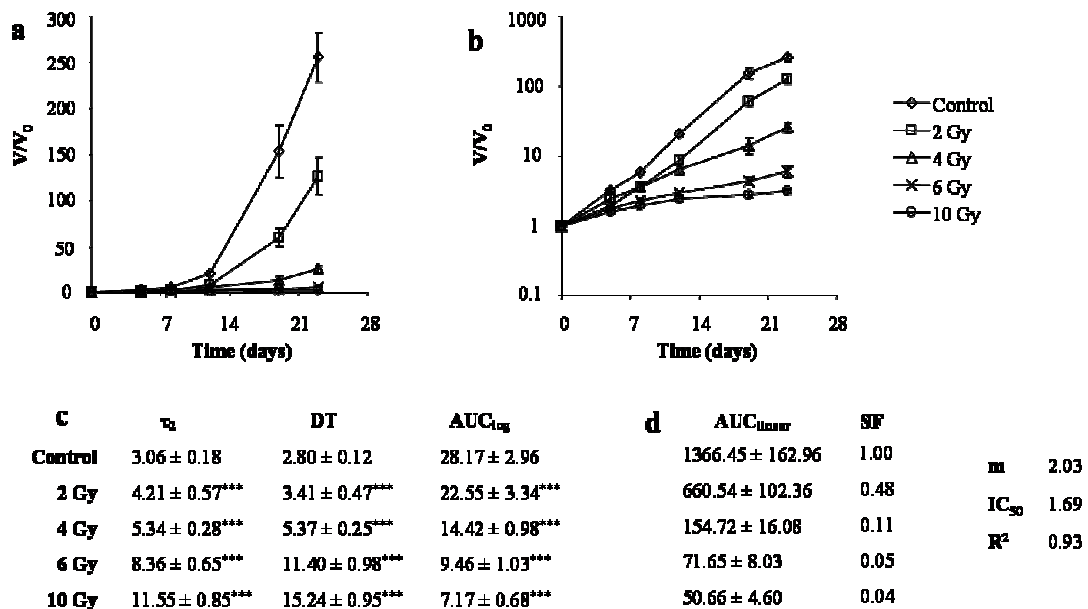


**Figure 58** The effect of  $\gamma$ -radiation on the growth of LNCaP spheroids

LNCaP spheroids were irradiated using a  $^{60}\text{Co}$  external beam. The  $V/V_0$  values are displayed on a linear scale (a) and on a logarithmic scale (b). Data are mean  $\pm$  SEM. (c)  $\tau_2$ , DT and  $\text{AUC}_{\log}$  values were calculated according to Section 6.3.4 and 6.3.5. Data are mean  $\pm$  SEM. The statistical significance of the differences in  $\tau_2$ , DT and  $\text{AUC}_{\log}$  values between groups was determined by non-parametric testing (Kruskal-Wallis followed by Mann-Whitney tests) using SPSS. The medians of the  $\tau_2$ , DT and  $\text{AUC}_{\log}$  values of the irradiated groups were compared with those of the control (\*). Three symbols indicate  $p < 0.001$ . (d) The surviving fraction SF was calculated using the  $\text{AUC}_{\text{linear}}$  values according Section 7.3.9.1. The median effect principle was applied to the SF values in order to calculate  $m$  and the  $\text{IC}_{50}$  of the effect of  $\gamma$ -radiation according to Section 3.3.5. The coefficient of determination  $R^2$  is a measure of the goodness of the fit of the linear regression of the median effect plot.

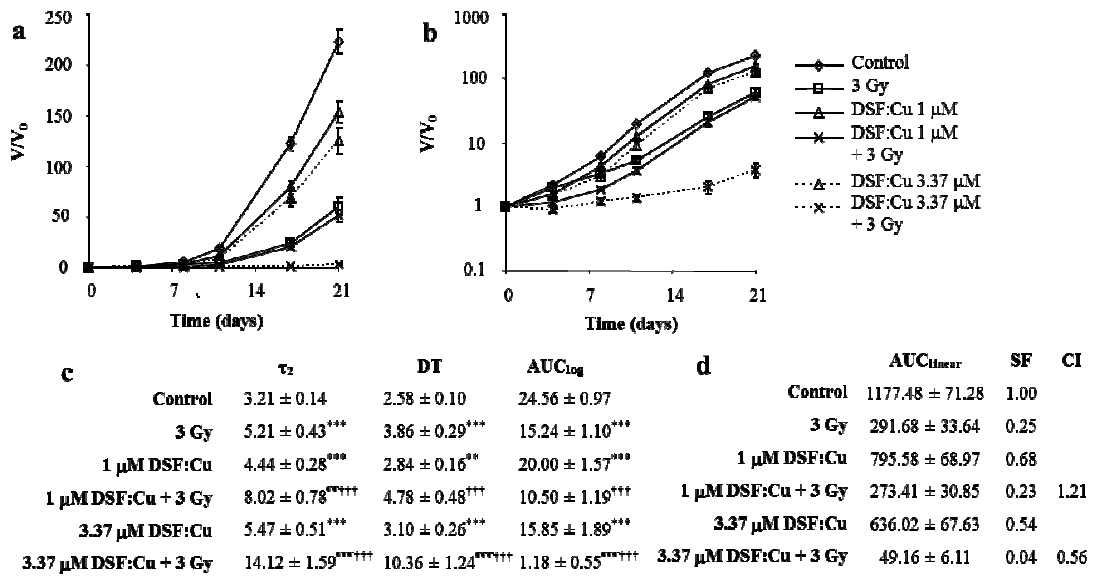


**Figure 59** The effect of DSF:Cu on the growth delay induced by  $\gamma$ -radiation in LNCaP spheroids.

LNCaP spheroids were treated with DSF:Cu in serum-free culture medium for 24 h or irradiated using a  $^{60}\text{Co}$  external beam. In the case of combination treatments, the irradiation of the spheroids was performed immediately after the start of the exposure of the spheroids to DSF:Cu. The  $V/V_0$  values are displayed on a linear scale (a) and on a log scale (b). Data are mean  $\pm$  SEM. (c)  $\tau_2$ , DT and AUC<sub>log</sub> values were calculated according to Section 6.3.4 and 6.3.5. Data are mean  $\pm$  SEM. The statistical significance of the differences in  $\tau_2$ , DT and AUC<sub>log</sub> values between groups was determined by non-parametric testing (Kruskal-Wallis followed by Mann-Whitney tests) using SPSS. The medians of  $\tau_2$ , DT and AUC<sub>log</sub> values of the groups treated with DSF:Cu or  $\gamma$ -radiation as single agents were compared with those of the untreated controls (\*). The medians of  $\tau_2$ , DT and AUC<sub>log</sub> values of the combinations of  $\gamma$ -radiation treatment with DSF:Cu were compared with those of  $\gamma$ -radiation treatment alone (¶) and to those of the drug treatment alone (†). Two symbols indicate  $p < 0.01$  and three symbols indicate  $p < 0.001$ . (d) The combination indices CI were calculated as explained in Section 7.3.9.2 using the AUC<sub>linear</sub> values of the combinations. The calculation was based on the parameters  $m$  and  $\text{IC}_{50}$  calculated for the single agents (Figure 57d and Figure 58d).

#### 7.4.2 Determination of the mechanism of [ $^{131}\text{I}$ ]MIP-1095 uptake in LNCaP spheroids

LNCaP spheroids were exposed to 0.37 MBq/ml [ $^{131}\text{I}$ ]MIP-1095 at 4°C for 0.25, 0.5, 1, 2 and 8 h. There is no internalisation of [ $^{131}\text{I}$ ]MIP-1095 at 4°C, thus, binding only and not internalisation was investigated in these conditions. Binding of [ $^{131}\text{I}$ ]MIP-1095 to PSMA was maximal (100% CPM) after 2 h exposure (Figure 60a). More than 90% of the maximal binding was reached within 15 min of exposure to [ $^{131}\text{I}$ ]MIP-1095. Based on these results, exposure to [ $^{131}\text{I}$ ]MIP-1095 for 2 h was used thereafter.

The dose-dependent binding of [ $^{131}\text{I}$ ]MIP-1095 to LNCaP spheroids was investigated at 4°C. The binding of [ $^{131}\text{I}$ ]MIP-1095 to PSMA increased with increasing radioactivity

concentrations of [<sup>131</sup>I]MIP-1095; a tendency toward saturation was indicated at 10 MBq/ml by the reduction of the slope (Figure 60b). There was a statistically significant reduction of the binding to PSMA in the presence of the binding inhibitor PMPA. At 0.1 MBq/ml [<sup>131</sup>I]MIP-1095, 10 μM and 100 μM PMPA inhibited 85% ( $p < 0.001$ ) and 90% ( $p < 0.001$ ) of the [<sup>131</sup>I]MIP-1095 binding to PSMA, respectively (Figure 60b). At 1 MBq/ml [<sup>131</sup>I]MIP-1095, 10 μM and 100 μM PMPA inhibited 55% ( $p < 0.01$ ) and 75% ( $p < 0.001$ ) of the binding, respectively (Figure 60b). At 10 MBq/ml [<sup>131</sup>I]MIP-1095, 10 μM and 100 μM PMPA inhibited 10% and 40% ( $p < 0.05$ ) of the [<sup>131</sup>I]MIP-1095 binding, respectively (Figure 60b). These data indicated the competitive nature of the [<sup>131</sup>I]MIP-1095 binding to PSMA.

Next, the internalisation of [<sup>131</sup>I]MIP-1095 into the intracellular space of LNCaP cells within the spheroids was investigated at 37°C. LNCaP spheroids were exposed to 0.1 MBq/ml [<sup>131</sup>I]MIP-1095 for 2 h. There was a 75% decrease in uptake at 4°C compared with that at 37°C ( $p < 0.01$ ) (Figure 60c). PMPA inhibited 95% of the uptake at 37°C ( $p < 0.01$ ), indicating that binding is required for internalisation (Figure 60c). Also, 3.37 μM DSF:Cu had no effect on the uptake of [<sup>131</sup>I]MIP-1095 by LNCaP spheroids (Figure 60c), suggesting that DSF:Cu is unlikely to decrease [<sup>131</sup>I]MIP-1095 efficacy.

Potassium cyanide (KCN), an inhibitor of the adenosine triphosphate (ATP) production by the mitochondrial respiratory chain, inhibited 70% of the uptake of [<sup>131</sup>I]MIP-1095 at 37°C ( $p < 0.001$ ) (Figure 60d). This reduction of the uptake by KCN was similar to that induced by exposure to [<sup>131</sup>I]MIP-1095 at 4°C (Figure 60d), suggesting that cellular metabolism and ATP was required for internalisation.

Chloroquine (CHQ) is an inhibitor of lysosomal degradation and of the recycling of the endosomes back to the cell membrane. It was added simultaneously with [<sup>131</sup>I]MIP-1095 in order to determine the involvement of endocytosis in the internalisation process of [<sup>131</sup>I]MIP-1095. CHQ inhibited 50% of the uptake of [<sup>131</sup>I]MIP-1095 at 37°C ( $p < 0.001$ ) (Figure 60d). However, there was a statistically significant increase in [<sup>131</sup>I]MIP-1095 uptake when spheroids were exposed to [<sup>131</sup>I]MIP-1095 with CHQ at 37°C compared with that at 4°C ( $p < 0.001$ ) (Figure 60d). This result may be explained as follows. CHQ was shown to reduce the uptake of antibodies by inhibition of the recycling of the endosomes to the cell membrane, but not by inhibition of the binding to the antigen<sup>285</sup>. Thus, CHQ allows a first round of binding and internalisation of [<sup>131</sup>I]MIP-1095 but prevents the recycling of

PSMA receptors back to the membrane, thereby inhibiting a second round of internalisation. This was consistent with the observation of a significantly greater uptake of [<sup>131</sup>I]MIP-1095 at 37°C compared with that at 4°C in the presence of CHQ ( $p < 0.001$ ).

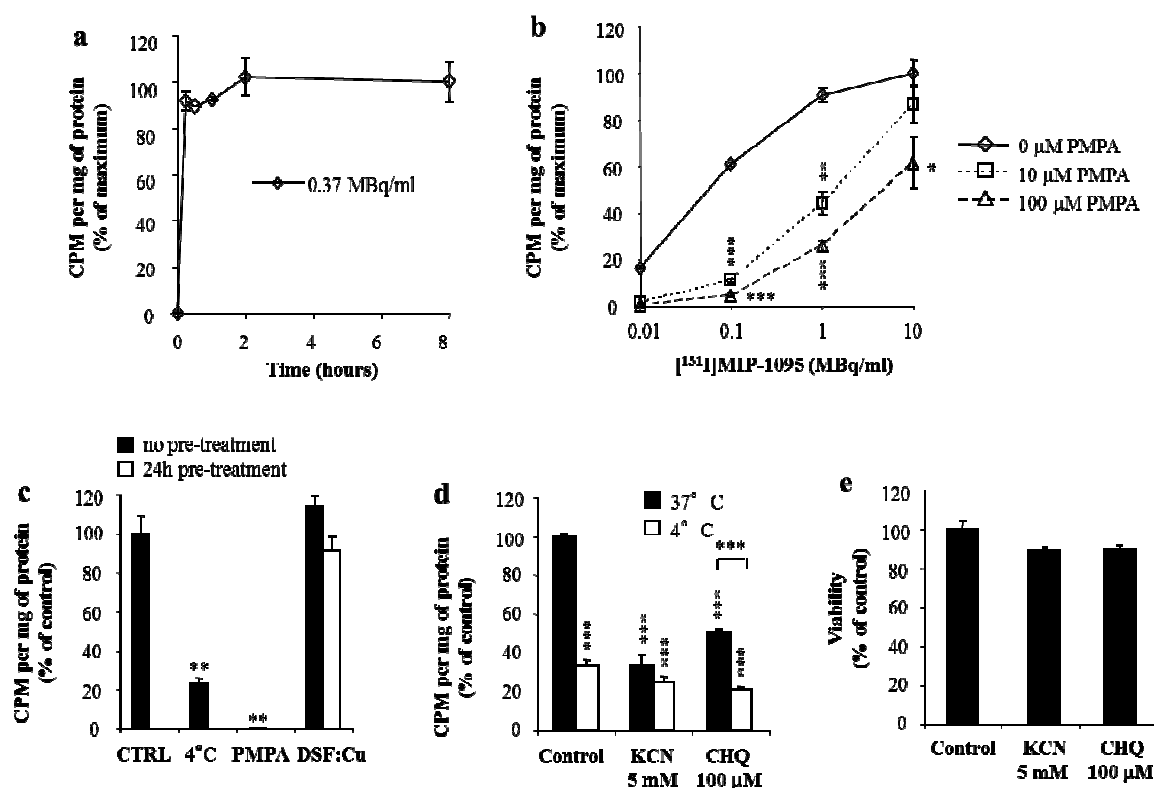


**Figure 60** The binding and internalisation of [<sup>131</sup>I]MIP-1095 to LNCaP spheroids

(a) LNCaP spheroids were exposed to 0.37 MBq/ml [<sup>131</sup>I]MIP-1095 at 4°C for 0.25, 0.5, 1, 2 and 8 h. (b) LNCaP spheroids were exposed to various radioactivity concentrations of [<sup>131</sup>I]MIP-1095 at 4°C for 2 h. The inhibitor of the binding of [<sup>131</sup>I]MIP-1095 to PSMA, PMPA, was added simultaneously with [<sup>131</sup>I]MIP-1095. (c) LNCaP spheroids were exposed to 0.1 MBq/ml [<sup>131</sup>I]MIP-1095 for 2 h at 37°C or at 4°C. LNCaP spheroids were exposed simultaneously to [<sup>131</sup>I]MIP-1095 and 3.37 μM DSF:Cu or 10 μM PMPA for 2 h. The pre-treatment consisted of exposure of LNCaP spheroids to DSF:Cu alone for 22 h immediately followed by exposure for 2 h to [<sup>131</sup>I]MIP-1095 in the presence of DSF:Cu. (d) LNCaP spheroids were exposed to 0.37 MBq/ml [<sup>131</sup>I]MIP-1095 for 2 h at 37°C or 4°C. LNCaP spheroids were treated with 5 mM potassium cyanide (KCN) or 100 μM chloroquine (CHQ) simultaneously with [<sup>131</sup>I]MIP-1095 without pre-treatment. (a, b, c and d) As indicated, the spheroids were pre-chilled to 4°C for 30 min prior to exposure to [<sup>131</sup>I]MIP-1095 at 4°C in order to avoid internalisation. (e) The MTT assay was carried out to determine the viability of LNCaP monolayers after 2 h treatment with 5 mM KCN or 100 μM CHQ. Statistical analyses: (b) the independent samples t-test was used to compare the mean binding of the PMPA-treated samples to that of their respective [<sup>131</sup>I]MIP-1095-treated samples without PMPA. (c, d and e) The independent samples t-test was used to compare the mean uptake value of each treatment with that of the control treatment, unless otherwise indicated by the horizontal bar. One symbol indicates  $p < 0.05$ , two symbols indicate  $p < 0.01$  and three symbols indicate  $p < 0.001$ .

If KCN and CHQ were toxic to LNCaP cells, the decrease in [<sup>131</sup>I]MIP-1095 uptake observed after such treatment would be due to their cytotoxicity since it was shown that reduced metabolic activity at 4°C or the lack of ATP production reduced [<sup>131</sup>I]MIP-1095 uptake. Thus, the viability of LNCaP monolayers was assessed using the MTT assay following treatment with KCN and CHQ for 2 h. There was no statistically significant decrease in viability when LNCaP monolayers were treated with KCN and CHQ for 2 h (Figure 60e), thus discounting KCN- and CHQ-induced cytotoxicity as the cause of reduced [<sup>131</sup>I]MIP-1095 uptake.

These results demonstrated the requirement of ATP for the internalisation of [<sup>131</sup>I]MIP-1095 by endocytosis. The duration of exposure for optimal [<sup>131</sup>I]MIP-1095 uptake was 2 h at 37°C. This duration was used in subsequent spheroid growth delay experiments.

#### **7.4.3 Determination of PSMA-specific [<sup>131</sup>I]MIP-1095-induced LNCaP spheroid growth delay**

In order to determine the PSMA-specificity of [<sup>131</sup>I]MIP-1095-induced delay of LNCaP spheroid growth, [<sup>131</sup>I]MIP-1095 was administered to LNCaP spheroids in the absence (Figure 61a) or in the presence of 10 µM (Figure 61b) or 100 µM PMPA (Figure 61c). There was a significant dose-dependent increase in  $\tau_2$  values in response to 0.37, 1 and 3.7 MBq/ml [<sup>131</sup>I]MIP-1095 (Table 10). Apart from the DT value of the group treated with 3.7 MBq/ml, the DT values increased in a dose-dependent manner with increasing [<sup>131</sup>I]MIP-1095 radioactivity concentrations (Table 10). Similarly, the AUC<sub>log</sub> values significantly decreased in a dose-dependent manner with increasing [<sup>131</sup>I]MIP-1095 concentrations up to 3.7 MBq/ml (Table 10). The  $\tau_2$  and AUC<sub>log</sub> values demonstrated the absence of a significantly increased growth delay when the radioactivity concentration of [<sup>131</sup>I]MIP-1095 was increased from 3.7 to 10 MBq/ml (Table 10). This was consistent with the tendency toward a plateau with respect to binding of [<sup>131</sup>I]MIP-1095 at a radioactivity concentration greater than 1 MBq/ml (Figure 60b).

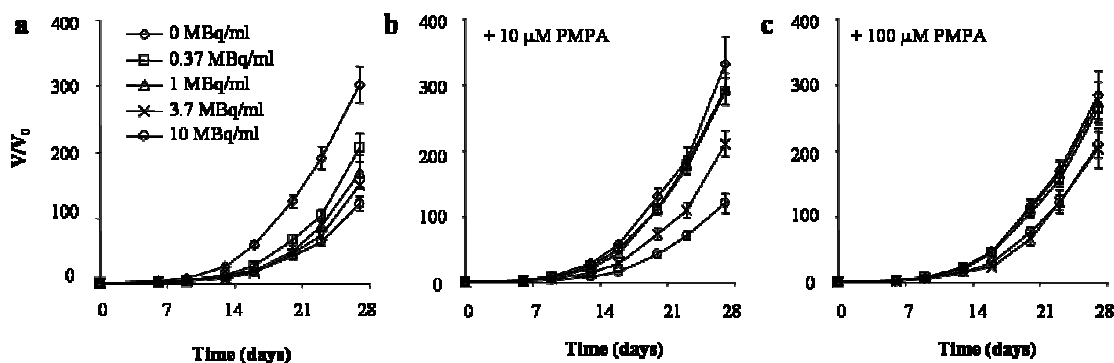


**Figure 61** The effect of [<sup>131</sup>I]MIP-1095 on the growth of LNCaP spheroids

LNCaP spheroids were treated with various concentrations of [<sup>131</sup>I]MIP-1095 for 2 h at 37°C in the presence or in the absence of the binding inhibitor PMPA. Data are mean ± SEM. Spheroids were exposed to (a) [<sup>131</sup>I]MIP-1095 alone, (b) [<sup>131</sup>I]MIP-1095 in the presence of 10 μM PMPA and (c) [<sup>131</sup>I]MIP-1095 in the presence of 100 μM PMPA. (d) SF values were calculated using the AUC<sub>linear</sub> values. The median effect principle was applied to the SF values in order to calculate m and the IC<sub>50</sub> of the effect of DSF:Cu according to Section 3.3.5. The coefficient of determination R<sup>2</sup> is a measure of the goodness of the fit of the linear regression of the median effect plot.

The τ<sub>2</sub> values of the groups treated with 0.37, 1 and 3.7 MBq/ml were significantly decreased in the presence of 10 and 100 μM PMPA, indicating that binding of [<sup>131</sup>I]MIP-1095 to PSMA is required for spheroid growth delay (Table 10). PMPA had no inhibitory effect on the increase in τ<sub>2</sub> value induced by 10 MBq/ml [<sup>131</sup>I]MIP-1095.

Although statistical significance was not always achieved, the DT values of the groups treated with 0.37 and 1 MBq/ml were reduced to untreated control levels by co-administration of 10 or 100 μM PMPA (Table 10). The DT values of LNCaP spheroids following treatments with 3.7 or 10 MBq/ml [<sup>131</sup>I]MIP-1095 were not significantly reduced by the inclusion of 10 μM PMPA in the incubation mixture (Table 10). Although the DT value following treatment with 10 MBq/ml [<sup>131</sup>I]MIP-1095 was significantly reduced by 100 μM PMPA, 100 μM PMPA failed to reduce the DT value following treatment with 3.7 MBq/ml (Table 10). The latter observations were contradictory and were most likely due to experimental error. Given more time, this experiment would be subjected to more rigorous evaluation.

The decreases in the AUC<sub>log</sub> values following treatment with 0.37, 1 and 3.7 MBq/ml [<sup>131</sup>I]MIP-1095 alone were significantly inhibited by treatment with 10 and 100 μM PMPA (Table 10). Treatment with 10 μM PMPA did not inhibit the decrease in AUC<sub>log</sub> value following exposure to 10 MBq/ml [<sup>131</sup>I]MIP-1095. However, an increase in the concentration of PMPA from 10 to 100 μM resulted in the inhibition of the decrease in AUC<sub>log</sub> value following treatment with 10 MBq/ml [<sup>131</sup>I]MIP-1095.

	$\tau_2$	DT	AUC <sub>log</sub>
<b>0 MBq/ml</b>	2.70 ± 0.40	3.19 ± 0.14	27.31 ± 1.49
<b>10 μM PMPA</b>	2.33 ± 0.22	3.18 ± 0.19	28.08 ± 1.76
<b>100 μM PMPA</b>	3.27 ± 0.28	3.20 ± 0.28	25.67 ± 0.80
<b>0.37 MBq/ml</b>	4.11 ± 0.38***	3.45 ± 0.28*	22.21 ± 2.24***
<b>0.37 MBq/ml + 10 μM PMPA</b>	2.77 ± 0.32†	3.19 ± 0.23	26.73 ± 2.38††
<b>0.37 MBq/ml + 100 μM PMPA</b>	3.04 ± 0.36†	3.21 ± 0.24	26.09 ± 2.31††
<b>1 MBq/ml</b>	4.14 ± 0.36***	3.74 ± 0.24***	21.40 ± 2.13***
<b>1 MBq/ml + 10 μM PMPA</b>	2.92 ± 0.28††	3.17 ± 0.27††	26.52 ± 2.29††
<b>1 MBq/ml + 100 μM PMPA</b>	2.73 ± 0.27††	3.33 ± 0.09††	26.32 ± 0.87††
<b>3.7 MBq/ml</b>	4.96 ± 0.57***	3.69 ± 0.39***	19.76 ± 2.16***
<b>3.7 MBq/ml + 10 μM PMPA</b>	3.95 ± 0.28†	3.43 ± 0.16	23.06 ± 1.22††
<b>3.7 MBq/ml + 100 μM PMPA</b>	3.34 ± 0.39†††	3.62 ± 0.39	23.57 ± 2.72††
<b>10 MBq/ml</b>	4.22 ± 0.46***	3.91 ± 0.38***	20.63 ± 2.04***
<b>10 MBq/ml + 10 μM PMPA</b>	4.83 ± 0.45	3.91 ± 0.33	19.55 ± 1.62
<b>10 MBq/ml + 100 μM PMPA</b>	4.02 ± 0.39	3.31 ± 0.28†††	23.18 ± 2.06††

**Table 10** The  $\tau_2$ , DT and AUC<sub>log</sub> values from Figure 61

The  $\tau_2$ , DT and AUC<sub>log</sub> values were calculated according to Section 6.3.4 and 6.3.5. The statistical significance of the differences in  $\tau_2$ , DT and AUC<sub>log</sub> values between groups was determined by non-parametric testing (Kruskal-Wallis followed by Mann-Whitney tests) using SPSS. The medians of  $\tau_2$ , DT and AUC<sub>log</sub> values of the groups treated with [<sup>131</sup>I]MIP-1095 alone were compared with that of the untreated controls (\*). The medians of  $\tau_2$ , DT and AUC<sub>log</sub> of the groups treated with [<sup>131</sup>I]MIP-1095 in the presence of PMPA were compared with those of the group treated with [<sup>131</sup>I]MIP-1095 alone (†). One symbol indicates p < 0.05, two symbols indicate p < 0.01 and three symbols indicate p < 0.001.

These results showed that 10 or 100 μM PMPA was able to prevent the inhibition of LNCaP growth following treatment with 0.37, 1 and 3.7 MBq/ml [<sup>131</sup>I]MIP-1095, demonstrating that the inhibition of the growth of spheroids by [<sup>131</sup>I]MIP-1095 is dependent on the binding to PSMA at these concentrations. However the effect of PMPA was lost at 10 MBq/ml [<sup>131</sup>I]MIP-1095. These data were consistent with the study of the

dose-dependent binding of [<sup>131</sup>I]MIP-1095 to PSMA (Figure 60b). Indeed, PMPA was less efficient at inhibiting the binding of 3.7 and 10 MBq/ml [<sup>131</sup>I]MIP-1095 to PSMA than the binding of [<sup>131</sup>I]MIP-1095 at radioactivity concentrations less than 3.7 MBq/ml (Figure 60b). Based on these data, a radioactivity concentration of 0.37 MBq/ml was chosen for the investigation of the effect of DSF:Cu on the growth delay induced by [<sup>131</sup>I]MIP-1095 in LNCaP spheroids. This concentration corresponded to a PSMA-specific growth delay, indicative of targeted radiotherapy.

It has been shown that [<sup>131</sup>I]MIP-1095 was a more potent inhibitor of the enzymatic activity of PSMA than PMPA: the K<sub>i</sub> values in LNCaP cells were 0.24 nM and 2.1 nM, respectively<sup>65,286</sup>. Based on the greater potency of [<sup>131</sup>I]MIP-1095 compared with that of PMPA and assuming that the difference in K<sub>i</sub> values reflected the differences in PSMA-binding affinity between [<sup>131</sup>I]MIP-1095 and PMPA, it was anticipated that PMPA concentration at least 10 times greater than that of [<sup>131</sup>I]MIP-1095 would inhibit 50% of the binding of [<sup>131</sup>I]MIP-1095 to PSMA. The molar concentration of 10 MBq/ml [<sup>131</sup>I]MIP-1095 was 638 nM. However, 10 μM PMPA, which corresponded to a 15-fold molar excess of PMPA compared with [<sup>131</sup>I]MIP-1095, only inhibited 15% of the binding of [<sup>131</sup>I]MIP-1095 to PSMA (Figure 60b). Moreover, 100 μM PMPA, which corresponded to a 150-fold molar excess of PMPA, only inhibited 40% of the binding of [<sup>131</sup>I]MIP-1095 to PSMA (Figure 60b). This could be explained by a difference in binding affinity between [<sup>131</sup>I]MIP-1095 and PMPA greater than that implied by the K<sub>i</sub> values. The K<sub>i</sub> values were measured using LNCaP cells membranes<sup>65,286</sup>. Thus it was possible that the use of LNCaP spheroids introduced complicating factors such as lipophilicity and penetrability which affected PMPA to a greater extent than [<sup>131</sup>I]MIP-1095.

#### **7.4.4 The effect of DSF:Cu in combination with [<sup>131</sup>I]MIP-1095 in LNCaP spheroids**

The effects of the single agents DSF:Cu and [<sup>131</sup>I]MIP-1095 on the growth delay of LNCaP spheroids were described in Figure 57 and Figure 61, respectively. The effect of the combination is shown in Figure 62. The statistically significant increase in τ<sub>2</sub> and DT values and the statistically significant decrease in AUC<sub>log</sub> values following treatment with DSF:Cu in combination with [<sup>131</sup>I]MIP-1095 compared with either [<sup>131</sup>I]MIP-1095 or DSF:Cu alone demonstrated the enhancement of [<sup>131</sup>I]MIP-1095 kill by DSF:Cu (Figure 62c). For instance, the τ<sub>2</sub> values were 2.82 ± 0.15, 5.62 ± 0.24 (p < 0.001), 4.13 ± 0.46 and 7.14 ± 0.60 (p < 0.001) days for untreated controls and the groups treated with 0.37 MBq/ml [<sup>131</sup>I]MIP-1095, 1 μM DSF:Cu and 3.37 μM DSF:Cu (Figure 62c). In contrast,

the  $\tau_2$  values of the combination of 1  $\mu\text{M}$  and 3.37  $\mu\text{M}$  DSF:Cu with 0.37 MBq/ml [ $^{131}\text{I}$ ]MIP-1095 were  $13.85 \pm 2.41$  ( $p < 0.001$ ) and  $12.37 \pm 1.63$  ( $p < 0.001$ ) days (Figure 62c). The CI values corresponding to the mixture of 1  $\mu\text{M}$  or 3.37  $\mu\text{M}$  DSF:Cu with 0.37 MBq/ml [ $^{131}\text{I}$ ]MIP-1095 were 0.05 or 0.25, respectively, indicating a supra-additive interaction between DSF:Cu and [ $^{131}\text{I}$ ]MIP-1095 (Figure 62d).

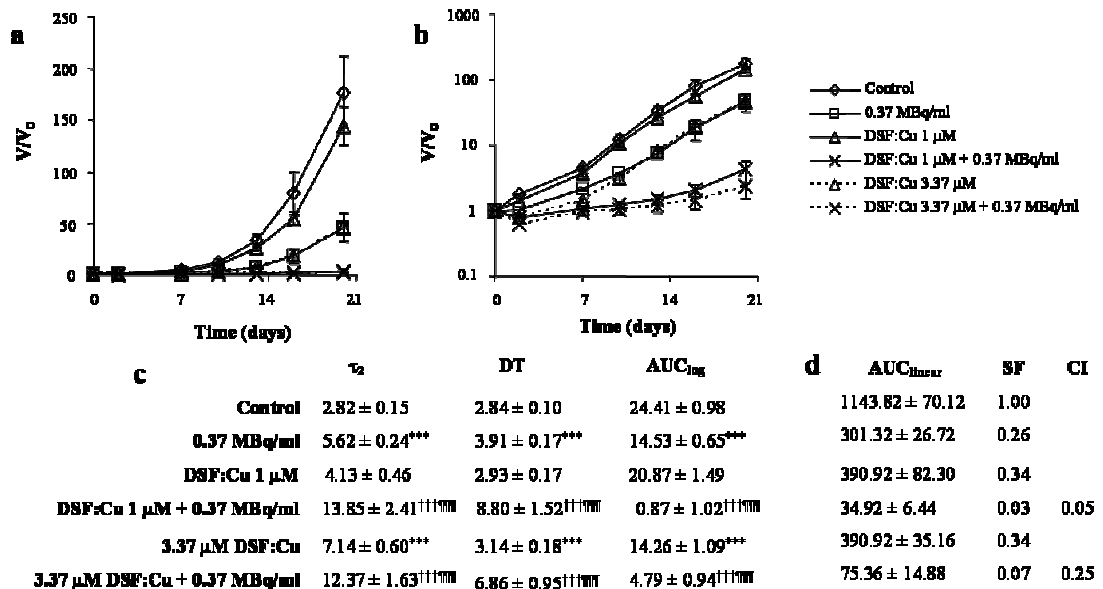


**Figure 62** The effect of DSF:Cu on the growth delay induced by [ $^{131}\text{I}$ ]MIP-1095 in LNCaP spheroids. LNCaP spheroids were treated with [ $^{131}\text{I}$ ]MIP-1095 for 2 h or with DSF:Cu for 24 h as single agent. For the combination of [ $^{131}\text{I}$ ]MIP-1095 and DSF:Cu, LNCaP spheroids were treated with [ $^{131}\text{I}$ ]MIP-1095 for 2 h in the presence of DSF:Cu, washed in culture medium and treated with DSF:Cu alone for a further 22 h. The  $V/V_0$  values are displayed on a linear scale (a) and on a logarithmic scale (b). Data are mean  $\pm$  SEM. (c)  $\tau_2$ , DT and AUC<sub>log</sub> values were calculated according to Section 6.3.4 and 6.3.5. Data are mean  $\pm$  SEM. The statistical significance of the differences in  $\tau_2$ , DT and AUC<sub>log</sub> values between groups was determined by non-parametric testing (Kruskal-Wallis followed by Mann-Whitney tests) using SPSS. The medians of  $\tau_2$ , DT and AUC<sub>log</sub> values of the groups treated with DSF:Cu or [ $^{131}\text{I}$ ]MIP-1095 as single agents were compared with those of the untreated control (\*). The medians of  $\tau_2$ , DT and AUC<sub>log</sub> values of the groups treated with a combination of [ $^{131}\text{I}$ ]MIP-1095 with DSF:Cu were compared with those of the group treated with [ $^{131}\text{I}$ ]MIP-1095 alone (¶) and to those of the group treated with DSF:Cu alone (†). Three symbols indicate  $p < 0.001$ . (d) The CI values were calculated as explained in Section 7.3.9.2 using the AUC<sub>linear</sub> values of the combinations. The calculation was based on the parameters  $m$  and  $\text{IC}_{50}$  calculated for the single agents (Figure 57d and Figure 61d).

#### 7.4.5 The effect of treatment schedules of DSF:Cu and [ $^{131}\text{I}$ ]MIP-1095 on the growth of LNCaP spheroids

It was previously shown, in Figure 60c, that the pre-treatment of LNCaP spheroids with 3.37  $\mu\text{M}$  DSF:Cu did not alter the internalisation of [ $^{131}\text{I}$ ]MIP-1095. Therefore, the effect of scheduling DSF:Cu and [ $^{131}\text{I}$ ]MIP-1095 administrations on the growth of LNCaP

spheroids was investigated (Figure 63). The simultaneous treatment of LNCaP spheroids with DSF:Cu and [<sup>131</sup>I]MIP-1095 resulted in a significant increase in  $\tau_2$  and DT values and a significant decrease in  $AUC_{\log}$  values compared with those of the groups treated with DSF:Cu or [<sup>131</sup>I]MIP-1095 as single agents (Figure 63c). For instance, the  $\tau_2$  values were  $2.10 \pm 0.26$ ,  $5.08 \pm 0.74$  and  $5.33 \pm 0.43$  days for untreated controls and the groups treated with 3.37  $\mu$ M DSF:Cu and 0.37 MBq/ml [<sup>131</sup>I]MIP-1095, respectively. In contrast, the  $\tau_2$  value of the group treated with the combination of 3.37  $\mu$ M DSF:Cu and 0.37 MBq/ml [<sup>131</sup>I]MIP-1095 was  $14.91 \pm 2.58$  (Figure 63c), indicating enhancement of [<sup>131</sup>I]MIP-1095-induced growth delay by DSF:Cu, as already reported in Figure 62.

The alternative schedules consisting of pre-treatment of DSF:Cu followed by treatment with [<sup>131</sup>I]MIP-1095, or *vice versa*, also resulted in a significant increase in  $\tau_2$  and DT values and a significant decrease in  $AUC_{\log}$  values compared with those of the groups treated with DSF:Cu or [<sup>131</sup>I]MIP-1095 as single agents (Figure 63c). Furthermore, there was no significant difference in the medians of  $\tau_2$  and  $AUC_{\log}$  values between the three combination schedules. However, the median of DT values of the combination schedule consisting of pre-treatment with DSF:Cu was significantly smaller than that of the simultaneous combination treatment of DSF:Cu and [<sup>131</sup>I]MIP-1095 ( $p < 0.001$ ). This may have indicated that pre-treatment with DSF:Cu did not potentiate [<sup>131</sup>I]MIP-1095-induced spheroid growth delay as efficiently as the simultaneous administration of both agents, which may have resulted in a quicker regrowth of the spheroids (Figure 63b).

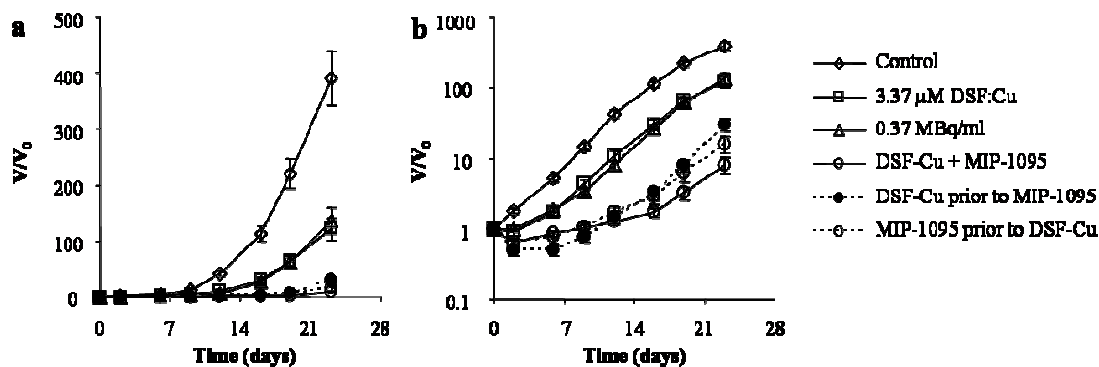


**Figure 63** The effect of treatment schedules of DSF:Cu and [<sup>131</sup>I]MIP-1095 on the growth of LNCaP spheroids

LNCaP spheroids were treated with DSF:Cu in serum-free culture medium for 24 h or with [<sup>131</sup>I]MIP-1095 for 2 h. In the first combination schedule examined, 3.37 μM DSF:Cu and 0.37 MBq/ml [<sup>131</sup>I]MIP-1095 were co-administered simultaneously for 2 h. Then unbound [<sup>131</sup>I]MIP-1095 was removed by three washes with culture medium and the spheroids were exposed to fresh culture medium containing DSF:Cu alone for a further 22 h. The second combination schedule consisted of a pre-treatment with 3.37 μM DSF:Cu alone for 24 h followed by treatment with 0.37 MBq/ml [<sup>131</sup>I]MIP-1095 alone for 2 h. Both drugs were removed by washing at the end of their respective incubation period. The third combination schedule consisted of a pre-treatment with 0.37 MBq/ml [<sup>131</sup>I]MIP-1095 alone for 2 h followed by treatment with 3.37 μM DSF:Cu for 24 h. Both drugs were removed by washing at the end of their respective incubation period. The V/V<sub>0</sub> values are displayed on a linear scale (a) and on a log scale (b). Data are mean ± SEM. (c)  $\tau_2$ , DT and AUC<sub>log</sub> values were calculated according to Section 6.3.4 and 6.3.5. Data are mean ± SEM. The statistical significance of the differences in  $\tau_2$ , DT and AUC<sub>log</sub> values between groups was determined by non-parametric testing (Kruskal-Wallis followed by Mann-Whitney tests) using SPSS. The medians of  $\tau_2$ , DT and AUC<sub>log</sub> values of the groups treated with DSF:Cu or [<sup>131</sup>I]MIP-1095 as single agents were compared with those of the untreated controls (\*). The medians of  $\tau_2$ , DT and AUC<sub>log</sub> values of the combinations of [<sup>131</sup>I]MIP-1095 treatment with DSF:Cu were compared with those of [<sup>131</sup>I]MIP-1095 treatment alone (¶) and to those of the drug treatment alone (†). Two symbols indicate p < 0.01 and three symbols indicate p < 0.001.

## 7.4.6 The effect of DSF:Cu in combination with [<sup>131</sup>I]mIBG on the growth of SK-N-BE(2c) and UVW/NAT spheroids

### 7.4.6.1 The effect of DSF:Cu on the growth of SK-N-BE(2c) and UVW/NAT spheroids

In SK-N-BE(2c) spheroids, the  $\tau_2$  values significantly increased in a dose-dependent manner following treatment with DSF:Cu alone. The  $\tau_2$  values were  $1.11 \pm 0.10$ ,  $1.57 \pm 0.21$  ( $p < 0.01$ ) and  $2.87 \pm 0.33$  days ( $p < 0.001$ ) for untreated control and for the groups treated with 0.337 and 3.37  $\mu\text{M}$  DSF:Cu, respectively (Figure 64c). However the DT values were not significantly increased by treatment with 0.337 or 3.37  $\mu\text{M}$  DSF:Cu, indicating regrowth after an initial delay in growth. A concentration of 33.7  $\mu\text{M}$  DSF:Cu sterilised SK-N-BE(2c) spheroids as indicated by the negative  $\text{AUC}_{\log}$  value (Figure 64c). The  $\text{IC}_{50}$  value for DSF:Cu treatment of SK-N-BE(2c) cells was 0.88  $\mu\text{M}$  (Figure 64d).

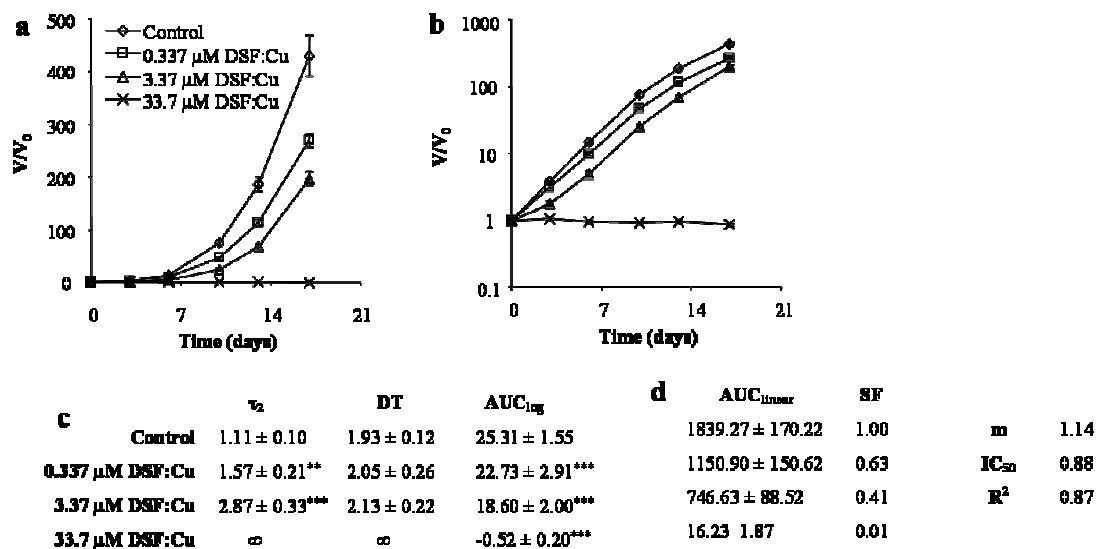


**Figure 64** The effect of DSF:Cu on the growth of SK-N-BE(2c) spheroids

SK-N-BE(2c) spheroids were treated with various concentrations of DSF:Cu for 24 h. The  $V/V_0$  values are displayed on a linear scale (a) and on a logarithmic scale (b). Data are mean  $\pm$  SEM. (c)  $\tau_2$ , DT and  $\text{AUC}_{\log}$  values were calculated according to Section 6.3.4 and 6.3.5.  $\infty$  indicates that a 2-fold increase in spheroid volume was not attained during the course of the experiment. Data are mean  $\pm$  SEM. The statistical significance of the differences in  $\tau_2$ , DT and  $\text{AUC}_{\log}$  values between groups was determined by non-parametric testing (Kruskal-Wallis followed by Mann-Whitney tests) using SPSS. The medians of  $\tau_2$ , DT and  $\text{AUC}_{\log}$  values of the DSF:Cu-treated groups were compared with those of the control (\*). Two symbols indicate  $p < 0.01$  and three symbols indicate  $p < 0.001$ . (d) SF values were calculated using the  $\text{AUC}_{\text{linear}}$  values according to Section 7.3.9.1. The median effect principle was applied to the SF values in order to calculate  $m$  and the  $\text{IC}_{50}$  of the effect of  $\gamma$ -radiation according to Section 3.3.5. The coefficient of determination ( $R^2$ ) is a measure of the goodness of the fit of the linear regression of the median effect plot.

In UVW/NAT spheroids, the  $\tau_2$  values were  $1.35 \pm 0.19$ ,  $3.34 \pm 0.28$  ( $p < 0.001$ ) and  $3.44 \pm 0.37$  days ( $p < 0.001$ ) for untreated control and for the groups treated with 10 and 20  $\mu\text{M}$  DSF:Cu, respectively (Figure 65c). However the DT values were not significantly increased by treatment with 10 and 20  $\mu\text{M}$  DSF:Cu which indicating regrowth after an initial delay in growth. A concentration of 100  $\mu\text{M}$  DSF:Cu sterilised UVW/NAT spheroids as indicated by the negative  $\text{AUC}_{\log}$  value (Figure 65c). The  $\text{IC}_{50}$  value for DSF:Cu in UVW/NAT spheroids was 10.01  $\mu\text{M}$  (Figure 65d).

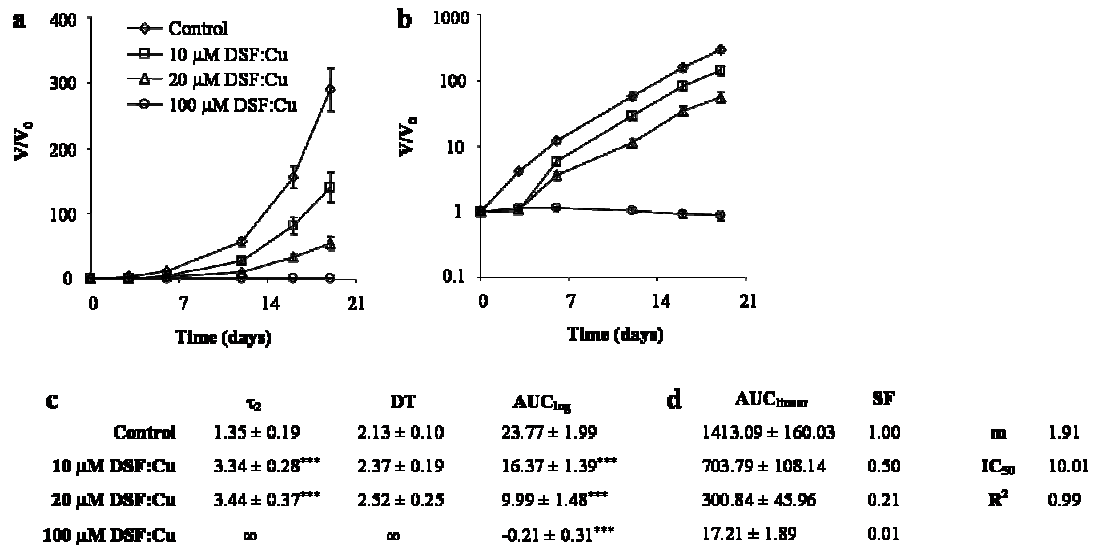


**Figure 65** The effect of DSF:Cu on the growth of UVW/NAT spheroids

UVW/NAT spheroids were treated with various concentrations of DSF:Cu for 24 h. The  $V/V_0$  values are displayed on a linear scale (a) and on a logarithmic scale (b). Data are mean  $\pm$  SEM. (c)  $\tau_2$ , DT and  $\text{AUC}_{\log}$  values were calculated according to Section 6.3.4 and 6.3.5.  $\infty$  indicates that there was not a 2-fold increase in spheroid volume. Data are mean  $\pm$  SEM. The statistical significance of the differences in  $\tau_2$ , DT and  $\text{AUC}_{\log}$  values between groups was determined by non-parametric testing (Kruskal-Wallis followed by Mann-Whitney tests) using SPSS. The medians of  $\tau_2$ , DT and  $\text{AUC}_{\log}$  values of the DSF:Cu-treated groups were compared with those of the control (\*). Three symbols indicate  $p < 0.001$ . (d) The surviving fraction (SF) was calculated using the  $\text{AUC}_{\text{linear}}$  values according to Section 7.3.9.1. The median effect principle was applied to the SF values in order to calculate m and the  $\text{IC}_{50}$  of the effect of  $\gamma$ -radiation according to Section 3.3.5. The coefficient of determination ( $R^2$ ) is a measure of the goodness of the fit of the linear regression of the median effect plot.

In both SK-N-BE(2c) and UVW/NAT spheroids, there was a significant increase in the  $\tau_2$  values without a significant increase in the DT values following treatment with DSF:Cu. This was consistent with the observation in LNCaP spheroids that DSF:Cu affected a sub-population of cells while the unaffected fraction was responsible for regrowth at the later timepoints (Figure 57).

#### 7.4.6.2 The effect of [<sup>131</sup>I]mIBG on the growth of SK-N-BE(2c) and UVW/NAT spheroids

The effect of [<sup>131</sup>I]mIBG as a single agent was studied in SK-N-BE(2c) (Figure 66) and UVW/NAT spheroids (Figure 67). In SK-N-BE(2c) spheroids, the  $\tau_2$  values significantly increased in a dose-dependent manner following treatment with [<sup>131</sup>I]mIBG alone. The  $\tau_2$  values were  $0.93 \pm 0.09$ ,  $1.15 \pm 0.08$  ( $p < 0.05$ ) and  $1.99 \pm 0.22$  days ( $p < 0.001$ ) for untreated control and for the groups treated with 1 and 5 MBq/ml [<sup>131</sup>I]mIBG, respectively (Figure 66c). The increase in DT values and the decrease in  $AUC_{\log}$  values were also directly related to [<sup>131</sup>I]mIBG radioactivity concentration (Figure 66c). The  $IC_{50}$  value for [<sup>131</sup>I]mIBG in SK-N-BE(2c) spheroids was 1.48 MBq/ml (Figure 66d).

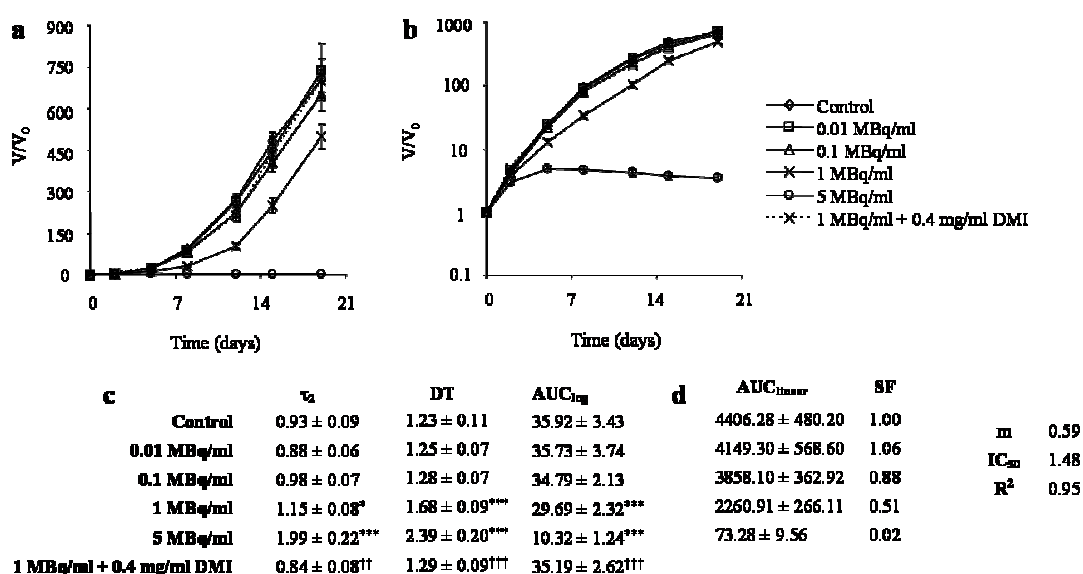


**Figure 66** The effect of [<sup>131</sup>I]mIBG on the growth of SK-N-BE(2c) spheroids

SK-N-BE(2c) spheroids were treated with [<sup>131</sup>I]mIBG for 2 h. Desipramine (DMI), an inhibitor of the cellular uptake of [<sup>131</sup>I]mIBG, was administered to the spheroids simultaneously with [<sup>131</sup>I]mIBG. Data are mean  $\pm$  SEM. The  $V/V_0$  values are displayed on a linear scale (a) and on a logarithmic scale (b). (c)  $\tau_2$ , DT and  $AUC_{\log}$  values were calculated according to Section 6.3.4 and 6.3.5. Data are mean  $\pm$  SEM. The statistical significance of the differences in  $\tau_2$ , DT and  $AUC_{\log}$  values between groups was determined by non-parametric testing (Kruskal-Wallis followed by Mann-Whitney tests) using SPSS. The median of  $\tau_2$ , DT and  $AUC_{\log}$  values of the [<sup>131</sup>I]mIBG-treated groups were compared with those of the control (\*). The medians of  $\tau_2$ , DT and  $AUC_{\log}$  values of the group treated with 1 MBq/ml [<sup>131</sup>I]mIBG in the presence of 0.4 mg/ml DMI were compared with those of the group treated with 1 MBq/ml [<sup>131</sup>I]mIBG alone ( $\dagger$ ). One symbol indicates  $p < 0.05$ , two symbols indicate  $p < 0.01$  and three symbols indicate  $p < 0.001$ . (d) SF values were calculated using the  $AUC_{linear}$  values according to Section 7.3.9.1. The median effect principle was applied to the SF values in order to calculate  $m$  and the  $IC_{50}$  of the effect of  $\gamma$ -radiation according to Section 3.3.5. The coefficient of determination  $R^2$  is a measure of the goodness of the fit of the linear regression of the median effect plot.

Secondly, the inhibitor of [<sup>131</sup>I]mIBG uptake, desipramine (DMI), was used to determine the NAT-specificity of growth inhibition by [<sup>131</sup>I]mIBG. The treatment with 0.4 mg/ml DMI abolished the growth delay induced by 1 MBq/ml [<sup>131</sup>I]mIBG (Figure 66c). The  $\tau_2$  values were  $0.93 \pm 0.09$ ,  $1.15 \pm 0.08$  and  $0.84 \pm 0.08$  days for untreated controls, the group treated with 1 MBq/ml [<sup>131</sup>I]mIBG alone and the group treated with 1 MBq/ml [<sup>131</sup>I]mIBG in the presence of 0.4 mg/ml DMI, respectively (Figure 66c). Moreover, the comparison of the medians of  $\tau_2$ , DT and  $AUC_{\log}$  values of the group treated with 1 MBq/ml [<sup>131</sup>I]mIBG alone with those of the group treated with 1 MBq/ml [<sup>131</sup>I]mIBG in the presence of 0.4 mg/ml DMI was statistically significant ( $p < 0.01$ ). This result demonstrated the NAT-specificity of growth inhibition by 1 MBq/ml [<sup>131</sup>I]mIBG. This radioactivity concentration was used in combination with DSF:Cu in subsequent experiments.

The evaluation of the effect of [<sup>131</sup>I]mIBG on the growth of UVW/NAT spheroids is depicted in Figure 67. The statistically significant increase in  $\tau_2$  and DT values and the statistically significant decrease in  $AUC_{\log}$  values following treatment of UVW/NAT spheroids with increasing radioactivity concentrations of [<sup>131</sup>I]mIBG demonstrated the dose-dependent effect of [<sup>131</sup>I]mIBG (Figure 67). For instance, the  $\tau_2$  values were  $1.25 \pm 0.10$ ,  $2.30 \pm 0.27$  ( $p < 0.001$ ) and  $3.07 \pm 0.52$  days ( $p < 0.001$ ) for untreated control and the group treated with 0.5 and 5 MBq/ml [<sup>131</sup>I]mIBG, respectively (Figure 67c). The  $IC_{50}$  value for [<sup>131</sup>I]mIBG was 0.46 MBq/ml in UVW/NAT spheroids (Figure 67d). Based on this result, 0.5 MBq/ml [<sup>131</sup>I]mIBG was used in combination with DSF:Cu in subsequent experiments.

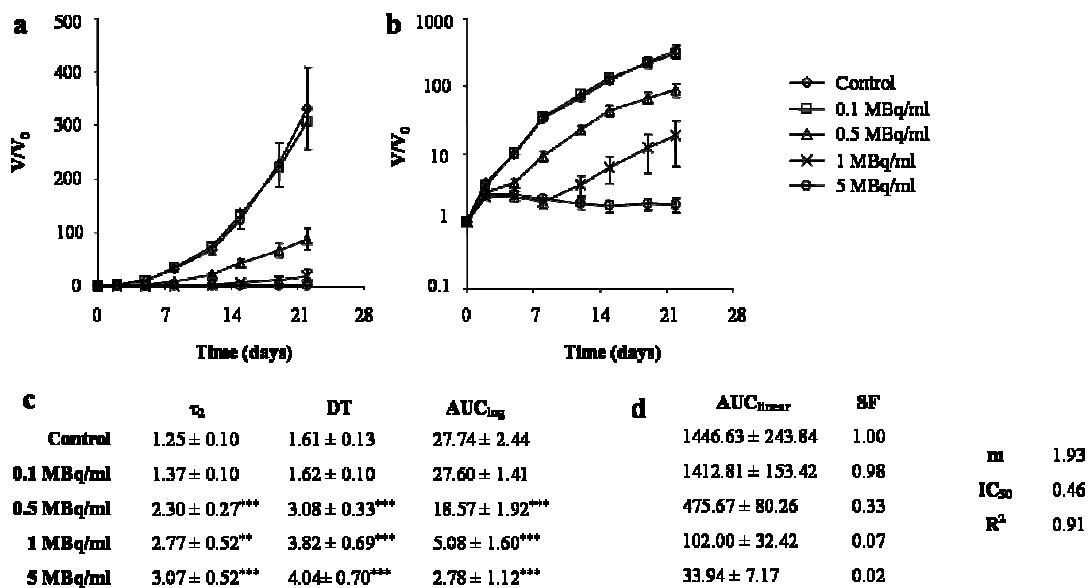
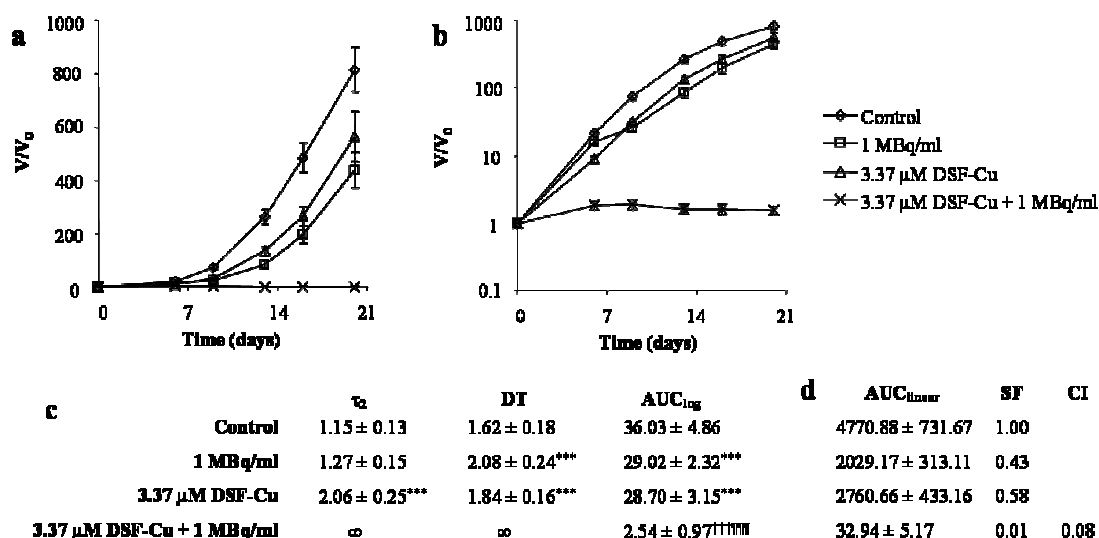


Figure 67 The effect of [<sup>131</sup>I]mIBG on the growth of UVW/NAT spheroids

UVW/NAT spheroids were treated with [<sup>131</sup>I]mIBG for 2 h. Data are mean ± SEM. The V/V<sub>0</sub> values are displayed on a linear scale (a) and on a logarithmic scale (b). (c) τ<sub>2</sub>, DT and AUC<sub>log</sub> values were calculated according to Section 6.3.4 and 6.3.5. Data are mean ± SEM. The statistical significance of the differences in τ<sub>2</sub>, DT and AUC<sub>log</sub> values between groups was determined by non-parametric testing (Kruskal-Wallis followed by Mann-Whitney tests) using SPSS. The median of τ<sub>2</sub>, DT and AUC<sub>log</sub> values of the [<sup>131</sup>I]mIBG-treated groups were compared with those of the control (\*). Two symbols indicate p < 0.01 and three symbols indicate p < 0.001. (d) SF values were calculated using the AUC<sub>linear</sub> values according to Section 7.3.9.1. The median effect principle was applied to the SF values in order to calculate m and the IC<sub>50</sub> of the effect of γ-radiation according to Section 3.3.5. The coefficient of determination R<sup>2</sup> is a measure of the goodness of the fit of the linear regression of the median effect plot.

#### 7.4.7 The effect of DSF:Cu in combination with [<sup>131</sup>I]mIBG in SK-N-BE(2c) and UVW/NAT spheroids

The combination of DSF:Cu and [<sup>131</sup>I]mIBG sterilised SK-N-BE(2c) spheroids as indicated by the failure to attain a doubling in spheroid volume over the course of the experiment (Figure 68c). The only quantifying parameter of spheroid growth was therefore the area under the curve. The AUC<sub>log</sub> value corresponding to treatment with the combination of DSF:Cu and [<sup>131</sup>I]mIBG (2.54 ± 0.97) was significantly smaller than those of the groups treated with either DSF:Cu alone (28.70 ± 3.15) (p < 0.001) or [<sup>131</sup>I]mIBG alone (29.02 ± 2.32) (p < 0.001) (Figure 68c), indicating enhancement of [<sup>131</sup>I]mIBG kill by DSF:Cu. The combination index was 0.08, indicative of a strong supra-additive interaction (Figure 68d).



**Figure 68** The effect of DSF:Cu on the growth delay induced by [<sup>131</sup>I]mIBG in SK-N-BE(2c) spheroids SK-N-BE(2c) spheroids were treated with [<sup>131</sup>I]mIBG for 2 h or with DSF:Cu for 24 h as single agents. For the combination of DSF:Cu with [<sup>131</sup>I]mIBG, SK-N-BE(2c) spheroids were treated with [<sup>131</sup>I]mIBG for 2 h in the presence of DSF:Cu, washed in PBS and treated with DSF:Cu alone for a further 22 h. The V/V<sub>0</sub> values are displayed on a linear scale (a) and on a logarithmic scale (b). Data are mean ± SEM. (c) τ<sub>2</sub>, DT and AUC<sub>log</sub> values were calculated according to Section 6.3.4 and 6.3.5. Data are mean ± SEM. ∞ indicated that

the spheroids failed to double their volume. The statistical significance of the differences in  $\tau_2$ , DT and  $AUC_{log}$  values between groups was determined by non-parametric testing (Kruskal-Wallis followed by Mann-Whitney tests) using SPSS. The medians of  $\tau_2$ , DT and  $AUC_{log}$  values of the groups treated with DSF:Cu or  $[^{131}\text{I}]\text{mIBG}$  as single agents were compared with those of the control (\*). The medians of  $\tau_2$ , DT and  $AUC_{log}$  values of the groups treated with a combination of  $[^{131}\text{I}]\text{mIBG}$  with DSF:Cu were compared with those of the groups treated with  $[^{131}\text{I}]\text{mIBG}$  alone (¶) and to those of the group treated with DSF:Cu alone (†). Three symbols indicate  $p < 0.001$ . (d) The CI values were calculated as explained in Section 7.3.9.2 using the  $AUC_{linear}$  values of the combination. The calculation was based on the parameters  $m$  and  $IC_{50}$  calculated for the single agents (Figure 64d and Figure 66d).

The combination of DSF:Cu and  $[^{131}\text{I}]\text{mIBG}$  sterilised UVW/NAT spheroids as indicated by the failure to attain a doubling in spheroid volume over the course of the experiment (Figure 69c). The  $AUC_{log}$  value corresponding to treatment with the combination of DSF:Cu and  $[^{131}\text{I}]\text{mIBG}$  ( $-0.42 \pm 1.09$ ) was significantly smaller than those of the groups treated with either DSF:Cu alone ( $28.50 \pm 2.89$ ) ( $p < 0.001$ ) or  $[^{131}\text{I}]\text{mIBG}$  alone ( $33.39 \pm 4.92$ ) ( $p < 0.001$ ) (Figure 69c), indicating enhancement of  $[^{131}\text{I}]\text{mIBG}$  kill by DSF:Cu. The combination index was 0.13, indicative of a strong supra-additive interaction (Figure 69d).

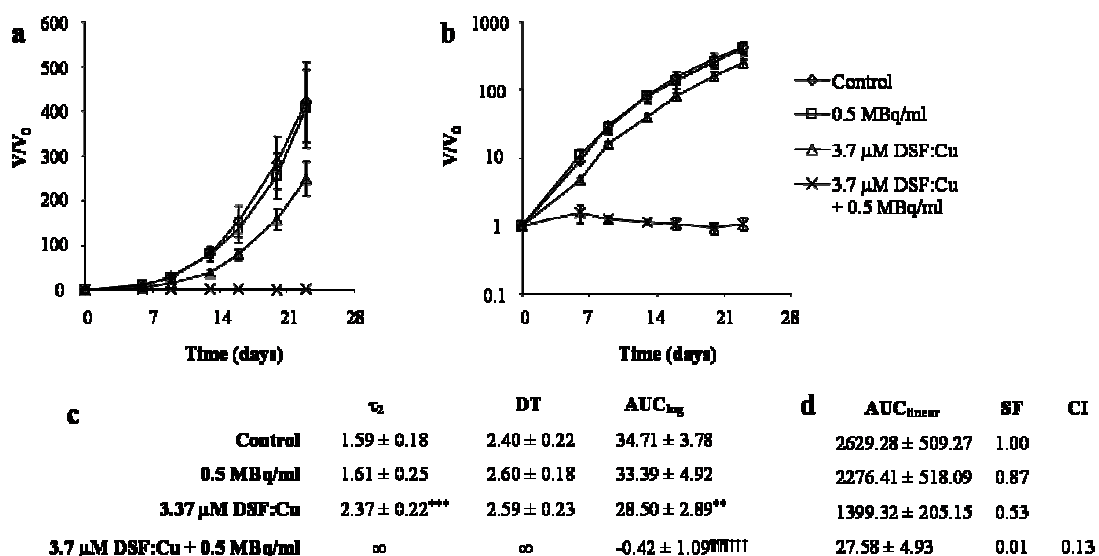


**Figure 69** The effect of DSF:Cu on the growth delay induced by  $[^{131}\text{I}]\text{mIBG}$  in UVW/NAT spheroids. UVW/NAT spheroids were treated with  $[^{131}\text{I}]\text{mIBG}$  for 2 h or with DSF:Cu for 24 h as single agents. For the combination of DSF:Cu with  $[^{131}\text{I}]\text{mIBG}$ , UVW/NAT spheroids were treated with  $[^{131}\text{I}]\text{mIBG}$  for 2 h in the presence of DSF:Cu, washed in culture medium and treated with DSF:Cu alone for a further 22 h. The  $V/V_0$  values are displayed on a linear scale (a) and on a logarithmic scale. Data are mean  $\pm$  SEM. (c)  $\tau_2$ , DT and  $AUC_{log}$  values were calculated according to Section 6.3.4 and 6.3.5. Data are mean  $\pm$  SEM.  $\infty$  indicated that the spheroids failed to double their volume. The statistical significance of the differences in  $\tau_2$ , DT and  $AUC_{log}$  values between groups was determined by non-parametric testing (Kruskal-Wallis followed by Mann-Whitney tests) using SPSS. The medians of  $\tau_2$ , DT and  $AUC_{log}$  values of the groups treated with DSF:Cu or  $[^{131}\text{I}]\text{mIBG}$  as single agents were compared with those of the control (\*). The medians of  $\tau_2$ , DT

and  $AUC_{\log}$  values of the groups treated with a combination of [ $^{131}\text{I}$ ]mIBG with DSF:Cu were compared with those of the groups treated with [ $^{131}\text{I}$ ]mIBG alone (¶) and to those of the group treated with DSF:Cu alone (†). Three symbols indicate  $p < 0.001$ . (d) The CI values were calculated as explained in Section 7.3.9.2 using the  $AUC_{\text{linear}}$  values of the combination. The calculation was based on the parameters  $m$  and  $IC_{50}$  calculated for the single agents (Figure 65d and Figure 67d).

These results demonstrated the strong synergism between DSF:Cu and two radiopharmaceuticals ([ $^{131}\text{I}$ ]MIP-1095 and [ $^{131}\text{I}$ ]mIBG) in spheroids derived from three cell lines, confirming the synergistic interaction between DSF:Cu and  $\gamma$ -radiation described in Section 4.4.3. Moreover, the finding of a supra-additive interaction between DSF:Cu and two radiopharmaceuticals in spheroids supported the strategy of using DSF:Cu as an adjuvant of targeted radiotherapy.

## 7.5 Discussion and summary of the results

The effect of [ $^{131}\text{I}$ ]MIP-1095 on the growth of LNCaP spheroids was characterised prior to the investigation of the combination with DSF:Cu. It was shown that the maximal PSMA-specific binding of [ $^{131}\text{I}$ ]MIP-1095 occurred at radioactivity concentrations less than 1 MBq/ml within 2 h (Figure 60a and Figure 60b). Moreover, the internalisation of [ $^{131}\text{I}$ ]MIP-1095 by endocytosis was demonstrated by co-incubation with CHQ, an inhibitor of the recycling of endosomes to the cell membrane (Figure 60d). The internalisation of [ $^{131}\text{I}$ ]MIP-1095 within endosomes would indicate that the retention of the radiopharmaceutical would be of greater duration than if [ $^{131}\text{I}$ ]MIP-1095 only bound to the PSMA receptor but was not intracellularly concentrated. In turn, prolonged intracellular retention should result in an increased absorbed radiation dose. Secondly, since [ $^{131}\text{I}$ ]MIP-1095 is trapped in the intracellular space of the targeted cells, thus reducing leakage, improved imaging of prostate carcinoma is expected. Accordingly, it has been shown that [ $^{123}\text{I}$ ]MIP-1072 and [ $^{123}\text{I}$ ]MIP-1095 were successfully used as imaging agents of prostate carcinomas<sup>61</sup>.

Moreover, it was also shown that internalisation was dependent on the metabolic status of the cells since KCN, an inhibitor of mitochondrial ATP production, inhibited intracellular concentration of [ $^{131}\text{I}$ ]MIP-1095 (Figure 60d). This result has therapeutic implications for the scheduling of [ $^{131}\text{I}$ ]MIP-1095 with radiosensitisers which may be cytotoxic in their own right. It is anticipated that a cytotoxic compound administered prior to [ $^{131}\text{I}$ ]MIP-1095 would reduce the metabolic activity of the target cells, thus leading to sub-optimal internalisation of [ $^{131}\text{I}$ ]MIP-1095. However, it was shown that 3.37  $\mu\text{M}$  DSF:Cu, which

was toxic to LNCaP spheroids (Figure 57, Figure 59 and Figure 62), did not inhibit the internalisation of [<sup>131</sup>I]MIP-1095 (Figure 60c). Although pre-treatment of LNCaP spheroids with DSF:Cu potentiated the growth delay induced by [<sup>131</sup>I]MIP-1095 (Figure 63), the enhancement was not as efficient as that induced by the simultaneous administration of DSF:Cu and [<sup>131</sup>I]MIP-1095 (Figure 63c). This was indicated by the significantly smaller DT value compared with that of the combination schedule consisting of the simultaneous administration of DSF:Cu and [<sup>131</sup>I]MIP-1095. Since both  $\tau_2$  and  $AUC_{\log}$  parameters did not significantly differ between the two schedules of administrations, the difference in DT value may have been an artefact due to the initial deep in the growth curve following the combination treatment consisting of pre-treatment with DSF:Cu followed by [<sup>131</sup>I]MIP-1095 (Figure 63c). Nevertheless, simultaneous administration of [<sup>131</sup>I]MIP-1095 and DSF:Cu induced a greater growth delay than the alternative schedules of delivery. After a single dose of disulfiram, maximal plasma concentration in patients is reached within 10 h<sup>161</sup>. Further investigation of the scheduling of administration of DSF:Cu with [<sup>131</sup>I]MIP-1095 is recommended in order to achieve optimal tumour concentration of both compounds at the same time.

The pattern of growth of spheroids was dependent on the treatment administered. DSF:Cu induced an initial growth delay followed by a proliferating phase parallel to that of the untreated control. This was manifest by increasing  $\tau_2$  values in response to increasing DSF:Cu concentrations while the DT values remained constant in LNCaP (Figure 57c), SK-N-BE(2c) (Figure 64c) and UVW/NAT spheroids (Figure 65c). This pattern is consistent with the initial killing of a sub-population of cells within spheroids whereas the unaffected cell fraction is responsible for the regrowth at later timepoints. In contrast,  $\gamma$ -radiation treatment did not induce growth delay in LNCaP spheroids (Figure 58). Instead, the growth rate of the proliferating phase was reduced from day 0, as indicated by the concomitant increases in  $\tau_2$  and DT values (Figure 58c). This pattern was consistent with the delivery of a dose of radiation to every cell of the spheroid. However, this experiment may represent a snapshot of the behaviour of the LNCaP cells soon after  $\gamma$ -radiation treatment; the spheroids may start to grow at a similar growth rate as the untreated control after 22 days (Figure 58).

The spheroid growth pattern following radiation treatment was dependent on the cell line used. [<sup>131</sup>I]MIP-1095 decreased the growth rate of LNCaP spheroids from day 0 without sterilising the spheroids up to 10 MBq/ml (Figure 61). The effect of  $\gamma$ -radiation in LNCaP

spheroids produced similar growth curve patterns in which the growth rate was affected from day 0 (Figure 58a). The SK-N-BE(2c) and UVW/NAT spheroid growth patterns following [<sup>131</sup>I]mIBG treatment were different from that of LNCaP spheroids following [<sup>131</sup>I]MIP-1095 treatment. [<sup>131</sup>I]mIBG sterilised SK-N-BE(2c) spheroids one week following treatment (Figure 66) or sterilised UVW/NAT spheroids 3 days following treatment (Figure 67). In both SK-N-BE(2c) and UVW/NAT spheroids, a phase of spheroid growth preceded sterilisation. This growth pattern after treatment with [<sup>131</sup>I]mIBG was also observed after treatment of SK-N-BE(2c) and UVW/NAT spheroids with  $\gamma$ -radiation (data not shown). The similarity of spheroid growth patterns between the two modes of radiation dose delivery (<sup>131</sup>I-labelled radiopharmaceutical or external beam  $\gamma$ -radiation) in three cell lines indicated that dose rate had negligible influence on regrowth delay of spheroids. LNCaP spheroids are slow growing (mean DT = 2.75 days) compared with SK-N-BE(2c) (mean DT = 1.36 days) and UVW/NAT (mean DT = 2.05 days). Although parameters other than growth rate influence response to radiation, the slower growth rate of LNCaP spheroids may explain in part the absence of sterilisation by 10 MBq/ml [<sup>131</sup>I]MIP-1095 compared with sterilisation after treatment of SK-N-BE(2c) and UVW/NAT spheroids with 5 MBq/ml [<sup>131</sup>I]mIBG<sup>287</sup>.

A radiosensitiser *in vitro* is defined as an agent which enhances the cell killing of a particular radiation dose<sup>82</sup>. In chapter 4, this definition was applied to radiation survival curves, in which radiosensitisation was demonstrated when the surviving fraction after  $\gamma$ -radiation treatment in the presence of DSF:Cu was lower than that after treatment with the same dose of  $\gamma$ -radiation alone. By extrapolation, in a spheroid growth delay experiment, radiosensitisation may be defined as the reduction of the area under the curve after radiation treatment in the presence of a radiosensitiser compared with the area under the curve after treatment with the same dose of radiation alone. A treatment may affect the growth of spheroids in various ways. A sub-population of cells within a spheroid may be especially susceptible or resistant to a treatment modality. For instance, a drug with poor penetrability would only be toxic to the external cellular layer of a spheroid, thus sparing more deeply located cells. This mode of action would lead to an initial delay in the growth of the treated spheroids compared with that of untreated spheroids with subsequent parallel growth curves. The parallelism of the growth curves of treated versus untreated spheroids at later timepoints results from the similar growth rate of the cells that have been unaffected by the treatment as that of the cells of untreated spheroids.

Alternatively, the totality of the cells within the spheroid may be affected by a treatment. If the treatment intensity is high enough, sterilisation occurs. Otherwise, the growth rate of all the cells in the spheroids is reduced, which results in the growth curve of treated spheroids deviating from that of the untreated control. Whether a treatment affects all or a smaller proportion of cells within a spheroid, the result is always the decrease in the area under the curve. The effect of DSF:Cu on the growth delay induced by radiation treatment was investigated in LNCaP, UVW/NAT and SK-N-BE(2c) spheroids using the following parameters:  $\tau_2$ , DT and  $AUC_{\log}$ . DSF:Cu potentiated the effect of  $\gamma$ -radiation, [ $^{131}\text{I}$ ]mIBG and [ $^{131}\text{I}$ ]MIP-1095 as indicated by a reduction in  $AUC_{\log}$  and an increase in  $\tau_2$  and DT values compared with radiation treatment alone in LNCaP, SK-N-BE(2c) and UVW/NAT spheroids.

Moreover, it is the purpose of the combination index and the isobologram methods of synergy analyses to quantify the effect of agent B upon A and, simultaneously, that of agent A upon B in the combination A+B. In all three cell lines, the CI values ranged from 0.08 to 0.56 for treatments consisting of 3.37  $\mu\text{M}$  DSF:Cu with external beam  $\gamma$ -radiation or targeted radiotherapy. This indicated supra-additivity regardless of the mode of radiation delivery or the cell line used (Figure 59, Figure 62, Figure 68 and Figure 69). In LNCaP spheroids, 1  $\mu\text{M}$  and 3.37  $\mu\text{M}$  DSF:Cu yielded CI values of 1.21 and 0.56, respectively, when given in combination with  $\gamma$ -radiation. This suggested that supra-additivity was more likely to occur at DSF:Cu concentrations higher than 1  $\mu\text{M}$ . The tendency toward synergy associated with increased concentrations of DSF:Cu was also observed in the analysis of DSF:Cu-induced radiosensitisation in SK-N-BE(2c) and UVW/NAT monolayers (Table 7).

The concentration of DSF:Cu (1  $\mu\text{M}$ ), which is achievable in the plasma in patients<sup>161</sup>, affected the growth of LNCaP spheroids in a manner that was dependent on the mode of radiation delivery with which it was combined. The CI value was 1.21 when combined with external  $\gamma$ -radiation treatment (Figure 59), suggesting infra-additivity, whereas the CI value was 0.05 when combined with targeted radiotherapy in the form of [ $^{131}\text{I}$ ]MIP-1095, suggesting supra-additivity (Figure 62). In these experiments, the effect of 3 Gy of  $\gamma$ -radiation and that of 0.37 MBq/ml [ $^{131}\text{I}$ ]MIP-1095 were similar with respect to cytotoxicity. SF values were 0.25 (Figure 59) and 0.26 (Figure 62), respectively. Thus, the effects of the combinations were comparable. These observations suggested that DSF:Cu was a better enhancer of the efficacy of targeted radiotherapy than that of external beam

radiotherapy. However, in a separate experiment determining the dose-response relationship of [ $^{131}\text{I}$ ]MIP-1095 in LNCaP spheroids (Figure 61), the SF value obtained following treatment with 0.37 MBq/ml [ $^{131}\text{I}$ ]MIP-1095 was 0.58, twice as much as in the combination experiment (Figure 62). This indicated that the effect of [ $^{131}\text{I}$ ]MIP-1095 as a single agent, depicted in the combination experiment (Figure 62), was greater than that observed in the evaluation of the dose-response relationship of [ $^{131}\text{I}$ ]MIP-1095 alone (Figure 61). The CI value is the sum of the ratios of the doses of each agent within the combination by their doses which induce the same effect as single agents. Since the CI value was calculated based on an effect of [ $^{131}\text{I}$ ]MIP-1095 as a single agent which was underestimated, the CI value of the combination of [ $^{131}\text{I}$ ]MIP-1095 with DSF:Cu was likely to be overestimated (Figure 62).

The second discrepancy of this dataset was the surviving fraction obtained after treatment of UVW/NAT with [ $^{131}\text{I}$ ]mIBG. The determination of the dose-response relationship of [ $^{131}\text{I}$ ]mIBG (Figure 67) and the evaluation of the potentiating effect of DSF:Cu in combination with [ $^{131}\text{I}$ ]mIBG yielded different surviving fraction values (Figure 69). The surviving fractions obtained in response to treatment with 0.5 MBq/ml [ $^{131}\text{I}$ ]mIBG alone were 0.33 and 0.87 in Figure 67 and Figure 69, respectively. Since the CI value of the combination of DSF:Cu and [ $^{131}\text{I}$ ]mIBG was calculated based on an effect of [ $^{131}\text{I}$ ]mIBG as a single agent which was overestimated (Figure 67), the CI value was likely to be underestimated. Thus, the combination of 0.5 MBq/ml [ $^{131}\text{I}$ ]mIBG with 3.37  $\mu\text{M}$  DSF:Cu should be even more supra-additive than indicated (Figure 69).

Despite the discrepancies observed in the calculations of the surviving fractions based on the  $\text{AUC}_{\text{linear}}$  values, generally there was agreement among experimental results. For instance, the surviving fractions in response to the treatment of LNCaP spheroids with 1  $\mu\text{M}$  DSF:Cu in the three separate experiments were 0.63, 0.68 and 0.74 (Figure 57d, Figure 59d and Figure 62d). Similarly, the  $\tau_2$  values of the untreated SK-N-BE(2c) spheroids were 1.11, 0.93 and 1.15 days and the DT values were 1.93, 1.23 and 1.62 days (Figure 64c, Figure 66c and Figure 68c). Due to time constraint, every determination of spheroid response to specific therapy was embodied in a single experiment. A maximum of 24 spheroids was evaluated in every treatment group. With the exception of the evaluation of the effect of DSF:Cu in combination with [ $^{131}\text{I}$ ]MIP-1095 on the growth of LNCaP spheroids (Figure 62), all other experimental determinations of potentiation of radiation-induced growth delay constituted single experiments. Nonetheless, regardless of cell line

(LNCaP, SK-N-BE(2c) or UVW/NAT), regardless of mode of radiation delivery (external beam or radiopharmaceutical) and regardless of the tumour cell culture (spheroids or monolayers), DSF:Cu consistently enhanced the radiation kill in a supra-additive manner.

The lack of reproducibility of the experiments resulted in the variability of the surviving fractions that was not suitable for the application of the median effect principle and the subsequent calculation of CI values. For instance, this was evident by the discrepancies between the surviving fraction calculated following treatment of UVW/NAT spheroids with 0.5 MBq/ml [<sup>131</sup>I]mIBG (SF = 0.33 Figure 67c versus SF = 0.87 Figure 69c). Thus, the calculation of a CI value based on individual spheroid growth delay experiments is not an accurate assessment of the efficacy of a combination treatment. A faster alternative method which measures the potentiation of the radiation kill would be as follows. First, the spheroids would be treated with drug alone, radiation alone or combination of drug and radiation. Secondly, the spheroids would be enzymatically dissociated into single cells and clonogenic assay performed. The median effect principle and the calculation of CI values would be directly applicable to the surviving fractions derived from clonogenic assay. However, LNCaP cells do not form colonies, thus such a method is not suitable for the determination of modulation of the toxicity of [<sup>131</sup>I]MIP-1095.

However, the determination of growth delay of spheroids is valuable in assessing subtle aspects of the efficacy of combination treatment. For instance, the comparison between the  $\tau_2$  and the DT values was used to elucidate the existence of an anti-tumour effect which was not immediately apparent but was manifest several days after the initiation of drug or radiation treatment. Spheroids, rather than cellular monolayers, allowed an assessment of the potential efficacy of novel therapy of microscopic metastases – the type of malignant disease against which targeted radionuclide treatment is expected to be most effective. In the final chapter, the use of the spheroid model is described for the comparison of the ability of various drugs to potentiate radiation-induced spheroid growth delay.

## 8 Comparison of the ability of drugs to potentiate the growth delay induced by $\gamma$ -radiation and [ $^{131}\text{I}$ ]MIP-1095 in spheroids

### 8.1 Introduction

A promising means of maximising the efficacy of targeted radiotherapy is by combination with radiosensitisers<sup>44,91</sup>. Clinical trials should be designed based on the *in vitro* assessment of the radiosensitising potential of chemotherapeutic agents. The latter studies should be carried out in spheroids which are representative of micrometastases in their prevascular stage of development. Moreover, these cellular aggregates are similar to the size class of malignant disease which is optimally sensitive to treatment with targeted radionuclides<sup>14</sup>.

The results of the screening of five radiosensitisers in LNCaP spheroids in combination with  $\gamma$ -radiation treatment and in combination with the radiopharmaceutical [ $^{131}\text{I}$ ]MIP-1095 will be presented. A description is provided of the variety of mechanisms underlying the radiosensitisation engendered by the series of drugs tested. Then, the modification of the growth delay induced by  $\gamma$ -radiation or [ $^{131}\text{I}$ ]MIP-1095 by each drug will be analysed by the  $\tau_2$ , DT and  $\text{AUC}_{\log}$  parameters as described in Section 6.3.4 and 6.3.5. In the last part of this chapter, an attempt is made to rank the enhancement of  $\gamma$ -radiation-induced and [ $^{131}\text{I}$ ]MIP-1095-induced spheroid growth delay by the drugs using the specific growth delay (SGD) value.

#### 8.1.1 Nutlin-3

The small molecule nutlin-3 (FW 581.49 g/mol) is a cis-imidazoline analogue which inhibits the interaction between murine double minute 2 (MDM2) and the tumour suppressor protein p53<sup>288</sup>. Under unstressed conditions, the binding of MDM2 to the transactivation domain of p53 inhibits p53 transcriptional activity. Furthermore, MDM2 is an ubiquitin ligase which promotes proteasomal degradation of p53. In response to radiation, the phosphorylation of p53 results in its release from MDM2. In turn, p53 triggers cell cycle arrest in G1 and promotes the repair of DNA damage. Alternatively, if the extent of DNA damage is greater than the capacity of the DNA repair machinery, radiation-induced p53 activation may result in apoptotic cell death<sup>289</sup>. Once activated, p53 also stimulates the transcription of the MDM2 gene. The resulting negative feedback prevents aberrant p53-induced apoptosis. It has been shown that the inhibition of MDM2 interaction with p53 by nutlin-3 radiosensitises tumour cells, presumably through increased apoptotic cell death<sup>290</sup>.

### 8.1.2 Olaparib

Poly(ADP-ribose)polymerase 1 (PARP-1) is a sensor of SSB and a signalling to the DNA repair machinery. PARP-1 is recruited at the site of DNA damage where it catalyses the binding of poly(ADP-ribose) polymers to histones, a process that requires the reduction of nicotinamide adenine dinucleotide (NAD<sup>+</sup>) to NADH. The branching structure of the positively charged ADP-ribose polymer opens up the chromatin structure, thus allowing access of the DNA repair machinery to the damaged sites and preventing DNA replication<sup>88</sup>. The small molecule olaparib (FW 435.08 g/mol) has a moiety similar to nicotinamide which confers inhibitory properties against PARP-1 enzymatic activity. Olaparib's  $K_i$  value is 5 nM<sup>291</sup>. Several studies have demonstrated the radiosensitising properties of olaparib in replicating cells, especially in those with a deficiency in the repair of DSB<sup>89,292</sup>. These studies suggest that the radiosensitising mechanism of olaparib was the increased rate of SSB conversion to DSB during DNA replication<sup>89,292</sup>.

### 8.1.3 AZD7762

The small molecule AZD7762 (FW 362.4 g/mol) is a thiophene carboxamide urea which inhibits the kinase activity of Chk1 with a  $K_i$  value of 3.6 nM<sup>293</sup>. Although data were not provided, the authors stated that AZD7762 inhibits Chk2 with the same potency as Chk1<sup>293</sup>. As a result of Chk1/2 inhibition, AZD7762 abrogates the G2 arrest machinery following treatment with gemcitabine<sup>293</sup>. AZD7762 has also been shown to radiosensitise a wide range of cell lines. In this report, the DEF values ranged from 1.05 to 1.2 in cell lines harbouring wild type p53 whereas the DEF values ranged from 1.21 to 1.7 in cell lines with a mutated version of p53<sup>294</sup>. The authors suggested that, due to the G2 arrest-inhibitory property of AZD7762, cells lacking a functional G1 arrest machinery, such as p53 mutated cells, would be more readily radiosensitised by treatment with AZD7762. However, a second study reported the radiosensitising effect of AZD7762 in the p53 wild type cell line H460 (human large cell lung carcinoma) as indicated by a DEF value of 1.5<sup>295</sup>. The observation of a DEF value of 1.5 in a p53 wild type cell line, which was in the same range as the DEF values obtained in p53 mutated cell lines (1.21 – 1.7) suggested that the p53 status of a cancer cell is not the only determinant of radiosensitisation induced by AZD7762.

### 8.1.4 Topotecan

The role of topoisomerase I is to alleviate the torsional stress generated as the replication fork advances during replication of DNA. Topoisomerase I cleaves one strand of DNA,

allowing the second strand to pass through the cleavage site, before re-sealing the nick. During this process, an intermediate state is created by the formation of a transient covalent bond between topoisomerase I and the cleaved strand of DNA, the so-called “cleavable complex”.

The small molecule topotecan (FW 457.9 g/mol) is a derivative of camptothecin, an alkaloid extract of the tree *Camptotheca acuminata* with antitumour properties<sup>296</sup>. The fork collision model has been described to explain topotecan cytotoxicity<sup>297</sup>. Topotecan binds to and stabilises the normally transient cleavable complex consisting of topoisomerase I and cleaved DNA. As the replication fork advances, the collision with the stalled cleavable complex (consisting of topotecan, topoisomerase I and cleaved DNA) results in the formation of DSB, leading to cell cycle arrest and cell death. Furthermore, topotecan has recently been shown to be a radiosensitiser<sup>92,298</sup>. It has also been observed that topoisomerase I is involved in the recruitment of the DNA repair machinery to sites of DNA strand breakage<sup>299</sup>. Therefore the radiosensitising mechanism of topotecan may not only result from the generation of DSB during DNA replication but may also be due to the inhibition of DNA repair.

### **8.1.5 Bortezomib**

The small molecule bortezomib (FW 384.24 g/mol) is a boron-based dipeptide with binding affinity for the 26S proteasome, the organelle responsible for the controlled enzymatic degradation of proteins. Bortezomib inhibits the catalytic activity of the 26S proteasome with a  $K_i$  value of 0.56 nM<sup>300</sup>. Many cellular pathways are regulated by the proteasome: inflammation, antigen presentation, cell cycle regulation and cell death. For instance, proteasomal degradation of I $\kappa$ B is required for the activation of the transcription factor NF- $\kappa$ B which is up-regulated in response to radiation treatment and is associated with radioresistance<sup>301</sup>. It has been demonstrated that bortezomib radiosensitises cancer cells via the prevention of NF- $\kappa$ B activation<sup>302</sup>, which resulted in apoptosis, and also via the down-regulation of the DNA damage response<sup>303</sup>.

### **8.1.6 Justification of the concentrations of the drugs examined**

The concentrations of the drugs used in the evaluation of the modulation of  $\gamma$ -radiation-induced or [<sup>131</sup>I]MIP-1095-induced spheroid growth delay were based on published reports and on the drug concentrations achievable in the plasma of patients (Table 11).

	Target $K_i$	Lowest radiosensitising concentration tested	Plasma concentration achieved
<b>Topotecan</b>	Topoisomerase I	10 nM	7.21-17.03 nM <sup>304</sup>
			2.23-9.06 nM <sup>305</sup>
			24.8 - 108.9 nM <sup>306</sup>
<b>Olaparib</b>	PARP-1 5.5 nM <sup>291</sup>	1 $\mu$ M	0.23 - 2.3 nM <sup>307</sup>
			5.75 $\mu$ M <sup>308</sup>
			11 $\mu$ M <sup>309</sup>
<b>Bortezomib</b>	26S proteasome 0.56 nM <sup>300</sup>	7.5 nM	205.60 nM <sup>310</sup>
			580 nM <sup>311</sup>
<b>Nutlin-3</b>	Mdm2-p53 80.3 nM <sup>288</sup>	10 $\mu$ M	clinical trial in progress
<b>AZD7762</b>	Chk1 3.6 nM <sup>293</sup>	Not radiosensitising at concentrations < 1 $\mu$ M	clinical trial in progress

**Table 11 The plasma concentrations of the evaluated drugs**

The  $K_i$  values, the reported peak plasma concentrations and the concentrations found to be radiosensitising in this chapter are presented. The lowest radiosensitising concentrations tested for every drug-will be described in the respective results Sections.

## 8.2 Aim

- determination and comparison of the capacity of cytotoxic drugs to enhance the growth delay of multicellular tumour spheroids following treatment with  $\gamma$ -radiation or [<sup>131</sup>I]MIP-1095

## 8.3 Materials and methods

### 8.3.1 Spheroid formation and analysis

See sections 6.3.1, 6.3.3, 6.3.4 and 6.3.5.

### 8.3.2 Combined treatments of drugs with $\gamma$ -radiation or [<sup>131</sup>I]MIP-1095

See sections 4.3.4.4 and 7.3.2.4.

### 8.3.3 Calculation of specific growth delay SGD

The growth rate of treated spheroids and untreated controls varied between experiments. Therefore, to enable comparison of the cytotoxicity of single-agent treatments between

separate experiments (drug alone or radiation alone), the specific growth delay resulting from single-agent treatment ( $SGD_{SA}$ ) was calculated using equation (23)<sup>269</sup>:

$$SGD_{SA} = (\tau_2 - \tau_{2 \text{ control}}) / \tau_{2 \text{ control}} \quad (23)$$

where the  $\tau_2$  value is the time required for a 2-fold increase in volume after a particular treatment, as described in Section 6.3.4, and  $\tau_{2 \text{ control}}$  is that of the respective untreated control.

Similarly, the effect of radiation alone varied between experiments. Thus, to enable the comparison of the enhancement of  $\gamma$ -radiation-induced and [<sup>131</sup>I]MIP-1095-induced growth delay by various drugs, the specific growth delay of a combination treatment ( $SGD_C$ ) was compared with the effect of radiation or [<sup>131</sup>I]MIP-1095 treatment alone and calculated using equation (24):

$$SGD_C = (\tau_2 - \tau_{2 \text{ radiation}}) / \tau_{2 \text{ radiation}} \quad (24)$$

where the  $\tau_2$  value is the time required for a 2-fold increase in volume after a particular combination treatment and  $\tau_{2 \text{ radiation}}$  is the  $\tau_2$  value of the  $\gamma$ -radiation or [<sup>131</sup>I]MIP-1095 treatment alone.

### **8.3.4 Statistical analysis of the drug-induced potentiation of $\gamma$ -radiation or [<sup>131</sup>I]MIP-1095**

See section 7.3.8.3.

### **8.3.5 Test for outlying results**

According to the Grubb's test<sup>312</sup>, an outlier is defined as a value within a dataset which deviates from the mean to a significantly greater extent than the standard deviation of the dataset. The Z-score is calculated according to equation (25):

$$Z\text{-score} = \text{ABS}(\text{mean} - \text{value}) / \text{SD} \quad (25)$$

where ABS is the absolute value and indicates that the Z-score is positive and SD is the standard deviation of the dataset containing the tested value.

Then, if the Z-score is greater than a critical Z value, the tested value is defined as an outlier. Examples of critical Z values are found in Table 12 and are depend on the number of observations (n) within the dataset and on the level of statistical significance.

Number of Observations <i>n</i>	5% Significance Level	2.5% Significance Level	1% Significance Level
3	1.15	1.15	1.15
4	1.46	1.48	1.49
5	1.67	1.71	1.75
6	1.82	1.89	1.94
7	1.94	2.02	2.10
8	2.03	2.13	2.22
9	2.11	2.21	2.32
10	2.18	2.29	2.41

**Table 12 Critical Z values at the 1%, 2.5% and 5% levels of significance for dataset containing n observations**

## 8.4 Results

### 8.4.1 Enhancement of the growth delay induced by $\gamma$ -radiation or [<sup>131</sup>I]MIP-1095

#### 8.4.1.1 Nutlin-3

It has been reported that 5 and 10  $\mu$ M nutlin-3 were required for the inhibition of the interaction of MDM2 with p53 which resulted in the increased expression of the p53-target gene p21 in LNCaP monolayers<sup>313</sup>. Secondly, the radiosensitising property of nutlin-3 has been demonstrated in monolayers using concentrations of 3 and 5  $\mu$ M<sup>314-316</sup>. Based on these studies, the potentiation of the growth delay induced by  $\gamma$ -radiation or [<sup>131</sup>I]MIP-1095 was carried out using nutlin-3 concentration of 10  $\mu$ M (Figure 70).

Increased growth delay by treatment with nutlin-3 was indicated by modification of  $\tau_2$ , DT and AUC<sub>log</sub> values. The toxicities of both  $\gamma$ -radiation (Figure 70a) and [<sup>131</sup>I]MIP-1095 (Figure 70b) were enhanced by inclusion of 10  $\mu$ M nutin-3 in combination treatments. The AUC<sub>log</sub> value of the combination of 10  $\mu$ M nutlin-3 with 3 Gy  $\gamma$ -radiation was  $3.96 \pm 1.09$  compared with  $15.58 \pm 1.46$  for 3 Gy  $\gamma$ -radiation alone ( $p < 0.001$ ) and  $21.57 \pm 1.15$  for 10  $\mu$ M nutlin-3 alone ( $p < 0.001$ ) (Figure 70c). Similarly, the AUC<sub>log</sub> value of the combination of 10  $\mu$ M nutlin-3 with 0.37 MBq/ml [<sup>131</sup>I]MIP-1095 was  $-3.25 \pm 0.75$  compared with  $12.86 \pm 0.44$  for 0.37 MBq/ml [<sup>131</sup>I]MIP-1095 alone ( $p < 0.001$ ) and  $19.20 \pm 1.20$  for 10  $\mu$ M nutlin-3 alone ( $p < 0.001$ ) (Figure 70d). These observations indicated

that nutlin-3 potentiated the growth delay induced by  $\gamma$ -radiation and [ $^{131}\text{I}$ ]MIP-1095 treatments.

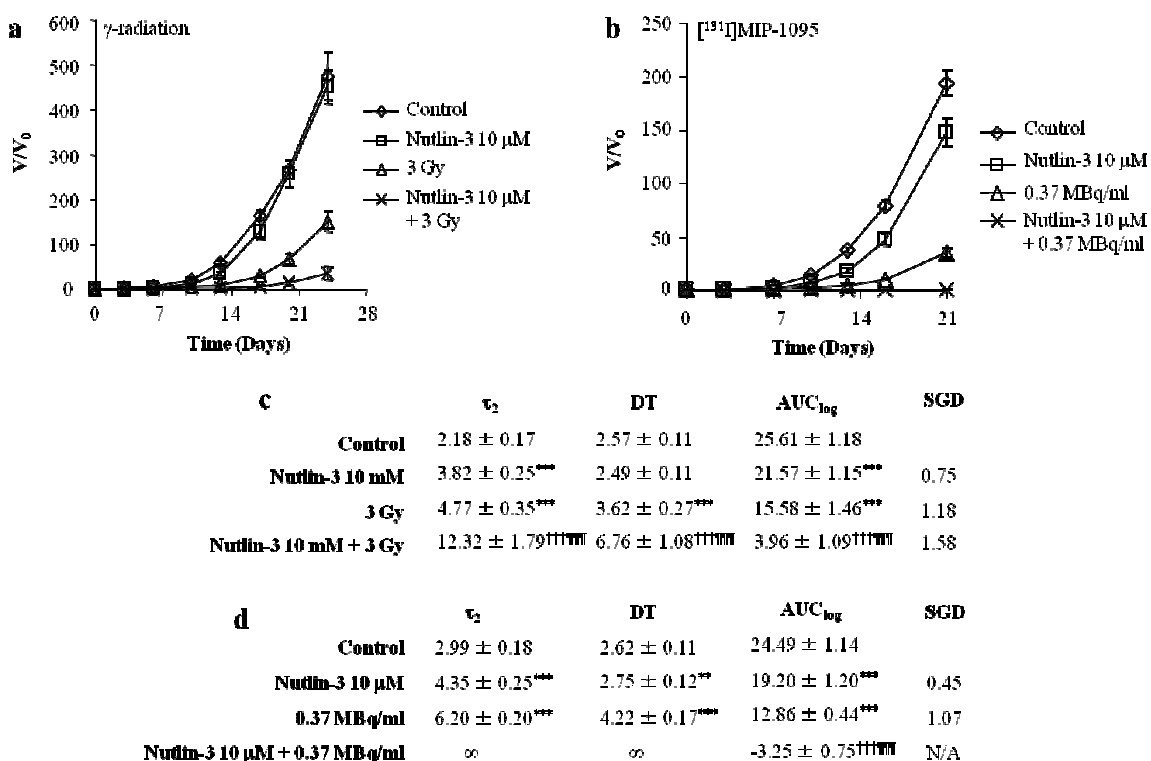


**Figure 70 Spheroid growth delay induced by treatment with  $\gamma$ -radiation, [ $^{131}\text{I}$ ]MIP-1095 or nutlin-3 as single agents or in combination**

(a) The potentiation of  $\gamma$ -radiation kill by nutlin-3 was investigated. LNCaP spheroids were exposed to 10  $\mu\text{M}$  nutlin-3 and immediately irradiated with 3 Gy  $\gamma$ -radiation using a  $^{60}\text{Co}$  source. The spheroids were then incubated for 24 h in culture medium containing 10  $\mu\text{M}$  nutlin-3. Data are mean  $\pm$  SEM. (b) The potentiation of [ $^{131}\text{I}$ ]MIP-1095 kill by nutlin-3 was investigated. LNCaP spheroids were simultaneously exposed to 10  $\mu\text{M}$  nutlin-3 and 0.37 MBq/ml [ $^{131}\text{I}$ ]MIP-1095. After 2 h, excess [ $^{131}\text{I}$ ]MIP-1095 was removed and the spheroids incubated in culture medium containing 10  $\mu\text{M}$  nutlin-3 for 22 h. (c) and (d)  $\tau_2$ , DT and AUC<sub>log</sub> values were calculated according to Section 6.3.4 and 6.3.5. Data are mean  $\pm$  SEM.  $\infty$  indicates that the spheroids failed to double in volume. The statistical significance of the differences in  $\tau_2$ , DT and AUC<sub>log</sub> values between groups was determined by non-parametric testing (Kruskal-Wallis followed by Mann-Whitney tests) using SPSS. The medians of  $\tau_2$ , DT and AUC<sub>log</sub> values of the groups treated with single agents were compared with those of the untreated control (\*). The medians of  $\tau_2$ , DT and AUC<sub>log</sub> values of the combination treatment were compared with those of the group treated with radiation alone (¶) and with those of the group treated with nutlin-3 alone (†). Two symbols indicate  $p < 0.01$  and three symbols indicate  $p < 0.001$ . The specific growth delay values corresponding to the single-agent treatments (SGD<sub>SA</sub>) and the specific growth delay of the combination treatments (SGD<sub>C</sub>) were calculated according to Section 8.3.3.

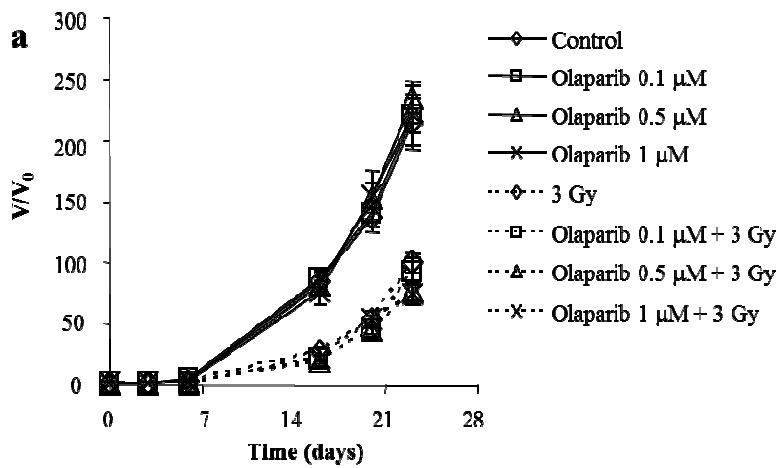
#### 8.4.1.2 Olaparib

Several authors have reported radiosensitisation by olaparib at concentrations ranging from 10 nM to 10  $\mu\text{M}$ <sup>89,292,317,318</sup>. Based on these results, the potential modulation of  $\gamma$ -radiation-

induced growth delay by olaparib was investigated at concentrations ranging from 0.1 to 1  $\mu\text{M}$  (Figure 71).

The  $\tau_2$ , DT and  $\text{AUC}_{\log}$  values of the groups treated with the combinations of 0.1, 0.5 or 1  $\mu\text{M}$  olaparib with 3 Gy  $\gamma$ -radiation were not significantly different from those of the group treated with 3 Gy  $\gamma$ -radiation alone (Figure 71b). For instance, the  $\tau_2$  values of the combinations ranged from  $4.43 \pm 0.37$  to  $4.76 \pm 0.33$  days compared with  $4.14 \pm 0.43$  days for 3 Gy  $\gamma$ -radiation alone (Figure 71b). This indicated that olaparib was not able to potentiate the toxicity induced by  $\gamma$ -radiation at concentrations less than 1  $\mu\text{M}$ .

Olaparib is an inhibitor of DNA damage repair. Therefore, in the absence of a DNA damaging agent such as radiation, olaparib as a single-agent treatment is unlikely to be cytotoxic (Figure 71). However, it was also possible that the absence of a growth delay in response to olaparib alone was due to insufficient concentration of drug. It has also been shown that the administration to patients of a single 400 mg dose of olaparib resulted in a peak plasma concentration of 11  $\mu\text{M}$  and it was well tolerated<sup>309</sup>. Thus, the investigation of the combination of olaparib with [<sup>131</sup>I]MIP-1095 was carried out with concentrations of olaparib of 1 and 10  $\mu\text{M}$  (Figure 72).



	$\tau_2$	DT	AUC <sub>log</sub>	SGD
<b>Control</b>	3.24 ± 0.38	2.98 ± 0.22	27.72 ± 2.26	0.00
<b>Olaparib 0.1 μM</b>	2.73 ± 0.39	2.97 ± 0.40	29.12 ± 3.94	-0.16
<b>Olaparib 0.5 μM</b>	2.97 ± 0.33	2.86 ± 0.30	28.71 ± 3.26	-0.08
<b>Olaparib 1 μM</b>	3.15 ± 0.53	2.98 ± 0.46	28.37 ± 4.71	-0.03
<b>3 Gy</b>	4.14 ± 0.43***	3.62 ± 0.35***	22.14 ± 2.90***	0.28
<b>Olaparib 0.1 μM + 3 Gy</b>	4.76 ± 0.33†††	3.68 ± 0.18†††	19.94 ± 2.28†††	0.15
<b>Olaparib 0.5 μM + 3 Gy</b>	4.56 ± 0.49†††	3.78 ± 0.36†††	19.59 ± 2.00†††	0.10
<b>Olaparib 1 μM + 3 Gy</b>	4.43 ± 0.37††	3.95 ± 0.28†††	21.50 ± 2.79†††	0.07

**Figure 71 Absence of enhancement of  $\gamma$ -radiation-induced spheroid growth delay by combined treatment with olaparib**

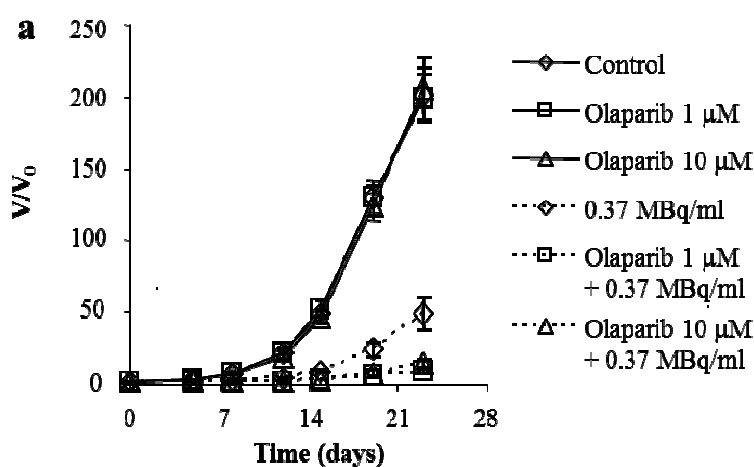
(a) The potentiation of  $\gamma$ -radiation kill by olaparib was investigated. LNCaP spheroids were exposed to 0.1, 0.5 or 1  $\mu$ M olaparib and immediately irradiated with 3 Gy  $\gamma$ -radiation using a  $^{60}\text{Co}$  source. The spheroids were then incubated for 24 h in culture medium containing 0.1, 0.5 or 1  $\mu$ M olaparib. Data are mean  $\pm$  SEM.

(b)  $\tau_2$ , DT and AUC<sub>log</sub> values were calculated according to Section 6.3.4 and 6.3.5. Data are mean  $\pm$  SEM. The statistical significance of the differences in  $\tau_2$ , DT and AUC<sub>log</sub> values between groups was determined by non-parametric testing (Kruskal-Wallis followed by Mann-Whitney tests) using SPSS. The medians of  $\tau_2$ , DT and AUC<sub>log</sub> values of the groups treated with single agents were compared with those of the untreated control (\*). The medians of  $\tau_2$ , DT and AUC<sub>log</sub> values of the combination treatment were compared with those of the group treated with radiation alone (¶) and with those of the group treated with olaparib alone (†). Two symbols indicate  $p < 0.01$  and three symbols indicate  $p < 0.001$ . The specific growth delay values corresponding to the single-agent treatments (SGD<sub>SA</sub>) and the specific growth delay of the combination treatments (SGD<sub>C</sub>) were calculated according to Section 8.3.3.

The spheroid growth delay induced by [ $^{131}\text{I}$ ]MIP-1095 was significantly enhanced by inclusion of 1  $\mu$ M or 10  $\mu$ M olaparib (Figure 72a), indicated by the significant modifications of  $\tau_2$ , DT and AUC<sub>log</sub> values following treatment with olaparib in combination with [ $^{131}\text{I}$ ]MIP-1095 compared with those of the group treated with [ $^{131}\text{I}$ ]MIP-1095 alone (Figure 72b). For instance, the  $\tau_2$  values were  $2.70 \pm 0.22$ ,  $2.98 \pm 0.26$  and  $6.32 \pm 0.91$  ( $p < 0.001$ ) following treatment with 1  $\mu$ M olaparib, 10  $\mu$ M olaparib and 0.37

MBq/ml [<sup>131</sup>I]MIP-1095, respectively (Figure 72b). In contrast, the  $\tau_2$  values of the treatments consisting of combination of [<sup>131</sup>I]MIP-1095 with 1 or 10  $\mu$ M olaparib were  $11.33 \pm 1.36$  and  $9.70 \pm 0.72$  days, respectively (Figure 72b).

The enhancement of toxicity induced by [<sup>131</sup>I]MIP-1095 following the inclusion of 1  $\mu$ M olaparib (Figure 72c) was in contrast with the absence of potentiation of  $\gamma$ -radiation-induced growth delay by 1  $\mu$ M olaparib (Figure 71c). This indicated that olaparib enhancement of radiation kill was dependent on the mode of delivery of radiation (external beam versus radiopharmaceutical). This will be discussed in further details in Section 8.5.



	$\tau_2$	DT	AUC <sub>log</sub>	SGD
<b>a</b>				
Control	$2.67 \pm 0.26$	$2.90 \pm 0.25$	$28.40 \pm 3.00$	
0.37 MBq/ml	$6.32 \pm 0.91^{***}$	$4.53 \pm 0.68^{***}$	$15.18 \pm 2.34^{***}$	1.36
Olaparib 1 $\mu$ M	$2.70 \pm 0.22$	$2.92 \pm 0.13$	$28.20 \pm 1.37$	0.01
Olaparib 10 $\mu$ M	$2.98 \pm 0.26$	$2.89 \pm 0.21$	$27.44 \pm 2.91$	0.11
Olaparib 1 $\mu$ M + 0.37 MBq/ml	$11.33 \pm 1.36^{†††***}$	$10.14 \pm 1.29^{†††***}$	$7.83 \pm 1.18^{†††***}$	0.79
Olaparib 10 $\mu$ M + 0.37 MBq/ml	$9.70 \pm 0.72^{†††***}$	$7.95 \pm 0.75^{†††***}$	$8.39 \pm 1.12^{†††***}$	0.53

**Figure 72 Spheroid growth delay induced by treatment with [<sup>131</sup>I]MIP-1095 or olaparib as single agents or in combination**

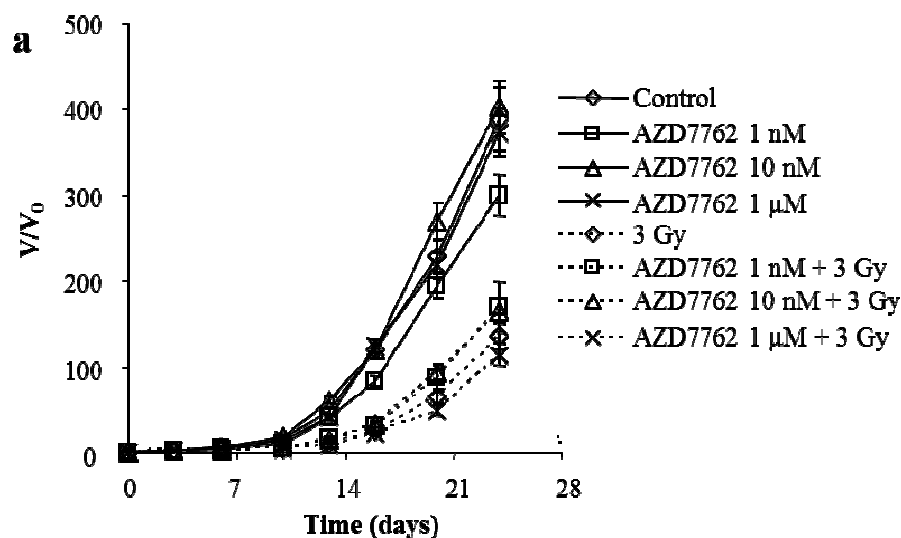
(a) The potentiation of [<sup>131</sup>I]MIP-1095 kill by olaparib was investigated. LNCaP spheroids were simultaneously exposed to 1 or 10  $\mu$ M olaparib and 0.37 MBq/ml [<sup>131</sup>I]MIP-1095. After 2 h, excess [<sup>131</sup>I]MIP-1095 was removed and the spheroids incubated in culture medium containing 1 or 10  $\mu$ M olaparib for 22 h. Data are mean  $\pm$  SEM. (b)  $\tau_2$ , DT and AUC<sub>log</sub> values were calculated according to Section 6.3.4 and 6.3.5. Data are mean  $\pm$  SEM. The statistical significance of the differences in  $\tau_2$ , DT and AUC<sub>log</sub> values between groups was determined by non-parametric testing (Kruskal-Wallis followed by Mann-Whitney tests) using SPSS. The medians of  $\tau_2$ , DT and AUC<sub>log</sub> values of the groups treated with single agents were compared with those of the untreated control (\*). The medians of  $\tau_2$ , DT and AUC<sub>log</sub> values of the combination treatment were compared with those of the group treated with radiation alone (¶) and with those of the group treated with olaparib alone (†). Two symbols indicate  $p < 0.01$  and three symbols indicate  $p <$

0.001. The specific growth delay values corresponding to the single-agent treatments ( $SGD_{SA}$ ) and the specific growth delay of the combination treatments ( $SGD_C$ ) were calculated according to Section 8.3.3.

#### **8.4.1.3 AZD7762**

The radiosensitisation of monolayers has been demonstrated at AZD7762 concentration of 100 nM<sup>295</sup>. Based on this report, the investigation of the modification of  $\gamma$ -radiation-induced spheroid growth delay by AZD7762 was carried out at concentrations ranging from 1 nM to 1  $\mu$ M (Figure 73).

The  $\tau_2$ , DT and  $AUC_{\log}$  values of the groups treated with the combinations of 1 nM, 10 nM or 1  $\mu$ M AZD7762 with 3 Gy  $\gamma$ -radiation were not significantly different from those of the group treated with 3 Gy  $\gamma$ -radiation alone (Figure 73b). For instance, the  $\tau_2$  values of the combinations ranged from  $4.05 \pm 0.27$  to  $5.33 \pm 0.52$  days compared with  $5.32 \pm 0.45$  days for 3 Gy  $\gamma$ -radiation alone (Figure 73b). This indicated that AZD7762 was not able to potentiate  $\gamma$ -radiation toxicity at concentrations less than 1  $\mu$ M.



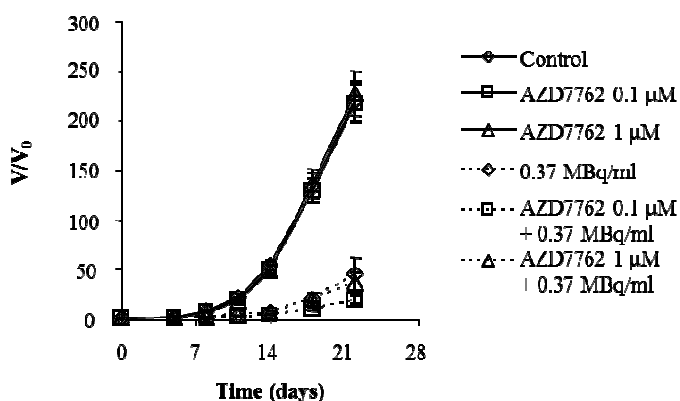
	$\tau_2$	DT	AUC <sub>log</sub>	SGD
<b>Control</b>	2.72 ± 0.19	2.62 ± 0.08	23.81 ± 0.88	
<b>AZD7762 1 nM</b>	3.33 ± 0.26	2.66 ± 0.03	21.84 ± 0.71	0.22
<b>AZD7762 10 nM</b>	2.01 ± 0.18	2.64 ± 0.16	25.46 ± 1.59	-0.26
<b>AZD7762 1 μM</b>	3.14 ± 0.24	2.58 ± 0.11	23.07 ± 1.16	0.15
<b>3 Gy</b>	5.32 ± 0.45 <sup>***</sup>	3.49 ± 0.26 <sup>***</sup>	14.65 ± 1.30 <sup>***</sup>	0.95
<b>AZD7762 1 nM + 3 Gy</b>	5.07 ± 0.50 <sup>††</sup>	3.35 ± 0.22	15.39 ± 1.40	-0.05
<b>AZD7762 10 nM + 3 Gy</b>	4.05 ± 0.27 <sup>†††††</sup>	3.21 ± 0.20 <sup>†††</sup>	17.72 ± 1.36 <sup>†††††</sup>	-0.24
<b>AZD7762 1 μM + 3 Gy</b>	5.33 ± 0.52 <sup>†††</sup>	3.73 ± 0.23 <sup>†††</sup>	14.54 ± 1.37 <sup>†††</sup>	0.00

**Figure 73 Absence of enhancement of  $\gamma$ -radiation-induced spheroid growth delay by combined treatment with AZD7762**

(a) The putative potentiation of  $\gamma$ -radiation kill by AZD7762 was investigated. LNCaP spheroids were exposed to 1 nM, 10 nM or 1  $\mu$ M AZD7762 and immediately irradiated with 3 Gy  $\gamma$ -radiation using a  $^{60}\text{Co}$  source. The spheroids were then incubated for 24 h in culture medium containing 1 nM, 10 nM or 1  $\mu$ M AZD7762. Data are mean  $\pm$  SEM. (b)  $\tau_2$ , DT and AUC<sub>log</sub> values were calculated according to Section 6.3.4 and 6.3.5. Data are mean  $\pm$  SEM. The statistical significance of the differences in  $\tau_2$ , DT and AUC<sub>log</sub> values between groups was determined by non-parametric testing (Kruskal-Wallis followed by Mann-Whitney tests) using SPSS. The medians of  $\tau_2$ , DT and AUC<sub>log</sub> values of the groups treated with single agents were compared with those of the untreated control (\*). The medians of  $\tau_2$ , DT and AUC<sub>log</sub> values of the combination treatment were compared with those of the group treated with radiation alone (¶) and with those of the group treated with AZD7762 alone (†). Two symbols indicate  $p < 0.01$  and three symbols indicate  $p < 0.001$ . The specific growth delay values corresponding to the single-agent treatments (SGD<sub>SA</sub>) and the specific growth delay of the combination treatments (SGD<sub>C</sub>) were calculated according to Section 8.3.3.

The effect of AZD7762 on the growth delay induced by [ $^{131}\text{I}$ ]MIP-1095 is depicted in Figure 74. The spheroid growth delay induced by [ $^{131}\text{I}$ ]MIP-1095 was not significantly enhanced by inclusion of 0.1  $\mu$ M or 1  $\mu$ M AZD7762 (Figure 74b). For instance, the  $\tau_2$

values were  $2.74 \pm 0.35$ ,  $2.95 \pm 0.23$  and  $6.06 \pm 0.97$  ( $p < 0.001$ ) following treatment with  $0.1 \mu\text{M}$  AZD7762,  $1 \mu\text{M}$  AZD7762 and  $0.37 \text{ MBq/ml}$  [ $^{131}\text{I}$ ]MIP-1095, respectively (Figure 74b). Similarly, the  $\tau_2$  values of the treatments consisting of combination of [ $^{131}\text{I}$ ]MIP-1095 with  $0.1$  or  $1 \mu\text{M}$  AZD7762 were  $7.23 \pm 0.69$  and  $7.13 \pm 1.31$  days, respectively (Figure 74b).



**b**

	$\tau_2$	DT	AUC <sub>log</sub>	SGD
Control	$2.43 \pm 0.23$	$2.79 \pm 0.05$	$27.95 \pm 1.81$	
0.37 MBq/ml	$6.06 \pm 0.97^{***}$	$5.00 \pm 0.85^{***}$	$13.20 \pm 2.15^{***}$	1.49
AZD7762 0.1 $\mu\text{M}$	$2.74 \pm 0.35$	$2.65 \pm 0.22$	$27.26 \pm 2.70$	0.13
AZD7762 1 $\mu\text{M}$	$2.95 \pm 0.23$	$2.68 \pm 0.03$	$26.73 \pm 0.75$	0.21
AZD7762 0.1 $\mu\text{M}$ + 0.37 MBq/ml	$7.23 \pm 0.69^{††}$	$6.05 \pm 0.61^{†††}$	$10.70 \pm 1.04^{†††}$	0.19
AZD7762 1 $\mu\text{M}$ + 0.37 MBq/ml	$7.13 \pm 1.31^{†††}$	$4.95 \pm 0.90^{†††}$	$14.32 \pm 2.37^{†††}$	0.18

**Figure 74 Absence of enhancement of [ $^{131}\text{I}$ ]MIP-1095-induced spheroid growth delay by combined treatment with AZD7762**

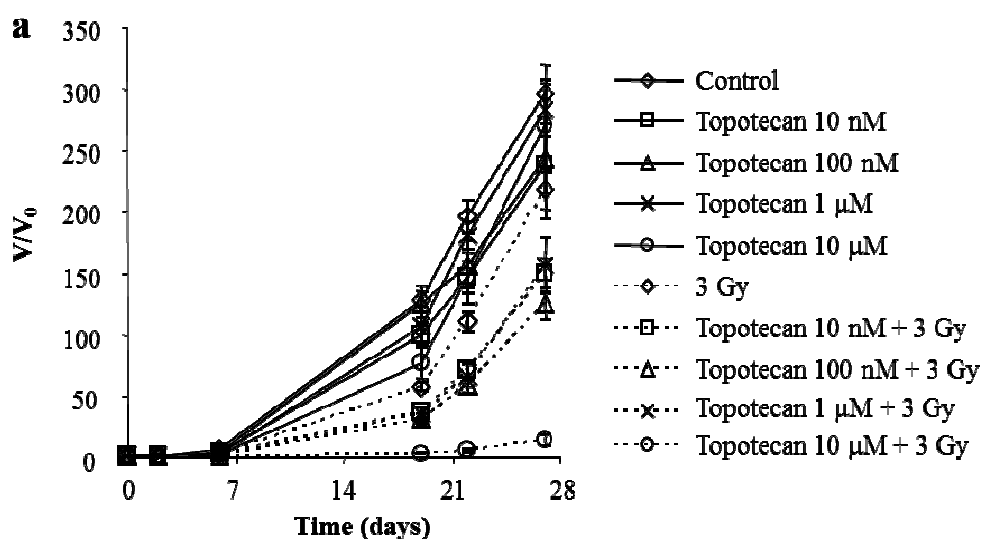
(a) The putative potentiation of [ $^{131}\text{I}$ ]MIP-1095 kill by AZD7762 was investigated. LNCaP spheroids were simultaneously exposed to  $0.1$  or  $1 \mu\text{M}$  AZD7762 and  $0.37 \text{ MBq/ml}$  [ $^{131}\text{I}$ ]MIP-1095. After 2 h, excess [ $^{131}\text{I}$ ]MIP-1095 was removed and the spheroids incubated in culture medium containing  $0.1$  or  $1 \mu\text{M}$  AZD7762 for 22 h. Data are mean  $\pm$  SEM. (b)  $\tau_2$ , DT and AUC<sub>log</sub> values were calculated according to Section 6.3.4 and 6.3.5. Data are mean  $\pm$  SEM. The statistical significance of the differences in  $\tau_2$ , DT and AUC<sub>log</sub> values between groups was determined by non-parametric testing (Kruskal-Wallis followed by Mann-Whitney tests) using SPSS. The medians of  $\tau_2$ , DT and AUC<sub>log</sub> values of the groups treated with single agents were compared with those of the untreated control (\*). The medians of  $\tau_2$ , DT and AUC<sub>log</sub> values of the combination treatment were compared with those of the group treated with radiation alone (¶) and with those of the group treated with AZD7762 alone (†). Two symbols indicate  $p < 0.01$  and three symbols indicate  $p < 0.001$ . The specific growth delay values corresponding to the single-agent treatments (SGD<sub>SA</sub>) and the specific growth delay of the combination treatments (SGD<sub>C</sub>) were calculated according to Section 8.3.3.

#### 8.4.1.4 Topotecan

Topotecan-induced radiosensitisation was demonstrated in monolayers at concentrations ranging from 5 to 100 nM<sup>319,320</sup>. However, concentrations of topotecan ranging from 10 nM to 10  $\mu$ M induced a modest reduction in the area under the  $V/V_0$  versus time curve of LNCaP spheroid growth. For instance, the  $AUC_{\log}$  value following treatment with 10  $\mu$ M topotecan was  $31.52 \pm 4.49$  days ( $p < 0.001$ ) compared with that of the untreated control ( $39.57 \pm 3.14$  days) (Figure 75). Based on these observations, the effect of topotecan on the growth delay induced by  $\gamma$ -radiation was investigated at concentrations ranging from 10 nM to 10  $\mu$ M (Figure 75).

The increase in  $\tau_2$  values and the decrease in  $AUC_{\log}$  values following treatment with the combinations of 10 nM, 100 nM, 1  $\mu$ M or 10  $\mu$ M topotecan with 3 Gy  $\gamma$ -radiation were significant in comparison with the  $\tau_2$ , and  $AUC_{\log}$  values of the group treated with 3 Gy  $\gamma$ -radiation alone and with those treated with topotecan alone (Figure 75b). For instance, the  $\tau_2$  values of the combinations ranged from  $4.51 \pm 0.25$  to  $8.02 \pm 1.51$  days compared with  $3.46 \pm 0.29$  days for the group treated with 3 Gy  $\gamma$ -radiation alone (Figure 75b). This indicated that topotecan was able to potentiate the toxicity induced by  $\gamma$ -radiation at concentrations less than 10  $\mu$ M in spheroids.

The conclusion of the analysis of the DT values conflicted with that obtained by the analysis of the  $\tau_2$  values. For instance, the DT values were  $3.70 \pm 0.17$ ,  $3.91 \pm 0.23$  and  $3.90 \pm 0.39$  days for the groups treated with the combinations of 3 Gy  $\gamma$ -radiation with 10 nM topotecan, 100 nM topotecan or 1  $\mu$ M topotecan, respectively (Figure 75b). The DT values of these combination were not significantly greater than that of the group treated with 3 Gy  $\gamma$ -radiation alone ( $3.49 \pm 0.27$  days) (Figure 75b), indicating the absence of the potentiation of  $\gamma$ -radiation toxicity by topotecan at concentrations less than 1  $\mu$ M. This was in contrast to the enhancement of  $\gamma$ -radiation kill by topotecan at these concentrations as determined by analysis of the  $\tau_2$  and  $AUC_{\log}$  values (Figure 75b). However, the combination of 10  $\mu$ M topotecan with 3 Gy  $\gamma$ -radiation resulted in the statistically significant increase in DT values ( $6.64 \pm 1.24$  days) compared with that of the group treated with 3 Gy  $\gamma$ -radiation alone ( $3.49 \pm 0.27$  days) ( $p < 0.001$ ) (Figure 75b). This indicated the potentiation of  $\gamma$ -radiation-induced growth delay at this level of topotecan toxicity (10  $\mu$ M).



	$\tau_2$	DT	AUC <sub>log</sub>	SGD
<b>Control</b>	1.79 ± 0.15	3.19 ± 0.21	39.57 ± 3.14	
<b>Topotecan 10 nM</b>	3.22 ± 0.31 <sup>***</sup>	3.23 ± 0.24	34.99 ± 3.46 <sup>***</sup>	0.80
<b>Topotecan 100 nM</b>	3.13 ± 0.31 <sup>***</sup>	2.96 ± 0.28	36.50 ± 6.81	0.75
<b>Topotecan 1 μM</b>	3.67 ± 0.34 <sup>***</sup>	3.03 ± 0.27	35.33 ± 3.51 <sup>***</sup>	1.05
<b>Topotecan 10 μM</b>	4.45 ± 0.66 <sup>***</sup>	3.31 ± 0.44	31.52 ± 4.49 <sup>***</sup>	1.49
<b>3 Gy</b>	3.46 ± 0.29 <sup>***</sup>	3.49 ± 0.27	32.89 ± 3.05 <sup>***</sup>	0.93
<b>Topotecan 10 nM + 3 Gy</b>	4.51 ± 0.25 <sup>†††***</sup>	3.70 ± 0.17 <sup>†††</sup>	27.84 ± 1.83 <sup>†††***</sup>	0.30
<b>Topotecan 100 nM + 3 Gy</b>	4.96 ± 0.26 <sup>†††***</sup>	3.91 ± 0.23 <sup>†††</sup>	25.94 ± 1.31 <sup>†††***</sup>	0.43
<b>Topotecan 1 μM + 3 Gy</b>	5.18 ± 0.55 <sup>†††***</sup>	3.90 ± 0.39 <sup>†††</sup>	26.24 ± 2.94 <sup>†††***</sup>	0.50
<b>Topotecan 10 μM + 3 Gy</b>	8.02 ± 1.51 <sup>†††***</sup>	6.64 ± 1.24 <sup>†††***</sup>	9.47 ± 2.16 <sup>†††***</sup>	1.32

**Figure 75 Spheroid growth delay induced by treatment with  $\gamma$ -radiation or topotecan as single agents or in combination**

(a) The potentiation of  $\gamma$ -radiation kill by topotecan was investigated. LNCaP spheroids were exposed to 10 nM, 100 nM, 1  $\mu$ M or 10  $\mu$ M topotecan and immediately irradiated with 3 Gy  $\gamma$ -radiation using a  $^{60}\text{Co}$  source. The spheroids were then incubated for 24 h in culture medium containing 10 nM, 100 nM, 1  $\mu$ M or 10  $\mu$ M topotecan. Data are mean  $\pm$  SEM. (b)  $\tau_2$ , DT and AUC<sub>log</sub> values were calculated according to Section 6.3.4 and 6.3.5. Data are mean  $\pm$  SEM. The statistical significance of the differences in  $\tau_2$ , DT and AUC<sub>log</sub> values between groups was determined by non-parametric testing (Kruskal-Wallis followed by Mann-Whitney tests) using SPSS. The medians of  $\tau_2$ , DT and AUC<sub>log</sub> values of the groups treated with single agents were compared with those of the untreated control (\*). The medians of  $\tau_2$ , DT and AUC<sub>log</sub> values of the combination treatment were compared with those of the group treated with radiation alone (¶) and with those of the group treated with topotecan alone (†). Two symbols indicate  $p < 0.01$  and three symbols indicate  $p < 0.001$ . The specific growth delay values corresponding to the single-agent treatments (SGD<sub>SA</sub>) and the specific growth delay of the combination treatments (SGD<sub>C</sub>) were calculated according to Section 8.3.3.

These observations indicated that concentrations of topotecan ranging from 10 nM to 1  $\mu$ M only transiently increased the growth delay induced by  $\gamma$ -radiation treatment. Spheroid regrowth was manifest from day 19 following combinations treatment consisting of 10 nM, 0.1  $\mu$ M and 1  $\mu$ M topotecan with 3 Gy  $\gamma$ -radiation (Figure 75b). In contrast, the combination treatment consisting of 10  $\mu$ M topotecan with 3 Gy  $\gamma$ -radiation induced a significant increase in DT values, indicative of a persistent potentiation of growth delay induced by  $\gamma$ -radiation (Figure 75b). These results indicated that radiosensitisation by topotecan was dose-dependent.

The spheroid growth delay induced by [ $^{131}$ I]MIP-1095 was also enhanced by treatment with 0.1  $\mu$ M and 1  $\mu$ M topotecan (Figure 76a). This was manifest by the significant modification of  $\tau_2$ , DT and AUC<sub>log</sub> values following treatment with 0.1 or 1  $\mu$ M topotecan in combination with [ $^{131}$ I]MIP-1095 compared with those of the group treated with [ $^{131}$ I]MIP-1095 alone (Figure 76b). For instance, the  $\tau_2$  values were  $3.25 \pm 0.17$ ,  $3.27 \pm 0.18$  and  $5.51 \pm 0.55$  ( $p < 0.001$ ) following treatment with 0.1  $\mu$ M topotecan, 1  $\mu$ M topotecan and 0.37 MBq/ml [ $^{131}$ I]MIP-1095, respectively (Figure 76b). In contrast, the  $\tau_2$  values corresponding to/resulting from the treatments consisting of combination of [ $^{131}$ I]MIP-1095 with 0.1 or 1  $\mu$ M topotecan were  $7.93 \pm 0.67$  and  $7.41 \pm 0.74$  days, respectively (Figure 76b).

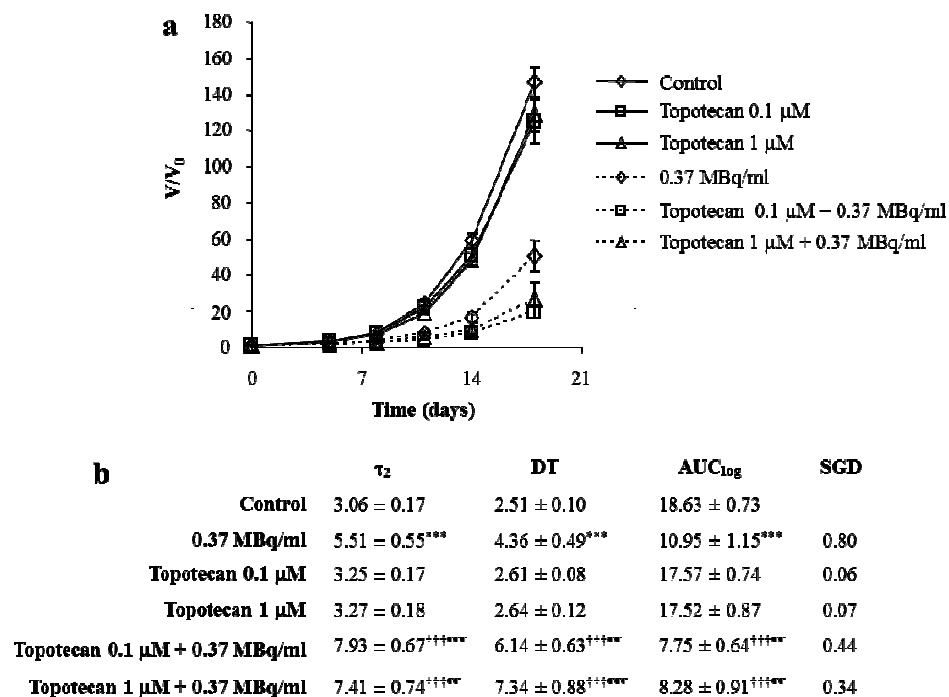
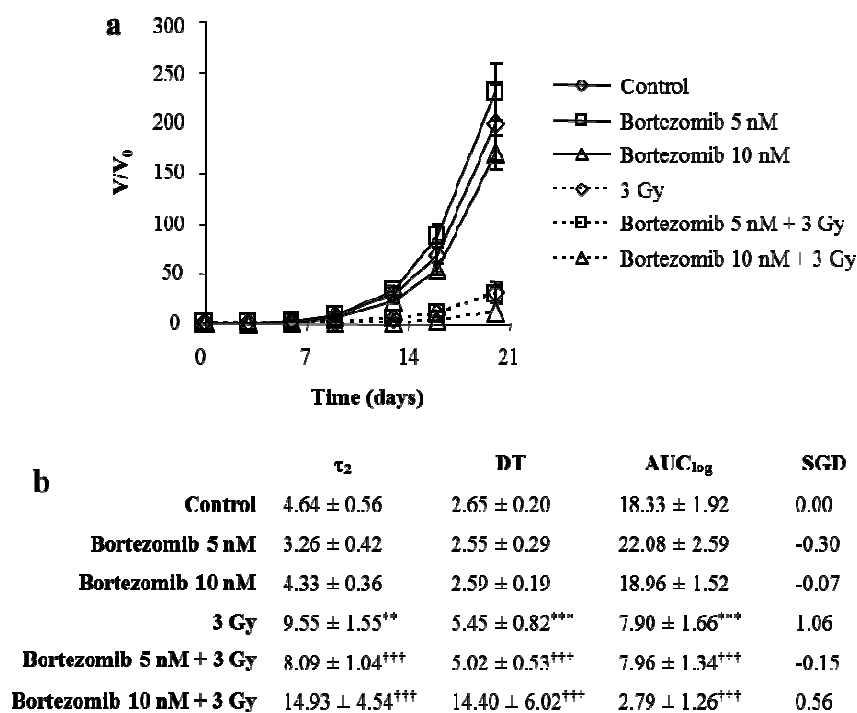


Figure 76 Spheroid growth delay induced by treatment with [ $^{131}$ I]MIP-1095 or topotecan as single agents or in combination

(a) The potentiation of  $[^{131}\text{I}]\text{MIP-1095}$  kill by topotecan was investigated. LNCaP spheroids were simultaneously exposed to 0.1 or 1  $\mu\text{M}$  topotecan and 0.37 MBq/ml  $[^{131}\text{I}]\text{MIP-1095}$ . After 2 h, excess  $[^{131}\text{I}]\text{MIP-1095}$  was removed and the spheroids incubated in culture medium containing 0.1 or 1  $\mu\text{M}$  topotecan for 22 h. Data are mean  $\pm$  SEM. (b)  $\tau_2$ , DT and  $\text{AUC}_{\log}$  values were calculated according to Section 6.3.4 and 6.3.5. Data are mean  $\pm$  SEM. The statistical significance of the differences in  $\tau_2$ , DT and  $\text{AUC}_{\log}$  values between groups was determined by non-parametric testing (Kruskal-Wallis followed by Mann-Whitney tests) using SPSS. The medians of  $\tau_2$ , DT and  $\text{AUC}_{\log}$  values of the groups treated with single agents were compared with those of the untreated control (\*). The medians of  $\tau_2$ , DT and  $\text{AUC}_{\log}$  values of the combination treatment were compared with those of the group treated with radiation alone ( $\text{\textcircled{D}}$ ) and with those of the group treated with topotecan alone ( $\text{\textcircled{+}}$ ). Two symbols indicate  $p < 0.01$  and three symbols indicate  $p < 0.001$ . The specific growth delay values corresponding to the single-agent treatments ( $\text{SGD}_{\text{SA}}$ ) and the specific growth delay of the combination treatments ( $\text{SGD}_{\text{C}}$ ) were calculated according to Section 8.3.3.

### 8.4.1.5 Bortezomib

The radiosensitising effect of bortezomib has previously been demonstrated in monolayers derived from cervical cancer cell lines at a concentration of 10 nM<sup>321</sup>. Based on this result, the effect of bortezomib on the growth delay induced by  $\gamma$ -radiation was evaluated using bortezomib concentrations of 5 and 10 nM (Figure 77).



**Figure 77 Absence of enhancement of  $\gamma$ -radiation-induced spheroid growth delay by combined treatment with bortezomib**

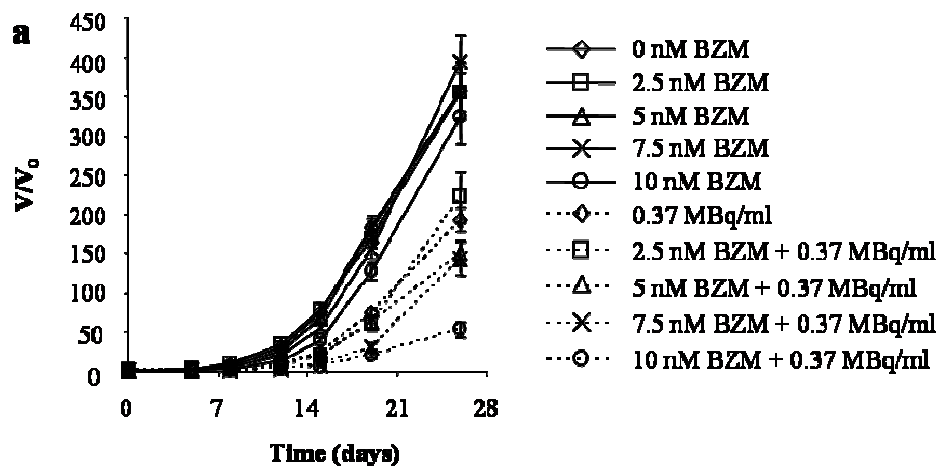
(a) The putative potentiation of  $\gamma$ -radiation kill by bortezomib was investigated. LNCaP spheroids were exposed to 5 nM or 10 nM bortezomib and immediately irradiated with 3 Gy  $\gamma$ -radiation using a  $^{60}\text{Co}$  source. The spheroids were then incubated for 24 h in culture medium containing 5 nM or 10 nM bortezomib. Data

are mean  $\pm$  SEM. (b)  $\tau_2$ , DT and  $AUC_{log}$  values were calculated according to Section 6.3.4 and 6.3.5. Data are mean  $\pm$  SEM. The statistical significance of the differences in  $\tau_2$ , DT and  $AUC_{log}$  values between groups was determined by non-parametric testing (Kruskal-Wallis followed by Mann-Whitney tests) using SPSS. The medians of  $\tau_2$ , DT and  $AUC_{log}$  values of the groups treated with single agents were compared with those of the untreated control (\*). The medians of  $\tau_2$ , DT and  $AUC_{log}$  values of the combination treatment were compared with those of the group treated with radiation alone (¶) and with those of the group treated with bortezomib alone (†). Two symbols indicate  $p < 0.01$  and three symbols indicate  $p < 0.001$ . The specific growth delay values corresponding to the single-agent treatments ( $SGD_{SA}$ ) and the specific growth delay of the combination treatments ( $SGD_C$ ) were calculated according to Section 8.3.3.

No significant potentiation of  $\gamma$ -radiation toxicity by simultaneous treatment with bortezomib was indicated from the analysis of  $\tau_2$ , DT and  $AUC_{log}$  values. The  $\tau_2$  values were  $9.55 \pm 1.55$  ( $p < 0.01$ ),  $3.26 \pm 0.42$  and  $8.09 \pm 1.04$  days for the groups treated with 3 Gy  $\gamma$ -radiation, 5 nM bortezomib and the combination of 3 Gy  $\gamma$ -radiation with 5 nM bortezomib, respectively (Figure 77b). Similarly, the  $\tau_2$  value of the group treated with 10 nM bortezomib in combination with 3 Gy  $\gamma$ -radiation ( $14.93 \pm 4.54$  days) was not significantly higher than that of the group treated with 3 Gy alone (Figure 77b). However, the growth delay induced by 3 Gy  $\gamma$ -radiation was unusually high in this particular experiment ( $\tau_2 = 9.55 \pm 1.55$  days); the average  $\tau_2$  value following 3 Gy irradiation from Figure 70, Figure 71, Figure 73 and Figure 75 was  $4.42 \pm 0.40$  days. Thus, any further reduction of the area under the curve induced by bortezomib would have been more difficult to discriminate from that induced by  $\gamma$ -radiation treatment alone. The Z-score, a measure of the deviation of a value from the mean in comparison with the standard deviation of the dataset (Section 8.3.5), was 1.712 which was higher than the critical Z-score (1.71), thus demonstrating that the  $\tau_2$  value following treatment with 3 Gy  $\gamma$ -radiation in this experiment was an outlying result at the 2.5% significance level<sup>312</sup>. Therefore, the observation of the absence of potentiation of the  $\gamma$ -radiation-induced growth delay by bortezomib is inconclusive.

The effect of bortezomib on the growth delay induced by [<sup>131</sup>I]MIP-1095 is depicted in Figure 78. The spheroid growth delay induced by [<sup>131</sup>I]MIP-1095 was enhanced by treatment with 7.5  $\mu$ M and 10  $\mu$ M bortezomib (Figure 78a). This observation was manifest by the significant modification of  $\tau_2$ , DT and  $AUC_{log}$  values following treatment with 7.5 or 10 nM bortezomib in combination with [<sup>131</sup>I]MIP-1095 compared with those of the group treated with [<sup>131</sup>I]MIP-1095 alone (Figure 78b). For instance, the  $\tau_2$  values were  $3.08 \pm 0.24$  ( $p < 0.001$ ),  $4.31 \pm 0.30$  ( $p < 0.001$ ) and  $4.86 \pm 0.28$  ( $p < 0.001$ ) following treatment

with 7.5 nM bortezomib, 10 nM bortezomib and 0.37 MBq/ml [<sup>131</sup>I]MIP-1095, respectively (Figure 78b). In contrast, the  $\tau_2$  values of the treatments consisting of combination of [<sup>131</sup>I]MIP-1095 with 7.5 or 10 nM bortezomib were  $7.82 \pm 0.66$  ( $p < 0.001$ ) and  $7.39 \pm 0.69$  days ( $p < 0.001$ ), respectively (Figure 78b).



<b>b</b>		$\tau_2$	DT	AUC <sub>log</sub>	SGD
	<b>Control</b>	$1.78 \pm 0.15$	$3.03 \pm 0.08$	$37.57 \pm 1.02$	
	<b>2.5 nM BZM</b>	$1.67 \pm 0.31$	$2.93 \pm 0.39$	$38.42 \pm 5.21$	-0.06
	<b>5 nM BZM</b>	$2.31 \pm 0.21^{**}$	$2.91 \pm 0.22$	$36.87 \pm 2.62$	0.29
	<b>7.5 nM BZM</b>	$3.08 \pm 0.24^{***}$	$2.81 \pm 0.12$	$35.56 \pm 2.24$	0.72
	<b>10 nM BZM</b>	$4.31 \pm 0.30^{***}$	$2.94 \pm 0.08$	$31.62 \pm 0.99^{***}$	1.41
	<b>0.37 MBq/ml</b>	$4.86 \pm 0.28^{***}$	$3.40 \pm 0.21^{**}$	$28.07 \pm 1.49^{***}$	1.72
	<b>2.5 nM BZM + 0.37 MBq/ml</b>	$5.43 \pm 0.24^{\dagger\dagger\dagger}$	$3.32 \pm 0.13$	$25.33 \pm 2.59^{\dagger\dagger\dagger}$	0.12
	<b>5 nM BZM + 0.37 MBq/ml</b>	$5.10 \pm 0.41^{\dagger\dagger\dagger}$	$3.75 \pm 0.37^{\dagger\dagger\dagger}$	$25.91 \pm 1.86^{\dagger\dagger\dagger}$	0.05
	<b>7.5 nM BZM + 0.37 MBq/ml</b>	$7.82 \pm 0.66^{\dagger\dagger\dagger\dagger\dagger\dagger}$	$3.93 \pm 0.35^{\dagger\dagger\dagger\dagger}$	$20.93 \pm 1.99^{\dagger\dagger\dagger\dagger\dagger}$	0.61
	<b>10 nM BZM + 0.37 MBq/ml</b>	$7.39 \pm 0.69^{\dagger\dagger\dagger\dagger\dagger\dagger}$	$4.88 \pm 0.43^{\dagger\dagger\dagger\dagger\dagger}$	$17.22 \pm 1.79^{\dagger\dagger\dagger\dagger\dagger\dagger}$	0.52

**Figure 78 Spheroid growth delay induced by treatment with [<sup>131</sup>I]MIP-1095 or bortezomib as single agents or in combination**

(a) The potentiation of [<sup>131</sup>I]MIP-1095 kill by bortezomib was investigated. LNCaP spheroids were simultaneously exposed to 2.5, 5, 7.5 or 10 nM bortezomib and 0.37 MBq/ml [<sup>131</sup>I]MIP-1095. After 2 h, excess [<sup>131</sup>I]MIP-1095 was removed and the spheroids incubated in culture medium containing 2.5, 5, 7.5 or 10 nM bortezomib for 22 h. Data are mean  $\pm$  SEM. (b)  $\tau_2$ , DT and AUC<sub>log</sub> values were calculated according to Section 6.3.4 and 6.3.5. Data are mean  $\pm$  SEM. The statistical significance of the differences in  $\tau_2$ , DT and AUC<sub>log</sub> values between groups was determined by non-parametric testing (Kruskal-Wallis followed by Mann-Whitney tests) using SPSS. The medians of  $\tau_2$ , DT and AUC<sub>log</sub> values of the groups treated with single agents were compared with those of the untreated control (\*). The medians of  $\tau_2$ , DT and AUC<sub>log</sub> values of the combination treatment were compared with those of the group treated with radiation alone (¶) and with those of the group treated with bortezomib alone (†). Two symbols indicate  $p < 0.01$  and three symbols indicate  $p < 0.001$ . The specific growth delay values corresponding to the single-agent treatments (SGD<sub>SA</sub>) and the specific growth delay of the combination treatments (SGD<sub>C</sub>) were calculated according to Section 8.3.3.

#### 8.4.2 Comparison of enhancement of [<sup>131</sup>I]MIP-1095-induced and $\gamma$ -radiation-induced growth delay by drugs

Olaparib is an inhibitor of DNA repair in response to radiation damage and AZD7762 inhibits the radiation-induced cell cycle arrest in G2. Drugs such as olaparib and AZD7762 which fall into the category of inhibitors of the cellular responses to radiation-induced damage exert cytotoxic effects only in combination with DNA damaging treatments such as radiation. Such drugs may be harmless as single agents at concentrations close to the  $K_i$  value corresponding to the inhibition of the target necessary for survival after radiation treatment (i.e. PARP-1 for olaparib and Chk1 for AZD7762). On the other hand, drugs may enhance radiation kill at concentrations which are toxic as single agents. For example, oxidising agents are toxic to cancer cells via the generation of oxidative stress which is also capable of enhancing radiation kill. Ideally, the comparison of the potentiation of radiation toxicity between two drugs should be performed at drug concentrations which induce an equivalent kill as single agents. However, the comparison of drugs which are cytotoxic as single agents with drug which are not cytotoxic as single agents demonstrates the difficulty of such a strategy.

The specific growth delay of a combination treatment  $SGD_C$  was used as a measure of the enhancement of  $\gamma$ -radiation- or [<sup>131</sup>I]MIP-1095-induced growth delay. The calculation of the  $SGD_C$  value allowed for the variation of the effect of radiation treatment alone among experiments. The  $SGD_C$  values of the combination treatments were calculated separately for every experiment. The graph presenting the  $SGD_C$  values of the combination of the drugs with 3 Gy  $\gamma$ -radiation against the  $SGD_{SA}$  values of each drug as single agent is shown in Figure 79a. Drugs, administered as single agents, that induce similar growth delays (similar  $SGD_{SA}$ ) can be ranked for radiosensitising potency at a given level of cytotoxicity. For instance, nutlin-3 and topotecan were equally toxic to LNCaP spheroids as indicated by the  $SGD_{SA}$  value of 0.75 (Figure 79a). At the toxicity level defined by  $SGD_{SA} = 0.75$ , the  $SGD_C$  for nutlin-3 was 1.58 whereas that of topotecan was 0.43, thus indicating the superior potentiation of  $\gamma$ -radiation-induced growth delay by nutlin-3 than by topotecan (Figure 79a). Similarly, olaparib and topotecan were equally toxic to LNCaP spheroids as indicated by the  $SGD_{SA}$  value of 0.1 (Figure 79b). At the toxicity level defined by  $SGD_{SA} = 0.1$ , the  $SGD_C$  for olaparib was 0.79 whereas that of topotecan was 0.44, thus indicating the superior potentiation of  $\gamma$ -radiation-induced growth delay by olaparib than by topotecan (Figure 79b).

Finally, the  $SGD_{SA}$  values of olaparib in the experiment evaluating the potentiation of the growth delay of  $\gamma$ -radiation (Figure 79a) were similar to those in the experiment evaluating the enhancement of the growth delay of [ $^{131}$ I]MIP-1095 (Figure 79b). For instance, the  $SGD_{SA}$  values following treatment with 0.1, 0.5 and 1  $\mu$ M olaparib were -0.16, -0.08 and -0.03, respectively, (Figure 79a), and those following treatment with 1 and 10  $\mu$ M olaparib were 0.01 and 0.11, respectively, (Figure 79b). This indicated that olaparib alone did not delay the growth of LNCaP spheroids at these concentrations and that the growth delays induced by olaparib in combination with  $\gamma$ -radiation or [ $^{131}$ I]MIP-1095 were comparable between the two experiments. Olaparib failed to potentiate the spheroid growth delay induced by  $\gamma$ -radiation, as indicated by  $SGD_C$  values ranging from 0.07 to 0.15 (Figure 79a), whereas olaparib enhanced the growth delay induced by [ $^{131}$ I]MIP-1095, as indicated by  $SGD_C$  values ranging from 0.53 to 0.79 (Figure 79b). Reasons for this contradictory result are discussed in Section 8.5.

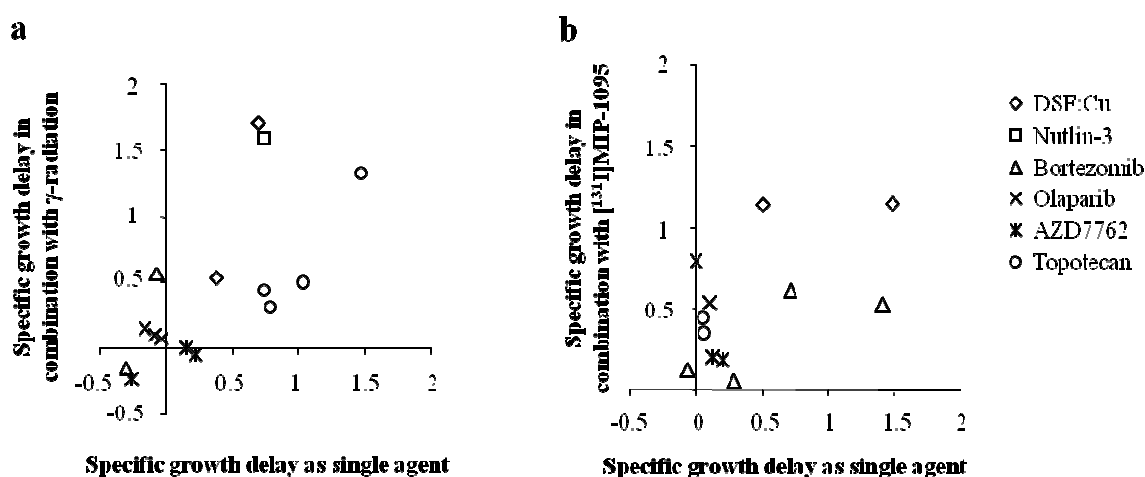


**Figure 79 Comparison of the enhancement of  $\gamma$ -radiation-induced or [ $^{131}$ I]MIP-1095-induced the growth delay by radiosensitising drugs**

For every drug concentration, the  $SGD_C$  value of the combination with  $\gamma$ -radiation (a) or [ $^{131}$ I]MIP-1095 (b) was plotted against the corresponding  $SGD_{SA}$  value of the effect of the drug as a single-agent.

## 8.5 Discussion and summary of the results

The statistical comparison of  $\tau_2$  values of combination treatments with those of single agent treatments demonstrated the enhancing effect of 10  $\mu$ M nutlin-3 (Figure 70b), 1 and 10  $\mu$ M olaparib (Figure 72), 0.1 and 1  $\mu$ M topotecan (Figure 76) and 7.5 and 10 nM bortezomib (Figure 78) on the growth delay induced by [ $^{131}$ I]MIP-1095. It also demonstrated the absence of an enhancing effect of 0.1 and 1  $\mu$ M AZD7762 (Figure 74)

and 2.5 and 5 nM bortezomib (Figure 78) on the growth delay induced by [<sup>131</sup>I]MIP-1095. Accordingly, the lowest SGD<sub>C</sub> values were calculated for AZD7762 and 2.5 and 5 nM bortezomib (SGD<sub>C</sub> range 0.05 - 0.19) whereas the highest SGD<sub>C</sub> values were calculated for 10 μM nutlin-3, 1 and 10 μM olaparib, 0.1 and 1 μM topotecan and 7.5 and 10 nM bortezomib (SGD<sub>C</sub> > 0.34) (Figure 70 to Figure 78). The agreement between the analysis of τ<sub>2</sub> values and SGD<sub>C</sub> was expected since the calculation of SGD<sub>C</sub> values is based on τ<sub>2</sub> values. With the exception of topotecan given in combination with γ-radiation, the analysis of DT values yielded results similar to those derived from τ<sub>2</sub> values with respect to the statistical significance of the potentiation of the growth delay induced by [<sup>131</sup>I]MIP-1095 following combination with the drugs. The τ<sub>2</sub> values are a measure of the early effect of the treatment since a doubling of the spheroid volume occurs within 3 to 4 days from the start of the monitoring period (3 to 4 weeks). DT values are a measure of the growth rate of the exponential growth of the spheroids over 3 to 4 weeks. Thus, the significant increase in DT values following combination treatment compared with single agent treatments demonstrated the persistence of the enhancement of the growth delay induced by [<sup>131</sup>I]MIP-1095 following combination with nutlin-3, olaparib and bortezomib.

The enhancement of the γ-radiation-induced spheroid growth inhibition by 0.01, 0.1 and 1 μM topotecan was only transient as indicated by the failure of the combination treatments to significantly increase the DT values (Figure 75). Upon increase of topotecan concentration to 10 μM, the analysis of the τ<sub>2</sub> and DT values showed that the enhancement of the γ-radiation-induced spheroid growth inhibition persisted over the course of the experiment. This example illustrated the merit of analysing both the growth delay and the growth rate of the exponential phase of spheroid growth for the determination of the enhancement of radiation treatment in a spheroid growth delay experiment.

Spheroids reaching a diameter of approximately 300 μm develop a non-proliferative, hypoxic and acidic core surrounded by a proliferative layer of cells<sup>254</sup>. These features of spheroids in an advanced stage of their growth have been shown to confer resistance to therapy<sup>258,261,262</sup>. In this chapter, LNCaP spheroids on average 100 μm diameter were treated with the drugs, γ-radiation or [<sup>131</sup>I]MIP-1095 as single agents or in combination. Therefore, the demonstration of the potentiation of the growth delay induced by γ-radiation or [<sup>131</sup>I]MIP-1095 was limited to spheroids which had not yet undergone internal morphological changes. Therefore, the clinical implications of the study reported in this chapter are that the drugs that enhanced the growth delay induced by [<sup>131</sup>I]MIP-1095 may

also retard the growth of juvenile malignant lesions which do not contain hypoxic and non-proliferative regions. Alternatively, the combinations of drugs with [<sup>131</sup>I]MIP-1095 may be used as second-line treatments when malignant lesions have been reoxygenated following cytoreductive therapy. A follow-up study would be the evaluation of the potentiating effect of the drugs on the growth delay induced by [<sup>131</sup>I]MIP-1095 in spheroids which have developed a hypoxic core surrounded by a proliferating region of cells using an experimental design similar to that used in Figure 54. This analysis would evaluate the ability of these combinations to overcome the putative resistance to treatment conferred by non-proliferative and hypoxic regions.

As explained in Sections 4.1.3, combination index and isobologram methods of synergy analysis enable the determination of supra-additive or infra-additive interaction between the components of combination therapy. The lack of time did not permit the repetition of these experiments. As explained in Section 7.5, repetitions are needed for the accurate application of the median effect principle and the subsequent calculation of CI values. Furthermore, the application of the combination index and isobologram methods requires the determination of a single-agent dose-response relationship for the two agents of the combination treatment. This is impossible in the case of drugs which do not have an effect on their own such as olaparib (PARP-1 inhibitor) or AZD7762 (Chk1 inhibitor). These two drugs are toxic only to cells which have experienced DNA damage since they specifically target DNA damage responses. Therefore, the combination index and isobologram methods of synergy analysis were not suitable for the comparison of the radiosensitising effects of these drugs.

The purpose of the screening of the radiosensitising properties of drugs is the treatment of prostate carcinoma in combination with [<sup>131</sup>I]MIP-1095. Therefore, it is important that the drug concentrations achievable in the plasma of patients are shown to enhance the growth delay induced by [<sup>131</sup>I]MIP-1095. Clinical studies in which the plasma concentrations of the drugs were measured are listed in Table 11. Olaparib and bortezomib enhanced [<sup>131</sup>I]MIP-1095-induced LNCaP spheroid growth delay at concentrations which are achievable in the plasma of patients (Table 11). No clinical trial involving nutlin-3 or AZD7762 has been reported. The highest topotecan concentration achieved in the plasma of patients was 108.9 nM (Table 11). The lowest concentration of topotecan found to radiosensitise LNCaP spheroids was 10 nM, though the radiosensitising effect was no longer observed 2 to 3 weeks after the end of the treatment (Figure 75). The enhancement of the [<sup>131</sup>I]MIP-1095-induced growth delay by topotecan was observed at a topotecan

concentration of 100 nM (Figure 76). Topotecan concentration of 100 nM constitutes the top end of the range of topotecan plasma concentration (Table 11). The investigation of the radiosensitising effect of topotecan at concentrations less than 100 nM in combination with [<sup>131</sup>I]MIP-1095 constitutes a follow-up experiment to the dataset presented in Figure 76.

Radiation delivered at a high dose rate (HDR) is more cytotoxic than radiation delivered at a low dose rate (LDR). The <sup>60</sup>Co source of  $\gamma$ -radiation used in these experiments corresponded to HDR (1 Gy/min), whereas radiation delivered using [<sup>131</sup>I]MIP-1095 corresponded to LDR (typically several Gy per hour<sup>322</sup>). The linear-quadratic equation which describes the effect of radiation on the survival of cells was described in Section 4.1.2. Briefly, the initial slope of the radiation survival curve results from single hit events in DNA whereas the bend of the radiation survival curve at high radiation doses results from multiple hit events. HDR results in a higher density of ionisations of DNA compared with LDR. Thus HDR results in a greater proportion of lethal DSB formation<sup>323</sup>.

Olaparib is an inhibitor of DNA repair of SSB via the abrogation of PARP-1 enzymatic activity. Since LDR radiation predominantly creates SSB, olaparib should be an efficient radiosensitiser when combined with LDR radiation such as radionuclide therapy. The observation that 1  $\mu$ M olaparib sensitised LNCaP spheroids to [<sup>131</sup>I]MIP-1095 treatment (Figure 72) but not to  $\gamma$ -radiation (Figure 71) treatments was consistent with this conjecture. Recently, the PARP-1 inhibitor PJ34 was shown to be a radiosensitiser in combination with LDR in the form of [<sup>131</sup>I]mIBG<sup>324</sup>.

However, it has been demonstrated that 0.5  $\mu$ M olaparib sensitised HeLa cells and mouse embryo fibroblasts (MEF) to HDR (7.5 Gy/min)<sup>292</sup>. The observation of the radiosensitising effect induced by olaparib in combination with HDR radiation in HeLa and MEF monolayers is in contrast to the absence of a radiosensitising effect in combination with HDR in LNCaP spheroids in the present study. The concentrations of olaparib used were similar: 0.5 versus 1  $\mu$ M. It is suggested that phenotypic differences between the cell lines arising from their respective genetic backgrounds and also from structural differences between monolayers and spheroids may explain this discrepancy.

Cancer cells halt their progression through the cell cycle in response to radiation treatment at the two major cell cycle checkpoints: G1 and G2. Furthermore, the p53 gene is the most commonly mutated gene in cancer<sup>325</sup>. Since p53 controls G1 arrest, inhibitors of G2 arrest

were developed in the expectation that they would constitute efficient treatments of p53-mutated tumours in combination with radiotherapy or other DNA damaging agents. Indeed, cancer cells with no functional checkpoint are more likely to carry DNA damage through S phase and mitosis than cells with only one functional checkpoint. Thus, cancer cells with no functional checkpoint should be more radiosensitive. Wild type p53 LNCaP spheroids were not radiosensitised by the Chk1 inhibitor AZD7762 regardless of the mode of delivery of radiation treatment ( $\gamma$ -radiation or [ $^{131}$ I]MIP1095) (Figure 73 and Figure 74). This result was consistent with the observation of an increased radiosensitising effect by AZD7762 in p53-mutated cancer cells compared with p53 wild type cells<sup>295</sup>. However, it could be argued that the failure of radiosensitisation by AZD7762 could be due to inadequate concentration. The evaluated concentrations of AZD762 depicted in Figure 73 and Figure 74 ranged from 1 nM to 1  $\mu$ M. However, supplementary experiments using 10  $\mu$ M AZD7762 in combination with 3 Gy  $\gamma$ -radiation did not result in the potentiation of the radiation-induced growth delay of LNCaP spheroids (data not shown). Furthermore, it has been demonstrated that 100 nM AZD7762 radiosensitised p53 wild type cells<sup>294,295</sup>. Therefore, the concentrations of AZD7762 in Figure 73 and Figure 74 (1 nM to 1  $\mu$ M) are similar to those previously examined. Moreover, the  $K_i$  value of Chk1 inhibition by AZD7762 is 3.6 nM<sup>293</sup>, suggesting that the concentration of AZD7762 used in the spheroid studies was sufficient for Chk1 inhibition.

The G2 arrest inhibitor, AZD7762, may still be a useful compound for the treatment of p53 wild type cancers but only in combination with inhibitors of the G1 arrest. For instance, nutlin-3, an inhibitor of the MDM2/p53 interaction, demonstrated a strong radiosensitising effect in LNCaP spheroids (Figure 70). The determination of the radiopotentiating effect of the perturbation of the G1 arrest mediated by nutlin-3 in combination with the inhibition of the G2 arrest mediated by AZD7762 is worthy of further investigation.

These data demonstrated that the disruption of the cell cycle is an efficient enhancing mechanism of the growth delay induced by [ $^{131}$ I]MIP-1095. Indeed, targeting the G2 checkpoint by DSF:Cu (Chapter 4 and 5), targeting the G1 checkpoint by nutlin-3 or inhibiting DNA replication by topotecan, all enhanced the effect of  $\gamma$ -radiation or that of [ $^{131}$ I]MIP-1095. The proteasome is involved in the degradation of proteins, such as cyclins, involved in cell cycle regulation. Thus, inhibition of the proteasome may also radiosensitise through disruption of cell cycle progression. In conclusion, there is a good prospect for the use of [ $^{131}$ I]MIP-1095 in combination with radiosensitising drugs for the

treatment of metastatic PCa. The demonstration of potentiation of the effect of [<sup>131</sup>I]MIP-1095 was the objective of the screening program. Further studies are required to quantify the enhancing effect of nutlin-3, topotecan and olaparib using a wider range of concentrations.

## 9 Summary and future work

The focus of this thesis was the elucidation of the mechanisms of DSF cytotoxicity and its radiomodifying properties. Furthermore, we have demonstrated, in spheroids, improved efficacy of radiopharmaceuticals by combination with cytotoxic drugs such as DSF but also nutlin-3, olaparib, topotecan and bortezomib, which potentially constitutes a treatment strategy in metastatic neuroblastoma and PCa.

The first part of the experimental work of this thesis evaluated the dependence on Cu of DSF cytotoxicity. It was shown that the biphasic response profile of DSF resulted from two different mechanisms of action (Figure 8). Equimolar concentrations of DSF and Cu (DSF:Cu) induced a hyperbolic dose-response relationship according to the median effect principle (Figure 15), which allowed the application of isobologram and combination index methods of synergy analysis in the ensuing chapters. Moreover, it was shown that DSF:Cu-induced cytotoxicity did not result from proteasome inhibition because it occurred at concentrations less than 1  $\mu\text{M}$ , which are clinically applicable, whereas proteasome inhibition occurred at concentrations greater than 1  $\mu\text{M}$  (Figure 17).

Secondly, the conflicting reports on the radiomodifying properties of DSF were explained by the wide range of DSF concentrations examined (0.1  $\mu\text{M}$  to 3 mM) and the lack of consideration of the presence of Cu in the culture medium. It was demonstrated that DSF:Cu, at concentrations less than 1  $\mu\text{M}$ , sensitised SK-N-BE(2c) and UVW/NAT cells to  $\gamma$ -radiation treatment delivered by external beam in a synergistic manner (Table 7). The hypothesised radiosensitising mechanism was the inhibition, by DSF:Cu, of DNA repair. This was suggested by the observation that DSF:Cu abrogated the G2 arrest following  $\gamma$ -radiation treatment, thus reducing time for DNA repair (chapter 5).

Furthermore, CDK1 is the most downstream molecular effector of G2 arrest. CDK1 activity depends on its phosphorylation status. CDK1 phosphorylated at tyrosine 15 (pCDK1<sup>15</sup>) is a marker of G2 arrest. If the radiosensitising action of DSF:Cu is the impediment of G2 arrest, then pCDK1<sup>15</sup> activity should be reduced following irradiation in the presence of DSF:Cu compared with radiation treatment alone. We are currently investigating how DSF:Cu modulates total levels of CDK1 and pCDK1<sup>15</sup> following radiation treatment in unsynchronised and synchronised cells. If the levels of pCDK1<sup>15</sup> appear to be modulated by DSF:Cu, the intention is to investigate the levels of the kinase Wee1 and phosphatase Cdc25C which control the phosphorylation status of CDK1.

Moreover, the application of the linear-quadratic model to  $\gamma$ -radiation survival curves allowed the formulation of the hypothesis that DSF:Cu increases the proportion of SSB but not DSB. To further investigate this conjecture, the analysis of the type of DNA damage produced by radiation in the presence of DSF:Cu could be carried out by comet assay in alkaline versus neutral conditions. Alkaline pH denatures DNA. Thus, in alkaline conditions, DNA molecules containing SSB (alkali-labile sites) give rise to the presence of DNA fragments of reduced size. In contrast, the comet assay performed in non-denaturing conditions at neutral pH measures the amount of DSB only because DNA molecules containing SSB do not result in DNA fragments of reduced size<sup>326</sup>. The observation of a “comet tail” in alkaline comet assay, indicative of the presence of SSB, but not in neutral comet assay, indicative of the absence of DSB, following irradiation in the presence of DSF:Cu would validate the conjecture formulated following the linear-quadratic evaluation of radiosensitisation by DSF:Cu.

The third part of this thesis was the investigation of the enhancement of the efficacy of two radiopharmaceuticals, [<sup>131</sup>I]mIBG and [<sup>131</sup>I]MIP-1095, with specificity for neuroblastoma and PCa, respectively. This study was carried out in multicellular tumour spheroids, *in vitro* models of avascular micrometastases, which are optimally suited for the investigation of the efficacy of radiopharmaceuticals. It was shown that DSF:Cu potentiated the spheroid growth delay induced by [<sup>131</sup>I]mIBG or [<sup>131</sup>I]MIP-1095 in a synergistic manner (chapter 7). Furthermore, olaparib, nutlin-3, topotecan and bortezomib also enhanced the spheroid growth delay induced by [<sup>131</sup>I]MIP-1095 (chapter 8).

Internal morphological changes in LNCaP spheroids at an advanced stage of development were more resistant to DSF:Cu treatment than juvenile spheroids (Figure 54). An important follow-up project to this thesis is the evaluation of the efficacy of combination treatments consisting of DSF:Cu with [<sup>131</sup>I]mIBG or [<sup>131</sup>I]MIP-1095 in developmentally advanced spheroids which had undergone internal morphological changes. This work is important to understand the impact of hypoxia, pH and heterogeneous proliferation status on the interaction of DSF:Cu with radiation. The putative demonstration of such a combination treatment able to sterilise spheroids at a more advanced stage of development would suggest that this combination may also target more advanced malignant lesions.

In conclusion, DSF is a promising drug for inclusion in combination with [<sup>131</sup>I]mIBG or [<sup>131</sup>I]MIP-1095 for the treatment of metastatic neuroblastoma or PCa, respectively. There is also a good prospect for the treatment of metastatic PCa with [<sup>131</sup>I]MIP-1095 in

combination with olaparib, nutlin-3, topotecan or bortezomib. It was recently reported by us that DSF enhanced efficacy of [<sup>131</sup>I]mIBG treatment in mice bearing SK-N-BE(2c) and UVW/NAT xenografts<sup>219</sup>. *In vitro* studies, using monolayers and spheroids, as well as animal models have suggested the benefit of DSF:Cu adjunct to radiotherapy. Furthermore, since DSF has only been used in the treatment of addictive behaviours in teenagers and adults, future studies should also include evaluation of the safety of DSF in children before inclusion of DSF in combination with [<sup>131</sup>I]mIBG for the treatment of metastatic neuroblastoma.

## 10 Appendix

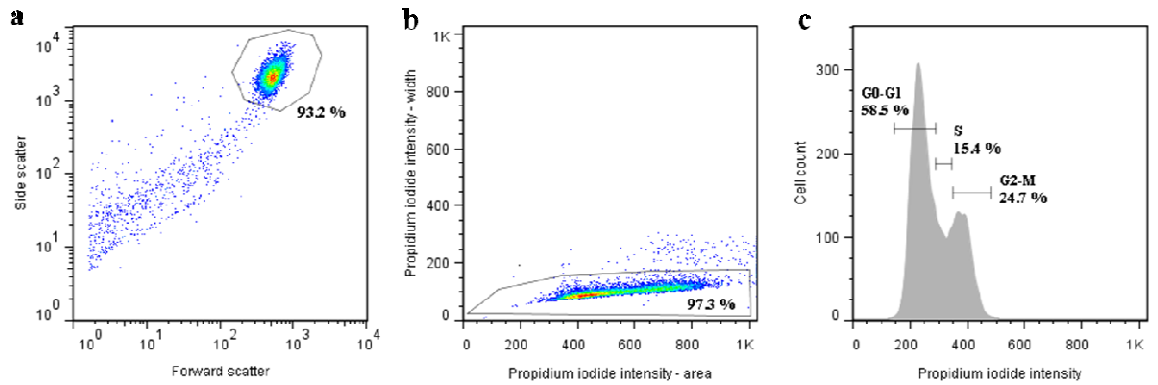


**Figure 80 FACS analysis carried out using FlowJo software**

(a) The side scatter and the forward scatter were used to select 93.2% of cells with homogeneous granularity and size, respectively. (b) The FL2 laser was used to detect propidium iodide fluorescence. The doublet discrimination features (area and width) were used to eliminate aggregated cells. 97.3% of fluorescence signal was detected from single cells. (c) Single cells with homogeneous granularity and size were then selected to construct a histogram showing their distribution according to intensity of propidium iodide signal, a measure of DNA content. The mean fluorescence determined from the G0-G1 peak was set at 200. 58.5% of cells were in the G0-G1 phase of the cell cycle. The mean fluorescence determined from the G2-M peak had a value of 400. 24.7% of cells were in the G2-M phase of the cell cycle. The S phase population of cells (15.4%) is represented by propidium iodide intensity ranging from 200 to 400.

## 11 List of references

- 1 Orlandi, F. *et al.* Treatment of medullary thyroid carcinoma: an update. *Endocrine-Related Cancer* **8**, 135-147 (2001).
- 2 Smith-Jones, P. M. Radioimmunotherapy of prostate cancer. *Q J Nucl Med Mol Imaging* **48**, 297-304 (2004).
- 3 Koppe, M. J., Bleichrodt, R. P., Oyen, W. J. & Boerman, O. C. Radioimmunotherapy and colorectal cancer. *Br J Surg* **92**, 264-276 (2005).
- 4 Modak, S. & Cheung, N. K. Antibody-based targeted radiation to pediatric tumors. *J Nucl Med* **46 Suppl 1**, 157S-163S (2005).
- 5 Bethge, W. A. & Sandmaier, B. M. Targeted cancer therapy using radiolabeled monoclonal antibodies. *Technology in Cancer Research & Treatment* **4**, 393-405 (2005).
- 6 Chatal, J. F. *et al.* Biodistribution of indium-111-labeled OC 125 monoclonal antibody intraperitoneally injected into patients operated on for ovarian carcinomas. *Cancer Res* **49**, 3087-3094 (1989).
- 7 Williams, L. E. *et al.* Tumor uptake as a function of tumor mass: a mathematic model. *J Nucl Med* **29**, 103-109 (1988).
- 8 Behr, T. M. *et al.* Cure of metastatic human colonic cancer in mice with radiolabeled monoclonal antibody fragments. *Clin Cancer Res* **6**, 4900-4907 (2000).
- 9 Mairs, R. J. *et al.* The distribution of alternative agents for targeted radiotherapy within human neuroblastoma spheroids. *Br J Cancer* **63**, 404-409 (1991).
- 10 Mairs, R. J., Angerson, W. J., Babich, J. W. & Murray, T. Differential penetration of targeting agents into multicellular spheroids derived from human neuroblastoma. *Prog Clin Biol Res* **366**, 495-501 (1991).
- 11 Meller, S. Targeted radiotherapy for neuroblastoma. *Arch Dis Child* **77**, 389-391 (1997).
- 12 O'Donoghue, J. A. Implications of nonuniform tumor doses for radioimmunotherapy. *J Nucl Med* **40**, 1337-1341 (1999).
- 13 Brechbiel, M. W. Targeted alpha-therapy: past, present, future? *Dalton Transactions*, 4918-4928 (2007).
- 14 Wheldon, T. E., Odonoghue, J. A., Barrett, A. & Michalowski, A. S. The Curability of Tumors of Differing Size by Targeted Radiotherapy Using I-131 or Y-90. *Radiotherapy and Oncology* **21**, 91-99 (1991).
- 15 Perkins, A. In vivo molecular targeted radiotherapy. *Biomed Imaging Interv J* **1**, e9 (2005).

- 16 Taylor, T. *et al.* Outcome after treatment of high-risk papillary and non-Hurthle-cell follicular thyroid carcinoma. *Ann Intern Med* **129**, 622-627 (1998).
- 17 Coleman, R. E. Clinical features of metastatic bone disease and risk of skeletal morbidity. *Clin Cancer Res* **12**, 6243s-6249s (2006).
- 18 Roque, I. F. M., Martinez-Zapata, M. J., Scott-Brown, M. & Alonso-Coello, P. Radioisotopes for metastatic bone pain. *Cochrane Database Syst Rev*, CD003347 (2011).
- 19 Witzig, T. E. *et al.* Randomized controlled trial of yttrium-90-labeled ibritumomab tiuxetan radioimmunotherapy versus rituximab immunotherapy for patients with relapsed or refractory low-grade, follicular, or transformed B-cell non-Hodgkin's lymphoma. *J Clin Oncol* **20**, 2453-2463 (2002).
- 20 Davis, T. A. *et al.* The radioisotope contributes significantly to the activity of radioimmunotherapy. *Clin Cancer Res* **10**, 7792-7798 (2004).
- 21 Kloppel, G. Tumour biology and histopathology of neuroendocrine tumours. *Best Pract Res Clin Endocrinol Metab* **21**, 15-31 (2007).
- 22 Plockinger, U. & Wiedenmann, B. Neuroendocrine tumors. Biotherapy. *Best Pract Res Clin Endocrinol Metab* **21**, 145-162 (2007).
- 23 Kwekkeboom, D. J. *et al.* Radiolabeled somatostatin analog [177Lu-DOTA0,Tyr3]octreotate in patients with endocrine gastroenteropancreatic tumors. *J Clin Oncol* **23**, 2754-2762 (2005).
- 24 Waldherr, C., Pless, M., Maecke, H. R., Haldemann, A. & Mueller-Brand, J. The clinical value of [90Y-DOTA]-D-Phe1-Tyr3-octreotide (90Y-DOTATOC) in the treatment of neuroendocrine tumours: a clinical phase II study. *Ann Oncol* **12**, 941-945 (2001).
- 25 Spix, C., Pastore, G., Sankila, R., Stiller, C. A. & Steliarova-Foucher, E. Neuroblastoma incidence and survival in European children (1978-1997): report from the Automated Childhood Cancer Information System project. *Eur J Cancer* **42**, 2081-2091 (2006).
- 26 Shimada, H. *et al.* The International Neuroblastoma Pathology Classification (the Shimada system). *Cancer* **86**, 364-372 (1999).
- 27 Cohn, S. L. *et al.* The International Neuroblastoma Risk Group (INRG) classification system: an INRG Task Force report. *J Clin Oncol* **27**, 289-297 (2009).
- 28 DuBois, S. G. *et al.* Metastatic sites in stage IV and IVS neuroblastoma correlate with age, tumor biology, and survival. *J Pediatr Hematol Oncol* **21**, 181-189 (1999).
- 29 Hara, J. Development of treatment strategies for advanced neuroblastoma. *Int J Clin Oncol* **17**, 196-203 (2012).

- 30 Matthay, K. K. *et al.* Treatment of high-risk neuroblastoma with intensive chemotherapy, radiotherapy, autologous bone marrow transplantation, and 13-cis-retinoic acid. Children's Cancer Group. *N Engl J Med* **341**, 1165-1173 (1999).
- 31 Yu, A. L. *et al.* Anti-GD2 antibody with GM-CSF, interleukin-2, and isotretinoin for neuroblastoma. *N Engl J Med* **363**, 1324-1334 (2010).
- 32 Carlin, S. *et al.* Development of a real-time polymerase chain reaction assay for prediction of the uptake of meta-[(131)I]iodobenzylguanidine by neuroblastoma tumors. *Clin Cancer Res* **9**, 3338-3344 (2003).
- 33 Hutchinson, R. J. *et al.* Long-term results of [131I]metaiodobenzylguanidine treatment of refractory advanced neuroblastoma. *J Nucl Biol Med* **35**, 237-240 (1991).
- 34 Klingebiel, T. *et al.* Treatment of neuroblastoma with [131I]metaiodobenzylguanidine: long-term results in 25 patients. *J Nucl Biol Med* **35**, 216-219 (1991).
- 35 Lashford, L. S. *et al.* Phase I/II study of iodine 131 metaiodobenzylguanidine in chemoresistant neuroblastoma: a United Kingdom Children's Cancer Study Group investigation. *J Clin Oncol* **10**, 1889-1896 (1992).
- 36 Lumbroso, J., Hartmann, O. & Schlumberger, M. Therapeutic use of [131I]metaiodobenzylguanidine in neuroblastoma: a phase II study in 26 patients. "Societe Francaise d'Oncologie Pediatrique" and Nuclear Medicine Co-investigators. *J Nucl Biol Med* **35**, 220-223 (1991).
- 37 Matthay, K. K. *et al.* Phase I dose escalation of 131I-metaiodobenzylguanidine with autologous bone marrow support in refractory neuroblastoma. *J Clin Oncol* **16**, 229-236 (1998).
- 38 Garaventa, A. *et al.* 131I-metaiodobenzylguanidine (131I-MIBG) therapy for residual neuroblastoma: a mono-institutional experience with 43 patients. *Br J Cancer* **81**, 1378-1384 (1999).
- 39 Matthay, K. K. *et al.* Phase II study on the effect of disease sites, age, and prior therapy on response to iodine-131-metaiodobenzylguanidine therapy in refractory neuroblastoma. *J Clin Oncol* **25**, 1054-1060 (2007).
- 40 Matthay, K. K. *et al.* Phase I dose escalation of iodine-131-metaiodobenzylguanidine with myeloablative chemotherapy and autologous stem-cell transplantation in refractory neuroblastoma: a new approaches to Neuroblastoma Therapy Consortium Study. *J Clin Oncol* **24**, 500-506 (2006).
- 41 de Kraker, J. *et al.* Iodine-131-metaiodobenzylguanidine as initial induction therapy in stage 4 neuroblastoma patients over 1 year of age. *Eur J Cancer* **44**, 551-556 (2008).

- 42 Mastrangelo, S., Rufini, V., Ruggiero, A., Di Giannatale, A. & Riccardi, R. Treatment of advanced neuroblastoma in children over 1 year of age: the critical role of (1)(3)(1)I-metaiodobenzylguanidine combined with chemotherapy in a rapid induction regimen. *Pediatr Blood Cancer* **56**, 1032-1040 (2011).
- 43 DuBois, S. G. *et al.* Phase I study of vincristine, irinotecan, and (1)(3)(1)I-metaiodobenzylguanidine for patients with relapsed or refractory neuroblastoma: a new approaches to neuroblastoma therapy trial. *Clin Cancer Res* **18**, 2679-2686 (2012).
- 44 Gaze, M. N., Gains, J. E., Walker, C. & Bomanji, J. B. Optimization of molecular radiotherapy with [131I]-meta Iodobenzylguanidine for high-risk neuroblastoma. *Q J Nucl Med Mol Imaging* **57**, 66-78 (2013).
- 45 Ferlay, J., Parkin, D. M. & Steliarova-Foucher, E. Estimates of cancer incidence and mortality in Europe in 2008. *Eur J Cancer* **46**, 765-781 (2010).
- 46 Parkin, D. M., Bray, F., Ferlay, J. & Pisani, P. Global cancer statistics, 2002. *CA Cancer J Clin* **55**, 74-108 (2005).
- 47 Holmberg, L. *et al.* Results from the Scandinavian Prostate Cancer Group Trial Number 4: a randomized controlled trial of radical prostatectomy versus watchful waiting. *J Natl Cancer Inst Monogr* **2012**, 230-233 (2012).
- 48 Huggins, C. & Hodges, C. V. Studies on prostatic cancer - I The effect of castration, of estrogen and of androgen injection on serum phosphatases in metastatic carcinoma of the prostate. *Cancer Research* **1**, 293-297 (1941).
- 49 Hirst, C. J., Cabrera, C. & Kirby, M. Epidemiology of castration resistant prostate cancer: a longitudinal analysis using a UK primary care database. *Cancer Epidemiol* **36**, e349-353 (2012).
- 50 Carducci, M. A. *et al.* A phase 3 randomized controlled trial of the efficacy and safety of atrasentan in men with metastatic hormone-refractory prostate cancer. *Cancer* **110**, 1959-1966 (2007).
- 51 Saad, F. *et al.* A randomized, placebo-controlled trial of zoledronic acid in patients with hormone-refractory metastatic prostate carcinoma. *J Natl Cancer Inst* **94**, 1458-1468 (2002).
- 52 Sternberg, C. N. *et al.* Multinational, double-blind, phase III study of prednisone and either satraplatin or placebo in patients with castrate-refractory prostate cancer progressing after prior chemotherapy: the SPARC trial. *J Clin Oncol* **27**, 5431-5438 (2009).
- 53 Fizazi, K. *et al.* Abiraterone acetate for treatment of metastatic castration-resistant prostate cancer: final overall survival analysis of the COU-AA-301 randomised, double-blind, placebo-controlled phase 3 study. *Lancet Oncol* **13**, 983-992 (2012).

- 54 Ryan, C. J. *et al.* Abiraterone in metastatic prostate cancer without previous chemotherapy. *N Engl J Med* **368**, 138-148 (2013).
- 55 Scher, H. I. *et al.* Increased survival with enzalutamide in prostate cancer after chemotherapy. *N Engl J Med* **367**, 1187-1197 (2012).
- 56 Robinson, M. B., Blakely, R. D., Couto, R. & Coyle, J. T. Hydrolysis of the Brain Dipeptide N-Acetyl-L-Aspartyl-L-Glutamate - Identification and Characterization of a Novel N-Acetylated Alpha-Linked Acidic Dipeptidase Activity from Rat-Brain. *Journal of Biological Chemistry* **262**, 14498-14506 (1987).
- 57 Luthi-Carter, R., Barczak, A. K., Speno, H. & Coyle, J. T. Molecular characterization of human brain N-acetylated alpha-linked acidic dipeptidase (NAALADase). *Journal of Pharmacology and Experimental Therapeutics* **286**, 1020-1025 (1998).
- 58 Rajasekaran, A. K., Anilkumar, G. & Christiansen, J. J. Is prostate-specific membrane antigen a multifunctional protein? *American Journal of Physiology-Cell Physiology* **288**, C975-C981 (2005).
- 59 Lapidus, R. G., Tiffany, C. W., Isaacs, J. T. & Slusher, B. S. Prostate-specific membrane antigen (PSMA) enzyme activity is elevated in prostate cancer cells. *Prostate* **45**, 350-354 (2000).
- 60 Wright, G. L. *et al.* Upregulation of prostate-specific membrane antigen after androgen-deprivation therapy. *Urology* **48**, 326-334 (1996).
- 61 Barrett, J. A. *et al.* First-in-Man Evaluation of 2 High-Affinity PSMA-Avid Small Molecules for Imaging Prostate Cancer. *J Nucl Med* **54**, 380-387 (2013).
- 62 Kahn, D. *et al.* A phase II study of [90Y] yttrium-capromab pendetide in the treatment of men with prostate cancer recurrence following radical prostatectomy. *Cancer Biother Radiopharm* **14**, 99-111 (1999).
- 63 Liu, H. *et al.* Monoclonal antibodies to the extracellular domain of prostate-specific membrane antigen also react with tumor vascular endothelium. *Cancer Res* **57**, 3629-3634 (1997).
- 64 Maresca, K. P. *et al.* A series of halogenated heterodimeric inhibitors of prostate specific membrane antigen (PSMA) as radiolabeled probes for targeting prostate cancer. *J Med Chem* **52**, 347-357 (2009).
- 65 Hillier, S. M. *et al.* Preclinical evaluation of novel glutamate-urea-lysine analogues that target prostate-specific membrane antigen as molecular imaging pharmaceuticals for prostate cancer. *Cancer Res* **69**, 6932-6940 (2009).
- 66 Halliwell, B. in *eLS* (John Wiley & Sons, Ltd, 2001).

- 67 Dai, J. M. *et al.* Microarray analysis of differentially expressed genes in mouse bone marrow tissues after ionizing radiation. *Int J Radiat Biol* **82**, 511-521 (2006).
- 68 Jeong, J. *et al.* Temporal cDNA microarray analysis of gene expression in human hepatocellular carcinoma upon radiation exposure. *Oncol Rep* **15**, 33-48 (2006).
- 69 Otomo, T., Hishii, M., Arai, H., Sato, K. & Sasai, K. Microarray analysis of temporal gene responses to ionizing radiation in two glioblastoma cell lines: up-regulation of DNA repair genes. *J Radiat Res* **45**, 53-60 (2004).
- 70 Sokolov, M. V., Smirnova, N. A., Camerini-Otero, R. D., Neumann, R. D. & Panyutin, I. G. Microarray analysis of differentially expressed genes after exposure of normal human fibroblasts to ionizing radiation from an external source and from DNA-incorporated iodine-125 radionuclide. *Gene* **382**, 47-56 (2006).
- 71 Boerma, M. *et al.* Microarray analysis of gene expression profiles of cardiac myocytes and fibroblasts after mechanical stress, ionising or ultraviolet radiation. *BMC Genomics* **6**, 6 (2005).
- 72 Rodningen, O. K., Overgaard, J., Alsner, J., Hastie, T. & Borresen-Dale, A. L. Microarray analysis of the transcriptional response to single or multiple doses of ionizing radiation in human subcutaneous fibroblasts. *Radiother Oncol* **77**, 231-240 (2005).
- 73 Vogel, C., Hager, C. & Bastians, H. Mechanisms of mitotic cell death induced by chemotherapy-mediated G2 checkpoint abrogation. *Cancer Res* **67**, 339-345 (2007).
- 74 Powell, S. & McMillan, T. J. DNA Damage and Repair Following Treatment with Ionizing-Radiation. *Radiotherapy and Oncology* **19**, 95-108 (1990).
- 75 Palcic, B., Brosing, J. W. & Skarsgard, L. D. Survival measurements at low doses: oxygen enhancement ratio. *Br J Cancer* **46**, 980-984 (1982).
- 76 Ward, J. F. DNA Damage Produced by Ionizing-Radiation in Mammalian-Cells - Identities, Mechanisms of Formation, and Reparability. *Progress in Nucleic Acid Research and Molecular Biology* **35**, 95-125 (1988).
- 77 Wallace, S. S. Enzymatic processing of radiation-induced free radical damage in DNA. *Radiat Res* **150**, S60-79 (1998).
- 78 Wallace, S. S., Murphy, D. L. & Sweasy, J. B. Base excision repair and cancer. *Cancer Lett* **327**, 73-89 (2012).
- 79 Svilar, D., Goellner, E. M., Almeida, K. H. & Sobol, R. W. Base excision repair and lesion-dependent subpathways for repair of oxidative DNA damage. *Antioxid Redox Signal* **14**, 2491-2507 (2011).
- 80 Mladenov, E. & Iliakis, G. Induction and repair of DNA double strand breaks: the increasing spectrum of non-homologous end joining pathways. *Mutation research* **711**, 61-72 (2011).

- 81 Chen, G. *et al.* Radiation-induced assembly of Rad51 and Rad52 recombination complex requires ATM and c-Abl. *J Biol Chem* **274**, 12748-12752 (1999).
- 82 Radiosensitisers. *Lancet* **2**, 638-640 (1972).
- 83 Farber, J. L. Mechanisms of Cell Injury by Activated Oxygen Species. *Environmental Health Perspectives* **102**, 17-24 (1994).
- 84 Gupte, A. & Mumper, R. J. Elevated copper and oxidative stress in cancer cells as a target for cancer treatment. *Cancer Treatment Reviews* **35**, 32-46 (2009).
- 85 Sharma, P. K., Bhardwaj, R., Dwarakanath, B. S. & Varshney, R. Metabolic oxidative stress induced by a combination of 2-DG and 6-AN enhances radiation damage selectively in malignant cells via non-coordinated expression of antioxidant enzymes. *Cancer Lett* **295**, 154-166 (2010).
- 86 Miller, W. H., Jr. Molecular targets of arsenic trioxide in malignant cells. *Oncologist* **7 Suppl 1**, 14-19 (2002).
- 87 Grimm, S. A. *et al.* Phase I study of arsenic trioxide and temozolomide in combination with radiation therapy in patients with malignant gliomas. *J Neurooncol* **110**, 237-243 (2012).
- 88 Chalmers, A. J. Poly(ADP-ribose) polymerase-1 and ionizing radiation: Sensor, signalling and therapeutic target. *Clinical Oncology* **16**, 29-39 (2004).
- 89 Dungey, F. A., Loser, D. A. & Chalmers, A. J. Replication-Dependent Radiosensitization of Human Glioma Cells by Inhibition of Poly(Adp-Ribose) Polymerase: Mechanisms and Therapeutic Potential. *International Journal of Radiation Oncology Biology Physics* **72**, 1188-1197 (2008).
- 90 Liu, X. *et al.* Potentiation of temozolomide cytotoxicity by poly(ADP)ribose polymerase inhibitor ABT-888 requires a conversion of single-stranded DNA damages to double-stranded DNA breaks. *Mol Cancer Res* **6**, 1621-1629 (2008).
- 91 Wong, J. Y. Systemic targeted radionuclide therapy: potential new areas. *Int J Radiat Oncol Biol Phys* **66**, S74-82 (2006).
- 92 McCluskey, A. G. *et al.* [I-131]meta-iodobenzylguanidine and topotecan combination treatment of tumors expressing the noradrenaline transporter. *Clinical Cancer Research* **11**, 7929-7937 (2005).
- 93 Gaze, M. *et al.* The early European experience of high activities of meta-iodobenzylguanidine and topotecan in neuroblastoma. *Pediatric Blood & Cancer* **49**, 554-554 (2007).
- 94 Carlsson, J., Aronsson, E. F., Hietala, S. A., Stigbrand, T. & Tennvall, J. Tumour therapy with radionuclides: assessment of progress and problems. *Radiotherapy and Oncology* **66**, 107-111 (2003).

- 95 Larsen, A. K., Ouaret, D., El Ouadrani, K. & Petitprez, A. Targeting EGFR and VEGF(R) pathway cross-talk in tumor survival and angiogenesis. *Pharmacol Ther* **131**, 80-90 (2011).
- 96 Jin, Q. & Esteva, F. J. Cross-talk between the ErbB/HER family and the type I insulin-like growth factor receptor signaling pathway in breast cancer. *J Mammary Gland Biol Neoplasia* **13**, 485-498 (2008).
- 97 Hellerstedt, B. A. & Pienta, K. J. The current state of hormonal therapy for prostate cancer. *CA Cancer J Clin* **52**, 154-179 (2002).
- 98 Steel, G. G. & Peckham, M. J. Exploitable Mechanisms in Combined Radiotherapy-Chemotherapy - Concept of Additivity. *International Journal of Radiation Oncology Biology Physics* **5**, 85-91 (1979).
- 99 Williams, E. E. Effects of alcohol on workers with carbon disulfide. *JAMA* **109**, 1471-1474 (1937).
- 100 Hald, J. & Jacobsen, E. A Drug Sensitising the Organism to Ethyl Alcohol. *Lancet* **255**, 1001-1004 (1948).
- 101 Martensen-larsen, O. Treatment of Alcoholism with a Sensitising Drug. *Lancet* **255**, 1004-1005 (1948).
- 102 Goldstein, M., Lauber, E. & McKereghan, M. R. Inhibition of Dopamine-Beta-Hydroxylase by Tropolone + Other Chelating Agents. *Biochemical Pharmacology* **13**, 1103-& (1964).
- 103 Petrakis, I. L. *et al.* Disulfiram treatment for cocaine dependence in methadone-maintained opioid addicts. *Addiction* **95**, 219-228 (2000).
- 104 Carroll, K. M., Nich, C., Ball, S. A., McCance, E. & Rounsavile, B. J. Treatment of cocaine and alcohol dependence with psychotherapy and disulfiram. *Addiction* **93**, 713-727 (1998).
- 105 Mutschler, J. *et al.* Disulfiram, an option for the treatment of pathological gambling. *Alcohol and alcoholism* **45**, 214-216 (2010).
- 106 Meyer, G. *et al.* Neuroendocrine response to casino gambling in problem gamblers. *Psychoneuroendocrinology* **29**, 1272-1280 (2004).
- 107 Schmidt, W. & Delint, J. Causes of Death of Alcoholics. *Quarterly Journal of Studies on Alcohol* **33**, 171-& (1972).
- 108 Lewison, E. F. Spontaneous regression of breast cancer. *Progress in clinical and biological research* **12**, 47-53 (1977).
- 109 Brar, S. S. *et al.* Disulfiram inhibits activating transcription factor/cyclic AMP-responsive element binding protein and human melanoma growth in a metal-dependent

- manner in vitro, in mice and in a patient with metastatic disease. *Molecular Cancer Therapeutics* **3**, 1049-1060 (2004).
- 110 Viola-Rhenals, M., Rieber, M. S. & Rieber, M. Suppression of survival in human SKBR3 breast carcinoma in response to metal-chelator complexes is preferential for copper-dithiocarbamate. *Biochem Pharmacol* **71**, 722-734 (2006).
- 111 Bradberry, S. M. & Vale, J. A. Therapeutic review: do diethyldithiocarbamate and disulfiram have a role in acute nickel carbonyl poisoning? *J Toxicol Clin Toxicol* **37**, 259-264 (1999).
- 112 Jones, S. G. & Jones, M. M. Structure-activity relationships among dithiocarbamate antidotes for acute cadmium chloride intoxication. *Environ Health Perspect* **54**, 285-290 (1984).
- 113 Nagai, M. *et al.* The oncology drug elesclomol selectively transports copper to the mitochondria to induce oxidative stress in cancer cells. *Free Radic Biol Med* **52**, 2142-2150 (2012).
- 114 Tardito, S. *et al.* Copper Binding Agents Acting as Copper Ionophores Lead to Caspase Inhibition and Paraptotic Cell Death in Human Cancer Cells. *J Am Chem Soc* (2011).
- 115 Sutton, H. C. & Winterbourn, C. C. On the Participation of Higher Oxidation-States of Iron and Copper in Fenton Reactions. *Free Radical Biology and Medicine* **6**, 53-60 (1989).
- 116 Szatrowski, T. P. & Nathan, C. F. Production of Large Amounts of Hydrogen-Peroxide by Human Tumor-Cells. *Cancer Research* **51**, 794-798 (1991).
- 117 Heikkila, R. E., Cabbat, F. S. & Cohen, G. In vivo Inhibition of Superoxide-Dismutase in Mice by Diethyldithiocarbamate. *Journal of Biological Chemistry* **251**, 2182-2185 (1976).
- 118 Wojtowicz, E. J. *et al.* Colorimetric determination of disulfiram in tablets: collaborative study. *J Assoc Off Anal Chem* **64**, 554-556 (1981).
- 119 Nagendra, S. N., Shetty, K. T., Subhash, M. N. & Guru, S. C. Role of glutathione reductase system in disulfiram conversion to diethyldithiocarbamate. *Life Sci* **49**, 23-28 (1991).
- 120 Cen, D. *et al.* Disulfiram induces apoptosis in human melanoma cells: a redox-related process. *Mol Cancer Ther* **1**, 197-204 (2002).
- 121 Chen, D., Cui, Q. Z. C., Yang, H. J. & Dou, Q. P. Disulfiram, a clinically used anti-alcoholism drug and copper-binding agent, induces apoptotic cell death in breast cancer cultures and xenografts via inhibition of the proteasome activity. *Cancer Research* **66**, 10425-10433 (2006).

- 122 Li, N. X. & Karin, M. Is NF-kappa B the sensor of oxidative stress? *Faseb Journal* **13**, 1137-1143 (1999).
- 123 Russo, S. M. *et al.* Enhancement of radiosensitivity by proteasome inhibition: Implications for a role of NF-kappa B. *International Journal of Radiation Oncology Biology Physics* **50**, 183-193 (2001).
- 124 Li, N. & Karin, M. Ionizing radiation and short wavelength UV activate NF-kappaB through two distinct mechanisms. *Proc Natl Acad Sci U S A* **95**, 13012-13017 (1998).
- 125 Honda, N., Yagi, K., Ding, G. R. & Miyakoshi, J. Radiosensitization by overexpression of the nonphosphorylation form of I kappa B-alpha in human glioma cells. *Journal of Radiation Research* **43**, 283-292 (2002).
- 126 Jang, J. H. & Surh, Y. J. Bcl-2 protects against Abeta(25-35)-induced oxidative PC12 cell death by potentiation of antioxidant capacity. *Biochem Biophys Res Commun* **320**, 880-886 (2004).
- 127 Gordon, G. J. *et al.* Inhibitor of apoptosis proteins are regulated by tumour necrosis factor-alpha in malignant pleural mesothelioma. *J Pathol* **211**, 439-446 (2007).
- 128 Jang, J. H. & Surh, Y. J. Bcl-2 attenuation of oxidative cell death is associated with up-regulation of gamma-glutamylcysteine ligase via constitutive NF-kappaB activation. *J Biol Chem* **279**, 38779-38786 (2004).
- 129 Wang, W., McLeod, H. L. & Cassidy, J. Disulfiram-mediated inhibition of NF-kappaB activity enhances cytotoxicity of 5-fluorouracil in human colorectal cancer cell lines. *Int J Cancer* **104**, 504-511 (2003).
- 130 Oridate, N. *et al.* Involvement of reactive oxygen species in N-(4-hydroxyphenyl)retinamide-induced apoptosis in cervical carcinoma cells. *J Natl Cancer Inst* **89**, 1191-1198 (1997).
- 131 Kyle, M. E., Serroni, A. & Farber, J. L. The inhibition of lipid peroxidation by disulfiram prevents the killing of cultured hepatocytes by allyl alcohol, tert-butyl hydroperoxide, hydrogen peroxide and diethyl maleate. *Chem Biol Interact* **72**, 269-275 (1989).
- 132 Burkitt, M. J. *et al.* Dithiocarbamate toxicity toward thymocytes involves their copper-catalyzed conversion to thiuram disulfides, which oxidize glutathione in a redox cycle without the release of reactive oxygen species. *Arch Biochem Biophys* **353**, 73-84 (1998).
- 133 Pande, V. & Ramos, M. J. Nuclear factor kappa B: a potential target for anti-HIV chemotherapy. *Curr Med Chem* **10**, 1603-1615 (2003).

- 134 Wiesener, N., Zimmer, C., Jarasch-Althof, N., Wutzler, P. & Henke, A. Therapy of experimental influenza virus infection with pyrrolidine dithiocarbamate. *Med Microbiol Immunol* (2011).
- 135 Sen, R. & Baltimore, D. Multiple Nuclear Factors Interact with the Immunoglobulin Enhancer Sequences. *Cell* **46**, 705-716 (1986).
- 136 Hayden, M. S., West, A. P. & Ghosh, S. NF-kappa B and the immune response. *Oncogene* **25**, 6758-6780 (2006).
- 137 Renoux, G. & Renoux, M. Thymus-Like Activities of Sulfur Derivatives on T-Cell Differentiation. *Journal of Experimental Medicine* **145**, 466-471 (1977).
- 138 Sauna, Z. E., Peng, X. H., Nandigama, K., Tekle, S. & Ambudkar, S. V. The molecular basis of the action of disulfiram as a modulator of the multidrug resistance-linked ATP binding cassette transporters MDR1 (ABCB1) and MRP1 (ABCC1). *Molecular Pharmacology* **65**, 675-684 (2004).
- 139 Loo, T. W., Bartlett, M. C. & Clarke, D. M. Disulfiram metabolites permanently inactivate the human multidrug resistance P-glycoprotein. *Mol Pharm* **1**, 426-433 (2004).
- 140 Pajic, M., Norris, M. D., Cohn, S. L. & Haber, M. The role of the multidrug resistance-associated protein 1 gene in neuroblastoma biology and clinical outcome. *Cancer Lett* **228**, 241-246 (2005).
- 141 van Brussel, J. P. & Mickisch, G. H. Multidrug resistance in prostate cancer. *Onkologie* **26**, 175-181 (2003).
- 142 Vanmaanen, J. M. S., Retel, J., Devries, J. & Pinedo, H. M. Mechanism of Action of Antitumor Drug Etoposide - a Review. *Journal of the National Cancer Institute* **80**, 1526-1533 (1988).
- 143 Wozniak, A. J., Glisson, B. S., Hande, K. R. & Ross, W. E. Inhibition of etoposide-induced DNA damage and cytotoxicity in L1210 cells by dehydrogenase inhibitors and other agents. *Cancer Res* **44**, 626-632 (1984).
- 144 Patel, J. M. Metabolism and Pulmonary Toxicity of Cyclophosphamide. *Pharmacology & Therapeutics* **47**, 137-146 (1990).
- 145 Hilton, J. Deoxyribonucleic acid crosslinking by 4-hydroperoxycyclophosphamide in cyclophosphamide-sensitive and -resistant L1210 cells. *Biochem Pharmacol* **33**, 1867-1872 (1984).
- 146 Hacker, M. P., Ershler, W. B., Newman, R. A. & Gamelli, R. L. Effect of disulfiram (tetraethylthiuram disulfide) and diethyldithiocarbamate on the bladder toxicity and antitumor activity of cyclophosphamide in mice. *Cancer Res* **42**, 4490-4494 (1982).

- 147 Bodenner, D. L., Dedon, P. C., Keng, P. C., Katz, J. C. & Borch, R. F. Selective protection against cis-diamminedichloroplatinum(II)-induced toxicity in kidney, gut, and bone marrow by diethyldithiocarbamate. *Cancer Res* **46**, 2751-2755 (1986).
- 148 Bouvet, D., Michalowicz, A., Crauste-Manciet, S., Brossard, D. & Provost, K. EXAFS and IR structural study of platinum-based anticancer drugs' degradation by diethyl dithiocarbamate. *Inorg Chem* **45**, 3393-3398 (2006).
- 149 Basinger, M. A. *et al.* Dithiocarbamate-induced biliary platinum excretion and the control of cis-platinum nephrotoxicity. *Toxicol Appl Pharmacol* **97**, 279-288 (1989).
- 150 Kast, R. E. & Belda-Iniesta, C. Suppressing glioblastoma stem cell function by aldehyde dehydrogenase inhibition with chloramphenicol or disulfiram as a new treatment adjunct: an hypothesis. *Curr Stem Cell Res Ther* **4**, 314-317 (2009).
- 151 Reya, T., Morrison, S. J., Clarke, M. F. & Weissman, I. L. Stem cells, cancer, and cancer stem cells. *Nature* **414**, 105-111 (2001).
- 152 Guo, R., Zhong, L. & Ren, J. Overexpression of aldehyde dehydrogenase-2 attenuates chronic alcohol exposure-induced apoptosis, change in Akt and Pim signalling in liver. *Clinical and Experimental Pharmacology and Physiology* **36**, 463-468 (2009).
- 153 Liu, P. *et al.* Cytotoxic effect of disulfiram/copper on human glioblastoma cell lines and ALDH-positive cancer-stem-like cells. *Br J Cancer* **107**, 1488-1497 (2012).
- 154 Lowndes, S. A. & Harris, A. L. The role of copper in tumour angiogenesis. *J Mammary Gland Biol Neoplasia* **10**, 299-310 (2005).
- 155 Finney, L., Vogt, S., Fukai, T. & Glesne, D. Copper and Angiogenesis: Unravelling a Relationship Key to Cancer Progression. *Clinical and Experimental Pharmacology and Physiology* **36**, 88-94 (2009).
- 156 Shiah, S. G., Kao, Y. R., Wu, F. Y. H. & Wu, C. W. Inhibition of invasion and angiogenesis by zinc-chelating agent disulfiram. *Molecular Pharmacology* **64**, 1076-1084 (2003).
- 157 Murai, R. *et al.* A novel screen using the Reck tumor suppressor gene promoter detects both conventional and metastasis-suppressing anticancer drugs. *Oncotarget* **1**, 252-264 (2010).
- 158 van der Jagt, M. F. *et al.* Correlation of reversion-inducing cysteine-rich protein with kazal motifs (RECK) and extracellular matrix metalloproteinase inducer (EMMPRIN), with MMP-2, MMP-9, and survival in colorectal cancer. *Cancer Lett* **237**, 289-297 (2006).
- 159 Chen, L. & Madura, K. Increased proteasome activity, ubiquitin-conjugating enzymes, and eEF1A translation factor detected in breast cancer tissue. *Cancer Res* **65**, 5599-5606 (2005).

- 160 Ren, S. *et al.* The p44S10 locus, encoding a subunit of the proteasome regulatory particle, is amplified during progression of cutaneous malignant melanoma. *Oncogene* **19**, 1419-1427 (2000).
- 161 Faiman, M. D., Jensen, J. C. & Lacoursiere, R. B. Elimination Kinetics of Disulfiram in Alcoholics after Single and Repeated Doses. *Clinical Pharmacology & Therapeutics* **36**, 520-526 (1984).
- 162 Stromme, J. H. Effects of diethyldithiocarbamate and disulfiram on glucose metabolism and glutathione content of human erythrocytes. *Biochem Pharmacol* **12**, 705-715 (1963).
- 163 Sauna, Z. E., Shukla, S. & Ambudkar, S. V. Disulfiram, an old drug with new potential therapeutic uses for human cancers and fungal infections. *Molecular Biosystems* **1**, 127-134 (2005).
- 164 Madan, A., Parkinson, A. & Faiman, M. D. Identification of the Human and Rat P450 Enzymes Responsible for the Sulfoxidation of S-Methyl N,N-Diethylthiolcarbamate (Detc-Me) - the Terminal Step in the Bioactivation of Disulfiram. *Drug Metabolism and Disposition* **23**, 1153-1162 (1995).
- 165 Eneanya, D. I., Bianchine, J. R., Duran, D. O. & Andresen, B. D. The Actions and Metabolic-Fate of Disulfiram. *Annual Review of Pharmacology and Toxicology* **21**, 575-596 (1981).
- 166 Rainey, J. M. Disulfiram Toxicity and Carbon-Disulfide Poisoning. *American Journal of Psychiatry* **134**, 371-378 (1977).
- 167 Bjornsson, E., Jerlstad, P., Bergqvist, A. & Olsson, R. Fulminant drug-induced hepatic failure leading to death or liver transplantation in Sweden. *Scandinavian Journal of Gastroenterology* **40**, 1095-1101 (2005).
- 168 Bessero, A. C., Daeopen, J. B. & Borruat, F. X. Optic neuropathy while taking disulfiram. *Journal Francais D Ophtalmologie* **29**, 924-928 (2006).
- 169 Borrett, D., Ashby, P., Bilbao, J. & Carlen, P. Reversible, Late-Onset Disulfiram-Induced Neuropathy and Encephalopathy. *Annals of Neurology* **17**, 396-399 (1985).
- 170 Filosto, M. *et al.* Disulfiram neuropathy: Two cases of distal axonopathy. *Clinical Toxicology* **46**, 314-316 (2008).
- 171 Fisher, C. M. Catatonia Due to Disulfiram Toxicity. *Archives of Neurology* **46**, 798-804 (1989).
- 172 Schmuecker, J. D., Meloy, J. R. & Williams, D. J. Disulfiram Toxicity and Catatonia in a Forensic Outpatient. *American Journal of Psychiatry* **149**, 1275-1276 (1992).
- 173 Wise, J. D. Disulfiram toxicity--a review of the literature. *J Ark Med Soc* **78**, 87-92 (1981).

- 174 Dupuy, O. *et al.* Disulfiram Toxicity - Report of 3 Cases. *Revue De Medecine Interne* **16**, 67-72 (1995).
- 175 Paul, S. M. *et al.* How to improve R&D productivity: the pharmaceutical industry's grand challenge. *Nature Reviews Drug Discovery* **9**, 203-214 (2010).
- 176 DiMasi, J. A., Hansen, R. W. & Grabowski, H. G. The price of innovation: new estimates of drug development costs. *Journal of Health Economics* **22**, 151-185 (2003).
- 177 Fojo, T. & Grady, C. Re: How Much Is Life Worth: Cetuximab, Non-Small Cell Lung Cancer, and the \$440 Billion Question Response. *Journal of the National Cancer Institute* **102**, 1207-U1121 (2009).
- 178 Cvek, B. Nonprofit drugs as the salvation of the world's healthcare systems: the case of Antabuse (disulfiram). *Drug Discov Today* (2012).
- 179 Kona, F. R., Buac, D. & Burger, A. M. Disulfiram, and disulfiram derivatives as novel potential anticancer drugs targeting the ubiquitin-proteasome system in both preclinical and clinical studies. *Curr Cancer Drug Targets* **11**, 338-346 (2011).
- 180 Vanbekkum, D. W. The Protective Action of Dithiocarbamates against the Lethal Effects of X-Irradiation in Mice. *Acta Physiologica Et Pharmacologica Neerlandica* **4**, 508-523 (1956).
- 181 Nemavarkar, P., Chourasia, B. K. & Pasupathy, K. Evaluation of radioprotective action of compounds using *Saccharomyces cerevisiae*. *J Environ Pathol Toxicol Oncol* **23**, 145-151 (2004).
- 182 Taylor, R. D., Maners, A. W., Salari, H., Baker, M. & Walker, E. M. Disulfiram as a Radiation Modifier. *Annals of Clinical and Laboratory Science* **16**, 443-449 (1986).
- 183 Evans, R. G., Engel, C., Wheatley, C. & Nielsen, J. Modification of the sensitivity and repair of potentially lethal damage by diethyldithiocarbamate during and following exposure of plateau-phase cultures of mammalian cells to radiation and cis-diamminedichloroplatinum(II). *Cancer Res* **42**, 3074-3078 (1982).
- 184 Rencova, J. *et al.* Reduction of subacute lethal radiotoxicity of polonium-210 in rats by chelating agents. *Int J Radiat Biol* **72**, 341-348 (1997).
- 185 Gandhi, N. M., Gopaldaswamy, U. V. & Nair, C. K. K. Radiation Protection by Disulfiram: Protection of membrane and DNA in vitro and in vivo against gamma-radiation. *Journal of Radiation Research* **44**, 255-259 (2003).
- 186 Kent, C. R. H. & Blekkenhorst, G. H. In vivo Radiosensitization by Diethyldithiocarbamate. *Radiation Research* **116**, 539-546 (1988).
- 187 Lin, P. S., Kwock, L. & Butterfield, C. E. Diethyldithiocarbamate Enhancement of Radiation and Hyperthermic Effects on Chinese-Hamster Cells In vitro. *Radiation Research* **77**, 501-511 (1979).

- 188 Stone, D., Lin, P. S. & Kwock, L. Radiosensitization of Human Erythrocytes by Diethyldithiocarbamate. *International Journal of Radiation Biology* **33**, 393-396 (1978).
- 189 Westman, G. & Marklund, S. L. Diethyldithiocarbamate, a Superoxide-Dismutase Inhibitor, Decreases the Radioresistance of Chinese-Hamster Cells. *Radiation Research* **83**, 303-311 (1980).
- 190 Eldjarn, L. *Sulfhydryl-disulfide protection mechanisms and the isolation of a possible target structure from mammalian cell nuclei.*, (1965).
- 191 Hospers, G. A., Eisenhauer, E. A. & de Vries, E. G. The sulfhydryl containing compounds WR-2721 and glutathione as radio- and chemoprotective agents. A review, indications for use and prospects. *Br J Cancer* **80**, 629-638 (1999).
- 192 Evans, R. G., Nielsen, J., Engel, C. & Wheatley, C. Enhancement of heat sensitivity and modification of repair of potentially lethal heat damage in plateau-phase cultures of mammalian cells by diethyldithiocarbamate. *Radiat Res* **93**, 319-325 (1983).
- 193 Evans, R. G., Engel, C. R., Wheatley, C. L., Nielsen, J. R. & Ciborowski, L. J. An in vivo study of the radioprotective effect of diethyldithiocarbamate (DDC). *Int J Radiat Oncol Biol Phys* **9**, 1635-1640 (1983).
- 194 Thomas, P. A., Fisenne, I., Chorney, D., Baweja, A. S. & Tracy, B. L. Human absorption and retention of polonium-210 from caribou meat. *Radiation Protection Dosimetry* **97**, 241-250 (2001).
- 195 Lovborg, H. *et al.* Inhibition of proteasome activity, nuclear factor-KappaB translocation and cell survival by the antialcoholism drug disulfiram. *Int J Cancer* **118**, 1577-1580 (2006).
- 196 Rivett, A. J. & Hearn, A. R. Proteasome function in antigen presentation: immunoproteasome complexes, Peptide production, and interactions with viral proteins. *Curr Protein Pept Sci* **5**, 153-161 (2004).
- 197 Bader, M. & Steller, H. Regulation of cell death by the ubiquitin-proteasome system. *Curr Opin Cell Biol* **21**, 878-884 (2009).
- 198 Liu, C. H., Goldberg, A. L. & Qiu, X. B. New insights into the role of the ubiquitin-proteasome pathway in the regulation of apoptosis. *Chang Gung Med J* **30**, 469-479 (2007).
- 199 Pahl, H. L. Activators and target genes of Rel/NF-kappa B transcription factors. *Oncogene* **18**, 6853-6866 (1999).
- 200 Li, N. & Karin, M. Is NF-kappaB the sensor of oxidative stress? *Faseb J* **13**, 1137-1143 (1999).
- 201 Mayo, M. W. & Baldwin, A. S. The transcription factor NF-kappaB: control of oncogenesis and cancer therapy resistance. *Biochim Biophys Acta* **1470**, M55-62 (2000).

- 202 Nakanishi, C. & Toi, M. Nuclear factor-kappaB inhibitors as sensitizers to anticancer drugs. *Nat Rev Cancer* **5**, 297-309 (2005).
- 203 Wang, C. Y., Cusack, J. C., Jr., Liu, R. & Baldwin, A. S., Jr. Control of inducible chemoresistance: enhanced anti-tumor therapy through increased apoptosis by inhibition of NF-kappaB. *Nat Med* **5**, 412-417 (1999).
- 204 Forman, H. J., York, J. L. & Fisher, A. B. Mechanism for the Potentiation of Oxygen-Toxicity by Disulfiram. *Journal of Pharmacology and Experimental Therapeutics* **212**, 452-455 (1980).
- 205 Cen, D. Z., Brayton, D., Shahandeh, B., Meyskens, F. L. & Farmer, P. J. Disulfiram facilitates intracellular Cu uptake and induces apoptosis in human melanoma cells. *Journal of Medicinal Chemistry* **47**, 6914-6920 (2004).
- 206 Wickström, M. *et al.* Pharmacological profiling of disulfiram using human tumor cell lines and human tumor cells from patients. *Biochemical Pharmacology* **73**, 25-33 (2007).
- 207 Pang, H., Chen, D., Cui, Q. C. & Dou, Q. P. Sodium diethyldithiocarbamate, an AIDS progression inhibitor and a copper-binding compound, has proteasome-inhibitory and apoptosis-inducing activities in cancer cells. *Int J Mol Med* **19**, 809-816 (2007).
- 208 Iljin, K. *et al.* High-throughput cell-based screening of 4910 known drugs and drug-like small molecules identifies disulfiram as an inhibitor of prostate cancer cell growth. *Clin Cancer Res* **15**, 6070-6078 (2009).
- 209 Zhang, H. *et al.* Disulfiram treatment facilitates phosphoinositide 3-kinase inhibition in human breast cancer cells in vitro and in vivo. *Cancer Res* **70**, 3996-4004 (2010).
- 210 (NIOSH), T. N. I. f. O. S. a. H. (1995).
- 211 Camakaris, J., Voskoboinik, I. & Mercer, J. F. Molecular mechanisms of copper homeostasis. *Biochem Biophys Res Commun* **261**, 225-232 (1999).
- 212 Brenner, A. J. & Harris, E. D. A quantitative test for copper using bicinchoninic acid. *Anal Biochem* **226**, 80-84 (1995).
- 213 Oh da, H. *et al.* Fetal bovine serum requirement for pyrrolidine dithiocarbamate-induced apoptotic cell death of MCF-7 breast tumor cells. *Eur J Pharmacol* **649**, 135-139 (2010).
- 214 Chou, T. C. Theoretical basis, experimental design, and computerized simulation of synergism and antagonism in drug combination studies. *Pharmacol Rev* **58**, 621-681 (2006).
- 215 Neshasteh-Riz, A. *et al.* Incorporation of iododeoxyuridine in multicellular glioma spheroids: implications for DNA-targeted radiotherapy using Auger electron emitters. *Br J Cancer* **75**, 493-499 (1997).

- 216 Mosmann, T. Rapid colorimetric assay for cellular growth and survival: application to proliferation and cytotoxicity assays. *J Immunol Methods* **65**, 55-63 (1983).
- 217 Chou, T. C. & Talalay, P. Quantitative-Analysis of Dose-Effect Relationships - the Combined Effects of Multiple-Drugs or Enzyme-Inhibitors. *Advances in Enzyme Regulation* **22**, 27-55 (1984).
- 218 Riccardi, C. & Nicoletti, I. Analysis of apoptosis by propidium iodide staining and flow cytometry. *Nature Protocols* **1**, 1458-1461 (2006).
- 219 Rae, C. *et al.* The role of copper in disulfiram-induced toxicity and radiosensitization of cancer cells. *J Nucl Med* **54**, 953-960 (2013).
- 220 Xiao, Z., Loughlin, F., George, G. N., Howlett, G. J. & Wedd, A. G. C-terminal domain of the membrane copper transporter Ctr1 from *Saccharomyces cerevisiae* binds four Cu(I) ions as a cuprous-thiolate polynuclear cluster: sub-femtomolar Cu(I) affinity of three proteins involved in copper trafficking. *J Am Chem Soc* **126**, 3081-3090 (2004).
- 221 Li, L., Yang, H., Chen, D., Cui, C. & Dou, Q. P. Disulfiram promotes the conversion of carcinogenic cadmium to a proteasome inhibitor with pro-apoptotic activity in human cancer cells. *Toxicol Appl Pharmacol* **229**, 206-214 (2008).
- 222 Adams, J. *et al.* Proteasome inhibitors: a novel class of potent and effective antitumor agents. *Cancer Res* **59**, 2615-2622 (1999).
- 223 Kaldis, P. & Reed, S. in *Cell Cycle Regulation Vol. 42 Results and Problems in Cell Differentiation* 147-181 (Springer Berlin Heidelberg, 2006).
- 224 Garba, I. H., Ubom, G. A. & Ejiogu, N. B. Serum copper concentration in adults with acute, uncomplicated falciparum malaria infection. *Biol Trace Elem Res* **113**, 125-130 (2006).
- 225 Moreno, T., Artacho, R., Navarro, M., Perez, A. & Ruiz-Lopez, M. D. Serum copper concentration in HIV-infection patients and relationships with other biochemical indices. *Sci Total Environ* **217**, 21-26 (1998).
- 226 Sullivan, J. F., Blotcky, A. J., Jetton, M. M., Hahn, H. K. & Burch, R. E. Serum levels of selenium, calcium, copper magnesium, manganese and zinc in various human diseases. *J Nutr* **109**, 1432-1437 (1979).
- 227 Bernier, J. L., Henichart, J. P. & Catteau, J. P. Design, synthesis and DNA-binding capacity of a new peptidic bifunctional intercalating agent. *Biochem J* **199**, 479-484 (1981).
- 228 Kirshner, J. R. *et al.* Elesclomol induces cancer cell apoptosis through oxidative stress. *Mol Cancer Ther* **7**, 2319-2327 (2008).

- 229 Wu, L., Zhou, L., Liu, D. Q., Vogt, F. G. & Kord, A. S. LC-MS/MS and density functional theory study of copper(II) and nickel(II) chelating complexes of elesclomol (a novel anticancer agent). *J Pharm Biomed Anal* **54**, 331-336 (2011).
- 230 Bonvini, P., Zorzi, E., Basso, G. & Rosolen, A. Bortezomib-mediated 26S proteasome inhibition causes cell-cycle arrest and induces apoptosis in CD-30+ anaplastic large cell lymphoma. *Leukemia* **21**, 838-842 (2007).
- 231 Ford, E. S. Serum copper concentration and coronary heart disease among US adults. *Am J Epidemiol* **151**, 1182-1188 (2000).
- 232 Squitti, R. *et al.* Ceruloplasmin (2-D PAGE) Pattern and Copper Content in Serum and Brain of Alzheimer Disease Patients. *Biomark Insights* **1**, 205-213 (2007).
- 233 Masuoka, J., Hegenauer, J., Van Dyke, B. R. & Saltman, P. Intrinsic stoichiometric equilibrium constants for the binding of zinc(II) and copper(II) to the high affinity site of serum albumin. *J Biol Chem* **268**, 21533-21537 (1993).
- 234 Johansson, B. Plasma protein binding of disulfiram and its metabolite diethylthiocarbamic acid methyl ester. *J Pharm Pharmacol* **42**, 806-807 (1990).
- 235 Hall, E. J. *Radiobiology for the Radiologist*. 6th edn, (Lippincott Williams & Wilkins, 2006).
- 236 Bleau, B. L. *Forgotten algebra*. 3rd edn, (Barron's Educationnal Series, Inc., 2003).
- 237 Cramp, W. A. Radiosensitization by copper ions, and consequent reversal of the oxygen effect. *Nature* **206**, 636-637 (1965).
- 238 Adams, G. E. Chemical Radiosensitization of Hypoxic Cells. *British Medical Bulletin* **29**, 48-53 (1973).
- 239 Bishop-Bailey, D. Tumour vascularisation: a druggable target. *Curr Opin Pharmacol* **9**, 96-101 (2009).
- 240 Fenton, B. M., Paoni, S. F., Lee, J., Koch, C. J. & Lord, E. M. Quantification of tumour vasculature and hypoxia by immunohistochemical staining and HbO<sub>2</sub> saturation measurements. *Br J Cancer* **79**, 464-471 (1999).
- 241 Hwang, A. & Muschel, R. J. Radiation and the G<sub>2</sub> phase of the cell cycle. *Radiat Res* **150**, S52-59 (1998).
- 242 Shin, J. S. *et al.* Serum starvation induces G<sub>1</sub> arrest through suppression of Skp2-CDK2 and CDK4 in SK-OV-3 cells. *Int J Oncol* **32**, 435-439 (2008).
- 243 Foijer, F. *et al.* Oncogenic pathways impinging on the G<sub>2</sub>-restriction point. *Oncogene* **27**, 1142-1154 (2008).
- 244 Kues, W. A. *et al.* Cell cycle synchronization of porcine fetal fibroblasts: effects of serum deprivation and reversible cell cycle inhibitors. *Biol Reprod* **62**, 412-419 (2000).

- 245 Yoshida, M. & Beppu, T. Reversible arrest of proliferation of rat 3Y1 fibroblasts in both the G1 and G2 phases by trichostatin A. *Exp Cell Res* **177**, 122-131 (1988).
- 246 Bunz, F. *et al.* Requirement for p53 and p21 to sustain G2 arrest after DNA damage. *Science* **282**, 1497-1501 (1998).
- 247 Kaufmann, W. K. & Paules, R. S. DNA damage and cell cycle checkpoints. *Faseb J* **10**, 238-247 (1996).
- 248 Tomita, M. Involvement of DNA-PK and ATM in radiation- and heat-induced DNA damage recognition and apoptotic cell death. *J Radiat Res* **51**, 493-501 (2010).
- 249 Vakifahmetoglu, H., Olsson, M. & Zhivotovsky, B. Death through a tragedy: mitotic catastrophe. *Cell Death Differ* **15**, 1153-1162 (2008).
- 250 Monazzam, A. *et al.* Application of the multicellular tumour spheroid model to screen PET tracers for analysis of early response of chemotherapy in breast cancer. *Breast Cancer Res* **9**, R45 (2007).
- 251 Harma, V. *et al.* A comprehensive panel of three-dimensional models for studies of prostate cancer growth, invasion and drug responses. *PLoS One* **5**, e10431 (2010).
- 252 Gati, I., Bergstrom, M., Muhr, C., Langstrom, B. & Carlsson, J. Application of (methyl-11C)-methionine in the multicellular spheroid system. *J Nucl Med* **32**, 2258-2265 (1991).
- 253 Olabiran, Y. *et al.* The selection of antibodies for targeted therapy of small-cell lung cancer (SCLC) using a human tumour spheroid model to compare the uptake of cluster 1 and cluster w4 antibodies. *Br J Cancer* **69**, 247-252 (1994).
- 254 Durand, R. E. Cellular oxygen utilization and radiation response of V-79 spheroids. *Adv Exp Med Biol* **159**, 419-434 (1983).
- 255 Acker, H., Holtermann, G., Bolling, B. & Carlsson, J. Influence of glucose on metabolism and growth of rat glioma cells (C6) in multicellular spheroid culture. *Int J Cancer* **52**, 279-285 (1992).
- 256 Walenta, S., Doetsch, J., Mueller-Klieser, W. & Kunz-Schughart, L. A. Metabolic imaging in multicellular spheroids of oncogene-transfected fibroblasts. *J Histochem Cytochem* **48**, 509-522 (2000).
- 257 Kwok, T. T. & Twentyman, P. R. The relationship between tumour geometry and the response of tumour cells to cytotoxic drugs--an in vitro study using EMT6 multicellular spheroids. *Int J Cancer* **35**, 675-682 (1985).
- 258 Durand, R. E. Chemosensitivity testing in V79 spheroids: drug delivery and cellular microenvironment. *J Natl Cancer Inst* **77**, 247-252 (1986).

- 259 Teicher, B. A., Kowal, C. D., Kennedy, K. A. & Sartorelli, A. C. Enhancement by hyperthermia of the in vitro cytotoxicity of mitomycin C toward hypoxic tumor cells. *Cancer Res* **41**, 1096-1099 (1981).
- 260 Thomlinson, R. H. & Gray, L. H. The Histological Structure of Some Human Lung Cancers and the Possible Implications for Radiotherapy. *British Journal of Cancer* **9**, 539-549 (1955).
- 261 West, C. M. Size-dependent resistance of human tumour spheroids to photodynamic treatment. *Br J Cancer* **59**, 510-514 (1989).
- 262 West, C. M., Sandhu, R. R. & Stratford, I. J. The radiation response of V79 and human tumour multicellular spheroids--cell survival and growth delay studies. *Br J Cancer* **50**, 143-151 (1984).
- 263 Rofstad, E. K. & Sutherland, R. M. Growth and radiation sensitivity of the MLS human ovarian carcinoma cell line grown as multicellular spheroids and xenografted tumours. *Br J Cancer* **59**, 28-35 (1989).
- 264 Kunz-Schughart, L. A., Freyer, J. P., Hofstaedter, F. & Ebner, R. The use of 3-D cultures for high-throughput screening: the multicellular spheroid model. *J Biomol Screen* **9**, 273-285 (2004).
- 265 West, G. W., Weichselbaum, R. & Little, J. B. Limited penetration of methotrexate into human osteosarcoma spheroids as a proposed model for solid tumor resistance to adjuvant chemotherapy. *Cancer Res* **40**, 3665-3668 (1980).
- 266 Oktem, G. *et al.* Effect of apoptosis and response of extracellular matrix proteins after chemotherapy application on human breast cancer cell spheroids. *Oncol Rep* **15**, 335-340 (2006).
- 267 Walker, K. A. *et al.* A tumour spheroid model for antibody-targeted therapy of micrometastases. *Br J Cancer* **58**, 13-16 (1988).
- 268 Emfietzoglou, D. *et al.* Liposome-mediated radiotherapeutics within avascular tumor spheroids: comparative dosimetry study for various radionuclides, liposome systems, and a targeting antibody. *J Nucl Med* **46**, 89-97 (2005).
- 269 Gaze, M. N., Mairs, R. J., Boyack, S. M., Wheldon, T. E. & Barrett, A. 131I-meta-iodobenzylguanidine therapy in neuroblastoma spheroids of different sizes. *Br J Cancer* **66**, 1048-1052 (1992).
- 270 Twentyman, P. R. Growth delay in small EMT6 spheroids induced by cytotoxic drugs and its modification by misonidazole pretreatment under hypoxic conditions. *Br J Cancer* **45**, 565-570 (1982).

- 271 Ballangrud, A. M., Yang, W. H., Dnistrian, A., Lampen, N. M. & Sgouros, G. Growth and characterization of LNCaP prostate cancer cell spheroids. *Clinical Cancer Research* **5**, 3171S-3176S (1999).
- 272 Yuhas, J. M., Li, A. P., Martinez, A. O. & Ladman, A. J. Simplified Method for Production and Growth of Multicellular Tumor Spheroids. *Cancer Research* **37**, 3639-3643 (1977).
- 273 Varghese, A. J., Gulyas, S. & Mohindra, J. K. Hypoxia-dependent reduction of 1-(2-nitro-1-imidazolyl)-3-methoxy-2-propanol by Chinese hamster ovary cells and KHT tumor cells in vitro and in vivo. *Cancer Res* **36**, 3761-3765 (1976).
- 274 H. G. Burkitt, B. Y., J. W. Heath. *Wheater's functional histology*. (1993).
- 275 Freshney, R. I. *Culture of animal cells. A manual of basic technique*. (Alan R. Liss, Inc., 1983).
- 276 Twentyman, P. R., Watson, J. V., Bleehen, N. M. & Rowles, P. M. Changes in cell proliferation kinetics occurring during the life history of monolayer cultures of a mouse tumour cell line. *Cell Tissue Kinet* **8**, 41-50 (1975).
- 277 Twentyman, P. R. & Bleehen, N. M. Changes in sensitivity to cytotoxic agents occurring during the life history of monolayer cultures of a mouse tumour cell line. *Br J Cancer* **31**, 417-423 (1975).
- 278 Kwok, T. T. & Twentyman, P. R. Effects of changes in oxygen tension, pH, and glucose concentration on the response to CCNU of EMT6 mouse tumor monolayer cells and multicellular spheroids. *Int J Radiat Oncol Biol Phys* **14**, 1221-1229 (1988).
- 279 Horoszewicz, J. S. *et al.* Lncap Model of Human Prostatic-Carcinoma. *Cancer Research* **43**, 1809-1818 (1983).
- 280 Singh, P. & Roberts, M. S. Local deep tissue penetration of compounds after dermal application: structure-tissue penetration relationships. *J Pharmacol Exp Ther* **279**, 908-917 (1996).
- 281 Yamada, K. *et al.* Concurrent use of Sr-89 chloride with zoledronic acid is safe and effective for breast cancer patients with painful bone metastases. *Exp Ther Med* **3**, 226-230 (2012).
- 282 Lewington, V. J. Cancer therapy using bone-seeking isotopes. *Phys Med Biol* **41**, 2027-2042 (1996).
- 283 Mairs, R. J., Gaze, M. N. & Barrett, A. The Uptake and Retention of Metaiodobenzyl Guanidine by the Neuroblastoma Cell-Line Nb1-G. *British Journal of Cancer* **64**, 293-295 (1991).

- 284 Bradford, M. M. A rapid and sensitive method for the quantitation of microgram quantities of protein utilizing the principle of protein-dye binding. *Anal Biochem* **72**, 248-254 (1976).
- 285 Tietze, C., Schlesinger, P. & Stahl, P. Chloroquine and ammonium ion inhibit receptor-mediated endocytosis of mannose-glycoconjugates by macrophages: apparent inhibition of receptor recycling. *Biochem Biophys Res Commun* **93**, 1-8 (1980).
- 286 Tiffany, C. W., Lapidus, R. G., Merion, A., Calvin, D. C. & Slusher, B. S. Characterization of the enzymatic activity of PSM: comparison with brain NAALADase. *Prostate* **39**, 28-35 (1999).
- 287 Bergonie, J. & Tribondeau, L. Interpretation of some results from radiotherapy and an attempt to determine a rational treatment technique. 1906. *Yale J Biol Med* **76**, 181-182 (2003).
- 288 Vassilev, L. T. *et al.* In vivo activation of the p53 pathway by small-molecule antagonists of MDM2. *Science* **303**, 844-848 (2004).
- 289 Fei, P. & El-Deiry, W. S. P53 and radiation responses. *Oncogene* **22**, 5774-5783 (2003).
- 290 Cao, C. *et al.* Radiosensitization of lung cancer by nutlin, an inhibitor of murine double minute 2. *Mol Cancer Ther* **5**, 411-417 (2006).
- 291 Menear, K. A. *et al.* 4-[3-(4-cyclopropanecarbonylpiperazine-1-carbonyl)-4-fluorobenzyl]-2H-phthalazin-1-one: a novel bioavailable inhibitor of poly(ADP-ribose) polymerase-1. *J Med Chem* **51**, 6581-6591 (2008).
- 292 Loser, D. A. *et al.* Sensitization to radiation and alkylating agents by inhibitors of poly(ADP-ribose) polymerase is enhanced in cells deficient in DNA double-strand break repair. *Mol Cancer Ther* **9**, 1775-1787 (2010).
- 293 Zabudoff, S. D. *et al.* AZD7762, a novel checkpoint kinase inhibitor, drives checkpoint abrogation and potentiates DNA-targeted therapies. *Mol Cancer Ther* **7**, 2955-2966 (2008).
- 294 Mitchell, J. B. *et al.* In vitro and in vivo radiation sensitization of human tumor cells by a novel checkpoint kinase inhibitor, AZD7762. *Clin Cancer Res* **16**, 2076-2084 (2010).
- 295 Vance, S. *et al.* Selective radiosensitization of p53 mutant pancreatic cancer cells by combined inhibition of Chk1 and PARP1. *Cell Cycle* **10**, 4321-4329 (2011).
- 296 Wall, M. E. *et al.* Plant Antitumor Agents. I. The Isolation and Structure of Camptothecin, a Novel Alkaloidal Leukemia and Tumor Inhibitor from *Camptotheca acuminata*. *J. Am. Chem. Soc.* **88**, 3888-3890 (1966).
- 297 Rothenberg, M. L. Topoisomerase I inhibitors: Review and update. *Annals of Oncology* **8**, 837-855 (1997).

- 298 Hedde, J. P. *et al.* A phase I/II trial of topotecan and radiation therapy for brain metastases in patients with solid tumors. *Int J Radiat Oncol Biol Phys* **68**, 839-844 (2007).
- 299 McCluskey, A. G., Boyd, M., Gaze, M. N. & Mairs, R. J. [I-131]MIBG and topotecan: A rationale for combination therapy for neuroblastoma. *Cancer Letters* **228**, 221-227 (2005).
- 300 Blackburn, C. *et al.* Characterization of a new series of non-covalent proteasome inhibitors with exquisite potency and selectivity for the 20S beta5-subunit. *Biochem J* **430**, 461-476 (2010).
- 301 Lee, S. J., Dimtchev, A., Lavin, M. F., Dritschilo, A. & Jung, M. A novel ionizing radiation-induced signaling pathway that activates the transcription factor NF-kappa B. *Oncogene* **17**, 1821-1826 (1998).
- 302 Tamatani, T. *et al.* Bortezomib-enhanced radiosensitization through the suppression of radiation-induced nuclear factor-kappaB activity in human oral cancer cells. *Int J Oncol* **42**, 935-944 (2013).
- 303 Jacquemont, C. & Taniguchi, T. Proteasome function is required for DNA damage response and fanconi anemia pathway activation. *Cancer Res* **67**, 7395-7405 (2007).
- 304 Forouzannia, A. *et al.* A phase I study of Topotecan, as a radiosensitizer, for thoracic malignancies. *Lung Cancer* **44**, 111-119 (2004).
- 305 Morgan, R. J. *et al.* Plasma and cerebrospinal fluid pharmacokinetics of topotecan in a phase I trial of topotecan, tamoxifen, and carboplatin, in the treatment of recurrent or refractory brain or spinal cord tumors. *Cancer Chemother Pharmacol* **66**, 927-933 (2010).
- 306 Verweij, J. *et al.* Phase I and pharmacokinetics study of topotecan, a new topoisomerase I inhibitor. *Ann Oncol* **4**, 673-678 (1993).
- 307 Sparidans, R. W. *et al.* Liquid chromatography-tandem mass spectrometric assay for the PARP-1 inhibitor olaparib in combination with the nitrogen mustard melphalan in human plasma. *J Chromatogr B Analyt Technol Biomed Life Sci* **879**, 1851-1856 (2011).
- 308 Rajan, A. *et al.* A phase I combination study of olaparib with cisplatin and gemcitabine in adults with solid tumors. *Clin Cancer Res* **18**, 2344-2351 (2012).
- 309 Yamamoto, N. *et al.* A Phase I, dose-finding and pharmacokinetic study of olaparib (AZD2281) in Japanese patients with advanced solid tumors. *Cancer Sci* **103**, 504-509 (2012).
- 310 Muscal, J. A. *et al.* A phase I trial of vorinostat and bortezomib in children with refractory or recurrent solid tumors: a Children's Oncology Group phase I consortium study (ADV0916). *Pediatr Blood Cancer* **60**, 390-395 (2013).

- 311 Moreau, P. *et al.* Pharmacokinetic, pharmacodynamic and covariate analysis of subcutaneous versus intravenous administration of bortezomib in patients with relapsed multiple myeloma. *Clin Pharmacokinet* **51**, 823-829 (2012).
- 312 Grubbs, F. E. Procedures for Detecting Outlying Observations in Samples. *Technometrics* **11**, 1-21 (1969).
- 313 Logan, I. R. *et al.* Analysis of the MDM2 antagonist nutlin-3 in human prostate cancer cells. *Prostate* **67**, 900-906 (2007).
- 314 Arya, A. K. *et al.* Nutlin-3, the small-molecule inhibitor of MDM2, promotes senescence and radiosensitises laryngeal carcinoma cells harbouring wild-type p53. *Br J Cancer* **103**, 186-195 (2010).
- 315 Supiot, S., Hill, R. P. & Bristow, R. G. Nutlin-3 radiosensitizes hypoxic prostate cancer cells independent of p53. *Mol Cancer Ther* **7**, 993-999 (2008).
- 316 Cao, C. *et al.* Radiosensitization of lung cancer by nutlin, an inhibitor of murine double minute 2. *Mol Cancer Ther* **5**, 411-417 (2006).
- 317 Miura, K. *et al.* The combination of olaparib and camptothecin for effective radiosensitization. *Radiat Oncol* **7**, 62 (2012).
- 318 Senra, J. M. *et al.* Inhibition of PARP-1 by olaparib (AZD2281) increases the radiosensitivity of a lung tumor xenograft. *Mol Cancer Ther* **10**, 1949-1958 (2011).
- 319 McCluskey, A. G. *et al.* [<sup>131</sup>I]meta-iodobenzylguanidine and topotecan combination treatment of tumors expressing the noradrenaline transporter. *Clin Cancer Res* **11**, 7929-7937 (2005).
- 320 Rave-Frank, M. *et al.* Combined effect of topotecan and irradiation on the survival and the induction of chromosome aberrations in vitro. *Strahlenther Onkol* **178**, 497-503 (2002).
- 321 Kamer, S., Ren, Q. & Dicker, A. P. Differential radiation sensitization of human cervical cancer cell lines by the proteasome inhibitor velcade (bortezomib, PS-341). *Arch Gynecol Obstet* **279**, 41-46 (2009).
- 322 Carlsson, J., Eriksson, V., Stenerlow, B. & Lundqvist, H. Requirements regarding dose rate and exposure time for killing of tumour cells in beta particle radionuclide therapy. *Eur J Nucl Med Mol Imaging* **33**, 1185-1195 (2006).
- 323 Dale, R. G. Dose-rate effects in targeted radiotherapy. *Phys Med Biol* **41**, 1871-1884 (1996).
- 324 McCluskey, A. G. *et al.* Inhibition of poly(ADP-Ribose) polymerase enhances the toxicity of <sup>131</sup>I-metaiodobenzylguanidine/topotecan combination therapy to cells and xenografts that express the noradrenaline transporter. *J Nucl Med* **53**, 1146-1154 (2012).

325 Petitjean, A. *et al.* Impact of mutant p53 functional properties on TP53 mutation patterns and tumor phenotype: lessons from recent developments in the IARC TP53 database. *Hum Mutat* **28**, 622-629 (2007).

326 Fairbairn, D. W., Olive, P. L. & O'Neill, K. L. The comet assay: a comprehensive review. *Mutation research* **339**, 37-59 (1995).